Galaxy Number Counts on the Light Cone

Ghosh, Basundhara

UNIVERSITÉ DE GENÈVE
Section de Physique — FACULTÉ DES SCIENCES
Department de Physique Théorique — Professeure Ruth DURRER

Galaxy number counts on the light cone

THÉSE

présentée à la Faculté des sciences de l'Université de Genève
pour obtenir le grade de
Docteur ès sciences, mention physique

par
Basundhara GHOSH
de
Chandannagar (Inde)

Thése N°5457

GENÈVE
Atelier de reproduction de la Section de Physique
2020

Abstract

This thesis aims to explore and emphasise on the significant relativistic contributions to observable galaxy number counts, and can be studied in two parts. The first two chapters deal with the treatment of the total galaxy number counts, without focusing on any particular relativistic contribution. We start by mathematically proving the frame-invariance of galaxy number counts in Einstein and Jordan frames, and then move on to computing the full-sky correlation function and power spectrum including all relativistic effects. From the third chapter onwards, we narrow down our interest to specific effects. The fourth chapter deals with modelling of the angular power spectra in the redshift space and also accounts for the intermediately nonlinear regime. In the fifth and sixth chapters, we establish the importance of including lensing corrections to the main signal of probes such as galaxy-galaxy lensing, and for measurements in case of tests of gravity like E_g statistics, respectively. Finally, we also talk about the shape and size correlations of galaxies occurring as a part of weak lensing data, arising out of the phenomenon of intrinsic alignment.

To my parents

Acknowledgements

First of all I would like to thank my supervisor Prof. Ruth Durrer for her immensely helpful guidance and faith in my abilities. She has been my pillar of strength and has always made herself available for questions and discussions whenever I needed. I also want to thank Prof. Martin Kunz, Prof. Camille Bonvin and Prof. Björn Malte Schäfer for their generous mentorship.

A lot of the credit for the successful completion of my PhD of course goes to my collaborators Ruth Durrer, Camile Bonvin, Vittorio Tansella, Elena Sellentin, Jérémie Francfort, Martin Kunz, Mona Jalilvand, Elisabetta Majerotto, Benjamin Bose and Björn Malte Schäfer.

I also want to thank all of my colleagues for providing the much-needed support and encouragement during my days in Geneva, especially Mona Jalilvand, Jérémie Francfort, Francesca Lepori, Charles Dalang, Farbod Hassani, Pierre Fleury, Viraj Nistane, Goran Jelic-Cizmek, William Matthewson, Lucie Khlat and Joyce Byun. All the interactions I have had with them and the rest of the group members have been very fruitful and uplifting. I thank Jérémie Francfort also for correcting the French introduction to this thesis.

I want to extend my gratitude to my hosts for their hospitality during my visit to their institutes, especially Anthony Challinor, Cora Uhlemann, Alan Heavens, Catherine Heymans, Qianli Xia, Aseem Paranjape, Subhabrata Majumdar and Björn Malte Schäfer.

I am grateful to the department secretaries Francine Gennai-Nicole, Cécile Jaggi-Chevalley and Angela Stark-Sanchez for helping out with bureaucratic requirements.

Finally, I express my gratitude to my parents, Buddhadeb Ghosh and Chitrali Ghosh, for believing in me and providing me with the necessary moral support, and to the other two most important people in my life, Gaurav Pratap Singh and Upasika Ghosh for always being there to boost me up when I faltered with self-doubt.

Jury Members

- Prof. Martin Kunz
  Département de Physique Théorique & Center for Astroparticle Physics, Université de Genève, 24 Quai E. Ansermet, CH-1211 Genève 4, Switzerland
- Prof. Lucas Lombriser
  Département de Physique Théorique & Center for Astroparticle Physics, Université de Genève, 24 Quai E. Ansermet, CH-1211 Genève 4, Switzerland
- Prof. Björn Malte Schäfer
  Zentrum für Astronomie der Universität Heidelberg (ZAH), Philosophenweg 12, Heidelberg, Germany
- Prof. Roy Maartens
  Faculty of Natural Science, University of the Western Cape, Robert Sobukwe Road, Bellville 7535, Republic of South Africa

I would like to thank them all for having accepted to be part of the Jury for my Thesis defense.

List of Publications

The following works have been considered as part of this thesis:

[281] V. Tansella, C. Bonvin, R. Durrer, B. Ghosh, & E. Sellentin, *The full-sky relativistic correlation function and power spectrum of galaxy number counts. Part I: theoretical aspects*, **JCAP 1803** (2018) 019, [arXiv: 1708.00492]

[115] B. Ghosh, R. Durrer, & E. Sellentin, *General Relativistic corrections in density-shear correlations*, **JCAP 1806** (2018) 008, [arXiv: 1801.02518]

[113] B. Ghosh & R. Durrer, *The observable E_g statistics*, **JCAP 1906** (2019) 010, [arXiv: 1812.09546]

[109] J. Francfort, B. Ghosh, & R. Durrer, *Cosmological Number Counts in Einstein and Jordan frames*, **JCAP 1909** (2019) 071, [arXiv: 1907.03606]

[163] M. Jalilvand, B. Ghosh, E. Majerotto, B. Bose, R. Durrer, & M. Kunz, *Non-linear contributions to angular power spectra*, **Phys.Rev.D** 101 (2020), [arXiv: 1907.13109]

[114] B. Ghosh, R. Durrer, & B. M. Schäfer, *Intrinsic and extrinsic correlations of galaxy shapes and sizes in weak lensing data*, [arXiv: 1812.09546]

Résumé

La cosmologie est l'étude de l'Univers dans son ensemble ainsi que des différentes étapes de son évolution conduisant á la forme que nous observons aujourd'hui. Bien que les philosophes et les scientifiques s'intéressent à la compréhension des propriétés des corps célestes depuis l'Antiquité, la cosmologie s'est développée comme un domaine d'étude approprié et scientifique principalement aprés que Einstein a postulé ses théories de la relativité au début des années 1900. Nous comprenons maintenant l'Univers macroscopique et sa dynamique à travers la théorie générale de la relativité, ainsi que les entités au niveau microscopique via le modèle standard de la physique des particules.

Dans le chapitre 1, nous introduisons le sujet général de la cosmologie et expliquons comment son étude a évolué au cours des siècles. Nous mentionnons de manière chronologique les découvertes significatives dans ce domaine et introduisons quelques concepts pertinents pour le reste de cette thèse. Nous discutons d'abord la formation des structures (galaxies) et évoquons brièvement la fonction de corrélation et le spectre de puissance (power spectrum). Nous expliquons ensuite la signification du comptage de galaxies (Galaxy Number Count) et concentrons notre attention sur deux contributions principales à cette quantité : les distorstions dues au décalage vers le rouge (redshift space distorsion) ainsi que l'effet de lentille (weak lensing). Nous introduison ensuite brièvement les théories dites Scalaire-Tenseur (Scalar-Tensor theories), ces dernières étant pertinentes pour décrire l'invariance du comptage des galaxies sous une transformation conforme de référentiel (invariance under conformal change of frames).

Dans le chapitre 2, nous reproduisons la référence [109], et montrons de manière mathématique cette invariance du comptage des galaxies sous une transformation conforme de référentiel. L'importance de ce travail réside dans l'intérêt d'étudier les théories dites de gravité modifiée qui vont au-delà de la théorie de la relativité générale. Dans les théories de type Scalaire-Tenseur, il est possible de passer du référentiel de Einstein à celui de Jordan via une transfromation conforme de la métrique. Nous calculons comment les quantités non-perturbées (background quantities) et comment les perturbations changent sous ce type de transformations. Nous trouvons que, bien que plusieurs sont soit indépendantes de la jauge (gauge-independent) soit indépendantes du rérérentiel (frame-independent), l'observable physique est bien le comptage des galaxies qui est à la fois indépendant de la jauge

et du référentiel.

Dans le chapitre 3, nous reproduisons la référence [281] et calculons ainsi la fonction de corrélation relativiste ciel plein (full-sky relativistic correlation function) et le spectre de puissance, en y incluant tous les effets relativistes, dans une tentative d'aller au-delà de l'approche d'approximation du ciel plat habituellement adoptée. Nous le faisons via deux approches : l'une impliquant le calcul direct de la fonction de corrélation, et l'autre via les spectres de puissance angulaire.

Dans le chapitre 4, nous reproduisons la référence [163], et cherchons une façon de modéliser le spectre de puissance angulaire (angular power spectra) C_ℓ dans le régime non-linéaire mais dans l'espace du décalage vers le rouge. Ce n'est pas chose facile car les méthodes analytiques existantes ne reproduisent pas précisément les résultats numériques qui sont, à ce jour, considérés comme la meilleure approche pour traiter les situations où les non-linéarités sont pertinentes. Nous étudions différentes méthodes perturbatives, en incluant par exemple une correction à une boucle (one-loop correction) et comparons les résultats avec les simulations à N corps (N-body simulations).

Dans le chapitre 5, nous reproduisons la référence [115], et portons notre attention sur l'effet de lentille en insistant sur l'importance des corrections dues à cet effet dans les analyses de type galaxie-galaxie (galaxy-galaxy probes). Nous discutons les contributions additionnelles au signal observé qui sont dues à la présence de matière entre les galaxies et l'observateur, ce qui induit un effet de lentille aditionnel. Nous ajoutons cette contribution au signal principal. Pour motiver nos résultats, nous utilisons un catalogue oùtilisant les *DES redshift bins* avec une distribution gaussienne, et répétons le même exercice pour des décalages vers le rouge plus élevés, qui seront mesurés par Euclid.

Dans le chapitre 6, nous reproduisons la référence [113], et étudions à nouveau les corrections dues à l'effet de lentille mais cette fois-ci pour le cas des statistiques E_g, ce qui constitue un test de la gravité à des échelles cosmologiques. Ces statistiques ne sont valables que dans le régime des perturbations linéaires, mais elles sont tout de même très utiles car elles permettent d'obtenir des mesures qui ne dépendent pas du biais (en supposant que la même population de galaxies est utilisée). Notre travail consiste à implémenter une méthode dans laquelle l'effet de lentille peut être incorporé dans les catalogues usuels et pour lesquels nous pouvons utiliser les spectres observables.

Dans le chapitre 7, nous reproduisons la référence [114], dans laquelle nous avons effectué un pas de plus et analysé les effets astrophysiques supplémentaires sur les lentilles faibles, à savoir les effets d'alignement intrinséque. Ces effets, qui résultent de l'interaction des galaxies avec leurs champs de cisaillement de marée (tidal shear fields) sont en quelque sorte analogues à la lentille elle-même. En étudiant leur contribution au signal total de lentille, décomposée en termes de corrélations de forme et de taille, nous obtenons des informations sur la façon dont il est utile de mesurer la forme, la taille ou les deux en même temps. Nous estimons aussi l'erreur introduite dans de telles mesures. Nous constatons que ces corrélations intrinséques ont les mêmes dépendances de paramétres, et ceci indépendamment du fait que le mécanisme sous-jacent soit la lentille ou l'alignement intrisèque. Nous

avons également constaté que l'estimation de la forme a un meilleur rapport signal sur bruit cumulé que l'estimation de la taille, bien qu'une combinaison des deux ne puisse pas entraîner une amélioration signific des mesures.

Notations

List of symbols used in the thesis

a	scale factor
H	Hubble parameter (H_0 denotes Hubble parameter today)
$\mathcal{H}$	comoving Hubble parameter $\mathcal{H} = aH$
h	reduced Hubble parameter $h = H_0/100$
η, η_0	conformal time (today)
t ,t_0	cosmic time (today)
χ	comoving distance $\chi = \eta_0 - \eta$
z	redshift
$\mathbf{n}$,$\hat{n}$	line-of-sight direction
$\mathbf{r}$	relative position of two objects $\mathbf{r} = \mathbf{x}_1 - \mathbf{x}_2$
Φ, Ψ	Bardeen potentials
δ, δ_m	density/matter density contrast in longitudinal gauge
D_g	gauge-invariant density fluctuation
Δ_g	observable galaxy number counts
$\mathbf{v}(\mathbf{x})$	velocity perturbation in longitudinal gauge
$v(x)$	velocity potential $\mathbf{v} = -\nabla v$
$V(k)$	defined as $v(k) = k^{-1}V(k)$
$D_1(z)$	matter growth function
$f(z)$	velocity growth rate
σ_v	velocity divergence
$P(k)$, $P_m(k)$	redshift-space power spectrum, linear matter power spectrum
$P_{NL}(k)$	non-linear redshift-space power spectrum
$\xi(\theta, z_1, z_2)$	two-point correlation function
$C_\ell(z_1, z_2)$	angular power spectrum
b	galaxy bias
s	magnification bias, change in size (only Chapter 7)
f_{evo}	evolution bias
ψ	lensing potential
κ	convergence
γ_1 and γ_2; γ	shear components; complex shear

ϵ	ellipticity
q_{ab}	second moments of brightness distribution
$\mathcal{P}_\ell(\mathrm{X})$	Legendre polynomials
$Y_{\ell m}(\theta, \phi)$	Spherical harmonics
$J_n(x)$	Bessel functions
$j_\ell(x)$	Spherical Bessel functions
δ_{ij}, δ^D	Kronecker and Dirac delta functions
ϵ_{ijk}	Levi-Civita tensor
Abbreviations	
(Λ)CDM	(Cosmological constant) Cold dark matter
FLRW	Freidmann-Lemaître-Robertson-Walker
GR	General relativity
CMB	Cosmic microwave background
LSS	Large-scale structures
BAO	Baryon acoustic oscillations
RSD	redshift-space distortion
iSW	Integrated Sachs-Wolfe
SPT	Standard perturbation theory
LPT	Lagrangian perturbation theory
EFT	Effective field theory
TNS	Taruya-Nishimichi-Saito

Contents

1

Introduction

> Philosophy [nature] is written in that great book which ever is before our eyes – I mean the universe – but we cannot understand it if we do not first learn the language and grasp the symbols in which it is written. The book is written in mathematical language, and the symbols are triangles, circles and other geometrical figures, without whose help it is impossible to comprehend a single word of it; without which one wanders in vain through a dark labyrinth.
>
> *Galileo Galilei*

Since time immemorial, humankind has been curious in unraveling the mysteries of the Universe. Cosmology as a subject of interest has always been of historical relevance, and any student or researcher in the field today still looks back in awe at the legacy of thinkers who propagated the study of cosmology. Around the 16th century BCE in early Mesopotamia, people came up with the concept of a cosmic ocean, whereby the main element of the universe was water on a flat circular surface, covered and enclosed on the edges by a firmament. Religions have also mentioned their own interpretation of how the Universe was formed. Interestingly, the ancient Hindu text called the *Rig Veda* written around the 12th century BCE has a section called the *Nasadiya Sukta* or the Hymn of Creation, which contemplates about the creation of the Universe, but doesn't provide any answers, through verses that imply that these facts are still unknown to humankind, and even the gods were born later than the universe itself. Although scientific cosmology occupied the centre stage

much later, it is exciting to see that cosmology has particularly been an area where both science and religion were earnest in their quest for an answer.

While ancient philosophers and thinkers had no tools for verification of their theories, over time we got lucky to have people who came up with intricately beautiful mathematics and scientific inventions for carrying out experiments and observations, that helped confirm or deny these theories. A hundred years before Isaac Newton formulated his classical theory of gravitation, Giordano Bruno thought of something that is central to the cosmological principle later devised in 1933 by Edward Milne, the fact that there are multiple star systems throughout the universe, and the solar system does not necessarily occupy the central position. Tycho Brahe and Johannes Kepler later formulated groundbreaking theories about the orbital motion of planets, which were later confirmed by Newton's inverse-square law.

The dawn of the new century saw a revolution in the understanding of space and time, through Einstein's pathbreaking papers on the special theory of relativity (1905) [99] and general theory of relativity (1915) [98]. Special relativity established space and time as entities that should be treated on the same footing and as part of the same continuum, and gave rise to the idea of a fourth intangible dimension for time. It also postulated that no object can travel faster than the speed of light, which has a finite value. General relativity traversed much more abstract concepts and complicated mathematics as it attempted to explain the curvature of this spacetime continuum brought about by gravity. The source of any gravitational field which carries the information about matter and energy, was attributed the energy-momentum tensor via an elegant formulation in the Einstein equation.

In 1922, Alexander Friedmann [110] and then Georges Lemaïtre [193] and Howard Robertson [240] in subsequent years, suggested that Einstein's equations can be used to explain an expanding universe, but Einstein was sceptical, being a believer in the staticness of the Universe. When Edwin Hubble demonstrated the distance-redshift relation that proved the expansion of the Universe [148], Einstein said that adding the cosmological constant to his equation to force a solution for a static universe was his "biggest blunder". However, contrary to Einstein's interpretation, according to Friedmann's work on the original Einstein equations, the cosmological constant was instrumental in explaining the expansion of the Universe.

In 1948, Alpher, Bethe and Gamow made a prediction [15] that the Universe in its early days must have been dominated by a primordial radiation, which suggested the existence of the cosmic microwave background (CMB). Some sixteen years after this, Arno Penzias and Robert Wilson detected some signals [237] at Bell Labs purely by accident that they thought to be a noise but could not be eliminated. Later people like Dicke, Peebles, Roll and Wilkinson interpreted it as a thermal relic from the Big Bang [90] (the term being coined by Fred Hoyle, who ironically was a believer of the steady state model), which supported Gamow's prediction. The CMB was eventually confirmed by NASA's COBE satellite [210] in 1990 to have a blackbody radiation, and was later found to have very tiny temperature anisotropies. The CMB portrays the Universe as it was 380,000 years after the Big Bang, and continues to be one of the most important probes to understand early universe phenomena and formation of structures. Over the years, surveys like WMAP [226] and Planck [102]

have improved upon the resolution of CMB observation, and have provided results in different areas of the electromagnetic spectrum.

Despite these revolutionary advancements, majority of the Universe still remains beyond our comprehension. Discussions on the existence of dark matter took place as early as 1933, when Fritz Zwicky showed that the Coma cluster of galaxies contained a lot of dark matter [317]. Now of course we know that dark matter is a component essential to the formation of galaxies, which in fact trace the underlying dark matter. But after Zwicky's discovery, there was a dry spell until the 1970s when Vera Rubin and Kent Ford rekindled interest in the cosmology community by measuring spiral galaxy rotation curves [255]. Subsequently, in the 1980s the abundance of cold dark matter over baryonic matter was established by a group of cosmologists [45, 82], and now we know that dark matter occupies $\sim 24\%$ of the observable Universe while baryons occupy a mere $\sim 5\%$. What about the remaining 71%? Well, that's another story.

The expansion of the Universe stands mysterious even a century after its proposition, the reason being that we don't really understand the force that drives it. It was only in the late 1990s that observations by the Hubble Space Telescope pointed at the accelerated expansion of the Universe, through a supernova called 1997ff ten billion light years away [121]. It hinted at the fact that after a certain decelerating phase in the Universe, accelerated expansion actually began, and can be attributed to the dominance of the dark energy component. However, postulating the properties of dark energy is not so simple, and existing issues like the cosmological constant problem render ΛCDM cosmology incapable of being hailed as the ultimate truth. As a result, the study of alternate theories of gravity have come up to the forefront recently, with a lot of different approaches like scalar-tensor theories, massive gravity, $f(R)$ gravity, K-essence and others being proposed [76]. Here in this thesis, we discuss scalar-tensor theory in some details (Chapter 2), and also talk about E_g statistics as a test of gravity on large cosmological scales (Chapter 6).

In the upcoming subsections of this introduction, we will try to have a better understanding of how structures are formed starting from primordial fluctuations, how we can obtain statistical measurements of objects in the sky, what we actually mean when we talk about "observable" quantities, and what general relativistic effects contribute to these observations.

1.1 Structure formation

The inflationary phase of the Universe plays a very important role in the structure formation later on, by planting the 'seeds' of initial inhomogeneities. The most plausible hypothesis is that the tiny perturbations due to quantum mechanical processes in the early universe stay quantum within the horizon (a conceptual boundary defining the observable universe), but as soon as they leave the horizon, they become classical and frozen, that is, the amplitude of the fluctuations remain unaltered although the they are stretched over large scales. This can be understood with respect to the fundamental concept of quantum field theory that vacuum is never completely empty, and virtual particles and antiparticles get created and annihilated

continuously. Due to the gigantic expansion that the baby universe underwent during inflation, some of such virtual particles might have gotten separated from their antiparticles by distances larger than the horizon, and failed to annihilate. They are understood to have remained as perturbations to the background. These quantum fluctuations get stretched on the superhorizon scales, and as they get "frozen in", their amplitude remains the same while their wavelength scales proportional to the scale factor a, a dimensionless quantity to parametrise the expansion of the universe. While we can say that the distance from our home to the grocery store is 200 metres, such measurements do not work for entities in the sky. What we observe via our telescopes on the sky are angles and redshifts, which we can eventually convert into metric distances that our brains can comprehend. These distances are mostly denoted in terms of mega-parsecs (Mpc) in the study of large-scale structures where $1\ Mpc = 3.26 \times 10^6$ light years. But in order to know what the number is in Mpc, we first need to measure the redshift z, which is obtained in terms of the emitted and observed frequencies: $1 + z = f_e/f_o$. The scale factor is related to the redshift as $a/a_0 = 1/(1 + z)$, where $a_0 = a(t_0)$ is the scale factor at present time t_0.

Thus it can be said that structure formation occurs due to gravitational instabilities and deviations from a homogeneous background FLRW metric. Considering the Newtonian formalism of structure formation, we can assume that the Universe is filled with an ideal fluid that is inhomogeneous and dissipationless, and describe it by some Newtonian hydrodynamical equations, which are applicable only to non-relativistic matter. However, a more correct treatment will be that using general relativity. This is because with the advent of precision cosmology, a better analysis of spacetime geometry is required, and we also need to study beyond ΛCDM models for which the Newtonian approach is insufficient. Moreover, even though Newtonian simulations are effective in the linear regime, general relativity is more suited to tackle nonlinearities. For this purpose, quite a few numerical codes have been formulated, among which Gevolution uses the weak field expansion in relativistic regime [8]. The usual Friedmann-Lemaître-Robertson-Walker metric is split into background and perturbation, and assuming zero spatial curvature, in the Poisson gauge looks like the following:

$$ds^2 = a^2(\tau)[-(1 + 2\Psi)d\tau^2 - 2B_i dx^i d\tau + (1 - 2\Phi)\delta_{ij}dx^i dx^j + h_{ij}dx^i dx^j] \qquad (1.1)$$

where a is the scale factor of the background, x^i the comoving coordinates, τ the conformal time, Φ and Ψ the Bardeen potentials, and B_i and h_{ij} are functions to be determined from the Einstein equations. We do not perform a perturbative treatment of the stress-energy tensor, and include only the terms that are linear in metric perturbation, and those that are quadratic with two spatial derivatives operating on Φ and Ψ. In this weak field approximation, the '00' part of the Einstein equations is:

$$(1 + 4\Phi)\Delta\Phi - 3\mathcal{H}\Phi' - 3\mathcal{H}^2\Psi + \frac{3}{2}(\nabla\Phi)^2 = -4\pi G a^2 \delta T^0_0 \qquad (1.2)$$

which is a generalised version of the Newtonian Poisson equation, and the 'ij' part

is:

$$\left(\delta^i_k\delta^j_l - \frac{1}{3}\delta_{kl}\delta^{ij}\right)\left[\frac{1}{2}h''_{ij} + \mathcal{H}h'_{ij} - \frac{1}{2}\Delta h_{ij} + B'_{(i,j)} + 2\mathcal{H}B_{(i,j)}\right.$$
$$\left.+(\Phi-\Psi)_{,ij} - 2(\Phi-\Psi)\Phi_{,ij} + 2\Phi_{,i}\Phi_{,j} + 4\Phi\Phi_{,ij}\right] = 8\pi G a^2\left(\delta_{ik}T^i_i - \frac{1}{3}\delta_{kl}T^i_i\right) \quad (1.3)$$

The metric can further be used to solve equations of motion for matter and study the evolution of the stress-energy tensor. In the simplest construction, the equations are solved at first or linear order, and the quantities in question (density, pressure, velocity, potential and entropy) are usually expressed as the sum of a background field plus a perturbed field, that is, we assume that the observed universe is not very different from one which is homogeneous, and the perturbations are very small in comparison to the background.

To have a simple picture, we can visualise galaxies as a system of particles in a six-dimensional phase space, where we can describe them in terms of a distribution function $f(\mathbf{x}, \mathbf{v})$. Using the equation of continuity, we can find the collisionless Boltzmann equation, which is as follows:

$$\frac{\partial f}{\partial t} + \mathbf{v}\cdot\nabla f - \nabla\Phi\cdot\frac{\partial f}{\partial \mathbf{v}} = 0 \quad (1.4)$$

Using this, we can obtain the *Jeans equation* for a collisionless fluid,

$$\nu\frac{\partial \bar{v}_j}{\partial t} + \bar{v}_i\nu\frac{\partial \bar{v}_j}{\partial x_i} = -\nu\frac{\partial\Phi}{\partial x_j} - \frac{\partial}{\partial x_i}(\nu\sigma^2_{ij}) \quad (j = 1, 2, 3) \quad (1.5)$$

where the acceleration and the kinematic viscosity on the left hand side and related to the gravity and the pressure on the right hand side. ν is the number density, $\bar{v}_j$ are the mean velocity components, Φ is the gravitational potential, and σ^2_{ij} is the velocity dispersion tensor.

Now in order for certain modes or perturbations to grow, they need to satisfy the Jeans criterion, whereby only the modes with wavelength larger than the Jeans length $\lambda_J = c_s\sqrt{\frac{\pi}{G\rho}}$ can grow, and these are called 'Jeans unstable' modes. Here c_s is the speed of sound and ρ is the average density. The modes smaller than this wavelength are 'Jeans stable' and merely show oscillatory behaviour. The fact that the Jeans length is proportional to the speed of sound c_s has important implications on the propagation of baryonic perturbations. In the early universe, the baryons are coupled with photons which are already constituted as a high pressure fluid, and this combination has a very high sound speed around $1.7 * 10^5$ km/sec. Due to high pressure, the baryon-proton fluid propagates as an expanding spherical sound wave from an overdense region. This continues until the era of recombination, after which the photons decouple from the baryons and travel outwards at the speed of light, leaving the baryons behind, which remain in a spherical shell along with the excess dark matter. This phenomenon gives rise to the *baryon acoustic oscillations* which act as standard rulers to study the expansion history of the Universe.

The perturbations which satisfy the Jeans criterion and are allowed to evolve, have a growing and a decaying mode as follows (+ for growth and - for decay):

$$\delta(t, \mathbf{k}) = \delta_+(\mathbf{k})D_+(t) + \delta_-(\mathbf{k})D_-(t) \tag{1.6}$$

δ being the overdensity. Here $D_+(t)$ is called the linear growth function, and grows simply as a power law $D_+(t) \propto a(t) \propto t^{2/3}$ in a matter dominated universe, suggesting that an expanding universe does not provide enough favourable environment for structure formation. The decaying mode changes with time as $D_1(t) \propto t^{-1}$. Since we will mostly talk about the growth of structure, we will stick to the conventional notation of D_+ in literature, that goes by D_1. Another quantity that we should introduce here for the sake of completion is the dimensional linear growth rate

$$f = \frac{d \ln D_1}{d \ln a} \tag{1.7}$$

which we will encounter many times throughout the thesis.

There are primarily two kinds of fluctuation modes, depending on the behaviour of entropy: the *adiabatic* one, where the fluctuations in matter and radiation components are coupled but with no spatial variation in entropy, and the *isocurvature* one, where entropy fluctuations exist but there is no net fluctuation in the energy density. Apart from the Jeans criterion that we talked about earlier, there can be other factors as well that suppress the growth of perturbations. For example, free streaming of collisionless hot dark matter particles can cause a serious damping effect, and the growth of baryonic perturbations can be hampered by the imperfect coupling between baryons and photons. The effect of these factors can be quantified through the transfer function $T(k)$, which can be defined in terms of the following relation:

$$\delta(t, \mathbf{k}) = \delta(t_{in}, \mathbf{k})T(k)\frac{D_1(t)}{D_1(t_{in})} \tag{1.8}$$

Thus the transfer function is essentially a measure of the deviations in the growth of the primordial perturbations during the radiation domination era and for modes inside the horizon. For early times, it is justified to assume very low overdensity ($\delta << 1$), which stands for linear approximations, but this fails when we enter late-time eras where nonlinearities become important ($\delta \lesssim 1$). Usually in such cases, we break up the overdensity into linear and nonlinear parts:

$$\delta(t, \mathbf{k}) = \delta_{lin}(t, \mathbf{k}) + \delta_{nl}(t, \mathbf{k}) \tag{1.9}$$

The way to deal with the nonlinear part is quite complicated and unfortunately there are no general analytic solutions. The best method is to employ expensive numerical simulations, and a large number of cosmologists are involved in finding better, faster and more precise ways of carrying out such simulations. Nonlinearities are fundamental to the formation of structures on the large scale, since the mixing of **k**-modes results in the construction of the cosmic web, whose components are sheets and filaments with nodes comprised of galaxy clusters.

1.1.1 Correlation function and power spectrum

For a quantitative understanding of the measurement of structures in the universe, we need to employ a stochastic treatment of the overdensity δ, the observable that contains all the information about the distribution of matter.[1] In order to measure the degree of galaxy clustering, let us look at some functions which help to quantify it deterministically. The two-point correlation function can be defined either for a spatial ($\xi(r)$) or angular ($w(\theta)$) distribution, and computes the excess probability over the random distribution, for the occurrence of galaxies at a distance of $r = |\mathbf{x} - \mathbf{x}'|$, where $\mathbf{x}$ and $\mathbf{x}'$ are the locations of the two galaxies with respect to the observer. In general, the two-point correlation function of an inhomogeneous universe can be defined in terms of the ensemble average over all densities which act as random fields:

$$\xi(\mathbf{r}, t, t') = \xi(\mathbf{x}, t, \mathbf{x}', t') = \langle \delta(\mathbf{x}, t)\delta(\mathbf{x}', t') \rangle \tag{1.10}$$

The Fourier transform of the correlation function, which is called the power spectrum, provides a spectral representation of the field via the superposition of various modes of different amplitudes that constitute the density field.

$$\langle \delta(\mathbf{k}, t)\delta(\mathbf{k}'^{*}, t') \rangle = (2\pi)^3 \delta_D(\mathbf{k} - \mathbf{k}') P(\mathbf{k}, t, t') \tag{1.11}$$

where

$$P(\mathbf{k}, t, t') = \int \xi(\mathbf{r}, t, t') e^{i\mathbf{k}\cdot\mathbf{r}} d^3\mathbf{r} \tag{1.12}$$

The three-dimensional Dirac delta function $\delta_D(\mathbf{k} - \mathbf{k}')$ in Eq. 1.11 is a direct result of the assumed homogeneity and isotropy of the Universe. For a small difference in t and t', we can consider an average time dependence $\bar{t} = \frac{t+t'}{2}$, which we continue denoting here as t for simplicity. Since $\xi(r, t)$ is a real function, we have $P(\mathbf{k}, t) = P^*(-\mathbf{k}, t)$, and also due to the isotropic nature of $\xi(\mathbf{r}, t)$, $P(\mathbf{k}, t) = P(k, t)$, thus making $P(k, t)$ a real function.

Along the lines of Eq. 1.8, we can write for the power spectrum:

$$P(k, t) = P_0(k) T^2(k) \left(\frac{D_1(t)}{D_1(t_{in})} \right)^2 \tag{1.13}$$

Depending on the survey, observers can choose to use either the correlation function or the power spectrum to analyse cosmological information. However, both of these approaches suffer from the shortcoming of not being directly observable, which means that they are dependent on a fiducial cosmology. The distance r that the correlation function depends on, is in turn defined in terms of the comoving distances $\chi(z_1)$ and $\chi(z_2)$, which can be obtained only when we consider a particular set of cosmological parameters. Needless to say, the power spectrum $P(\mathbf{k}, t)$ which is derived as a Fourier transform of $\xi(\mathbf{r}, t)$ is also affected by these parameters. Apart from this, these approaches are limited only to density and redshift

[1] A word of caution: we will soon explain in the next section why δ is not an actual observable and there is more to the story.

space distortions, and do not implicitly take into account lensing and other large-scale relativistic effects. We will see in the next section how these extra effects come into the picture. Another issue is that the usual domain of using the correlation function and the power spectrum is that of the flat-sky approximation which will be inadequate as large-scale surveys aiming to probe much higher redshifts ($z \geq 2$) will become functional. Thus, in Chapter 3, we make an attempt to calculate the full-sky relativistic correlation function and power spectrum of galaxy number counts.

To counteract these problems, we can adopt a third mechanism using the angular power spectrum. As all information about an observed galaxy is essentially obtained from its subtended angle in the sky and its redshift, the correlation function depends on the relative distance between the two galaxies, and the angle between their direction in the sky (due to statistical isotropy), that is we have a function of the form $\xi(\theta, z_1, z_2)$. When we express this in terms of the angular power spectrum, the redshift information manifests in the angular power spectrum as $C_\ell(z_1, z_2)$, where ℓ denotes the multipoles (see Eq. 3.1). The advantages and disadvantages of using C_ℓ over correlation function and power spectrum have been further discussed in Chapter 3, while in Chapter 4 we work exclusively with the concept of angular power spectrum with this idea in mind that it is more convenient to include relativistic effects in its case.

1.2 Observable galaxy number counts

As stated earlier in Section 1.1, for measuring distances in the sky we need to take the help of redshift z. The other relevant quantity is the angle that the object subtends on our telescope, say, θ. This angle helps to determine the direction in which the object is observed, and finally we can say that the number of galaxies can be counted on a patch of the sky at a particular redshift z and direction $\mathbf{n}$. Let us denote this quantity as $N(\mathbf{n}, z)d\Omega_{\mathbf{n}}dz$ (see Fig.1.1). The next step is to average over the angles and get the redshift distribution of the galaxies, that is, $\langle N\rangle(z)dz$. The redshift density perturbation can be obtained from this in terms of the number density of galaxies and the physical survey volume density, both per redshift bin per solid angle:

$$\delta_z(\mathbf{n}, z) = \frac{N(\mathbf{n}, z) - \langle N\rangle(z)}{\langle N\rangle(z)} - \frac{\delta V(\mathbf{n}, z)}{V(z)} \tag{1.14}$$

The important point here is that volume perturbations also exist since there is a distortion of the solid angle and the redshift bin as light propagates from the source to the observer. Thus the truly observed galaxy number counts turn out to be

$$\Delta(\mathbf{n}, z) \equiv \frac{N(\mathbf{n}, z) - \langle N\rangle(z)}{\langle N\rangle(z)} = \delta_z(\mathbf{n}, z) + \frac{\delta V(\mathbf{n}, z)}{V(z)} \tag{1.15}$$

Following the detailed derivations of the right hand side as done in [46], we arrive at an elaborate mathematical expression for the observable galaxy number counts, which includes all the possible relativistic effects:

$$\Delta(\mathbf{n}, z) = D_g + \Phi + \Psi + \frac{1}{\mathcal{H}}\left[\dot{\Phi} + \partial_r(\mathbf{V}\cdot\mathbf{n})\right]$$

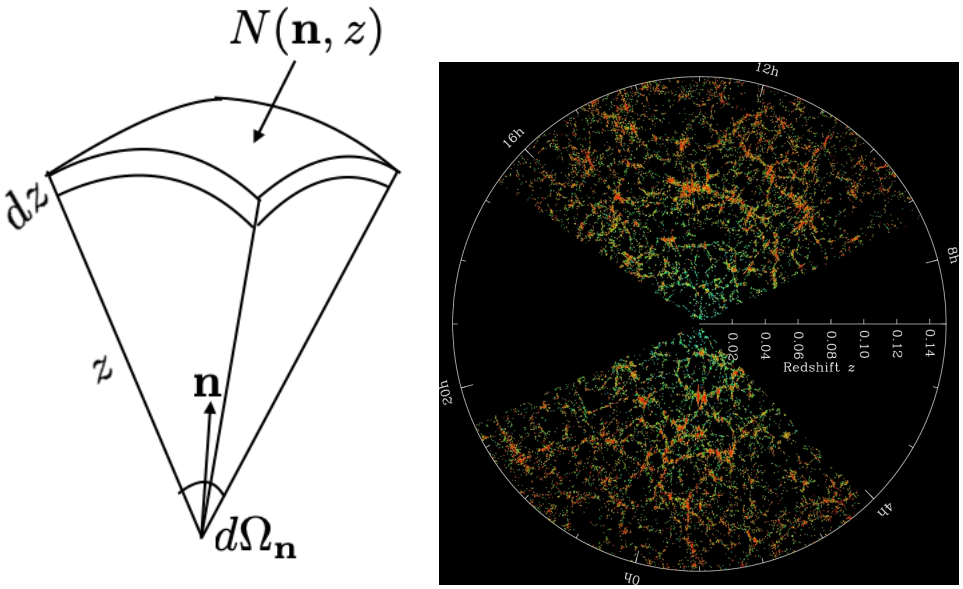

Figure 1.1: Left panel: Schematic diagram showing the number of galaxies in a patch of the sky $N(\mathbf{n}, z)d\Omega_{\mathbf{n}}dz$. Right panel: The Sloan Digital Sky Survey (SDSS) map of distribution of galaxies, where the Earth is at the central point, and each point represents a galaxy.

$$+\left(\frac{\dot{\mathcal{H}}}{\mathcal{H}^2}+\frac{2}{r_S\mathcal{H}}\right)\left(\Psi+\mathbf{V}\cdot\mathbf{n}+\int_0^\chi d\lambda(\dot{\Phi}+\dot{\Psi})\right)$$
$$+\frac{1}{\chi}\int_0^\chi d\lambda\left[2-\frac{\chi-\chi'}{\chi'}\Delta_\Omega\right](\Phi+\Psi) \tag{1.16}$$

Let us have an overall idea of what these terms stand for:

- D_g: It is a gauge-invariant density fluctuation, which has been introduced and elaborately explained in [94].
- $\frac{1}{\mathcal{H}}\partial_r(\mathbf{V}\cdot\mathbf{n})$: This is the redshift space distortion that we will discuss in more details in Section 1.2.1.
- $\left(\frac{\dot{\mathcal{H}}}{\mathcal{H}^2}+\frac{2}{\chi\mathcal{H}}\right)\mathbf{V}$: The Doppler term is essentially an effect explained by the special theory of relativity, which should not be confused with the simple cosmological redshift. While redshift arises due to the expansion of space and does not depend on the motion of the object emitting photons, in case of Doppler shift, the wavelength of the emitted photons changes depending on the position of the source in motion.
- $\left(\frac{\dot{\mathcal{H}}}{\mathcal{H}^2}+\frac{2}{\chi\mathcal{H}}\right)\left(\Psi+\int_0^\chi d\lambda(\dot{\Phi}+\dot{\Psi})\right)$: The Sachs-Wolfe like terms (ordinary and integrated) determine the strength of the gravitational field that affects the energy of photons reaching from a source to the observer. The ordinary Sachs-Wolfe effect describes the effect of gravitational potential at the last

scattering surface and is directly related to the primordial CMB, and the integrated Sachs-Wolfe effect deals with time-dependent potentials that photons encounter during their propagation from the last scattering surface to the observer.

- $\frac{1}{\chi}\int_0^\chi d\lambda \left[-\frac{\chi-\chi'}{\chi'}\Delta_\Omega\right](\Phi+\Psi)$: The lensing distortion term will be elaborately discussed in Section 1.2.2.
- $\frac{2}{\chi}\int_0^\chi d\lambda(\Phi+\Psi)$: This term corresponds to the Shapiro time delay, also called gravitational time delay. As the name suggests, it is simply the fact that gravitational potentials might inhibit the travelling photons, causing them to arrive at the observer point with a delay compared to the expected time of arrival. This acts as a test of general relativity in the solar system, and has been performed using radar signals sent from the Earth to Venus and back, leading to the observation of time delay due to the presence of the massive body that is the Sun.

The redshift space distortions (RSD), along with the density contrast, are called the standard terms, since they are manifest in the observed number counts even if large-scale relativistic effects are not relevant at the smaller scales we are interested in. The effects that are direct results of Einstein's theory of general relativity are represented by the subsequent terms denoting gravitational lensing, Doppler effect, integrated Sachs-Wolfe effect and Shapiro time delay. In this thesis, we will mainly focus on weak gravitational lensing, and RSD to certain extent.

1.2.1 Redshift space distortions

The most intuitive way to find the location of a galaxy cluster based on its redshift information is via its Hubble expansion factor ($\chi = z/H_0$, for $z << 1$). However, this argument fails at larger redshifts, and along with that, peculiar velocities of the galaxies within the cluster also need to be taken into account. This additional contribution results in something called the redshift space distortion, which manifests as an alteration of the observed overdensity. In an overdense region, the galaxies that are closer to us along the line of sight appear to be moving closer to the central overdensity and thus away from us. Similarly, those that are away from us appear to be moving towards the central overdensity, and thus effectively towards us. This leads to the impression of an overall squashing along the line-of-sight direction, giving rise to a quadrupole moment. What we seem to see then is an increase in the density of the cluster along the line of sight, accounted for in the extra term that appears on the right hand side of Eq. 1.17. This is called the Kaiser effect. Thus the power spectrum in the redshift space including the Kaiser term is as follows:

$$P(k,\mu,\bar{z}) \;=\; D_1^2(\bar{z})\left[b(\bar{z})+f(\bar{z})\mu^2\right]^2 P_m(k) \tag{1.17}$$

where D_1 and f are the growth functions as defined in Section 1.1, $\mu = \cos(\mathbf{k},\mathbf{n})$ and $P_m(k)$ is the linear matter power spectrum. While this might seem straightforward, as we enter nonlinear regimes, where the collapse of overdense regions has already

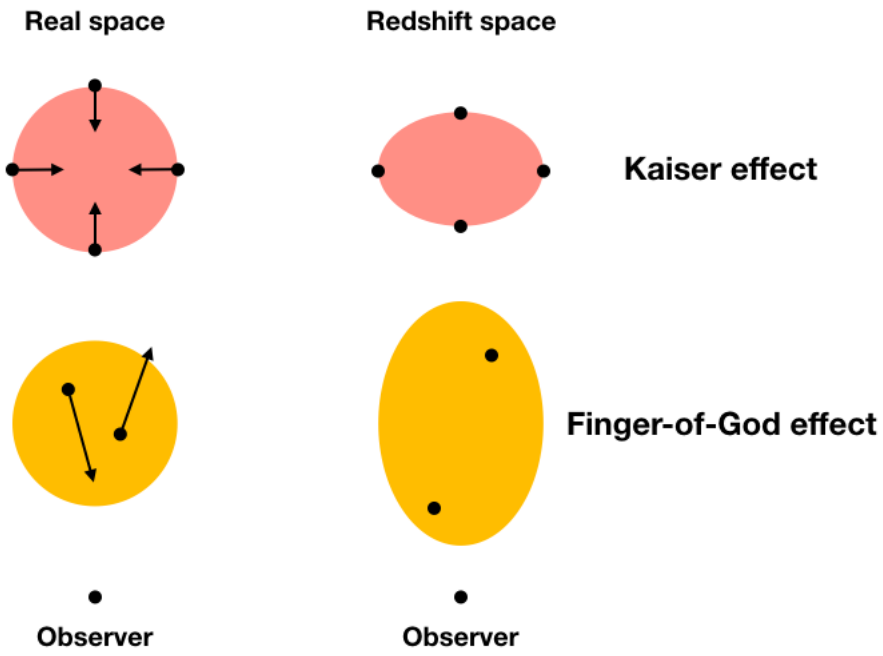

Figure 1.2: A simple illustration to show how the Kaiser effect and the FoG effect cause distortions in observed galaxy clusters along the line-of-sight direction.

taken place, the peculiar velocities are not so well-behaved anymore, and redshift space distortions do not behave in the conventional manner. The more collapsed the object is, the stronger is the velocity dispersion and the effect of nonlinearities. In this case, the quadrupole moment and the linear overdensity have opposite signs, and the object appears to be elongated along the line of sight. This is called a Finger of God (FoG) effect, and needs to be dealt with caution when one looks at structures in the quasi-linear regime, where the Kaiser effect also coexists. In the nonlinear regime, the Kaiser power spectrum is a sum of the auto-correlations of the density (δ) and the velocity divergence ($\theta = \nabla \cdot \mathbf{v}/H(z) = f(z)\delta(k,z)$) power spectra, and also the cross-correlations between them.

$$P_{NL}(k,\mu,\bar{z}) \quad = \quad P_{\delta\delta}(k,\bar{z}) + 2\mu^2 P_{\delta\theta}(k,\bar{z}) + \mu^4 P_{\theta\theta}(k,\bar{z}) \tag{1.18}$$

For taking into account the FoG effect, one needs to add a damping factor to the nonlinear power spectrum, which is conventionally of a Gaussian or a Lorentzian form:

$$D_{FoG}[x] = \begin{cases} \exp(-x^2), & : \text{Gaussian} \\ 1/(1+x^2), & : \text{Lorentzian} \end{cases} \tag{1.19}$$

where $x = k\mu\sigma_v$. The velocity dispersion σ_v is a free parameter that can be determined by fitting with simulations and observations.

1.2.2 Weak gravitational lensing

Gravitational lensing has been strongly attracting the attention of the cosmology community, because of the plethora of information it holds about the large-scale structure. It has also proved to be a test of general relativity since it is a direct consequence of the curvature of spacetime as postulated by Einstein. The first official test of general relativity was carried out in 1919 by Arthur Eddington who teamed up with Frank Watson Dyson to measure the deflection of starlight during total solar eclipse on the 29th of May. The deflection angle was found to be closer in agreement to the value predicted by Einstein's theory, which was twice the expected Newtonian value. Lensing is also one of the most useful cosmological probes and helps to have a better understanding of the underlying matter distribution, especially dark matter tracers like galaxies. It manifests in primarily three different ways as follows:

- Strong lensing: When the lens is very massive and compact, and the source is lying very close to the lens, the bending of light can be extreme, due to which it takes different paths while reaching the observer. This results in multiple images of the same source being observed. If the source, lens and the observer are exactly aligned, it gives rise to a unique image called the Einstein ring.

- Weak lensing: As the name suggests, weak lensing is less stronger than strong lensing, and apparently does nothing too fancy except for stretching and distorting the source image (shear), or magnifying it (convergence). However, it has wide applications in the study of the statistical properties of the large-scale structure of the universe, and we will talk about it in more details.

- Microlensing: This kind of lensing is useful for observing objects that emit little to no light, for example, exoplanets. The lens involved has a very low mass, and passes by the source in a small amount of time, which can help us detect the change in brightness of the source. In the case of exoplanets, the amount of light visible from an object changes periodically, and hence microlensing is essentially a transient phenomenon.

In case of weak lensing, when light from an object passes through a gravitational field, the resulting image formed on our telescope undergoes certain changes. In Fig. 1.3 photons travel from the source plane to the observer plane, but also pass through the lens plane along the way. If the lens plane was not present, the angular position η of the extended source would have appeared at the angular position β. But the lens plane deflects the position of the source by an deflection angle α, due to which the position of the lens is seen to be at an angle θ. Thus, the lens equation turns out to be:

$$\beta = \theta - \alpha(\theta) \tag{1.20}$$

If we map the lens plane to the source plane, we can construct the following Jacobian matrix:

$$A_{ab} = \frac{\partial \beta_a}{\partial \theta_b} = \delta_{ab} - \frac{\partial \alpha_a}{\partial \theta_b} \tag{1.21}$$

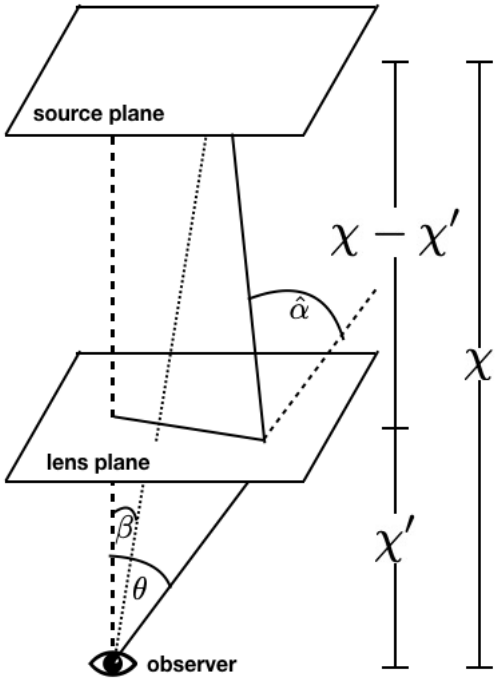

Figure 1.3: Schematic diagram to demonstrate the phenomenon of weak lensing, inspired from [26]

where a and b denote angular coordinates. We can also define a lensing potential ψ that characterises an extended distribution of matter. Here, χ and χ' are the comoving distances of the observer to the source plane and to the lens plane respectively. The deflection angle along a particular coordinate is the gradient of the lensing potential transverse to the photon direction:

$$\alpha_a = \partial_a \psi(\vec{\theta}, \chi) = \partial_a \frac{2}{c^2} \int_0^{\chi} d\chi' \frac{\chi - \chi'}{\chi \chi'} \Phi(\chi' \vec{\theta}, \chi') \tag{1.22}$$

where Φ is the gravitational potential. We can define a matrix A, whose elements are in terms of the convergence κ and shear elements γ_1 and γ_2.

$$A = \begin{pmatrix} 1 - \kappa - \gamma_1 & -\gamma_2 \\ -\gamma_2 & 1 - \kappa + \gamma_1 \end{pmatrix} \tag{1.23}$$

The convergence can be expressed as the Laplacian of the lensing potential:

$$\kappa = \frac{1}{2}(\partial_1 \partial_1 + \partial_2 \partial_2)\psi = \frac{1}{2}\nabla^2 \psi \tag{1.24}$$

The shear components are given as follows:

$$\gamma_1 = \frac{1}{2}(\partial_1 \partial_1 - \partial_2 \partial_2)\psi, \quad \gamma_2 = \partial_1 \partial_2 \psi \tag{1.25}$$

and the complex shear is a helicity-2 object:

$$\gamma = \gamma_1 + i\gamma_2 \tag{1.26}$$

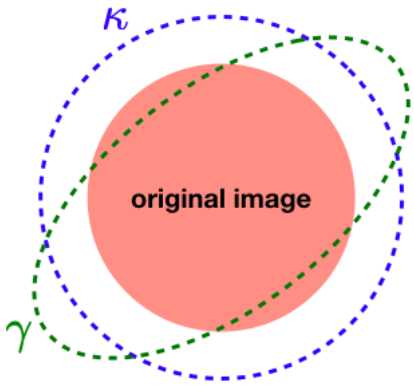

Figure 1.4: The pink sphere is the original image of a galaxy, which appears magnified and distorted after being subjected to weak lensing. The blue dotted circle represents the magnification expressed through convergence κ, and the green dotted ellipse is for the change in shape given by the shear γ.

- Magnification: The quantity associated with the magnification caused by weak lensing is the convergence κ. As seen in Eq. 1.23, κ is included in the diagonal part of the matrix, and thus corresponds to an isotropic change in the size of the image.
- Shape distortion: The trace-free part of the matrix A quantifies the anisotropic amount of stretching or distortion via the complex quantity called shear (Eq. 1.26).

As intriguing the phenomenon of weak lensing is, there is more to the story. Lensing signals also include some systematic effects that are often neglected due to their small magnitude, but are important nonetheless if we want to use lensing as an accurate probe of cosmological scales. These effects which are called intrinsic alignments, are mainly astrophysical effects that arise due to nearby galaxies being subjected to the same tidal field. As a result of such environmental effects, galaxies close to each other get aligned in a particular direction, which adds some extra information to the observed lensing signal. As such, if we correlate the ellipticities of two galaxies ϵ_i and ϵ_j, we actually get a resultant sum of the following correlations:

$$\langle \epsilon_i \epsilon_j \rangle = \langle \gamma_i \gamma_j \rangle + \langle \epsilon_i^s \epsilon_j^s \rangle + \langle \gamma_i \epsilon_j^s \rangle + \langle \epsilon_i^s \gamma_j \rangle \tag{1.27}$$

where ϵ_i^s and ϵ_j^s are the intrinsic ellipticities. This arises due to the fact that intrinsically galaxies are not perfectly circular, their non-negligible ellipticities being related to the observed ellipticity after weak lensing as follows:

$$\epsilon = \frac{\epsilon^s + g}{1 + \epsilon^s g*} \approx \epsilon^s + \gamma \tag{1.28}$$

g being the reduced shear, $g = \kappa/1 - \gamma$. While the left hand side of Eq. 1.27 denotes the observed ellipticity, the right hand side can be decomposed in three different kind of contributions:

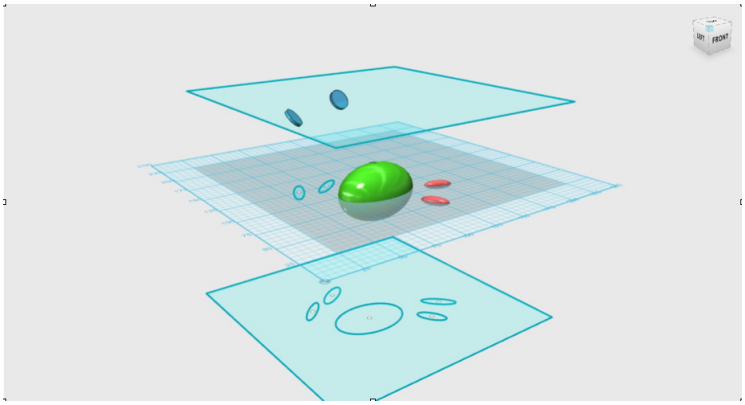

Figure 1.5: A schematic diagram showing the intrinsic alignment contamination of a gravitational lensing signal (courtesy: [171]). The topmost plane is that of the source, the middle one of the lens and the bottom one of the observer. The blue discs are the background source galaxies, and the green ellipsoid is the intermediate matter structure that deflects the light from the source. The alignment of the galaxy images tangentially with respect to the lens gives rise to the GG signal. The red ellipsoids show galaxies that are close to the lens structure and get pointed towards it, causing another kind of alignment that results in the II signal. Finally the GI signal arises out of the anti-alignment of images of galaxies close to the lens, with the images of background galaxies that are gravitationally sheared.

- the GG signal ($\langle\gamma_i\gamma_j\rangle$)is the pure shear correlation necessary for analysis of data.
- the II signal ($\langle\epsilon_i^s\epsilon_j^s\rangle$) is the intrinsic ellipticity correlation, and
- the GI+IG signal ($\langle\gamma_i\epsilon_j^s\rangle + \langle\epsilon_i^s\gamma_j\rangle$) is the correlation between the shear acting on one galaxy and the intrinsic ellipticity of another.

Depending on the type of galaxy (spiral or elliptical), the response of their shape and alignment to the tidal shear can be studied through two different types of model (quadratic or linear). While in case of spiral galaxies, the shape of galaxies is determined by the orientation of the angular momentum which can be traced back to the effects of tidal torquing, elliptical galaxies respond more directly to the tidal shear by undergoing anisotropic deformations due to the second derivative of the gravitational potential. A detailed review of this can be found in [171]. We study about intrinsic alignments and their contribution in weak lensing observations in Chapter 7.

1.3 Scalar-tensor theory

Although most of the discussions in this thesis have been done in the context of general relativity, we also study some other dark energy models like scalar-tensor theory. This is because the cosmological observations are true not only in the Einsteinian

theory but for all theories where photons follow the null geodesic. Apart from the fact that physical observables are gauge-independent, we also need to establish their frame-independence, something that we can explore in the context of scalar-tensor theory, where the usual Einstein frame can be made to undergo a conformal transformation into the Jordan frame. This is the subject of Chapter 2. Let us try to develop an understanding of this, for which we follow the approach of [111].

In a scalar-tensor theory, we can write the Lagrangian of a scalar field in a four-dimensional curved space-time, where it enters the picture non-trivially via a *nonminimal coupling* with the tensor gravitational fields, whereby it also gets included in the matter sector of the Lagrangian.

$$\mathcal{L}_J = \sqrt{-g}\left[\varphi_J^{\gamma}\left(R - \omega_J \frac{1}{\varphi_J^2} g^{\mu\nu}\partial_\mu\varphi_J\partial_\mu\varphi_J\right) + L_{\text{matter}}(\varphi_J, \Psi)\right] \tag{1.29}$$

Here the subscript J refers to quantities in the Jordan frame. φ_J^{γ} is Jordan's scalar field, γ and ω_J are constants, and Ψ represents a matter field. We can show that the choice of γ doesn't affect the fact that the first two terms on the right hand side contain no dimensional constant, and thus a simplified version of this in the prototype Brans-Dicke [54] formalism can be written:

$$\mathcal{L}_{BD} = \sqrt{-g}\left(\varphi R - \omega\frac{1}{\varphi} g^{\mu\nu}\partial_\mu\varphi\partial_\mu\varphi + L_{\text{matter}}(\Psi)\right) \tag{1.30}$$

The first term on the right hand side of Eq.(1.30) is the nonminimal coupling term, which is analogous to the usual Einstein-Hilbert term:

$$\mathcal{L} = \sqrt{-g}\frac{1}{16\pi G}R \tag{1.31}$$

We can redefine the scalar field in Eq.(1.30) to express the Lagrangian into a canonical form, such that the apparent singularity due φ and the multiplicativity of ω can be bypassed. For this we introduce a scalar field ϕ and a dimensionless constant ζ such that

$$\varphi = \frac{1}{2}\zeta\phi^2, \quad \varphi > 0 \tag{1.32}$$

and

$$\epsilon\zeta^{-1} = 4\omega \tag{1.33}$$

Then the new and simplified Brans-Dicke form becomes:

$$\mathcal{L}_{BD} = \sqrt{-g}\left(\frac{1}{2}\zeta\phi^2 R - \frac{1}{2}\epsilon g^{\mu\nu}\partial_\mu\varphi\partial_\mu\varphi + L_{\text{matter}}\right) \tag{1.34}$$

A non-minimal coupling can be removed by subjecting the metric $g_{\mu\nu}$ to a conformal transformation, as follows:

$$g_{\mu\nu} \to g_{*\mu\nu} = \Omega^2(x)g_{\mu\nu}$$

where $\Omega^2(x)$ is a spacetime dependent function of the scalar field ϕ, and can be expressed as a function F such that $\Omega^2(x) = F(\phi)$. The Lagrangian of Eq.(1.29) undergoes a conformal transformation to give us the usual Einstein-Hilbert action in the Einstein frame, where the matter part of the Lagrangian does not contain any scalar field.

The rest of the thesis is structured as follows. Chapter 2 is based on a recent work where we have studied the frame invariance of the number counts in Einstein and Jordan frames, and found that it holds true in the case of scalar-tensor theory of gravity. Chapter 3 will talk in detail about the calculation of the full-sky relativistic correlation function and power spectrum. Chapter 4 is based on our computations of nonlinear contributions to angular power spectra in the redshift space, where we have used a flat-sky approximation and compared different perturbation theory approaches with simulations, to assess their reliability in modelling the angular power spectrum with better accuracy. In the chapters after this, we focus our attention to weak lensing. In Chapter 5, we look at the general relativistic corrections on the correlation between tangential shear and galaxy number counts, which is also called galaxy-galaxy lensing. In Chapter 6, we test the contribution of the lensing corrections in case of E_g statistics, which is a test of gravity at large scales, as explained previously in this introduction. Chapter 7 is based on a work that aims to forecast the measurement of intrinsic and extrinsic shape-size correlations of galaxies in weak lensing measurements.

2

Cosmological Number Counts in Einstein and Jordan frames

Based on:
[109] J. Francfort, B. Ghosh, & R. Durrer, *Cosmological Number Counts in Einstein and Jordan frames*, **JCAP 1909** (2019) 071, [arXiv: 1907.03606]

In Section 1.2, we introduced the concept of observable galaxy number counts, and stressed on the fact that the matter density power spectrum is not a directly observable quantity. It is important to note that, by definition, a physical observable is supposed to be gauge-invariant and frame-invariant. While we intuitively say that this will be true for the number counts Δ_g (denoted in this work as Δ for simplicity), we want to show explicitly how this happens. We adopt two descriptions using two different models - general relativity, and scalar tensor theory (introduced in Section 1.3) - and check if the physics of cosmological observables remains the same in the Einstein and Jordan frames. For this, our aim is to describe the cosmology along with perturbations in both the frames. Testing for different background quantities like density, pressure and redshift, and perturbed quantities like matter density, velocity, Bardeen and lensing potentials, redshift-space density and volume perturbations, we find that many of these are either gauge-independent or frame-independent but not both. As expected, we find that the galaxy number counts do turn out to be both gauge and frame-independent and are proved to be good observables.

Abstract: Even though we know that physical observations are frame independent, the frame dependence of cosmological perturbations is relatively subtle and has led to confusion in the past. In this paper we show that while the (unobservable) matter power spectrum is frame dependent, the observable number counts are not. We also determine how the frame dependence of the power spectrum depends on scale.

2.1 Introduction

From the point of view of fundamental physics the problem of dark energy is very puzzling. Cosmological data, especially the accelerated expansion of the Universe, can be fit relatively well with the standard ΛCDM cosmological model. However, the value of the cosmological constant Λ corresponds to a vacuum energy density

$$\rho_\Lambda = \frac{\Lambda}{8\pi G} \simeq \left(3 \times 10^{-3}\text{eV}\right)^4 \tag{2.1}$$

which cannot be explained by any fundamental theory. Assuming that the vacuum energy scale should be of the order of the cutoff scale of the theory and setting this scale to the Planck scale, one finds that the cosmological constant proposed in the ΛCDM model is about 120 orders of magnitude smaller than this naively guessed value. Probably the worst guess in the history of physics.

Of course the cosmological constant cannot be computed in quantum field theory and it acquires very large corrections at each order in perturbation theory, but the fact that the measured value is so much smaller than any naive guess, is suggestive of the fact that there might be a theoretical reason (maybe coming from quantum gravity) which requests it to vanish. In this case, the observed cosmic acceleration which has led to its introduction must have another origin.

This and similar ideas have prompted many workers in the field to consider theories of gravity which modify Einstein gravity in the infrared regime. The simplest modifications are the so-called scalar-tensor theories which allow, in addition to the metric, for a scalar field with a universal coupling to matter. These theories can be formulated equivalently in the so-called Einstein or Jordan frame.

It is clear that theories which can be transformed into each other by a pure conformal frame transformation describe the same physics and therefore the predicted outcome for every experiment must be equal. However, the interpretation of the experiment might be very different: for example, in the 'Einstein frame', we can interpret the scale factor as a scalar field which is coupled to matter. In this case, the redshift of spectral lines of far away sources is no longer interpreted as an effect due to the expansion of the Universe, but due to a growth of coupling constants such that the present transition energies are higher than those in the past which reach us from far away sources. Hence the Einstein frame physicist does not see an expanding Universe, as in the case of a 'Jordan frame' physicist, but growing coupling constants. Nevertheless, the measured redshift of spectral lines is the same for both, the Einstein frame physicist and the Jordan frame physicist.

This difference of the interpretation of the physics at work in the two frames has led to considerable confusion in the literature. In the present paper we want to contribute hopefully not to the confusion but to the elucidation of the issue. An important point is the fact that one may only consider truly measurable or observable quantities. By laying down a dictionary which translates between background quantities and perturbation variables in both frames, we shall show that the customary density fluctuations or the matter power spectrum are not observables and are actually frame dependent. However, the galaxy number counts which are the true observables, which on small scales, reduce to the density fluctuations and redshift space distortions, are frame independent. We shall also show that, a bit like gauge dependence, frame dependence becomes negligible on small scales.

The rest of this paper is structured as follows. In Section 2.2 we present our dictionary. Most of what we say there can be found in previous literature, see, e.g. [66, 69, 273, 85, 111]. For this reason we shall defer most derivations to an Appendix. The original part of this section is our discussion of the scale dependence of the frame effects in different variables. In Section 2.3 we apply our findings to the number counts. This section is novel and is the main point of the present work. In Section 2.4 we conclude.

Conventions and notations:
We work with the $(-,+,+,+)$ convention.
The coordinates are $(t, \mathbf{x})$ with t being the conformal time and $\mathbf{x}$ the conformal distance, and $\mathcal{H}$ the conformal Hubble factor.
Quantities in Einstein frame are given without indication, e.g. $\mathcal{H}$, while quantities in Jordan frame are marked by a tilde, e.g. $\tilde{\mathcal{H}}$.
The index 0 means *at the background level*, and is not related to any value today (this avoids having a too cluttered notation like $\bar{\tilde{X}}$).
The scalar field is denoted as ϕ and the Bardeen potentials are Ψ and Φ, while φ is the lensing potential.
The letter k is used for the kinetic term of the scalar field. In order to avoid confusion, we use q for the momentum.

2.2 Einstein and Jordan frame - A dictionary

2.2.1 Conformal relationships

We want to consider conformally related metrics[1],

$$\mathrm{d}s^2 = F\mathrm{d}\tilde{s}^2\,, \tag{2.2}$$

where F is a positive function which may depend on spacetime position.

Length scales in these metrics are related by $\ell = \sqrt{F}\tilde{\ell}$. This means that a given spacetime interval will measure ℓ *units* in Einstein frame, but $\tilde{\ell}$ *units* in Jordan frame. Using units with $c = \hbar = k_{\mathrm{Boltzmann}} = 1$, this relation also holds for times

[1]Recall quantities without/with tilde are in Einstein/Jordan frame.

while masses and temperatures are related via $m = \tilde{m}/\sqrt{F}$ and $T = \tilde{T}/\sqrt{F}$. In these units a mass is given by the inverse of the corresponding Compton wavelength and is also equal to the energy mc^2, while a temperature is given by the mean kinetic energy of one degree of freedom at this temperature.

If F is a constant, the two metrics are related by a change of units. The important remark then is that measurements are always comparisons, i.e., we only can measure *ratios* between quantities. Usually a measurement is the ratio between the quantity we are interested in and some reference length scale ℓ_R or its inverse.

The interesting case is a dynamical F, which may, e.g., depend on a scalar field, $F(\phi)$. In this case, the two conformally related metrics describe the same physics only if we correctly adjust the kinetic term of the scalar field ϕ and its coupling to matter. In this case the frame dependence of energies and frequencies, at first sight, seems to imply a frame dependence of the redshift, the ratio of the frequency a photon emitted at x_1 and the one received at x_2. The relation between these frequencies in the two frames is $\nu = \tilde{\nu}/\sqrt{F}$, so that one might naively infer the redshift $(1+z) = \nu(x_1)/\nu(x_2) = \tilde{\nu}(x_1)\sqrt{F(x_1)}/\left(\tilde{\nu}(x_2)\sqrt{F(x_2)}\right) = (1+\tilde{z})\sqrt{F(x_2)/F(x_2)}$. However, when 'measuring' a frequency at the source we 'compare' it with a standard frequency or standard length $\ell_R(x_1)$ so that what we truly measure is

$$(1+z) = \frac{\nu(x_1)\ell_R(x_1)}{\nu(x_2)\ell_R(x_2)} = \frac{\tilde{\nu}(x_1)\tilde{\ell}_R(x_1)}{\tilde{\nu}(x_2)\tilde{\ell}_R(x_2)}\,, \tag{2.3}$$

which is frame *independent*. Some more intuitive explanations are given in the Appendix 2.A. The important point again is that measuring means comparing. Hence the frame dependence of quantities is very subtle and it is sometimes not sufficient to compare dimensionless quantities if they involve measurements at different spacetime points. More details on this point are given in Appendix 2.C.

We want to describe cosmology with perturbations in both Jordan and Einstein frame. We consider General Relativity with a scalar field and matter. The actions in the two frames are given by

$$\mathcal{S} = \int \sqrt{-g}\left(\frac{R}{16\pi G} - \frac{1}{2}k(\phi)(\nabla\phi)^2 - V + \mathcal{L}_m(\psi,\phi)\right)\,\mathrm{d}^4x, \tag{2.4}$$

and

$$\tilde{\mathcal{S}} = \int \sqrt{-\tilde{g}}\left(\frac{F(\phi)\tilde{R}}{16\pi G} - \frac{1}{2}\tilde{k}(\phi)(\tilde{\nabla}\phi)^2 - \tilde{V} + \tilde{\mathcal{L}}_m(\psi,\phi)\right)\,\mathrm{d}^4x. \tag{2.5}$$

Here $\mathcal{L}_m$ is the matter Lagrangian and ψ stands collectively for all matter fields. In order to describe the same theory, the variables in Jordan frame (with tilde) and Einstein frame have to be related by

$$g_{\mu\nu} = F\tilde{g}_{\mu\nu}, \quad \tilde{g}^{\mu\nu} = Fg^{\mu\nu}, \quad g = F^4\tilde{g}, \tag{2.6}$$

$$V = F^{-2}\tilde{V}, \tag{2.7}$$

$$k = \frac{3}{16\pi G}\left(\frac{F'}{F}\right)^2 + \frac{\tilde{k}}{F}, \qquad \text{and} \tag{2.8}$$

$$\mathcal{L}_m \;=\; F^{-2}\tilde{\mathcal{L}}_m. \tag{2.9}$$

A derivation of the only non-trivial relation, Eq (2.8), can be found e.g., in [300]. The energy momentum tensor in Jordan frame is given by

$$\tilde{T}_{\mu\nu} = \frac{2}{\sqrt{\tilde{g}}}\frac{\partial(\sqrt{\tilde{g}}\tilde{\mathcal{L}}_m)}{\partial\tilde{g}^{\mu\nu}}. \tag{2.10}$$

The quantity in the numerator is frame-independent, while $\sqrt{\tilde{g}}$ adds a factor of F^{-2} and $\partial\tilde{g}^{\mu\nu}$ adds a factor of F when converting to Einstein frame so that the whole fraction is multiplied by F. The energy-momentum tensors are therefore related as

$$\tilde{T}_{\mu\nu} = FT_{\mu\nu}, \quad \tilde{T}^{\mu}_{\nu} = F^2T^{\mu}{}_{\nu}, \quad \tilde{T}^{\mu\nu} = F^3T^{\mu\nu}. \tag{2.11}$$

This is coherent as $\rho \sim T^0_0$ and we then obtain $\tilde{\rho} = F^2\rho$, which we expect since ρ has dimension 4 when counting energy and inverse length dimensions as positive.

Important remark: In what follows, we will define the Jordan frame as the frame where ℓ_R is constant and we choose units such that its value is unity. This implies $\ell_R = \sqrt{F}$ in Einstein frame and $\tilde{\ell}_R = 1$ in Jordan frame. From now on, we will only write $\ell(x) \equiv \sqrt{F}$ to refer to the reference length in Einstein frame.

2.2.2 Background variables

We now consider a Friedmann-Lemaître Universe with metrics

$$\mathrm{d}s^2 \;=\; a^2(-\mathrm{d}t^2 + \gamma_{ij}\mathrm{d}x^i\mathrm{d}x^j) \qquad \text{and} \tag{2.12}$$

$$\mathrm{d}\tilde{s}^2 \;=\; \tilde{a}^2(-\mathrm{d}t^2 + \gamma_{ij}\mathrm{d}x^i\mathrm{d}x^j) \qquad \text{with } a = \sqrt{F_0}\tilde{a} \tag{2.13}$$

in Einstein and Jordan frame respectively. Here t is conformal time and a and $\tilde{a}$ are the scale factors in Einstein and Jordan frame respectively, while $F_0 \equiv F(\phi_0(t))$, where ϕ_0 is the background value of the scalar field. Note that we do not put the subscript 0 on V and k, and the subscript will be also omitted on ρ and P when there is no possible confusion. Moreover, $F_0' \equiv \mathrm{d}F_0/\mathrm{d}\phi_0$ in what follows. Similarly, we define $\ell_0(t)$ as the background value for the reference length. The comoving Hubble parameters are related by

$$\tilde{\mathcal{H}} = \frac{\dot{\tilde{a}}}{\tilde{a}} = \frac{1}{\sqrt{F_0}a}\frac{\mathrm{d}(\sqrt{F_0}a)}{\mathrm{d}t} = \frac{\dot{a}}{a} - \frac{\dot{\phi}_0F_0'}{2F_0} = \mathcal{H} - \frac{\dot{\phi}_0F_0'}{2F_0} = \mathcal{H} - \frac{\dot{\ell}_0}{\ell_0}\,. \tag{2.14}$$

The above relation can be understood easily as follows. Let's suppose that the Universe is static in Jordan frame, hence $\tilde{\mathcal{H}} = 0$, but that $\dot{\ell} > 0$. This means that all lengths appear to be expanding in Einstein frame, or said differently, that the standard ruler in Einstein frame is shrinking. In Einstein frame, the Universe seems to be expanding, hence $\mathcal{H} > 0$.

The matter content in a Friedmann universe is (for symmetry reasons) of the perfect-fluid form,

$$(T^{\mu}_{\nu}) = \mathrm{diag}(-\rho_0, P_0, P_0, P_0), \tag{2.15}$$

and the same form holds in Jordan frame. Density and pressure of the two frames are related as

$$\rho = F^{-2}\tilde{\rho}\,, \qquad P = F^{-2}\tilde{P}\,, \tag{2.16}$$

which is a simple consequence of (2.11) (this relationship holds at the background and at the perturbation level).

For energy momentum 'conservation' we shall assume that the fluid in Jordan frame does not interact with ϕ. This is equivalent to assuming that $\tilde{\mathcal{L}}_m$ is independent of ϕ, i.e. $\tilde{\mathcal{L}}_m(\psi,\phi) \equiv \tilde{\mathcal{L}}_m(\psi)$. In this case Jordan frame fluid satisfies the ordinary conservation equation,

$$\nabla^\mu \tilde{T}_{\mu\nu} = 0, \tag{2.17}$$

while in Einstein frame, the coupling to ϕ via the factor F leads to (see e.g. [300])

$$\nabla^\mu T_{\mu\nu} = -\nabla_\nu \phi \frac{F'}{2F} T, \tag{2.18}$$

where T is the trace of the energy-momentum tensor in Einstein frame. At the background level, as usual, only energy 'conservation' is relevant and the conservation Eq. (2.17) and (2.18) yield

$$\dot{\tilde{\rho}} = -\left(\tilde{\rho} + \tilde{P}\right) 3\tilde{\mathcal{H}}, \tag{2.19}$$

$$\dot{\rho} = -3\mathcal{H}(\rho + P) - \rho\frac{\dot{\phi}F'}{2F} + P\frac{3\dot{\phi}F'}{2F}\,. \tag{2.20}$$

The background Einstein equations in Einstein frame read

$$3\mathcal{H}^2 = 8\pi G_N \left(a^2\rho + \frac{\dot{\phi_0}^2 k}{2} + a^2 V\right), \tag{2.21}$$

$$\mathcal{H}^2 - 2\frac{a\ddot{a}}{\dot{a}^2} = 8\pi G_N \left(a^2 P + \frac{\dot{\phi_0}^2 k}{2} - a^2 V\right). \tag{2.22}$$

They correspond to the usual Friedmann equations, with the energy density and the pressure of matter and a scalar field, as measured in Einstein frame.

In Jordan frame, these equations become

$$3\tilde{\mathcal{H}}^2 = \frac{8\pi G_N}{F_0}\left(\tilde{a}^2\tilde{\rho} + \frac{\dot{\phi_0}^2\tilde{k}}{2} + \tilde{a}^2\tilde{V}\right) - 3\tilde{\mathcal{H}}\frac{\dot{\phi}_0 F_0'}{F_0}, \tag{2.23}$$

$$\tilde{\mathcal{H}}^2 - 2\frac{\tilde{a}\ddot{\tilde{a}}}{\dot{\tilde{a}}^2} = \frac{8\pi G_N}{F_0}\left(\tilde{a}^2\tilde{P} + \frac{\dot{\phi_0}^2\tilde{k}}{2} - \tilde{a}^2\tilde{V}\right) + \tilde{\mathcal{H}}\frac{\dot{\phi}_0 F_0'}{F} + \frac{\ddot{\phi}_0 F_0'}{F_0} + \frac{\dot{\phi_0}^2 F_0''}{F_0} \tag{2.24}$$

We note that Newton's constant appears with a scaling factor F_0^{-1} which is expected, as it has dimension of a length square. The first terms on the right are the density and the pressure as measured in Jordan frame. Moreover, the additional terms are the signature of the non-minimal coupling between the scalar field and gravity.

It is straightforward to check that these two sets of equations are equivalent if one makes use of the *dictionary*.

2.2.3 Perturbations

We will now consider scalar perturbations at first order. First, note that, if we work in a gauge where the metric is diagonal, this feature will hold in both frames thanks to the conformal relationship (2.2). Hence, we consider only scalar perturbations, since a scalar field only generates scalar perturbations at first order. Therefore vector and tensor perturbations are not affected by a conformal transformation if properly normalized. We use the Newtonian (or longitudinal) gauge, where the perturbed metrics are given by

$$(g_{\mu\nu}) = a^2\,\mathrm{diag}(-1-2\Psi, 1-2\Phi, 1-2\Phi, 1-2\Phi), \tag{2.25}$$
$$(\tilde{g}_{\mu\nu}) = \tilde{a}^2\,\mathrm{diag}(-1-2\tilde{\Psi}, 1-2\tilde{\Phi}, 1-2\tilde{\Phi}, 1-2\tilde{\Phi}),\ , \tag{2.26}$$

where $\Phi,\ \Psi$ and $\tilde{\Phi},\ \tilde{\Psi}$ respectively are the Bardeen potentials in Einstein and Jordan frames. Second, the scalar field is also perturbed, $\phi(t,\mathbf{x}) = \phi_0(t)+\delta\phi(t,\mathbf{x})$, while the conformal factor is now $F(t,\mathbf{x}) = F_0(t) + F'\delta\phi(t,\mathbf{x})$ (a prime indicates a derivative with respect to the scalar field). We also have for the reference length

$$\ell(x) = \ell_0(t) + \delta\ell(x) = \sqrt{F_0}\left(1 + \frac{\delta\phi F_0'}{2F_0}\right). \tag{2.27}$$

The *dictionary* for the Bardeen potentials is

$$\Psi = \tilde{\Psi} + \frac{F_0'\delta\phi}{2F_0} = \tilde{\Psi} + \frac{\delta\ell}{\ell}, \quad \Phi = \tilde{\Phi} - \frac{F_0'\delta\phi}{2F_0} = \tilde{\Phi} - \frac{\delta\ell}{\ell}. \tag{2.28}$$

The denominator containing ℓ can be evaluated at the background or at the perturbed level, the difference is of second order. Note that the sum of the Bardeen potentials is frame invariant. This is very satisfactory as they are actually the potential for the Weyl tensor from scalar perturbations which is conformally invariant, see, e.g. [96]. This also means that the lensing potential, given by

$$\varphi(\mathbf{n}, z) = \int_0^{r(z)} \mathrm{d}r \frac{r(z)-r}{r(z)r}\left[\Phi(r\mathbf{n}, t_{now}-r) + \Psi(r\mathbf{n}, t_{now}-r)\right], \tag{2.29}$$

is frame independent. This confirms the naive expectation that gravitational lensing which describes the deflection of light is conformally invariant.

The difference of the Bardeen potentials, however is the anisotropic stress tensor which is not frame invariant.

Note that even though the Bardeen potentials are gauge invariant, i.e. invariant under linearized coordinate transformation, they are not frame invariant and therefore not directly observable.

Let us now turn to the energy-momentum tensors. For simplicity we consider only perfect fluid matter, without anisotropic stress, such that the perturbed tensors are of the form

$$T^{\mu}{}_{\nu} = (\rho_0 + \delta\rho)u^\mu u_\nu + (P_0 + \delta P)\left(u^\mu u_\nu + \delta^\mu{}_\nu\right), \tag{2.30}$$
$$\tilde{T}^{\mu}{}_{\nu} = (\tilde{\rho}_0 + \delta\tilde{\rho})\tilde{u}^\mu \tilde{u}_\nu + (\tilde{P}_0 + \delta\tilde{P})\left(\tilde{u}^\mu \tilde{u}_\nu + \delta^\mu{}_\nu\right). \tag{2.31}$$

The *dictionary* relating the perturbations in both frames is given by

$$\delta(x) = \frac{\rho(x) - \rho_0(t)}{\rho_0(t)} = \frac{F^2\tilde{\rho}(x) - F_0^{-2}\tilde{\rho}_0(t)}{F_0^{-2}\tilde{\rho}_0(t)} \tag{2.32}$$

$$= \frac{F_0^{-2}\tilde{\rho}(x)\left(1 - 2\frac{F_0'\delta\phi}{F_0}\right) - F_0^{-2}\tilde{\rho}(t)}{F_0^{-2}\tilde{\rho}(t)} \tag{2.33}$$

$$= \tilde{\delta}(x) - 2\delta\phi\frac{F_0'}{F_0} = \tilde{\delta}(x) - 4\frac{\delta\ell}{\ell}\,. \tag{2.34}$$

The same holds for the pressure perturbation, namely

$$\frac{\delta P(x)}{P_0} = \frac{\delta\tilde{P}(x)}{\tilde{P}_0} - 4\frac{\delta\ell}{\ell}\,. \tag{2.35}$$

Eq. (2.34) can be understood as follows: if $\tilde{\delta} = 0$ (Jordan frame), then matter is distributed uniformly on a given time slice. However, at a given spatial position, ℓ may be slightly larger than on the rest of the time slice (then the standard ruler is smaller). Lengths appear larger, and hence energies smaller. The minus sign is then in agreement with the fact that, at this particular position, the energy density will appear smaller in Einstein frame.

Let us finally express the velocity of the fluid. This needs some care. We use that the velocity is normalized in either frame, $\tilde{u}^2 = \tilde{u}^\mu\tilde{u}^\nu\tilde{g}_{\mu\nu} = u^2 = u^\mu u^\nu g_{\mu\nu} = -1$, so that one has

$$\tilde{u}^\mu = \sqrt{F}u^\mu = \ell u^\mu = \frac{1}{\tilde{a}}\left(1 - \tilde{\Psi}, \tilde{\boldsymbol{v}}\right), \tag{2.36}$$

Here the $\tilde{u}^0$ term is fixed by the normalization and we have defined the velocity perturbation in Jordan frame, $\tilde{\boldsymbol{v}}$. In Einstein frame we obtain

$$u^\mu = \ell^{-1}\tilde{u}^\mu \tag{2.37}$$

$$= \ell_0^{-1}\left(1 - \frac{\delta\ell}{\ell}\right)\tilde{a}^{-1}(1 - \tilde{\Psi}, \tilde{\mathbf{v}}) \tag{2.38}$$

$$= a^{-1}\left(1 - \left(\tilde{\Psi} + \frac{\delta\ell}{\ell}\right), \tilde{\mathbf{v}}\right) \;=\; a^{-1}(1 - \Psi, \mathbf{v}). \tag{2.39}$$

where we have used Eq. (2.28) relating Ψ and $\tilde{\Psi}$ and the fact that $\mathbf{v}$ is already first order. Hence the peculiar velocity is not modified (at first order), which is quite intuitive for a dimensionless local quantity.

We also want to compute the redshift perturbation in Einstein frame. This is possible by taking the usual formula, see e.g. [46], and taking into account that the *measured* frequency is $(k \cdot u)\ell$ we obtain in longitudinal gauge

$$\delta z(\mathbf{n}, z_0) = -(1 + z_0)\left(\Psi + \mathbf{n}\cdot\mathbf{v} + \int_0^{r(z_0)} \mathrm{d}r(\dot{\Psi} + \dot{\Phi}) \; - \frac{\delta\ell}{\ell}\right), \tag{2.40}$$

where $r(z)$ denotes the conformal distance at the background redshift z_0. Here all the terms are evaluated at emission, $(t(z_0), r(z_0)\boldsymbol{n})$ (we assume the observer to be

situated at $\mathbf{x} = 0$). As usual, we omit terms at the observer which add only a monopole or a dipole contribution to the final results. Note that the terms with Ψ and $\delta\phi$ add up, and accordingly to the relation between the Bardeen potentials in both frames (2.28), they simply give $\tilde{\Psi}$ which makes this relation frame invariant. The sum in the integral is, as mentioned, frame invariant, hence the redshift perturbation is frame independent. Interestingly it is not gauge invariant, see [46]. This comes from the fact that the split into $z = z_0 + \delta z$ depends on the time slice i.e. on the chosen gauge.

The density perturbation and therefore also the matter power spectrum, $P(q) = |\delta(q)|^2$ is frame dependent. Note also that in cosmology q is the comoving wave number which is frame independent, hence Fourier transforms do not affect the frame dependence of first order perturbation variables.

2.2.4 Perturbed conservation equations

Let us determine the perturbed 'conservation' equations. We have seen that already at the background level, matter in Einstein frame is interacting with the scalar field and $\nabla^\mu T_\mu{}^\nu \neq 0$. We now perturb these equations at first order (see appendix for more details). Here, we follow the idea presented in [273].

In Einstein frame, the conservation equations read[2]

$$\begin{aligned}
\dot{\delta} + 3\mathcal{H}\left(c_s^2 - \omega\right)\delta + (1+\omega)\nabla\cdot\mathbf{v} - 3(1+\omega)\dot{\Phi} &= (3\omega-1)\left(\frac{F_0'}{2F_0}\delta\phi\right)^\bullet + \frac{3F_0'\dot{\phi}}{2F_0}\left(c_s^2-\omega\right)\delta \\
&= (3\omega-1)\left(\frac{\delta\ell}{\ell}\right)^\bullet + 3\frac{\dot{\ell}}{\ell}\left(c_s^2-\omega\right)\delta, \quad (2.41)\\
\dot{\mathbf{v}} + \mathcal{H}(1-3\omega)\mathbf{v} + \boldsymbol{\nabla}\Psi + \frac{c_s^2}{(1+\omega)}\nabla\delta &= \frac{1-3\omega}{1+\omega}\frac{\boldsymbol{\nabla}\delta\ell}{\ell_0} + (1-3\omega)\frac{\dot{\ell}_0}{\ell_0}\mathbf{v}. \quad (2.42)
\end{aligned}$$

Considering the same equations in Jordan frame, one can use the various equations in the *dictionary* to obtain the usual relations

$$\begin{aligned}
\dot{\tilde{\delta}} + 3\tilde{\mathcal{H}}\tilde{\delta}\left(c_s^2-\omega\right) + \nabla\cdot\mathbf{v} - 3\dot{\tilde{\Phi}}(1+\omega) &= 0, \quad (2.43)\\
\dot{\mathbf{v}} + \tilde{\mathcal{H}}\mathbf{v}(1-3\omega) + \nabla\tilde{\Psi} + c_s^2\frac{\nabla\tilde{\delta}}{(1+\omega)} &= 0. \quad (2.44)
\end{aligned}$$

Note that, as expected, these equations are the usual ones without coupling to the scalar field ϕ, see e.g. [96]. In Einstein frame, the right hand side is the effect of the coupling between matter and the scalar field. In the second equation, they can be interpreted as the *fifth force*, which refers to any force modifying the usual geodesic equation. In the case of a Universe filled with radiation only ($\omega = c_s^2 = 1/3$), the equations are not modified. This is simply a consequence of the fact that massless particles are invariant under conformal transformations.

[2]We use the usual notation $P_0 = \omega\rho_0$ and $\delta P = c_s^2\delta\rho$, with ω and c_s^2 frame invariant.

2.2.5 Perturbed Einstein equations

Regarding the perturbations, in Einstein frame, one has $\Phi = \Psi$ if the anisotropic stress can be neglected. From now on, we will also assume vanishing pressure, since we are mainly interested in a ΛCDM Universe with a scalar field at redshifts $0 < z < 6$ where the fluid matter is pressureless [3]. The perturbed Poisson equation (00 constraint) is[4]

$$\Delta\Phi - 4\pi G a^2 \rho\,(\delta - 3\mathcal{H}v) = 4\pi G\left(\left(3\mathcal{H}k\dot{\phi} + \frac{k'}{2}\dot{\phi}^2 + \frac{a^2V'}{2}\right)\delta\phi + k\dot{\phi}\dot{\delta\phi} - k\dot{\phi}^2\Phi\right) \quad (2.45)$$

The perturbed scalar $(0i)$ constraint is

$$\dot{\Phi} + \mathcal{H}\Phi + 4\pi G a^2 \rho v = 4\pi G k\dot{\phi}\delta\phi. \quad (2.46)$$

The scalar dynamical equation is

$$\ddot{\Phi} + 3\mathcal{H}\dot{\Phi} - \mathcal{H}^2\Phi + 2\frac{\ddot{a}}{a}\Phi = 4\pi G\left(\frac{1}{2}k'\dot{\phi}^2\delta\phi - a^2V'\delta\phi + k\dot{\phi}\dot{\delta\phi} - k\dot{\phi}^2\Phi\right). \quad (2.47)$$

In Jordan frame, the equations are quite long. We give the full expressions in Appendix 2.B. Here we just state that the off diagonal part of the dynamical equations in Jordan frame yield

$$\tilde{\Phi} - \tilde{\Psi} = 2\frac{\delta\ell}{\ell}, \quad (2.48)$$

which is in agreement with Eqs. (2.28).

2.2.6 Scaling of the frame dependence

In this section, we investigate the frame dependence of different quantities depends on the considered wavelength. As shown by the dictionary for the density perturbation (2.34), the difference is given by the quantity $\delta\ell/\ell$. We estimate its order of magnitude. We will assume that we work on subhorizon scales such that $q \gg \mathcal{H}$, and for example $(q^2 + \mathcal{H}^2)\Phi \sim q^2\Phi$. The power spectrum of the matter perturbation is $\mathcal{P}(q) \sim \delta^2$. Hence, the power spectra $\mathcal{P}, \tilde{\mathcal{P}}$ in both frames are related as

$$\tilde{\mathcal{P}} \sim \mathcal{P} + 8\delta \cdot \frac{\delta\ell}{\ell} + 16\left(\frac{\delta\ell}{\ell}\right)^2. \quad (2.49)$$

In order to evaluate the last terms, we will use the Einstein equations and make several assumptions. We work now in Einstein frame. We have at our disposal two scales: a time/length scale given by $\mathcal{H}^{-1}$, and a momentum given by q. Assuming there is no other scale governing the evolution of the scalar field, we can estimate that

$$\dot{\phi} \sim \mathcal{H}\phi, \quad \dot{\delta\phi} \sim \mathcal{H}\delta\phi. \quad (2.50)$$

[3] Adding it does not lead to any principal difficulties, but the equations become just more cumbersome.

[4] As usual for scalar perturbations, we introduce the velocity potential v with $\mathbf{v} = \nabla v$.

Moreover, we will suppose that F is a polynomial function in ϕ such that $F' \sim F/\phi$, and the same for k (the coefficient of the kinetic term).
Taking the dynamical perturbed Einstein's equation (2.47), we can estimate

$$\mathcal{H}^2\Phi \sim \mathcal{H}^2\frac{\delta\phi}{\phi}, \tag{2.51}$$

where we used the first Friedmann equation (2.23) to evaluate $4\pi Gk\dot{\phi}^2 \sim 4\pi Ga^2V \sim \mathcal{H}^2$.
The conclusion is that the relative perturbation of the scalar field scales roughly as the Bardeen potentials

$$\Phi \sim \frac{\delta\phi}{\phi}. \tag{2.52}$$

This implies that the difference between the two density perturbations, δ and $\tilde{\delta}$ scales in the same way:

$$\frac{\delta\ell}{\ell} \sim \frac{\delta\phi F'}{F} \sim \frac{\delta\phi}{F}\frac{F}{\phi} \sim \Phi. \tag{2.53}$$

Performing the same order of magnitude evaluation on the perturbed Poisson equation (2.45), we can estimate the relation between the Bardeen potential and the density perturbations on subhorizon scales,

$$q^2\Phi \sim \mathcal{H}^2\delta. \tag{2.54}$$

By combining the three previous relationships, we find

$$\frac{\delta\ell}{\ell} \sim \left(\frac{\mathcal{H}}{q}\right)^2\delta. \tag{2.55}$$

If we now turn our attention to the relation between the two power spectra in equation (2.50), we obtain the order of magnitude relation

$$\tilde{\mathcal{P}} \sim \mathcal{P}\left(1 + \mathcal{O}\left(\left[\frac{\mathcal{H}}{q}\right]^2\right)\right). \tag{2.56}$$

This shows that, even if the power spectrum is frame dependent, hence not an observable, the difference at small scales is negligible. In galaxy surveys, on small, widely subhorizon scales frame effects can therefore be neglected. It is also on these scales that thew number counts can be expressed in terms of the power spectrum. On large scales, $q \sim \mathcal{H}$, however frame effects are as important as other relativistic effects. We shall now show that, as it must be for a true observable, in the galaxy number counts all frame effects cancel.

2.3 Cosmological number counts

2.3.1 Number count in Jordan frame

In this section, we will follow the notation of [46]. See Appendix for more details. In Jordan frame, as the value of ℓ is constant, the same formula holds, namely

$$\tilde{\Delta}(\mathbf{n}, z) = \tilde{\delta}_z(\mathbf{n}, z) + \frac{\delta\tilde{V}(\mathbf{n}, z)}{\tilde{V}(z)} \tag{2.57}$$

Here $\tilde{\Delta}$ is the number count, which is actually observed in galaxy survey, δ_z is the density perturbation **in redshift space**, and is **not** the usual density perturbation of the energy-momentum tensor and δV is the volume perturbation. We will show that both these terms are not frame invariant, but all the frame dependent terms cancel, and we shall find that the number counts are frame invariant.

2.3.2 Number counts in Einstein frame

The main issue in Einstein frame is the variation of the ruler. Recall that, in this frame, we have a function $\ell(x)$ defining the size of our ruler at a given spacetime point. The computations need to be modified to take this into account. Regarding density perturbations in redshift space, we need to take into account that density is related to N and V by $\rho = mN/V$. Here, for simplicity we assume a Universe made out of particles (galaxies) of fixed mass m of which we find N in the volume V. In Jordan frame, or in the usual formulation of General Relativity, this mass is constant and it cancels in all expressions. However, this is not true in our Einstein frame where the ruler is not constant[5]. We can then compute the redshift density perturbations taking into account that the mass scales like $m \propto \ell^{-1}$:

$$\delta_z(\mathbf{n}, z) = \frac{\rho(\mathbf{n}, z) - \rho_0(z)}{\rho_0(z)} = \frac{\frac{N(\mathbf{n},z)\ell(\mathbf{n},z)^{-1}}{V(\mathbf{n},z)} - \frac{N_0(z)\ell_0(z)^{-1}}{V_0(z)}}{\frac{N_0(z)\ell_0(z)^{-1}}{V_0(z)}} \tag{2.58}$$

$$= \Delta(\mathbf{n}, z) + \frac{\delta z}{\ell_0}\frac{\mathrm{d}\ell_0}{\mathrm{d}z_0} - \frac{\delta\ell}{\ell_0} - \frac{\delta V}{V_0}. \tag{2.59}$$

More details are given in Appendix 2.C. The important point is that, in the second equality, we use that $\rho = mN/V$, and the mass in Einstein frame scales as ℓ^{-1}, hence the appearance of this factor. Moreover, note that here we want to isolate the number count, hence we only need to convert the masses m to the number of galaxies N, which brings exactly one factor of ℓ^{-1}. The volume V is still measured in Einstein frame, hence we do not have factors of ℓ^3 appearing which would convert it to Jordan frame.

[5]Note that for dimensional reasons, one should actually take the ratio with the reference length in Jordan frame l_J. As this value is constant, we can simply omit it, because it cancels in all the ratios.

The formula for the number counts in Einstein frame is then given by

$$\Delta(\mathbf{n}, z) = \delta_z(\mathbf{n}, z) + \frac{\delta V(\mathbf{n}, z)}{V(z)} - \frac{\delta z}{\ell_0}\frac{\mathrm{d}\ell_0}{\mathrm{d}z_0} + \frac{\delta \ell}{\ell_0}. \tag{2.60}$$

To relate it to the number count in Jordan frame, we need to relate the corresponding density perturbation in the redshift space, δ_z and the volume fluctuation δV. We can perform this computation in two ways.

We first present a naive and quick version, before giving the detailed derivation in the next two sections. Consider a physical quantity f in Einstein frame whose energy dimension is n. We can relate the perturbation in Einstein and in Jordan frame as (see derivation in Appendix

$$\frac{\delta f}{f} \equiv \frac{\delta f(\mathbf{n}, z)}{f_0(z)} = \frac{\delta \tilde{f}}{\tilde{f}} + n\frac{\delta z}{\ell_0}\frac{\mathrm{d}\ell_0}{\mathrm{d}z_0} - n\frac{\delta \ell}{\ell}. \tag{2.61}$$

We know that $\delta\rho$ and V have energy dimensions 4 and -3 respectively. Hence, their sum for the number count in Eq. (2.60) gives

$$\delta_z(\mathbf{n}, z) + \frac{\delta V(\mathbf{n}, z)}{V(z)} = \tilde{\Delta}(\mathbf{n}, z) + \frac{\delta z}{\ell_0}\frac{\mathrm{d}\ell_0}{\mathrm{d}z_0} - \frac{\delta \ell}{\ell_0}, \tag{2.62}$$

where we have used the definition of $\tilde{\Delta}$ (2.57). This precisely cancels the remaining last term of Eq. (2.60) .

This derivation is somewhat dangerous as e.g. conformal time t and distance r even though they usually do have dimensions do not transform in this way while the dimensionless Bardeen potentials do transform. However, considering the metrics (2.25) and (2.26) we realize that Ψ and $\tilde{\Psi}$ correspond to changes in physical time intervals while Φ and $\tilde{\Phi}$ correspond to changes in the inverse physical distance (at first order) this explains their behavior under conformal transformations given in (2.28). Because of this subtlety we now present a more formal derivation of the same result.

Density perturbation

We want to show how we can obtain the relation (2.61), but this time by following the approach of [46]. As shown, the density in redshift space is given by

$$\delta_z(\mathbf{n}, z) = \frac{\delta\rho(\mathbf{n}, z)}{\bar{\rho}(z_0)} - \frac{\mathrm{d}\rho_0}{\mathrm{d}z_0}\frac{\delta z(\mathbf{n}, z)}{\rho_0(z_0)}. \tag{2.63}$$

The first term is simply the relative energy perturbation given by the dictionary equation for δ (2.34).

The second term of (2.63) is more tricky. As both z and z_0 are frame independent, δz must to be so as well. Considering the definition in (2.3) including the ruler-dependence, the redshift in Einstein term picks up a factor ℓ. The second term can be evaluated using the conservation equation (2.20) (with $P = 0$) and the time

derivative of z_0. This last quantity is obtained directly from the definition of z, (2.3) and we find[6]

$$\frac{\mathrm{d}z_0}{\mathrm{d}t} = -(1+z_0)\left(\mathcal{H} - \frac{F_0'\dot{\phi}_0}{2F_0}\right) = -(1+z_0)\tilde{\mathcal{H}}. \tag{2.64}$$

The last equality uses the dictionary between $\mathcal{H}$ and $\tilde{\mathcal{H}}$. As z_0 and t are frame-invariant, so is this derivative. Combining the previous results yields

$$\delta_z = \tilde{\delta}_z - 4\frac{\delta\ell}{\ell_0} + 4\frac{\mathrm{d}\ell_0}{\mathrm{d}z_0}\frac{\delta z}{\ell_0}, \tag{2.65}$$

where we use the chain rule to go from one derivative to another (recall $\ell_0 = \sqrt{F_0}$), and

$$\tilde{\delta}_z = \tilde{\delta} - \frac{3\delta z}{1+z_0}. \tag{2.66}$$

Note that Eq. (2.65) is in agreement with (2.61), with $n = 4$.

Volume perturbation

We will briefly present the relation of the volume perturbations and mention which corrections need to be taken into account in Einstein frame. The most important point is that, in this frame, we do *not* have that $a^{-1} = 1 + z_0$ (where a is the scale factor at the emission). Recall the time derivative of z_0 given by Eq. (2.64). Then, Eq. (14) of [46] contains a prefactor of the form

$$\frac{a^3}{1+z}\frac{1}{\mathcal{H} - \frac{\dot{\phi}_0 F_0'}{2F_0}} = \frac{\ell^3}{(1+z)^4}\frac{1}{\mathcal{H} - \frac{\dot{\phi}_0 F_0'}{2F_0}}. \tag{2.67}$$

The remaining steps are as in Ref. [46], provided we include this correction. Hence we find

$$\frac{\delta\tilde{V}}{\tilde{V}_0} = \frac{\delta V}{V_0} + 3\frac{\delta\ell}{\ell_0} - 3\frac{\mathrm{d}\ell_0}{\mathrm{d}z_0}\frac{\delta z}{\ell_0}\,. \tag{2.68}$$

Note that the factor ℓ^3 exactly brings the factors predicted by Eq. (2.61) with $n = 3$.

2.4 Conclusions

In this paper we have studied the frame dependence of cosmological perturbation variables. We have shown that gauge invariance does not guarantee frame invariance (consider, e.g., the Bardeen potentials) and that, on the other hand, there are gauge dependent quantities (e.g. redshift, velocities) which are frame invariant. We have finally shown that the physical, observable number counts are frame invariant, while the density power spectrum is not. This remains true when adding redshift space distortions since velocities are frame independent. However, the frame dependence is relevant only on large scales, comparable to the Hubble scale, where density

[6]Recall that both a **and** ℓ are time dependent.

fluctuations are not directly observable but acquire relativistic corrections. We have also shown that the lensing potential, which is a weighted integral of the sum of the Bardeen potentials is frame independent.

We summarize the gauge and frame dependence of the interesting variables in the final table below. While we do not spell out the gauge dependence which can be found e.g. in [96], we explicitly give the relation between the corresponding quantities in Einstein and Jordan frame.

Table 2.1: Gauge and frame dependence of various quantities.

Quantity	Gauge dependent	Frame dependent	
Background			
Density ρ_0	Yes	Yes	$\rho_0 = F_0^{-2}\tilde{\rho}_0$
Pressure P_0	Yes	Yes	$P_0 = F_0^{-2}\tilde{P}_0$
Redshift z_0	Yes	No	
Observed redshift z	No	No	
Perturbations			
Density δ	Yes	Yes	$\delta = \tilde{\delta} - 4\delta\ell/\ell$
Velocity $\boldsymbol{v}$	Yes	No	
Bardeen pot. Ψ	No	Yes	$\Psi = \tilde{\Psi} + \delta\ell/\ell$
Bardeen pot. Φ	No	Yes	$\Phi = \tilde{\Phi} - \delta\ell/\ell$
Lensing potential φ	No	No	
Redshift density δ_z	No	Yes	$\delta_z = \tilde{\delta}_z - 4\frac{\delta\ell}{\ell} + 4\frac{\mathrm{d}\ell}{\mathrm{d}z}\frac{\delta z}{\ell}$
Volume perturbation $\delta V/V$	No	Yes	$\delta V/V = \delta\tilde{V}/\tilde{V} + 3\frac{\delta\ell}{\ell} - 3\frac{\mathrm{d}\ell}{\mathrm{d}z}\frac{\delta z}{\ell}$
Number counts $\Delta(\boldsymbol{n}, z)$	No	No	

APPENDIX

2.A Some explanations

We give here further intuitive explanations for some of the equations of the paper.

Let us recall the new definition of the redshift given by (2.3). We consider a photon emitted at position e and received at position r:

$$(1+z) = \frac{\nu_e \ell_e}{\nu_r \ell_r} = \frac{\lambda_r \ell_e}{\lambda_e \ell_r}\,. \tag{2.A69}$$

Here ℓ represents the measured length of a given, fixed physical process, i.e. our ruler. Let's consider two examples.

- First, suppose that $\lambda_r = \lambda_e$ but $\ell_e > \ell_r$. With the usual definition of z, this would mean there is no redshift, because both wavelengths are measured equal. However, in the framework of conformal frames, we have

  $$1 + z = \frac{\ell_e}{\ell_r} \tag{2.A70}$$

  which implies that $z > 0$. This is due to the fact that the ruler which is used is expanding with the considered wave, hence its wavelentgh is seen to be constant. Because the ruler is expanding, the reference length, which is itself not being stretched, appears smaller and smaller hence $\ell_e > \ell_r$.

- On the other hand, one can consider a process where $\lambda_e < \lambda_r$ and $\ell_e < \ell_r$ such that both ratios cancel and give $z = 0$. This means that the ruler is expanding, hence the measured reference length appears smaller, but the wavelength of the travelling photon also appears to be decreasing. In fact, nothing is being redshifted, the only modification is that the ruler is being stretched.

The second point illustrates the following interesting fact: If the physical process which is used to define ℓ is also undergoing the same 'redshift', we would naively think that $z = 0$. This is why it is important that the comparisons are made *locally*: at each spacetime point, one has to reproduce the reference physical process in their laboratory, and calibrate in this way the values for $\ell(x)$.

Let us now turn our attention to the conservation equations in Einstein frame (2.20). Consider a box filled with matter only. We assume for simplicity that $\tilde{\mathcal{H}} = 0$ in Jordan frame, and suppose that $\dot{\ell} > 0$, which means that the standard ruler in Einstein frame is shrinking. We can have in mind a fixed box of a given size, and inside a ruler that is getting smaller over time.

By using the *dictionary* for the Hubble factors (2.14), we find $\mathcal{H} = (\dot{\phi}F')/(2F) = \dot{\ell}/\ell$ and Eq. (2.20) reads

$$\dot{\rho} = -\rho\left(\frac{3\dot{\ell}}{\ell} + \frac{\dot{\ell}}{\ell}\right) - P\left(\frac{3\dot{\ell}}{\ell} - \frac{3\dot{\ell}}{\ell}\right) = -\rho\left(\frac{3\dot{\ell}}{\ell} + \frac{\dot{\ell}}{\ell}\right) < 0 \tag{2.A71}$$

First, we note that we have two contributions: the first one is the usual term corresponding to the (apparent) volume expansion of the box, while the second term corresponds to the (apparent) decreasing masses: $\dot{\ell} > 0$ and $m \propto \ell^{-1}$, the masses appear to get smaller in Einstein frame. Regarding the pressure, it is interesting to note that both terms cancel. This should not be a surprise, since the contribution of the pressure to the variation of the energy is given by $W = -P\delta V$. But in this case, the true volume (the volume of the box, measured in Jordan frame) is not varying.

2.B Perturbed Einstein equations in Jordan frame

In Jordan frame, the perturbed Poisson equation (00 eqn.) reads

$$\begin{aligned}\Delta\tilde{\Phi} - \frac{4\pi G\tilde{a}^2\rho}{F}\left(\tilde{\delta} - 3\tilde{\mathcal{H}}v\right) &= \frac{4\pi G}{F_0}\left(\left(3\tilde{\mathcal{H}}\tilde{k}\dot{\phi} + \frac{\tilde{k}'}{2}\dot{\phi}^2 + \frac{a^2\tilde{V}'}{2}\right)\delta\phi + \frac{3}{2}\tilde{k}\dot{\phi}\dot{\delta\phi} - \tilde{k}\dot{\phi}^2\tilde{\Phi}\right)\\ &- \frac{4\pi G}{F_0}\left(\tilde{a}^2\tilde{\rho}_0\frac{F_0'}{F_0}\delta\phi - \frac{\tilde{k}}{2}\dot{\phi}^2F_0'\delta\phi + \tilde{a}^2\tilde{V}\frac{F_0'}{F_0}\delta\phi\right)\\ &+ \frac{F_0'}{2F_0}\left(\Delta\delta\phi - 3\tilde{\mathcal{H}}^2\delta\phi + 3\tilde{\mathcal{H}}\dot{\phi}\tilde{\Phi} + 3\phi\dot{\tilde{\Phi}}\right) + \frac{\dot{\phi}F_0''}{2F_0}\dot{\delta\phi}\end{aligned} \tag{2.B72}$$

The perturbed scalar $(0i)$ constraint is

$$\dot{\tilde{\Phi}} + \tilde{\mathcal{H}}\tilde{\Phi} + \frac{4\pi G\tilde{a}^2\tilde{\rho}}{F_0}v = \frac{4\pi Gk\dot{\phi}}{F_0}\delta\phi + \frac{F_0'}{2F_0}\left(\tilde{\mathcal{H}}\delta\phi + \frac{F_0'}{F_0}\dot{\phi}\delta\phi - \dot{\phi}\tilde{\Phi} + \dot{\delta\phi}\right) + \frac{F_0''}{2F_0}\dot{\phi}\delta\phi \tag{2.B73}$$

The trace of the dynamical equation is

$$\begin{aligned}\ddot{\Phi} + 3\tilde{\mathcal{H}}\dot{\Phi} - \tilde{\mathcal{H}}^2\Phi + 2\frac{\ddot{a}}{a}\Phi &= \frac{4\pi G}{F_0}\left(\frac{k}{2}\dot{\phi}\dot{\delta\phi} - k\dot{\phi}^2\Phi - a^2V'\delta\phi + \frac{1}{2}k'\dot{\phi}^2\delta\phi\right)\\ &+ \frac{4\pi G}{F_0}\left(\tilde{a}^2\tilde{V}\left(\frac{F_0'}{F_0}\right)^2\delta\phi + \frac{\tilde{k}}{2}\dot{\phi}^2\frac{F_0'}{F_0^2}\right)\\ &- \frac{F_0'}{2F_0}\left(2\tilde{\mathcal{H}}^2 - 4\frac{\ddot{a}}{a} + \tilde{\mathcal{H}}\frac{F_0'}{F_0}\dot{\phi} + \left(\frac{F_0'}{F_0}\right)^2\dot{\phi}^2\right)\delta\phi\\ &+ \frac{F_0'}{2F_0}\left(3\tilde{\mathcal{H}} + \dot{\phi}\right)\dot{\delta\phi} + \frac{F_0'}{2F_0}\ddot{\delta\phi}\\ &- \frac{F_0'}{2F_0}\left(2\tilde{\mathcal{H}}\dot{\phi}\Phi + 2\ddot{\phi}\Phi + 3\dot{\phi}\dot{\Phi}\right)\\ &+ \frac{F_0''}{2F_0}\left(3\tilde{\mathcal{H}}\dot{\phi}\delta\phi + \ddot{\phi}\delta\phi + \frac{F_0'}{F_0}\dot{\phi}^2\delta\phi + \ddot{\phi}\dot{\delta\phi} - \dot{\phi}^2\Phi\right)\\ &+ \frac{F_0^{(3)}}{2F_0}\dot{\phi}^2\delta\phi\,,\end{aligned} \tag{2.B74}$$

while its traceless part simply yields

$$\tilde{\Phi} - \tilde{\Psi} = 2\frac{\delta\ell}{\ell}\,. \tag{2.B75}$$

2.C Some derivations

We present the derivation of Eq. (2.61). Consider a physical quantity f with energy dimension n.

$$\frac{\delta f}{f} \equiv \frac{\delta f(\mathbf{n},z)}{f_0(z)} = \frac{f(\mathbf{n},z)-f_0(z)}{f_0(z)} \tag{2.C76}$$

$$= \frac{\tilde{f}(\mathbf{n},z)\ell(\mathbf{n},z)^{-n} - \tilde{f}_0(z)\ell_0(z)^{-n}}{f_0(z)\ell_0(z)^{-n}} \tag{2.C77}$$

$$= \frac{\tilde{f}(\mathbf{n},z)\ell_0(z)^{-n}\left(1+n\frac{\delta z}{\ell_0}\frac{\mathrm{d}\ell_0}{\mathrm{d}z_0}-n\frac{\delta\ell}{\ell}\right) - \tilde{f}_0(z)\ell_0(z)^{-n}}{f_0(z)\ell_0(z)^{-n}} \tag{2.C78}$$

$$= \frac{\delta\tilde{f}}{\tilde{f}} + n\frac{\delta z}{\ell_0}\frac{\mathrm{d}\ell_0}{\mathrm{d}z_0} - n\frac{\delta\ell}{\ell}. \tag{2.C79}$$

The first and second equality are definitions. To go to the second line, we use the *dictionary* to go from Einstein to Jordan frame. To go to the third line, we use that $\ell(\mathbf{n},z) = \ell_0(z_0) + \delta\ell(\mathbf{n},z)$ and $z = z_0 + \delta z$ to get both contributions. This can be understood by observing Fig. 2.1. The point A is at the observed coordinate $(\mathbf{n},z)$, but is located on the time slice corresponding to z_0. Hence, the perturbation δf is given with respect to $f_0(z_0)$.
We can understand the two corrections as follows: suppose that $\delta z > 0$, as shown in the figure, and that the derivative in the last term is positive, namely ℓ_0 decreases over time, which is equivalent to saying that the standard ruler is getting larger over time. This implies that length will appear smaller and energies bigger in Einstein frame. Hence the $+n$ in the first term to take into account this correction. Now suppose that $\delta\ell > 0$, which means that lengths appear larger and energy smaller at the considered point that on the time slice, hence the $-n$ of the second term.

The relationship involving the number count in Jordan frame goes as follows:

$$\delta_z(\mathbf{n},z) = \frac{\rho(\mathbf{n},z)-\rho_0(z)}{\rho_0(z)} \tag{2.C80}$$

$$= \frac{\frac{N(\mathbf{n},z)\ell(\mathbf{n},z)^{-1}}{V(\mathbf{n},z)} - \frac{N_0(z)\ell_0(z)^{-1}}{V_0(z)}}{\frac{N_0(z)\ell_0(z)^{-1}}{V_0(z)}} \tag{2.C81}$$

$$= \frac{\frac{N(\mathbf{n},z)\ell_0(z_0)^{-1}\left(1-\frac{\delta\ell}{\ell_0}\right)}{V_0(z)+\delta V(\mathbf{n},z)} - \frac{N_0(z)\ell_0(z)^{-1}}{V_0(z)}}{\frac{N_0(z)\ell_0(z)^{-1}}{V_0(z)}} \tag{2.C82}$$

$$= \frac{N(\mathbf{n},z)\ell_0(z)^{-1}\left(1+\frac{\delta z}{\ell_0}\frac{\mathrm{d}\ell_0}{\mathrm{d}z_0}\right)\left(1-\frac{\delta\ell}{\ell_0}\right)\frac{1}{V_0(z)}\left(1-\frac{\delta V}{V_0}\right) - \frac{N_0(z)\ell_0(z)^{-1}}{V_0(z)}}{\frac{N_0(z)\ell_0(z)^{-1}}{V_0(z)}} \tag{2.C83}$$

$$= \Delta(\mathbf{n},z) + \frac{\delta z}{\ell_0}\frac{\mathrm{d}\ell_0}{\mathrm{d}z_0} - \frac{\delta\ell}{\ell_0} - \frac{\delta V}{V}. \tag{2.C84}$$

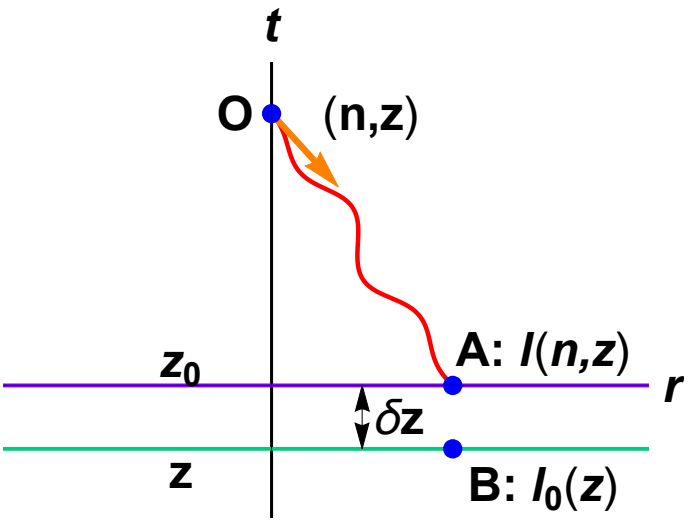

Figure 2.1: Schematic view of the photon trajectory. The distance is displayed horizontally and the time vertically. The photon is emitted at A, on the timeslice corresponding to z_0, and is received at O.

The first equality is the definition of the density perturbation. For the second equality, we use that $\rho = mN/V$ and use the fact that the measured mass of N particles in Einstein frame is proportional to ℓ^{-1}. Note that we only *convert* the mass, because at the end we would like to obtain the number count, which involves N. We do not want to convert the volume here. In the third equality, we use that $\ell(\mathbf{n}, z) = \ell(z_0) + \delta\ell(\mathbf{n}, z)$ (the logic is the same as in the previous derivation). In the fourth equality, we use $z = z_0 + \delta z$. In the final equality we simplify the expression.

By using the definition for the redshift density perturbation given in (2.63), we can finally write the number counts as

$$\Delta(\mathbf{n}, z) = \frac{\delta\rho}{\bar{\rho}(z_0)} - \frac{\mathrm{d}\rho_0}{\mathrm{d}z_0}\frac{\delta z}{\rho_0(z_0)} + \frac{\delta V}{V} - \frac{\delta z}{\ell_0}\frac{\mathrm{d}\ell_0}{\mathrm{d}z_0} + \frac{\delta\ell}{\ell_0}. \tag{2.C85}$$

Let us present an intuitive explanation for each of these terms. Keep in mind that all the perturbed quantities are evaluated at the point with observed coordinates $(\mathbf{n}, z)$, which is physically located at B in Fig. 2.1. The question we ask is: *Why is the number count not equal to the density perturbation?* Let's consider one term after another. In what follows, we will consider that $\delta z > 0$, as shown for example in the Fig. 2.1.

- The first term is due to the fact the galaxy is located at z_0 but we compare it with the background value at the observed redshift, namely $\rho_0(z)$ to obtain the number count. However, $\delta\rho$ is computed from the background value $\rho_0(z_0)$. We have in our example $\rho_0(z_0) < \rho_0(z)$, so the number count will be slightly smaller than the density perturbation. This can be mathematically understood because the derivative of ρ_0 in the first term is positive, and we choose $\delta z > 0$ for our example, hence the term is positive but contributes negatively because of the minus sign.

- The second term is due to the volume perturbation. Let's suppose that $\delta V > 0$, namely the physical volume at the point of the emission is slightly *larger* than on the rest of the time slice. The number count is not affected by any volume distortion, but the density is reduced. Hence, the number count should be bigger than the density perturbation.

- The third and the fourth term are the two corrections to the first two terms, their interpretation being given above.

3

The full-sky relativistic correlation function and power spectrum of galaxy number counts

Based on:
[281] V. Tansella, C. Bonvin, R. Durrer, B. Ghosh, & E. Sellentin, *The full-sky relativistic correlation function and power spectrum of galaxy number counts. Part I: theoretical aspects*, **JCAP 1803** (2018) 019, [arXiv: 1708.00492]

Now that we have established that the galaxy number counts are good observables and are frame-independent, it is necessary for us to have a clear understanding of what we are observing and measuring in the sky. However, simulating the observed data is often computationally expensive, and we resort to reasonable approximations. One such approximation is the flat-sky approximation (also called the distant observer approximation) which provides us with a simplified version of the two-point statistics like the correlation function and power spectrum. In this approximation we assume that we are effectively looking at only one direction in the sky while correlating two objects, and that the directions $\mathbf{n}_1$ and $\mathbf{n}_2$ for two objects can essentially be treated as a single direction $\mathbf{n}$ ($\mathbf{n}_1 = \mathbf{n}_2 = \mathbf{n}$). But we need to explore scenarios beyond approximations in order to get a more accurate picture, and that is what we do here. We derive a full-sky correlation function inclusive of all possible relativistic effects, using two different methods - one via the angular power spectra or C_ℓ's, and the other without using them, which is computationally much faster. This is useful for obtaining a three-dimensional information of the large-scale structure, which isn't provided by the C_ℓ's. From the correlation function, we obtain the power spectrum by taking the Fourier transform. We study how different relativistic effects contribute at different redshifts, and find that while large-scale effects such as Sachs-Wolfe terms are more significant at smaller redshifts, the lensing term is more important at higher redshifts. We also compute the correlation function and power spectrum multipoles, whereby we find that the correction due to lensing increases with redshift for both the monopole and the quadrupole, and eventually for the hexadecapole as well. This suggests that the lensing contribution is absolutely in need of being considered for current and upcoming surveys which aim to probe higher redshifts, and this issue has been taken up further in Chapters 5 and 6.

Abstract: We derive an exact expression for the correlation function in redshift shells including all the relativistic contributions. This expression, which does not rely on the distant-observer or flat-sky approximation, is valid at all scales and includes both local relativistic corrections and integrated contributions, like gravitational lensing. We present two methods to calculate this correlation function, one which makes use of the angular power spectrum $C_\ell(z_1, z_2)$ and a second method which evades the costly calculations of the angular power spectra. The correlation function is then used to define the power spectrum as its Fourier transform. In this work theoretical aspects of this procedure are presented, together with quantitative examples. In particular, we show that gravitational lensing modifies the multipoles of the correlation function and of the power spectrum by a few percent at redshift $z = 1$ and by up to 30% and more at $z = 2$. We also point out that large-scale relativistic effects and wide-angle corrections generate contributions of the same order of magnitude and have consequently to be treated in conjunction. These corrections are particularly important at small redshift, $z = 0.1$, where they can reach 10%. This means in particular that a flat-sky treatment of relativistic effects, using for example the power spectrum, is not consistent.

3.1 Introduction

Upcoming redshift surveys of the distribution of galaxies [189, 19, 201, 3, 13, 60] are going to probe the large-scale structure of the universe at high redshift and for wide patches of the sky with unprecedented precision. To exploit the information delivered by these surveys in an optimal way, it is crucial to have reliable theoretical predictions of the signal. Redshift surveys generally associate two quantities to each galaxy they detect: the direction from which photons are received, $\boldsymbol{n}$, and the redshift z. It has therefore been argued in the past [130, 131, 275, 276, 245, 46], that galaxy correlation functions are truly functions of two redshifts and an angle. The angular-redshift power spectrum is then given by $C_\ell(z_1, z_2)$. This quantity has been introduced in [46, 67], where it has also been shown that due to relativistic projection effects, the linear power spectrum is not simply given by density fluctuations and redshift-space distortions, but it acquires several additional terms from lensing, ordinary and integrated Sachs Wolfe terms, gravitational redshift, Doppler terms, and Shapiro time delay. These projection effects had been previously identified in [310, 309].

Subsequently, linear Boltzmann codes like CAMB [197] and CLASS [41] have been generalized to calculate this galaxy count angular power spectrum [88, 86]. To determine the $C_\ell(z_1, z_2)$ observationally, one correlates the number of galaxies in a redshift bin around z_1 and in a small solid angle around direction $\boldsymbol{n}_1$ with those in a redshift bin around z_2 and in a small solid angle around direction $\boldsymbol{n}_2$. Due to statistical isotropy, the resulting correlation function only depends on the angle θ between $\boldsymbol{n}_1$ and $\boldsymbol{n}_2$, $\cos\theta = \boldsymbol{n}_1 \cdot \boldsymbol{n}_2$ and is related to the angular power spectrum in

the well known way,

$$\xi(\theta, z_1, z_2) = \frac{1}{4\pi}\sum_\ell (2\ell+1) C_\ell(z_1, z_2) L_\ell(\cos\theta)\,, \tag{3.1}$$

where L_ℓ denotes the Legendre polynomial of degree ℓ.

Before the introduction of the $C_\ell(z_1, z_2)$'s, cosmologists have mainly concentrated on determining the correlation function and the power spectrum in Fourier space. In comoving gauge, on sub-horizon scales the latter is given by [175]

$$\begin{aligned} P_g(k,\nu,\bar{z}) &= D_1^2(\bar{z})\left[b(\bar{z}) + f(\bar{z})(\hat{\mathbf{k}}\cdot\boldsymbol{n})^2\right]^2 P_m(k) \qquad (3.2)\\ &= D_1^2(\bar{z})\left[b^2 + \frac{2bf}{3} + \frac{f^2}{5} + \left(\frac{4bf}{3} + \frac{4f^2}{7}\right)L_2(\nu) + \frac{8f^2}{35}L_4(\nu)\right] P_m(k)\,. \end{aligned}$$

Here $\bar{z}$ is the mean redshift or the survey, $P_m(k)$ is the matter density power spectrum today, $D_1(\bar{z})$ is the growth factor normalized to $D_1(0) = 1$, $b(\bar{z})$ is the galaxy bias and

$$f(\bar{z}) = -\frac{D_1'}{D_1}(1+\bar{z}) = \frac{d\ln D_1}{d\ln(a)}\,, \tag{3.3}$$

is the growth rate, where the prime denotes the derivative with respect to the redshift $\bar{z}$. The direction cosine ν is the cosine of the angle between $\mathbf{k}$ and the observation direction $\boldsymbol{n}$ (in the literature this direction cosine is often denoted as μ but here we reserve μ for the corresponding angle in real space and in order to avoid confusion we denote it by ν in Fourier space).

Equation (3.2) has an interesting property: projecting out the monopole, quadrupole and hexadecapole in ν, one can directly measure the bias b and the growth rate f. This has been exploited in previous observations and has led to the best determinations of f so far (see [77, 230, 6, 9, 14, 258] and refs. therein). It is clear that the form (3.2) of the power spectrum can only be valid if the bins are not too far apart in the sky. Eq. (3.2) indeed implicitly assumes that the galaxies are observed in *one* single direction $\boldsymbol{n}$ so that a 'flat-sky approximation' with a well defined angle ν is a reasonably good approximation.

An observable alternative to the power spectrum, which is routinely used in galaxy surveys is the correlation function $\xi(r, \mu, \bar{z})$, where r denotes the separation between the galaxies, μ is the orientation of the pair with respect to the direction of observation $\boldsymbol{n}$ and $\bar{z}$ is the mean redshift of the survey. The correlation function is observed in terms of z_1, z_2 and θ. To express it in terms of r, μ and $\bar{z}$, the redshifts z_1 and z_2 have to be converted into comoving distances and a direction cosine μ has to be defined.

Neglecting spatial curvature we can use the cosine law to express r in terms of the comoving distances to z_1 and z_2,

$$r(z_1, z_2, \theta) = \sqrt{\chi(z_1)^2 + \chi(z_2)^2 - 2\chi(z_1)\chi(z_2)\cos\theta}\,, \tag{3.4}$$

where

$$\chi(z) = \frac{1}{H_0}\int_0^z \frac{dz}{\sqrt{\Omega_m(1+z)^3 + \Omega_X g_X(z)}}\,. \tag{3.5}$$

Here Ω_m is the matter density parameter and $\Omega_X g_X(z)$ is the dark energy density in units of the critical density today; g_X is normalized to $g_X(0) = 1$. Hence the correlation function $\xi(r, \mu, \bar{z})$, as well as the power spectrum, are not directly observable: they both require the use of a fiducial cosmology to calculate r and $\chi(z)$. If the redshift is small, $z \ll 1$, we can write $\chi(z) \simeq z/H_0$, and the dependence on H_0 is taken into account by measuring cosmological distances in units of Mpc$/h$, where Mpc denotes a megaparsec ($\simeq 3.1 \times 10^6$ light years) and $h = H_0/100\,\mathrm{km/s/Mpc}$. However, in present and upcoming catalogues which go out to $z = 2$ and more, this is no longer sufficient and r depends in a non-trivial way on the dark matter and dark energy density, on the dark energy equation of state and on curvature (which is set to zero in this work for simplicity). Fortunately this dependence can be accounted for by introducing correction parameters, which allow for deviations from the fiducial cosmology, see e.g. [303]. In the flat-sky approximation, the standard correlation function takes the simple form [128]

$$\xi^{\mathrm{st}}(r, \mu, \bar{z}) = D_1^2(\bar{z}) \left[\left(b^2 + \frac{2bf}{3} + \frac{f^2}{5} \right) c_0(r) - \left(\frac{4bf}{3} + \frac{4f^2}{7} \right) c_2(r) L_2(\mu) + \frac{8f^2}{35} L_4(\mu) c_4(r) \right] , \tag{3.6}$$

with

$$c_\ell(r) = \frac{1}{2\pi^2} \int dk\, k^2 P_m(k) j_\ell(rk) \,. \tag{3.7}$$

Note that the terms containing the growth factor f come from the Jacobian transforming real space positions $\boldsymbol{x}$ into redshifts [1].

In Appendix 3.D we derive the general relation between the $c_\ell(r)$ and the corresponding pre-factors of the Legendre polynomials in the power spectrum.

Expressions (3.2) and (3.6) are currently used to analyse redshift surveys [2]. These expressions are sufficiently accurate to place meaningful constraints on cosmological parameters with current data. They may however not be sufficient to analyse future surveys since they suffer from two important limitations: first they are based on the flat-sky (sometimes also called distant-observer) approximation. And second they take into account only density fluctuations and redshift-space distortions. They neglect lensing which is relevant especially when the redshifts z_1 and z_2 are significantly different. They also neglect all the relativistic projection effects which are relevant on large scales (close to horizon scale). These expressions are therefore

[1] We point out that the original derivation of redshift-space distortion from [175] contains a contribution proportional to $\boldsymbol{n} \cdot \mathbf{v} = v_r$. This term does contribute to the monopole and quadrupole and it consequently modifies (3.6). It is however neglected in most redshift-space distortion analysis and therefore we do not consider it as 'standard' and we do not include it in (3.6). We include it however in the relativistic corrections, along with the other Doppler corrections, which are of the same order of magnitude (see Eq. (3.12)). Note that, as discussed in more detail in Section 3.2.2, this specific contribution has been studied in detail in [275, 276, 234, 245] and its impact on the correlation function was found to be important at small redshift and large separation.

[2] Note that these expressions are valid in the linear regime only. Theoretical models accounting for non-linearities have been developed and are used to extend the constraints to non-linear scales, see e.g. [106].

only an approximate description of what we are observing, which is also reflected by the fact that they are gauge-dependent.

Due to these limitations, one would be tempted to use the angular power spectrum instead of Eqs. (3.2) and (3.6) to analyse future redshift surveys. The gauge-invariant $C_\ell(z_1, z_2)$'s account indeed for all observable effects. They are directly observable and do not rely on the flat-sky approximation. And they can be determined numerically within a few seconds with sub-percent accuracy. Unfortunately they are not fully satisfactory for several reasons:

- If we want to profit optimally from *spectroscopic* redshift information from a survey like the one that will be generated by Euclid [189], DESI [13] or the SKA [60], we need several thousand redshift slices leading to several million $C_\ell(z, z')$ spectra. For an MCMC parameter estimation this is simply prohibitive. Even if one spectrum is calculated within a few seconds, calculating the millions of spectra $\sim 10^5$ times would take months even if highly parallelized.

- In each spectroscopic redshift bin we then only have a few 1000 galaxies, less than one per square degree, and the observed spectra would have very large shot noise $\propto 1/N$, allowing only computation up to very low ℓ.

- One of the big advantages of $\xi(r, \mu)$ and $P(k, \nu)$ is that the growth rate $f(z)$ can be simply determined by isolating the monopole, quadrupole and hexadecapole components in an expansion of P and ξ in Legendre polynomials in μ and ν respectively. With the C_ℓ's on the other hand there is no simple way to isolate redshift-space distortions since each multipole ℓ is a non-trivial combination of density and velocity.

Hence even though the C_ℓ's are very convenient theoretically, they are not fully satisfactory from an observational point of view. In this paper we therefore derive general expressions for the correlation function and the power spectrum, that can be used as theoretical models for future surveys. Our work builds on the result of several papers, which have studied the impact of some of the relativistic effects on the correlation function and on the power spectrum. In [165, 312], expressions for the flat-sky power spectrum including all non-integrated relativistic effects have been derived. In [151, 200, 150] the lensing contribution to the flat-sky power spectrum and the flat-sky correlation function has been studied in detail. Refs. [275, 276, 234] have derived full-sky expressions for density and redshift-space (RSD) contributions to the correlation function, which have then be further developed in [245, 256, 34, 311]. These expressions have been re-derived using an alternative method in [57]. Ref. [252] has studied in detail the relation between the full-sky and flat-sky density and RSD for both the correlation function and the power spectrum. In [48] the full-sky calculation of [275, 276, 234] has been extended to include gravitational redshift and Doppler terms, which are especially relevant in the case of multiple populations of galaxies. Ref. [34] further expands the formalism introduced in [275] by computing theoretical expressions for the wide-angle corrections including also the integrated

terms and Ref. [248] numerically evaluates all the non-integrated relativistic terms in the full-sky. In [249] the integrated terms in the correlation function are plotted for the first time for two values of the angle θ. The theoretical expressions in these works rely on an expansion of the correlation function in Tripolar Spherical Harmonics which on the one hand is a powerful tool to obtain simple expressions in the full-sky but on the other hand hides some properties of the correlation function enforced by isotropy.[3]

Here we generalise and complete these results. We first derive a full-sky expression for the correlation function including all local and integrated contributions, in which isotropy of the perturbations is explicit. In particular, we provide a detailed study of the gravitational lensing contribution to the correlation function which does not rely on the flat-sky or Limber approximation. We discuss how these full-sky contributions modify the simple multipole expansion of Eq. (3.6). This represents the first analysis of the full-sky lensing contributions to the multipoles of the correlation function, which is most relevant when extracting the growth factor. In this aspect as in several other ways, this analysis goes beyond the pioneering work of [249].

In the second part of this work we use the correlation function to calculate the power spectrum, which we define as the Fourier transform of the full-sky correlation function. In this way the power spectrum does not rely explicitly on the flat-sky approximation. However, it has an unambiguous interpretation only in this limit. Comparing the full-sky and flat-sky derivations, we find that relativistic effects and wide-angle corrections [4] are of the same order of magnitude and they have therefore to be treated in conjunction. This leads us to the conclusion that relativistic effects cannot be consistently studied in the flat-sky and that the correlation function is therefore more adapted than the power spectrum to investigate these effects.

This paper is the first part of this study where we present the theoretical derivation and some numerical results. An exhaustive numerical study, including also the effects of the new terms on cosmological parameter estimation, is deferred to a future publication [95]. Of course, there are many studies estimating cosmological parameters using the $C_\ell(z_1, z_2)$, see for example [86, 246, 221, 59, 87]. However as argued above, these can mainly be used for large, photometric redshift bins while within such bins, in order to profit optically from spectroscopic redshift information, a correlation function or power spectrum analysis is required.

The remainder of the present work is structured as follows: in the next section we describe how we obtain the redshift-space correlation function from the angular correlation function. As already discussed above, the procedure of course depends on the cosmological model. We shall describe two possibilities: to go either over the $C_\ell(z_1, z_2)$ spectra or to obtain $\xi(r, \mu, \bar{z})$ directly from the density fluctuations, velocity fluctuations and the Bardeen potentials in Fourier space. In Section 3.3 we study the power spectrum. In Section 3.4 we discuss the implications of our findings

[3] Whether in flat-sky or full-sky the correlation function depends on three variables: two distances and one angle ($\xi(\chi_1, \chi_2, \theta)$ or $\xi(\bar{\chi}, r, \cos\alpha)$ in this work), one distance and two angles ($\xi(\theta, \gamma, r)$ in [275], $\xi(\chi_2, \theta, \phi)$ in [248]) or three distances ($\xi(\chi_1, \chi_2, r)$). When ξ is expanded in Tripolar Spherical Harmonics one obtains a function $\xi(\boldsymbol{x}_1, \boldsymbol{x}_2)$ and the three physical variables are in general not directly inferred.

[4] Here we call wide-angle corrections the difference between the flat-sky and full-sky expressions.

for future surveys and we conclude. Several technical derivations are relegated to 5 appendices.

3.2 The correlation function

The galaxy number counts including relativistic corrections have been derived in [46, 67] with the following result

$$\Delta_g(\boldsymbol{n}, z) = \Delta^{\rm den} + \Delta^{\rm rsd} + \Delta^{\rm len} + \Delta^{\rm d1} + \Delta^{\rm d2} + \Delta^{\rm g1} + \Delta^{\rm g2} + \Delta^{\rm g3} + \Delta^{\rm g4} + \Delta^{\rm g5}\,, \quad (3.8)$$

where

$$\begin{aligned}
\Delta^{\rm den} &= b\delta_c(\chi(z)\boldsymbol{n}, z)\,, && (3.9)\\
\Delta^{\rm rsd} &= -\mathcal{H}^{-1}\partial_r v_r\,, && (3.10)\\
\Delta^{\rm len} &= \frac{5s-2}{2\chi}\int_0^{\chi(z)} d\lambda \frac{\chi-\lambda}{\lambda}\Delta_\Omega(\Phi+\Psi), && (3.11)\\
\Delta^{\rm d1} &= -\left(\frac{\dot{\mathcal{H}}}{\mathcal{H}^2} + \frac{2-5s}{\mathcal{H}\chi} + 5s - f_{\rm evo}\right) v_r\,, && (3.12)\\
\Delta^{\rm d2} &= -(3-f_{\rm evo})\mathcal{H}v\,, && (3.13)\\
\Delta^{\rm g1} &= \left(1 + \frac{\dot{\mathcal{H}}}{\mathcal{H}^2} + \frac{2-5s}{\mathcal{H}\chi} + 5s - f_{\rm evo}\right)\Psi\,, && (3.14)\\
\Delta^{\rm g2} &= (5s-2)\Phi\,, && (3.15)\\
\Delta^{\rm g3} &= \mathcal{H}^{-1}\dot{\Phi} && (3.16)\\
\Delta^{\rm g4} &= \frac{2-5s}{\chi}\int_0^{\chi(z)} d\lambda(\Phi+\Psi)\,, && (3.17)\\
\Delta^{\rm g5} &= \left(\frac{\dot{\mathcal{H}}}{\mathcal{H}^2} + \frac{2-5s}{\mathcal{H}\chi} + 5s - f_{\rm evo}\right)\int_0^{\chi(z)} d\lambda(\dot{\Phi}+\dot{\Psi})\,. && (3.18)
\end{aligned}$$

Here δ_c is the matter density fluctuation in comoving gauge, v_r is the radial component of the velocity in longitudinal gauge, v is the velocity potential such that $\boldsymbol{v} = -\nabla v$, $v_r = -\partial_r v$; hence v has the dimension of a length (we later define V via its Fourier transform, $\hat{v} = k^{-1}V(k)$, so that $V(\boldsymbol{x})$ is dimensionless). Φ and Ψ are the Bardeen potentials and Δ_Ω denotes the Lapacian on the sphere of directions $\boldsymbol{n}$. The galaxy bias is denoted by b, s is the magnification bias and $f_{\rm evo}$ is the evolution bias. These biases generally depend on redshift. The magnification bias s comes from the fact that in general we do not observe all galaxies but only those which are brighter than the flux limit of our instrument. Due to lensing and to some relativistic effects, some fainter galaxies may make it into our surveys. This is taken into account by s which is proportional to the logarithmic derivative of the galaxy luminosity function at the flux limit of our survey, see [67, 88] for more details.

The terms $\Delta^{\rm den}$ and $\Delta^{\rm rsd}$ are the density and redshift-space distortion terms usually taken into account. In the following we call the sum of these two terms the

'standard terms'. $\Delta^{\rm len}$ represents the lensing term, also often called magnification. This term has already been measured with quasars at large redshift, see e.g. [216], but it is usually neglected in galaxy surveys, since it is subdominant at low redshift. $\Delta^{\rm d1}$ is the Doppler contribution. Note that here we have used Euler's equation to derive this term. In all generality this term contains a contribution from gravitational redshift, proportional to $\partial_r\Psi/\mathcal{H}$, which can be rewritten in terms of the velocity v_r using Euler equation, see e.g. [48]. $\Delta^{\rm d2}$ is a velocity term which comes from transforming the longitudinal gauge density into the comoving density. $\Delta^{\rm g1}$, $\Delta^{\rm g2}$ and $\Delta^{\rm g3}$ are relativistic effects, given by the gravitational potentials at the source. As such they are sometimes called 'Sachs-Wolfe' terms. $\Delta^{\rm g4}$ denotes the so-called Shapiro time-delay contribution and $\Delta^{\rm g5}$ is the integrated Sachs-Wolfe term.

In the following we will sometimes group together the relativistic non-integrated terms (d1, d2, g1, g2, g3). The lensing term is treated separately since its calculation is different. The relativistic integrated terms (g4 and g5) are neglected in our numerical results since their contribution is largely subdominant with respect to the lensing term.

3.2.1 Using C_ℓ's

We start by deriving the correlation function of (3.8), using the angular power spectrum C_ℓ. Using Eqs. (3.1) and (3.4) we can write

$$\xi(r,\bar z,\theta)=\frac{1}{4\pi}\sum_\ell(2\ell+1)C_\ell(\bar z-\Delta z,\bar z+\Delta z)L_\ell(\cos\theta)\,, \tag{3.19}$$

where Δz is given by ($\bar H=H(\bar z)$, $\bar\chi=\chi(\bar z)$)

$$\Delta z(r,\bar z,\theta)=\frac{\bar H\sqrt{r^2-2\bar\chi^2(1-\cos\theta)}}{\sqrt{2(1+\cos\theta)}}\in\left[0,r\bar H/2\right]\,. \tag{3.20}$$

This is a simple consequence of (3.4) setting $z_{1,2}=\bar z\pm\Delta z$ and approximating $\chi_{1,2}=\chi(\bar z\pm\Delta z)\simeq\chi(\bar z)\pm\Delta z/H(\bar z)$. This function is the same full correlation function as the one given in Eq. (3.1), but now expressed in terms of the variables $r,\bar z$ and θ instead of z_1,z_2 and θ. We shall use the same symbol ξ to denote it.

Usually, the correlation function is not considered as a function of $r,\bar z$ and the opening angle θ between the two directions which are correlated, but as a function of $r,\bar z$ and the angle with a fictitious but fixed line-of-sight between the two directions of observation. If θ is small enough, redshift-space distortions are proportional to the $\cos^2$ of the angle with this fictitious direction. To mimic this situation we introduce

$$r_\parallel \;=\; \chi_2-\chi_1\;\simeq\;2\Delta z/H(\bar z)\;\le\;r\,, \tag{3.21}$$

$$\mu \;=\; \frac{r_\parallel}{r}\,,\qquad -1\le\mu\le1\qquad\text{and}\qquad r_\perp\;=\;\sqrt{r^2-r_\parallel^2}\,. \tag{3.22}$$

Writing $\bar\chi=(\chi_1+\chi_2)/2$ and using Eq. (3.21) we obtain

$$\cos\theta=\frac{2\bar\chi^2-r^2+\frac12\mu^2r^2}{2\bar\chi^2-\frac12\mu^2r^2}=\frac{2\bar\chi^2-r_\perp^2-\frac12r_\parallel^2}{2\bar\chi^2-\frac12r_\parallel^2}\equiv c(\bar z,r,\mu)\,. \tag{3.23}$$

Note that $\bar{\chi}$ and $\chi(\bar{z})$ are not exactly the same but in what follows we neglect this difference which is of order $(\Delta z)^2/\mathcal{H}(\bar{z})$. With this, the correlation function, $\xi(r, \bar{z}, \theta)$ can be written as a function of $\bar{z}$, $r_\parallel$ and $r_\perp$ (or, equivalently, $\bar{z}, r$ and μ)

$$\xi(r_\parallel, r_\perp, \bar{z}) = \frac{1}{4\pi}\sum_\ell (2\ell+1) C_\ell\left(\bar{z} - \frac{r_\parallel \bar{H}}{2}, \bar{z} + \frac{r_\parallel \bar{H}}{2}\right) L_\ell\left(c(\bar{z}, r, \mu)\right) \quad (3.24)$$

$$= \langle \Delta(\boldsymbol{x}_1, \bar{z} - \Delta z)\Delta(\boldsymbol{x}_2, \bar{z} + \Delta z)\rangle\,. \quad (3.25)$$

Note that, again, we have re-expressed ξ in different variables.

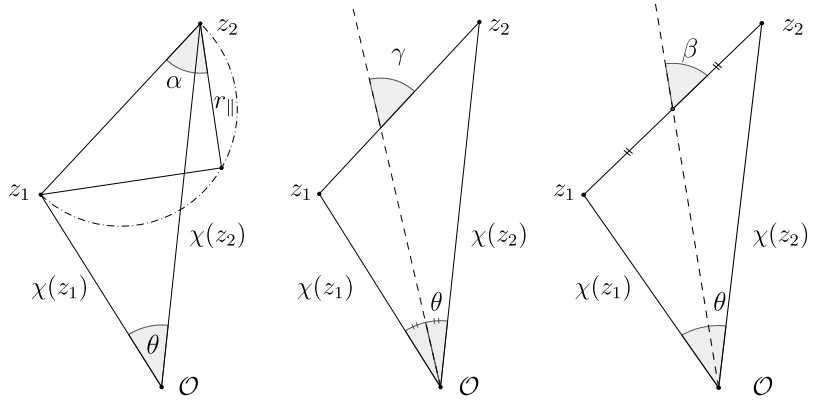

Figure 3.1: The definitions of the angles α (left panel, $r_\parallel = \chi_2 - \chi_1$), γ (middle panel) and β (right panel) as discussed in the text.

Expression (3.24) is valid as long as Δz is small so that $\Delta z \simeq r_\parallel H(\bar{z})/2 = (\chi_2 - \chi_1)H(\bar{z})/2$ is a good approximation. Expression (3.25) however, is valid for all possible values of $r_\parallel = \chi(\bar{z}+\Delta z) - \chi(\bar{z}-\Delta z)$ and $r = \sqrt{(\boldsymbol{x}_1 - \boldsymbol{x}_2)^2}$, $r_\perp = \sqrt{r^2 - r_\parallel^2}$ where $\boldsymbol{x}_1 = \chi(\bar{z} - \Delta z)\boldsymbol{n}_1$, $\boldsymbol{x}_2 = \chi(\bar{z} + \Delta z)\boldsymbol{n}_2$ such that $c(\bar{z}, r, \mu) = \boldsymbol{n}_1 \cdot \boldsymbol{n}_2$. For a given cosmology, fixing $r_\parallel$ and $\bar{z}$ is therefore equivalent to fixing z_1 and z_2 while $r_\perp$ then fixes $\cos\theta$. Given a cosmological background model, there is a one-to-one correspondence between the model-independent angular correlation function (3.1) and the model-dependent correlation function (3.25).

The angle α, given by $\mu = \cos\alpha$ defined by Eq. (3.22), is the angle between the line r connecting $\boldsymbol{x}_1$ and $\boldsymbol{x}_2$ and the line connecting the intersection of the circle around $\boldsymbol{x}_2$ with radius $r_\parallel = \mu r$ and the Thales circle over r (see Fig. 3.1, left panel). This angle is not very intuitive and it is not what observers use. In practice the angles used are either β, the angle between r and the line dividing r into two equal halves (see Fig. 3.1, right panel) or γ, the angle between the line bisecting the angle θ and r (see Fig. 3.1, middle panel). Using elementary geometry we can express the angles β and γ in terms of θ, χ_1 and χ_2 (see Appendix 3.A for a derivation):

$$\cos\beta = \mu f_\beta(\theta, \chi_1, \chi_2)\,, \qquad \cos\gamma = \mu f_\gamma(\theta, \chi_1, \chi_2)\,, \quad (3.26)$$

$$f_\beta = \frac{\chi_1 + \chi_2}{\sqrt{\chi_1^2 + \chi_2^2 + 2\chi_1\chi_2\cos\theta}}\,, \qquad f_\gamma = \frac{\sqrt{1+\cos\theta}}{\sqrt{2}}\,. \quad (3.27)$$

In the small angle approximation, $\theta \to 0$, both functions behave as

$$f_{\beta,\gamma} = 1 + \mathcal{O}(\theta^2)\,.$$

If $r_\parallel \neq 0$, i.e. $\chi_1 \neq \chi_2$, we can express $c(\bar{z}, r, \mu)$ in terms of $\bar{z}, r, \cos\beta$ as

$$c(\bar{z}, r, \cos\beta) = \frac{1}{2\chi_1\chi_2}\left[\frac{(\chi_1^2-\chi_2^2)^2}{r^2\cos^2\beta} - \chi_1^2 - \chi_2^2\right]. \tag{3.28}$$

Here $\chi_{1,2}$ are given in terms of $\bar{\chi}$ and r by solving the equations

$$\bar{\chi} \;=\; (\chi_1+\chi_2)/2 \qquad \text{and} \qquad r^2 \;=\; \chi_1^2+\chi_2^2-2\chi_1\chi_2\cos\theta\,. \tag{3.29}$$

If we want to express the correlation function in terms of $\bar{z}$, r and $\cos\beta$, we have to solve the system (3.28,3.29). A short calculation gives

$$\cos\theta \;=\; 1 - \frac{8r^2\bar{\chi}^2(1-\cos^2\beta)}{16\bar{\chi}^4 - r^2\cos^2\beta(8\bar{\chi}^2-r^2)}\,, \qquad \chi_{1,2} \;=\; \bar{\chi} \pm \sqrt{\bar{\chi}^2 - \frac{4\bar{\chi}^2-r^2}{2(1+\cos\theta)}} \tag{3.30}$$

$$r_\parallel \;=\; \chi_2-\chi_1 = 2\sqrt{\bar{\chi}^2 - \frac{4\bar{\chi}^2-r^2}{2(1+\cos\theta)}}\,. \tag{3.31}$$

Inserting $\cos\theta$ from (3.30) and $r_\parallel$ from (3.31) in (3.24), we can express the correlation function as a function of $r, \bar{z}$ and $\cos\beta$. In terms of γ we find

$$\cos\theta \;=\; 1 - \frac{r^2}{2\bar{\chi}^2}(1-\cos^2\gamma)\,. \tag{3.32}$$

In the small angle limit, all three angles, α, β and γ coincide. In Section 3.2.2 we will see that the angle which gives the result closest to the flat-sky limit is the angle μ. For this reason and due to its simplicity in what follows we express both, the correlation function and the power spectrum in terms of the projection along and transverse to the line-of-sight using the angle α with $\cos\alpha = \mu = (\chi_2-\chi_1)/r = r_\parallel/r$. As explained above, for small angles this is equivalent to choosing β or γ, but for large angles, the expressions in terms of μ are simpler.

In Fig. 3.2 we show the correlation function at $\bar{z} = 1$ as a function of $r_\parallel$ and $r_\perp$. In all figures, we use the cosmological parameters: $h^2\Omega_m = 0.14$, $h^2\Omega_b = 0.022$, $h = 0.676$, $A_s = 2.215 \times 10^{-9}$ at $k_* = 0.05$ Mpc^{-1}, $n_s = 0.961$, $b(z) = 1$, $f_{\rm evo} = 0$ and $s = 0$ unless otherwise stated. In the left panel of Fig. 3.2 we include only the density, in the middle panel we also consider redshift-space distortions (RSD) and in the right panel we include also the lensing term. While the pure density term is spherically symmetric with a well visible baryon acoustic oscillation (BAO) feature at $r \sim 100$Mpc, the RSD removes power for small $r_\perp$ and adds power at large $r_\perp$. Also the maximal amplitude has more than doubled due to RSD [5]. Finally the lensing term adds a very significant amount of power for large $r_\parallel$ and small $r_\perp$.

[5]Note that we have chosen $b = 1$. For larger values of b, the importance of redshift-space distortion with respect to the density contribution is reduced.

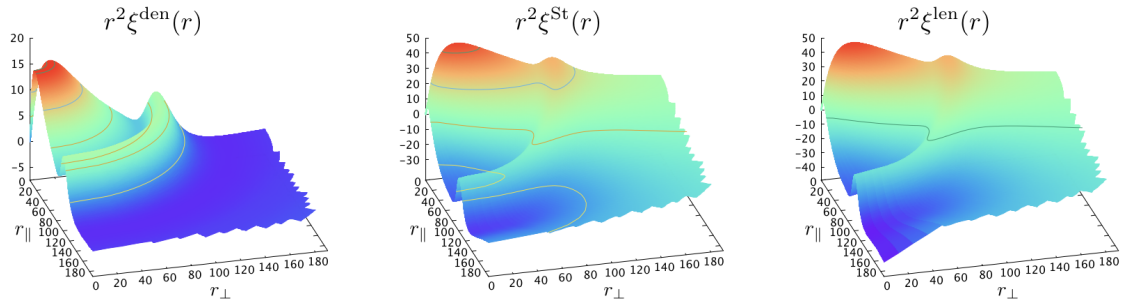

Figure 3.2: The correlation function at redshift $\bar{z} = 1$ as a function of $r_\parallel$ and $r_\perp$. The left panel contains only the density contribution, $\xi^{\rm den}$, the middle panel contains also RSD, $\xi^{\rm st}$, and the right panel contains also the lensing term, $\xi^{\rm st+len}$.

This is the case when a foreground density fluctuations lenses a structure at higher redshift along its line of sight. The additional relativistic contributions are very small and become visible only on very large scales, as we shall see in the rest of this paper and as has already been anticipated in several papers, e.g. Refs. [46, 67].

In Fig. 3.3 we show fractional differences for $\mu = 0$ (left) and $\mu = 1$ (right)

$$\Delta\xi^A \equiv \frac{\xi^A - \xi^{\rm st}}{\xi^{\rm st}}\,, \tag{3.33}$$

where

$$\xi^A = \left\langle \left(\Delta^{\rm st} + \Delta^A\right)(\boldsymbol{n}_1, z_1)\left(\Delta^{\rm st} + \Delta^A\right)(\boldsymbol{n}_2, z_2)\right\rangle . \tag{3.34}$$

In this way we show separately the contribution of each correction A with respect to the standard term, including its correlation with density and redshift-space distortion. The middle panel shows $\Delta\xi^A$ for $A =$ lensing and the lower panel for all the non-integrated relativistic effects, namely the terms d1, d2, g1, g2 and g3 (see Eqs. (3.8) to (3.18) for a definition of the various relativistic terms). Finally, as reference, we plot in the top panel the fractional difference due to redshift-space distortion, namely $\Delta\xi^{\rm rsd} = (\xi^{\rm st} - \xi^{\rm den})/\xi^{\rm den}$.

Not surprisingly, for $\mu = 0$ the lensing term is very small apart from a small effect on the acoustic peaks. For $\mu = 1$ however, at large scales $r > 150\,$Mpc, lensing becomes the dominant term. As also noted in [200], it increases linearly with distance. Comparing our full-sky calculation of the lensing (orange) with the flat-sky expression (blue) derived in [200] and in Appendix 3.E (see Eq. (3.E132)) we see that for $\mu = 1$ the two expressions agree very well, which is not surprising because in this case $\boldsymbol{n}_1 = \boldsymbol{n}_2$ and flat-sky is a good approximation. The only source of difference in this case comes from the fact that the flat-sky result uses Limber approximation whereas the full-sky result is exact. This difference is very small, showing that Limber approximation for $\mu = 1$ is very good. For $\mu = 0$ on the other hand we see a non-negligible difference between the flat-sky and full-sky result. We will discuss this in more detail in Section 3.2.2.

From the bottom panel, we see that the non-integrated relativistic terms generate a correction of the order of the percent at large separation $r \sim 350\,$Mpc$/h$.

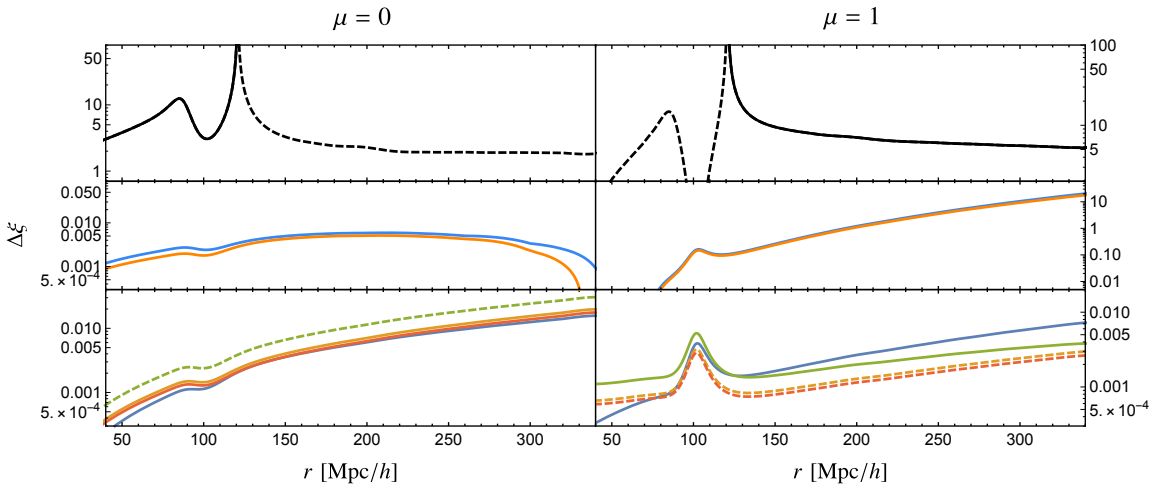

Figure 3.3: The relative difference $\Delta\xi$ at redshift $\bar{z} = 1$ for $\mu = 0$ (left panels) and $\mu = 1$ (right panels). *Top panels:* $\Delta\xi^{\rm rsd} = (\xi^{\rm st} - \xi^{\rm den})/\xi^{\rm den}$. *Middle panels:* fractional difference induced by lensing $\Delta\xi^{\rm lensing}$ (full-sky in orange and flat-sky in blue). *Bottom panels:* $\Delta\xi^A$ where $A =:$ d1 (blue), d2 (orange), g1 (green) and g2 (red). The contribution g3 is subdominant (see Eqs. (3.8) to (3.18) for a definition of the various relativistic terms). Negative contributions are dashed.

Naively we would expect the Doppler term (d1: blue) to dominate over the other relativistic effects because it is proportional to the peculiar velocity and contains therefore one more factor $k/\mathcal{H}$ than the terms proportional to the potentials (see e.g. Eqs. (3.36) to (3.45) below). However, as shown in [48] (see also Appendix 3.B), the correlation of this term with the standard term $\langle\Delta^{\rm d1}\Delta^{\rm st}\rangle$ exactly vanishes in the flat-sky because it is totally anti-symmetric. The contribution that we see in Fig. 3.3 is therefore due to the correlation $\langle\Delta^{\rm d1}\Delta^{\rm d1}\rangle$, which is a factor $\mathcal{H}/k$ smaller, hence $\sim \langle\Delta^{\rm st}\Psi\rangle$ and to the full-sky contributions to $\langle\Delta^{\rm d1}\Delta^{\rm st}\rangle$, which are of the order $r/\chi\langle\Delta^{\rm d1}\Delta^{\rm st}\rangle \sim \langle\Delta^{\rm d1}\Delta^{\rm d1}\rangle \sim \langle\Delta^{\rm st}\Psi\rangle$. Consequently, with one population of galaxies the Doppler contribution to the correlation function is of the same order of magnitude as the gravitational potential contributions (d2, g1 and g2). Only in the case where one cross-correlates two populations of galaxies, the Doppler contribution strongly dominates over the other relativistic contributions, because in this case $\langle\Delta^{\rm d1}\Delta^{\rm st}\rangle$ does not vanish in the flat-sky.

For $\mu = 0$, the Sachs-Wolfe like term (g1) dominates over the other corrections at all scales. For $\mu = 1$ this term still dominates at small separation, but at large separation the full-sky corrections to the Doppler term become important and dominates over g1. Interestingly the second Sachs-Wolfe like term (g2) and the second Doppler term (d2) are nearly equal for both values of μ. It is easy to derive from the continuity and the Poisson equations that in a matter dominated Universe $(\mathcal{H}/k)V = -(2/3)\Phi$, hence $\Delta_\ell^{\rm d2} = \Delta_\ell^{\rm g2}$ if $s = 0$, see Eqs. (3.40) and (3.42). At lower redshifts, when Λ-domination sets in, we expect this equality to be less precise. The relativistic terms not shown in Fig. 3.3 are the Shapiro time delay (g4) and the

integrated Sachs-Wolfe term (g5). These integrated terms are always subdominant with respect to the lensing term.

Let us also note that the difference between the flat-sky standard term and the full-sky standard term is of the same order of magnitude as the relativistic terms depicted in the bottom panel of Fig. 3.3. It is therefore not consistent to use the flat-sky approximation for the standard terms when investigating relativistic effects.

Finally we should point out that in this work we present the *theoretical* contributions of relativistic effects on the correlation function and the power spectrum (see Figs. 3.3, 3.8, 3.11, 3.16 and 3.17). To estimate the *observational* impact of these terms one should build a realistic estimator and proceed with signal-to-noise analysis, forecasts and constraints for a specific survey. Such studies have been performed for the angular power spectrum C_ℓ in [86, 246, 247, 59, 87, 199] and for the anti-symmetric part of the correlation function ξ_g in [49]. In a future work [95], we will develop this for the multipoles of the correlation function and the power spectrum. This will allow us to compare the observational impact of the relativistic effects on the angular power spectrum with their impact on the multipoles of the correlation function and power spectrum, which are the standard observables currently used in large-scale structure surveys to measure the growth rate f.

3.2.2 Direct determination of the correlation function

In the calculation of the correlation function presented in the previous section, we still need all the $C_\ell(z_1, z_2)$ for an accurate calculation. Hence the reason (1) given in the introduction for the use of the correlation function and the power spectrum is not satisfied: the calculation is not simplified. To compute the correlation function for thousands of spectroscopic redshifts in an MCMC would still take months even if very highly parallelised. In this section we show how to improve this. The method explained in this section reduces the calculation of several thousand $C_\ell(z_1, z_2)$'s into just several terms. This results in a very significant speed up so that the computation becomes feasible.

We expand on a method introduced in [57] which avoids the computation of $C_\ell(z_1, z_2)$ but requires integrations in k-space and over the line-of-sight, as we shall see. In this method, no flat-sky approximation is performed, and the correlation function is therefore exact, within linear perturbation theory. We start from expression (3.1) for the correlation function and use that the $C_\ell(z_1, z_2)$ are of the form (see [88]),

$$C_\ell(z_1, z_2) \;=\; \sum_{A,B} C_\ell^{AB}(z_1, z_2)\,, \qquad C_\ell^{AB}(z_1, z_2) \;=\; 4\pi \int \frac{dk}{k} \mathcal{P}_\mathcal{R}(k) \Delta_\ell^A(k, z_1) \Delta_\ell^B(k, z_2)\,. \tag{3.35}$$

Here $\mathcal{P}_\mathcal{R}$ denotes the primordial power spectrum, determined by the amplitude A_s and the primordial spectral index n_s:

$$\mathcal{P}_\mathcal{R}(k) = \frac{1}{2\pi^2} A_s \left(\frac{k}{k_*}\right)^{n_s - 1}\,,$$

and Δ_ℓ^A, Δ_ℓ^B are the Fourier-Bessel transforms of the terms defined in (3.9) to (3.18). More precisely

$$\Delta_\ell^{\rm den} = b(z) S_D j_\ell(k\chi)\,, \tag{3.36}$$

$$\Delta_\ell^{\rm rsd} = \frac{k}{\mathcal{H}} S_V j_\ell''(k\chi)\,, \tag{3.37}$$

$$\Delta_\ell^{\rm len} = \left(\frac{2-5s}{2}\right) \frac{\ell(\ell+1)}{\chi} \int_0^\chi \partial\lambda \frac{\chi-\lambda}{\lambda} (S_\phi + S_\psi) j_\ell(k\lambda)\,, \tag{3.38}$$

$$\Delta_\ell^{\rm d1} = \left(\frac{\dot{\mathcal{H}}}{\mathcal{H}^2} + \frac{2-5s}{\chi\mathcal{H}} + 5s - f_{\rm evo}\right) S_V j_\ell'(k\chi)\,, \tag{3.39}$$

$$\Delta_\ell^{\rm d2} = -(3 - f_{\rm evo}) \frac{\mathcal{H}}{k} S_V j_\ell(k\chi) = \Delta^{\rm d2}(z,k) j_\ell(k\chi)\,, \tag{3.40}$$

$$\Delta_\ell^{\rm g1} = \left(1 + \frac{\dot{\mathcal{H}}}{\mathcal{H}^2} + \frac{2-5s}{\chi\mathcal{H}} + 5s - f_{\rm evo}\right) S_\psi j_\ell(k\chi) = \Delta^{\rm g1}(z,k) j_\ell(k\chi)\,, \tag{3.41}$$

$$\Delta_\ell^{\rm g2} = (-2 + 5s) S_\phi j_\ell(k\chi) = \Delta^{\rm g2}(z,k) j_\ell(k\chi)\,, \tag{3.42}$$

$$\Delta_\ell^{\rm g3} = \frac{1}{\mathcal{H}} \dot{S}_\phi j_\ell(k\chi) = \Delta^{\rm g3}(z,k) j_\ell(k\chi)\,, \tag{3.43}$$

$$\Delta_\ell^{\rm g4} = \frac{2-5s}{\chi} \int_0^\chi \partial\lambda (S_\phi + S_\psi) j_\ell(k\lambda)\,, \tag{3.44}$$

$$\Delta_\ell^{\rm g5} = \left(\frac{\dot{\mathcal{H}}}{\mathcal{H}^2} + \frac{2-5s}{\chi\mathcal{H}} + 5s - f_{\rm evo}\right) \int_0^\chi \partial\lambda (\dot{S}_\phi + \dot{S}_\psi) j_\ell(k\lambda)\,. \tag{3.45}$$

Here j_ℓ are the spherical Bessel functions and the functions $S_X(z,k)$ are the transfer functions for the variable X which we specify in Appendix 3.B. Over-dots indicate derivatives with respect to conformal time. For the evolution bias $f_{\rm evo}$, the magnification bias s and the galaxy bias b we follow the conventions of [88]. From these expressions one also infers the scaling of the different terms with respect to the density term. On sub-Hubble scales, $k > \mathcal{H}$, the scaling of these terms with powers of $\mathcal{H}/k$ is a simple consequence of Newtonian physics. The continuity equation implies $S_V \sim (\mathcal{H}/k) S_D$ and the Poisson equation yields $S_\phi \sim S_\psi \sim (\mathcal{H}/k)^2 S_D$, we see that the density, RSD and lensing terms dominate, while the Doppler term d1 is suppressed by one factor of $(\mathcal{H}/k)$, and all other terms are suppressed by $(\mathcal{H}/k)^2$. For this reason all relativistic terms apart from lensing are strongly suppressed on sub-horizon scales and we call them 'large-scale contributions'. Most of them are relevant only on very large scales close to $\mathcal{H}(z)^{-1}$. Exceptions to this rule are $\Delta_\ell^{\rm d1}$ and $\Delta_\ell^{\rm g1}$ which contain a pre-factor $1/(\chi\mathcal{H})$ which becomes large at very low redshift where χ is small. On super horizon scales all the transfer functions S_X are typically of the same order but they become gauge dependent.

Using these expressions, the correlation function ξ can be written as

$$\xi = \sum_{A,B} \xi^{AB} \qquad \text{with} \qquad \xi^{AB}(\theta, z_1, z_2) = \int \frac{dk}{k}\, \mathcal{P}_\mathcal{R}\; Q_k^{AB}(\theta, z_1, z_2)\,, \tag{3.46}$$

where we define

$$Q_k^{AB}(\theta, z_1, z_2) \equiv \sum_\ell (2\ell+1)\Delta_\ell^A(k, z_1)\Delta_\ell^B(k, z_2)L_\ell(\cos\theta)\,. \tag{3.47}$$

In most of the terms Q_k^{AB} we have a sum of the form

$$\sum_\ell (2\ell+1)L_\ell(\cos\theta)j_\ell(k\chi_1)j_\ell(k\chi_2) \;\; = \;\; j_0(kr)\,, \tag{3.48}$$

where $r = \sqrt{\chi_1^2 + \chi_2^2 - 2\chi_1\chi_2\cos\theta}$ (see e.g. [4] (10.1.45)). Inserting (3.48) into (3.46) we can easily calculate the correlation function for these terms avoiding the numerically costly sum over the C_ℓ's. The redshift-space distortion and the Doppler term give rise to contributions that are slightly different because they contain first and second derivatives of the spherical Bessel functions with respect to $k\chi_1$ and $k\chi_2$. These terms can however be treated in a very similar way using recurrence relations for the spherical Bessel function. For this we define

$$\zeta^{ij} \equiv \sum_\ell (2\ell+1) j_\ell^{(i)}(k\chi_1) j_\ell^{(j)}(k\chi_2) L_\ell(\cos\theta) = \sum_\ell (2\ell+1) j_\ell^{(i)}(x_1) j_\ell^{(j)}(x_2) L_\ell(\cos\theta)\,, \tag{3.49}$$

where we have set $x_i = k\chi_i$ and $j_\ell^{(i)}(x) = \frac{\partial^i}{\partial x^i} j_\ell(x)$. Using

$$\zeta^{ij}(x_1, x_2) = \zeta^{ji}(x_2, x_1) \quad \text{and} \quad \frac{\partial^{n+m}}{\partial x_1^n \partial x_2^m}\zeta^{ij} = \zeta^{i+n, j+m},$$

we can determine explicit expressions for the ζ^{ij} for $i, j \in \{0, 1, 2\}$. They are all given in Appendix 3.B.

The only coefficients that do not fall into this category are the ones in $\Delta_\ell^{\rm len}$ which contain additional factors ℓ and $(\ell+1)$ (see Eq. (3.38)). These terms can however be computed using the identity

$$\triangle_\Omega L_\ell(\cos\theta) = -\ell(\ell+1)L_\ell(\cos\theta)\,.$$

They are given by

$$\zeta^{\rm LL} \equiv \sum_\ell (2\ell+1)\ell^2(\ell+1)^2 j_\ell(x_1) j_\ell(x_2) L_\ell(\cos\theta) = \triangle_\Omega^2\, \zeta^{00}\,, \tag{3.50}$$

$$\zeta^{i{\rm L}} \equiv \sum_\ell (2\ell+1)\ell(\ell+1) j_\ell^{(i)}(x_1) j_\ell(x_2) L_\ell(\cos\theta) = -\triangle_\Omega\, \zeta^{i0}\,, \tag{3.51}$$

where LL denotes the correlation of lensing with itself and iL the cross-correlation of lensing with one of the other terms. With this we can build all the functions Q_k^{AB} and hence, with Eq. (3.46), the correlation function. The complete list of Q_k^{AB} is given in Appendix 3.B. Here we just report the dominant contributions, i.e. the contributions which are not suppressed with additional powers of $\mathcal{H}/k$ with respect to the density term:

$$Q^{\rm den}(\theta, z_1, z_2) = b(z_1)b(z_2)S_D(z_1)S_D(z_2)\,\zeta^{00}(k\chi_1, k\chi_2)\,,$$

$$
\begin{aligned}
Q^{\rm rsd}(\theta,z_1,z_2) &= \frac{k^2}{\mathcal{H}_1\mathcal{H}_2}S_V(z_1)S_V(z_2)\,\zeta^{22}(k\chi_1,k\chi_2)\,,\\
Q^{\rm len}(\theta,z_1,z_2) &= \frac{(2-5s)^2}{4\chi_1\chi_2}\int_0^{\chi_1}\int_0^{\chi_2}\partial\lambda\partial\lambda'\left[\frac{(\chi_1-\lambda)(\chi_2-\lambda')}{\lambda\lambda'}S_{\phi+\psi}(\lambda)S_{\phi+\psi}(\lambda')\zeta^{LL}(k\lambda,k\lambda')\right],\\
Q^{\text{den-rsd}}(\theta,z_1,z_2) &= \frac{kb(z_1)}{\mathcal{H}_2}S_D(z_1)S_V(z_2)\,\zeta^{02}(k\chi_1,k\chi_2)\,,\\
Q^{\text{den-len}}(\theta,z_1,z_2) &= b(z_1)S_D(z_1)\left(\frac{2-5s}{2\chi_2}\right)\int_0^{\chi_2}\partial\lambda\left[\frac{\chi_2-\lambda}{\lambda}\Big(S_\phi(\lambda)+S_\psi(\lambda)\Big)\,\zeta^{0L}(k\chi_1,k\lambda)\right],\\
Q^{\text{rsd-len}}(\theta,z_1,z_2) &= \frac{k}{\mathcal{H}_1}S_V(z_1)\left(\frac{2-5s}{2\chi_2}\right)\int_0^{\chi_2}\partial\lambda\left[\frac{\chi_2-\lambda}{\lambda}\Big(S_\phi(\lambda)+S_\psi(\lambda)\Big)\,\zeta^{2L}(k\chi_1,k\lambda)\right].
\end{aligned}
$$

Note that here and in the following we suppress the argument θ in the functions $\zeta^{\rm AB}(k\chi_1,k\chi_2,\theta)$ for simplicity. The correlation function is then given by Eq. (3.46). For example, the correlation function including only the standard terms is given by

$$
\begin{aligned}
\xi^{\rm st} =& \int\frac{dk}{k}\,\mathcal{P}_{\mathcal{R}}\Big[Q^{\rm den}(\theta,z_1,z_2)+Q^{\text{den-rsd}}(\theta,z_1,z_2)+Q^{\text{rsd-den}}(\theta,z_1,z_2)+Q^{\rm rsd}(\theta,z_1,z_2)\Big]\\
=&\frac{2A_s}{9\pi^2\Omega_m^2}D_1(z_1)D_1z_2)\int\frac{dk}{k}\Big[b(z_1)b(z_2)\zeta^{00}(k\chi_1,k\chi_2)-b(z_1)f(z_2)\zeta^{02}(k\chi_1,k\chi_2)\\
&-b(z_2)f(z_1)\zeta^{02}(k\chi_2,k\chi_1)+f(z_1)f(z_2)\zeta^{22}(k\chi_1,k\chi_2)\Big]\left(\frac{k}{H_0}\right)^4\left(\frac{k}{k_*}\right)^{n_s-1}T^2(k)\,.
\end{aligned}
\tag{3.52}
$$

For the second equal sign we made use of the transfer functions given in Appendix 3.B. Eq. (3.52) is expressed in terms of the redshift z_1 and z_2 and the angle θ. It can however easily be written in terms of a mean redshift $\bar{z}$, the separation of the galaxies r and the orientation of the pair using Eqs. (3.21),(3.22),(3.23).

The correlation function obtained in this way agrees with the full-sky expressions derived in [275, 276, 234] for the standard terms and in [48] for the Doppler term. This method has however the advantage that it can be used to calculate also expressions for the integrated terms valid in the full-sky. Since the lensing is the dominant correction, it is important to have an accurate expression for this term valid at all scales and not relying on the Limber approximation.

μ and r dependence of the correlation function

Let us first discuss the full-sky correlation function as a function of μ and r. In Fig. 3.4 we show the lensing contribution

$$
\xi^{\rm lensing} = \big\langle\big(\Delta^{\rm st}+\Delta^{\rm lensing}\big)(\boldsymbol{n}_1,z_1)\big(\Delta^{\rm st}+\Delta^{\rm lensing}\big)(\boldsymbol{n}_2,z_2)\big\rangle-\big\langle\Delta^{\rm st}(\boldsymbol{n}_1,z_1)\Delta^{\rm st}(\boldsymbol{n}_2,z_2)\big\rangle\,,
\tag{3.53}
$$

as a function of μ and r. We compare the full-sky result (solid lines) with the flat-sky result (dashed lines) derived in [151] and given in Eq. (3.E132). In the top left panel we show the cross-correlation between density and lensing, whereas in the top right panel we show the lensing-lensing correlation. We see that the

flat-sky expression for the lensing-lensing agrees extremely well with the full-sky expression. The density-lensing cross-correlation is however significantly different in the flat-sky and full-sky, even at small separation. This can be understood in the following way. The flat-sky result assumes not only that $\boldsymbol{n}_1 = \boldsymbol{n}_2$, but it also uses the Limber approximation, which implies that only correlations at the same redshift contribute to the correlation function. Hence instead of integrating the lensing along the line-of-sight as is done in the full-sky expression, the flat-sky expression correlates the density at position z_2 with the lensing from the same redshift. This can be seen by looking at Eq. (3.E123), where the integral along the line-of-sight has been replaced by the function $\delta(\chi_2 - \lambda)$. This approximation is quite good for values of μ close to 1, i.e. when the galaxies are behind each other, but it is very bad when μ becomes small and for small separations r. In such cases, the density δ is correlated with the gravitational potentials generated by that same density Φ and Ψ and therefore the correlation is non-negligible even when the two redshifts are not exactly the same. As a result the flat-sky expression, which ignores this direct correlation, strongly underestimates the density-lensing correlation. Since the density-lensing cross-correlation is negative whereas the lensing-lensing is positive, this means that the flat-sky result overestimates the total correlation function, as shown in the bottom left panel of Fig. 3.4. The bottom right panel shows the total lensing contribution as a function of separation for various values of μ. In general we find that the relative difference between the flat-sky and full-sky result is of the order of 20 percents and it can become much larger in some configurations.

In all these plots we do not calculate the lensing contribution when μ is exactly equal to 1. This value is indeed not physical since it would correspond to a galaxy situated exactly behind the other, which we can of course not see. Numerically this value is also problematic because it requires the computation of the correlation function between points that are exactly at the same position. This correlation function diverges if one uses the linear power spectrum and it has to be regularised by non-linear effects which suppress the power spectrum on very small scales, where fluctuations are damped. The largest value that we take is therefore $\mu = 0.9997895$. This value ensures us that the line-of-sight from the most distant galaxy passes sufficiently far away from the closest galaxy to avoid being absorbed by it. In the following when we discuss about the parallel correlation function or when we show plots for $\mu = 1$, this has to be understood as $\mu = 0.9997895$. Finally let us mention that we do not include the correlation between redshift-space distortion and lensing. This correlation is exactly zero in the flat-sky approximation and we do expect it to remain very small in the full-sky [6].

So far we have calculated all the flat-sky and full-sky correlation functions using the linear power spectrum. Since we are mainly interested in correlations at large separations, this is a very well motivated approximation for all the non-integrated terms. We have indeed checked that all the large-scale relativistic contributions change by at most 2-3 percents at small scales if we use the halo-fit power spectrum instead of the linear one to calculate the correlation function. For the lensing con-

[6] We have checked numerically that at $\bar{z} \sim 1$ the RSD-lens contribution to the angular power spectrum is 3 to 4 orders of magnitude smaller than the δ-lens term.

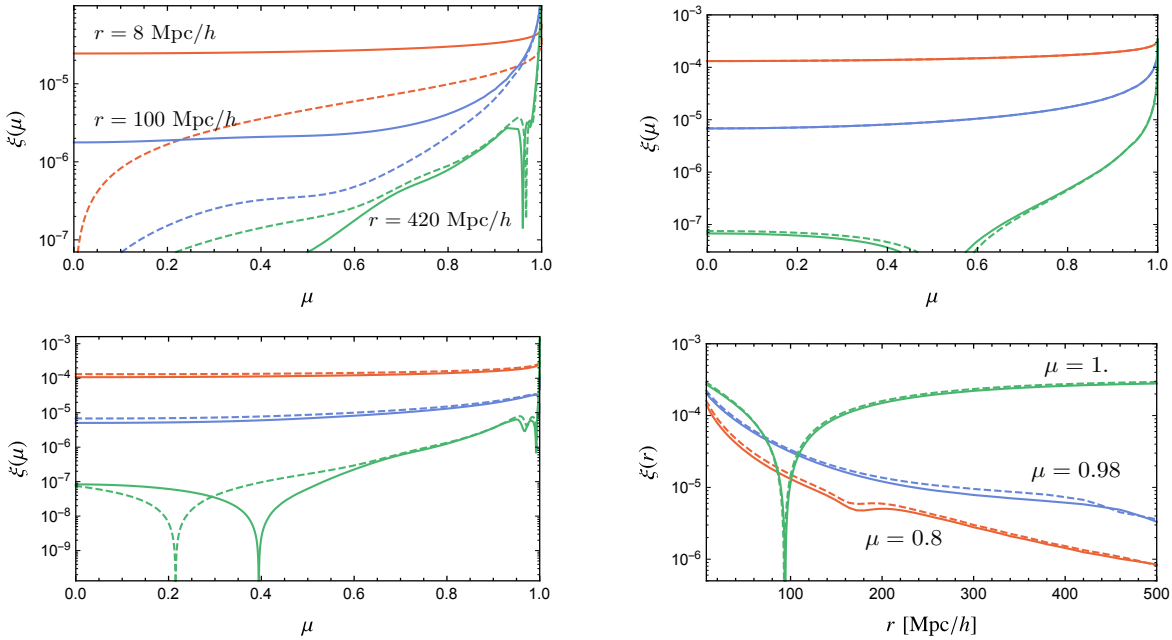

Figure 3.4: Top panels: correlation between density and lensing (left) and lensing-lensing (right) at $\bar{z} = 1$, as a function of μ and for fixed separation $r = 8\,\mathrm{Mpc}/h$ (orange), $r = 100\,\mathrm{Mpc}/h$ (blue) and $r = 420\,\mathrm{Mpc}/h$ (green). Solid lines show the full-sky result and dashed lines the flat-sky result using Limber approximation. Bottom panels: total lensing contribution as a function of μ (left) and r (right) at $\bar{z} = 1$.

tribution on the other hand, non-linearities are important even at large separation, as already pointed out in [151, 200, 150]. This is due to the fact that lensing is sensitive not only to correlations between the two positions of the galaxy, but also to all correlations between the two lines-of-sight from these galaxies. When μ is large, these two lines-of-sight are close to each other at least in the vicinity of the observer, even when r is large, and consequently non-linear effects are important. Lensing has the property to mix large and small separations and a full-sky non-linear treatment is therefore necessary.

The simplest way to calculate the full-sky lensing non-linearly is to use the Poisson equation to relate the gravitational potentials along the line-of-sight to the density (this equation is indeed valid also in the non-linear regime) and to use halo-fit to calculate the non-linear density power spectrum. This procedure can however not be implemented exactly because the full-sky lensing requires the density power spectrum at different redshifts along the two lines-of-sight $P_m(k, z, z')$ where z and z' can take any values between 0 and z_1 and z_2. Halo-fit gives an expression for the power spectrum only when $z = z'$. Note that this problem does not arise in the calculation of the flat-sky expression which uses Limber approximation and therefore neglects correlations coming from $z \neq z'$. In order to overcome this problem we use the following approximate procedure: we calculate the non-linear power spectrum at

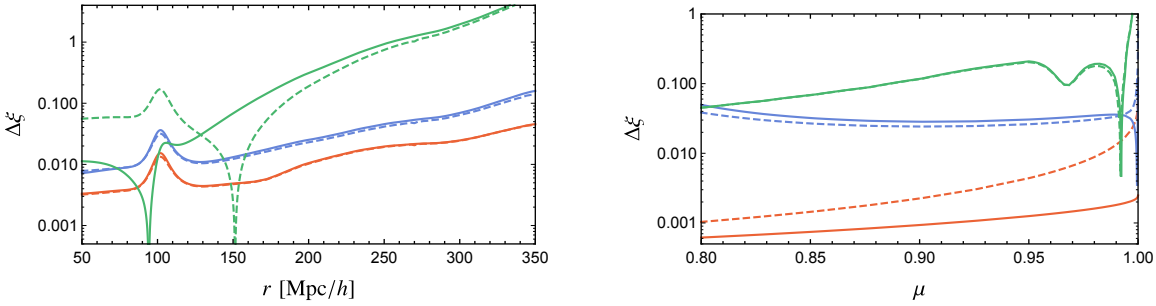

Figure 3.5: Fractional differences $\Delta\xi^{\rm lensing}$ at redshift $\bar{z} = 1$ using the full-sky formalism. The solid lines show the fractional difference using the linear transfer function and the dashed line is using halofit. In the *left panel* we show $\Delta\xi^{\rm lensing}$ as a function of separation r for fixed values of μ: $\mu = 1$ (green), $\mu = 0.98$ (blue) and $\mu = 0.8$ (orange), and in the *right panel* we show it as a function of μ for fixed separation: $r = 8{\rm Mpc}/h$ (orange), $r = 100{\rm Mpc}/h$ (blue) and $r = 420{\rm Mpc}/h$ (green).

a middle redshift along the line-of-sight z_* and then evolve it using the linear growth rate $D_1(z)$ along the photon trajectory. This is of course not completely correct because in the non-linear regime density does not evolve with the linear growth rate, but it gives us a good approximation of the true non-linear lensing contribution. To determine which z_* is the most appropriate, we use the flat-sky approximation [7]. We checked that our result behaves in a consistent way when we vary z_*, which gives us confidence in this approximation (see Fig. 3.19 in Appendix 3.C for more detail).

In Fig. 3.5 we show the fractional difference with respect to the standard term due to the full-sky lensing in the linear and non-linear regime $\Delta\xi^{\rm lensing}$. Contrary to Fig. 3.3 where the fractional difference of all the terms was calculated with respect to the full-sky standard term, here we show the fractional difference with respect to the flat-sky standard term given in Eq. (3.6). In this way Fig. 3.5 can be directly interpreted as the fractional error that one makes when using the standard flat-sky correlation function instead of the full-sky observable correlation function containing lensing [8]. Clearly, lensing becomes very important at large separation and large μ. Neglecting it in this regime can therefore impact the determination of cosmological

[7] More precisely we do the following: we calculate the flat-sky contribution using the correct non-linear power spectrum integrated along the line-of-sight (remember that in the flat-sky we can do that since we have only one line-of-sight). Then we use the same approximation as in the full-sky to calculate also the flat-sky and we compare the correct flat-sky result with the approximate flat-sky result for various values of z_*. This allows us to find the best z_*. For $z = 1$ we find $z_* = 0.42$ and for $z = 2$, $z_* = 0.73$.

[8] Note that to calculate the flat-sky standard expression in the non-linear regime we use the linear continuity equation to relate the velocity to the density and then we use halo-fit for the density power spectrum. This procedure is not completely correct as the continuity equation is also modified in the non-linear regime. Current data analyses use a more sophisticated procedure to calculate the non-linear redshift-space distortions, based on [106]. Our procedure is however conservative since it tends to overestimate the impact of non-linearities on redshift-space distortions and therefore to underestimate the relative importance of lensing.

parameters in a significant way. We defer a detailed study of this impact to a future work [95]. Comparing linear and non-linear results, we find that for $\mu = 1$, the non-linear result is very different from the linear one at all separations up to $250\,\mathrm{Mpc}/h$. For $r \leq 150\,\mathrm{Mpc}/h$, the non-linear lensing is significantly enhanced with respect to the linear regime. At larger separation however, the tendency is reversed. This reflects the fact that non-linearities move power from small to large k. On the right panel we see that at small separation, $r = 8\,\mathrm{Mpc}/h$, the non-linear lensing is significantly larger than the linear one for all μ. In summary, Fig. 3.5 shows that lensing cannot be neglected at redshift 1 and that it has to be calculated in the full-sky non-linear regime, because it mixes small scales (where non-linearities are important) and large scales (where full-sky effects are important).

Multipole expansion of the correlation function

The correlation function is in general a function of separation r and orientation μ. However, the dependence in μ of the standard flat-sky expression (3.6) is very simple, since it is given by $L_2(\mu)$ and $L_4(\mu)$ only. This simple dependence has been exploited to measure directly the growth rate f. In practice this means that each pair of galaxies is weighted either by $L_0(\mu) = 1$, $L_2(\mu)$ or $L_4(\mu)$. The average over all orientations is then performed, allowing one to measure the coefficient in front of each of the L_ℓ, i.e. the monopole, quadrupole and hexadecapole.

In the full-sky regime the dependence of redshift-space distortions on μ becomes more complicated, first due to the fact that $\boldsymbol{n}_1$ and $\boldsymbol{n}_2$ are not parallel (wide-angle effects) and second because the growth rate and bias are evolving with time $f(z_1) \neq f(z_2)$. In addition, the large-scale relativistic effects and the integrated effects have their own μ-dependence, which cannot be simply expressed in terms of $L_2(\mu)$ and $L_4(\mu)$ as we saw in Fig. 3.4. As a consequence the multipole expansion of the full-sky observable correlation function differs from the flat-sky standard expansion. Firstly the monopole, quadrupole and hexadecapole of the full-sky standard term differ from the flat-sky ones. Secondly, these multipoles get corrections from the relativistic and lensing contributions. And finally, due to wide-angle effects and lensing, the multipoles beyond $\ell = 4$ no longer vanish.

In Fig. 3.6 we show the impact of wide-angle effects on the monopole, quadrupole and hexadecapole. Since the standard terms are almost not affected by non-linearities above $20\,\mathrm{Mpc}/h$, we calculate these multipoles using the linear power spectrum. In black we show the flat-sky multipoles from density and redshift-space distortions, that are simply given by the coefficients in front of $L_\ell(\mu)$ in Eq. (3.6). In blue, purple and green we show the full-sky multipoles from density and redshift-space distortions obtained from expression (3.52), which we multiply by the appropriate

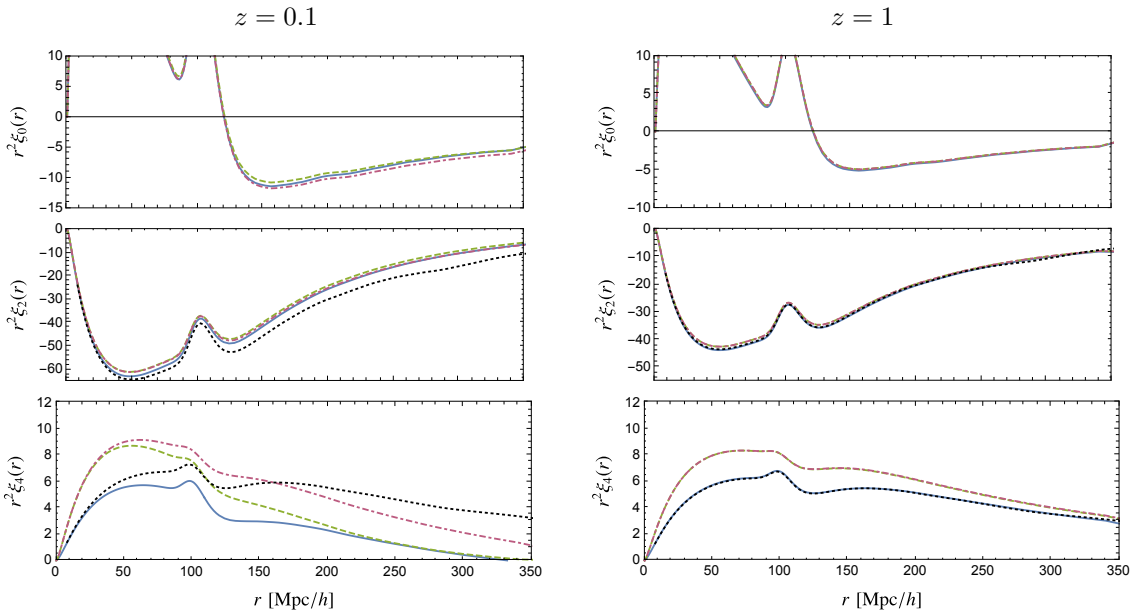

Figure 3.6: The multipoles from density and redshift-space distortions, $\xi^{\rm st}$, at redshift $\bar{z} = 0.1$ (left) and $\bar{z} = 1$ (right). We show the monopole (top) quadrupole (middle) and hexadecapole (bottom) for different definitions of the angle in the full-sky: μ (blue, solid), $\cos\gamma$ (purple, dash-dotted) and $\cos\beta$ (green, dashed) and we compare this with the flat-sky multipoles obtained from (3.6) (black, dotted).

Legendre polynomial and numerically integrate over directions [9]

$$\xi_\ell(r,\bar{z}) = \frac{1}{2\ell+1}\int_{-1}^{1}\xi(r,\bar{z},\sigma)L_\ell(\sigma)d\sigma\,. \tag{3.54}$$

As discussed in Section 3.2.1, in the full-sky there is no unique way to define the orientation of the pairs of galaxies. We therefore calculate the multipoles for different choices: $\sigma = \cos\beta$, $\sigma = \cos\gamma$ and $\sigma = \mu$. The amplitude of the multipoles depends on this choice, as can be seen from the different colours in Fig. 3.6. At redshift $\bar{z} = 1$ (right), we find that the monopole differs only at very large scales by a few percent, while the quadrupole also differs at intermediate scales by a few percent. The hexadecapole is significantly different at most scales. At redshift $\bar{z} = 0.1$ (left) the difference is much more important, up to 10% on the quadrupole at intermediate scales already. And the hexadecapole is very different at most scales. As already pointed out in [275, 276, 234, 245, 256, 34, 311] it is therefore important to account for wide-angle effects when interpreting the multipoles. We also see in Fig 3.6 that the angle which is closest to the flat-sky result is nearly always μ and especially it

[9] Note that the multipoles defined in Eq. (3.54) completely differ from the multipoles defined in [249] (see their Eq. (17)). The multipoles in (3.54) are defined at fixed galaxy separation r and they correspond to what observers are measuring in redshift surveys. The multipoles in [249] are on the contrary defined at fixed angular separation θ (see their Fig. 1). As a consequence they mix different separations r and have completely different properties.

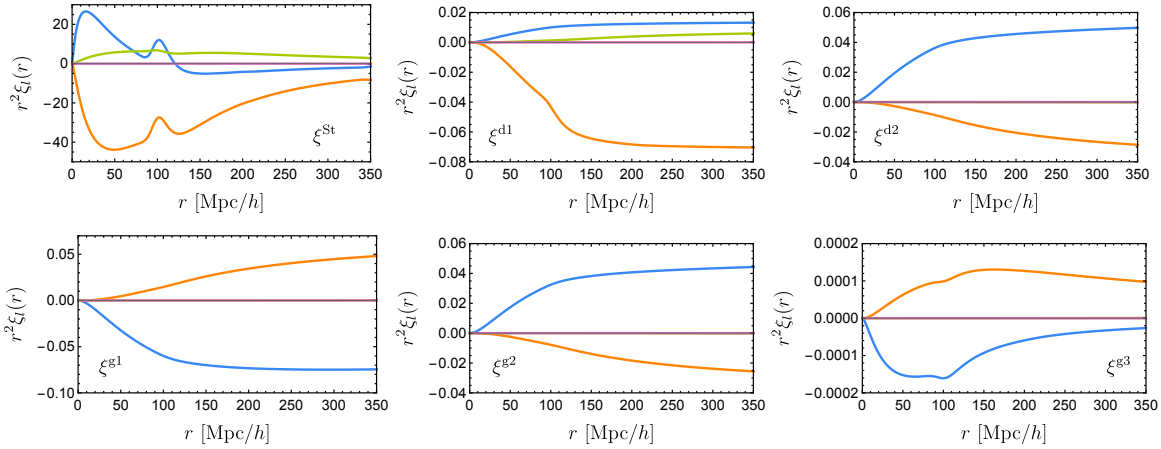

Figure 3.7: We show the multipoles of different contributions to the full-sky correlations function at $\bar{z} = 1$. The monopole (blue), quadrupole (orange), hexadecopole (green) and $\ell = 6$ purple.

is always μ for $\bar{z} = 1$. Note that in [252], expressions for the dominant wide-angle corrections to the monopole, quadrupole and hexadecapole have been derived for various choices of angles.

In Fig. 3.7 we show the multipoles from all the non-integrated contributions in the full-sky linear regime. We use the angle μ for this figure. Each plot represents a different relativistic contribution (see Eqs. (3.9) to (3.18) for a definition of the terms). As in Figs. 3.3 and 3.5, this encompasses the correlation of the term with itself as well as its cross-correlation with the standard term (density and redshift-space distortion). One would naively expect that the dominant contribution would come from the Doppler term d1 correlated with the standard term. However, as discussed in Section 3.2.1, this contribution exactly vanishes in the flat-sky approximation. It would contribute only to a dipole, which cannot be seen with one population of galaxies, due to its anti-symmetry (indeed only even multipoles exist in this case). As a consequence to measure the dominant dipole one needs to cross-correlate two populations of galaxies, as discussed in [48, 49, 112, 125].

However, as discussed in Section 3.2.1, in the full-sky the Doppler-standard correlation does not exactly vanish and it contributes to the even multipoles. The amplitude of this term is then of the same order of magnitude as the d1-d1 correlation and as the other relativistic terms (for example g1 correlated with density). This is evident from the various panels in Fig. 3.7, where we see that all the non-integrated relativistic terms generate multipoles of the same order of magnitude. The only exception is g3 which is much smaller. This is not surprising since at $z = 1$ the universe is still matter dominated and the gravitational potential is nearly constant. For the same reason also d2 and g2 are very similar.

The Doppler contribution is the only one which generates a non-negligible hexadecapole. This comes from the correlation of d1 with redshift-space distortions which contains 3 gradient of the potential. In the flat-sky this gives rise to a μ^3-

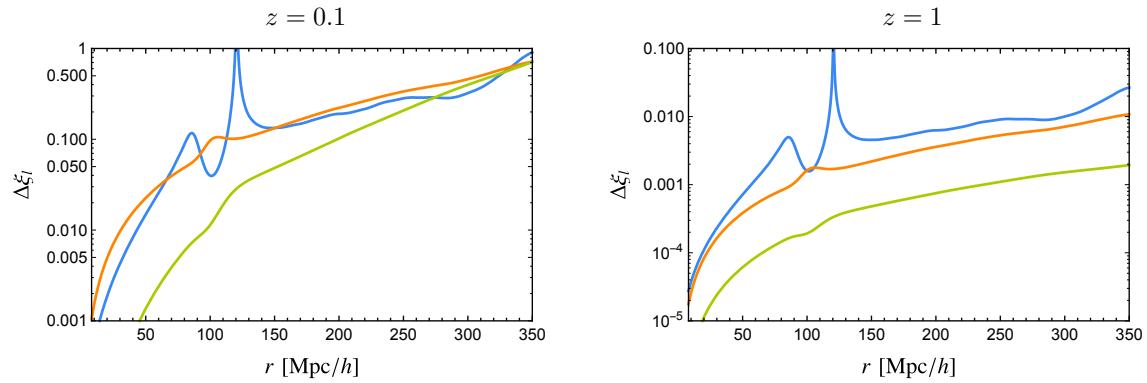

Figure 3.8: Fractional difference generated by the sum of the non-integrated relativistic effects on the monopole (blue), quadrupole (orange) and hexadecapole (green). The relativistic multipoles are calculated in the full-sky linear regime, whereas the standard multipoles are calculated in the flat-sky linear regime, to reproduce the theoretical prediction currently used.

dependence, which again vanishes for symmetry reason, but in the full-sky one obtains an additional factor $\mu \cdot r/\chi$ which leads to an hexadecapole [10]. In the flat-sky the other relativistic terms (d2, g1, g2 and g3) generate only a monopole and quadrupole, due to their correlation with redshift-space distortion. In the full-sky they do generate higher multipoles, but again those are suppressed by powers of r/χ and are consequently negligible.

In Fig. 3.8 we plot the fractional difference due to all non-integrated effects with respect to the standard flat-sky multipoles

$$\Delta\xi_\ell^{\rm rel} = \frac{\xi_\ell^{\rm rel}}{\xi_\ell^{\rm st,flat-sky}}\,, \tag{3.55}$$

where $\xi_\ell^{\rm rel}$ contains the correlation of all the non-integrated relativistic terms with themselves as well as their correlation with the standard term, i.e. they come from

$$\langle\Delta^{\rm st}\Delta^{\rm rel}\rangle + \langle\Delta^{\rm rel}\Delta^{\rm st}\rangle + \langle\Delta^{\rm rel}\Delta^{\rm rel}\rangle = \langle\Delta^{\rm st+rel}\Delta^{\rm st+rel}\rangle - \langle\Delta^{\rm st}\Delta^{\rm st}\rangle\,. \tag{3.56}$$

At $\bar{z} = 1$ (right panel), the relativistic terms modify the monopole by a few percent at separations $\geq 300\,{\rm Mpc}/h$. The impact of these terms on parameter estimation is therefore probably negligible at high redshift. At $\bar{z} = 0.1$ however (left panel) the relativistic contribution to the multipoles is non-negligible at most scales. The contributions to the monopole and quadrupole are already of a few percent at $50\,{\rm Mpc}/h$. At $100\,{\rm Mpc}/h$ these contributions reach 10% and they quickly increase with separation.

The large amplitude of the relativistic terms at small redshift is due to one specific term in the Doppler contribution, namely the one proportional to $1/(\mathcal{H}\chi)$

[10] This can been seen for example by expanding $\alpha_1 - \alpha_2$ in powers of r/χ in the expression ζ^{12} in Appendix 3.B.

(see Eq. (3.12)). The correlation of the Doppler term with itself has roughly the following amplitude:

$$1/(\mathcal{H}\chi)^2(\mathcal{H}/k)^2\langle\Delta^{\rm den}\Delta^{\rm den}\rangle \sim (r/\chi)^2\langle\Delta^{\rm den}\Delta^{\rm den}\rangle\,,$$

where we have used that k corresponds to $1/r$. At small redshift and large separation, this suppression is not very strong. For example at $\bar{z} = 0.1$, $\chi = 433\,\mathrm{Mpc}/h$ and therefore the amplitude of the Doppler term at $r = 200\,\mathrm{Mpc}/h$ is roughly $(r/\chi)^2\langle\Delta^{\rm den}\Delta^{\rm den}\rangle \sim 0.2\langle\Delta^{\rm den}\Delta^{\rm den}\rangle$, i.e. 20% of the standard term. The same argument applies to the full-sky Doppler-standard correlation which contributes at the same level. The other relativistic terms on the other hand are more strongly suppressed. For example, the correlation g1-standard has the following amplitude: $1/(\mathcal{H}\chi)(\mathcal{H}/k)^2\langle\Delta^{\rm den}\Delta^{\rm den}\rangle \sim (r/\chi)r\mathcal{H}\langle\Delta^{\rm den}\Delta^{\rm den}\rangle$. At $\bar{z} = 1$, $\mathcal{H} \sim 1/\chi$ and the Doppler contribution is similar to the g1 contribution, as already discussed. At $\bar{z} = 0.1$ however, $\mathcal{H}$ is significantly smaller than $1/\chi$ and therefore the Doppler contribution is enhanced with respect to the g1 contribution. Note that the importance of this Doppler effect on the correlation function has already been studied in detail in [234] and further discussed in [245, 256]. These references, however, do not include the other Doppler terms or lensing.

This result is especially relevant for a survey like the SKA that will cover wide parts of the sky from $z = 0$ to 2 and will therefore be strongly affected by the Doppler term at low redshift. In a forthcoming publication we will study the impact of this effect on the measurement of cosmological parameters, in particular on the measurement of the growth rate f from the monopole and quadrupole. Note that, as discussed above, such a study has to be performed using the full-sky formalism, since full-sky effects (from the Doppler-density correlation) contribute at the same level.

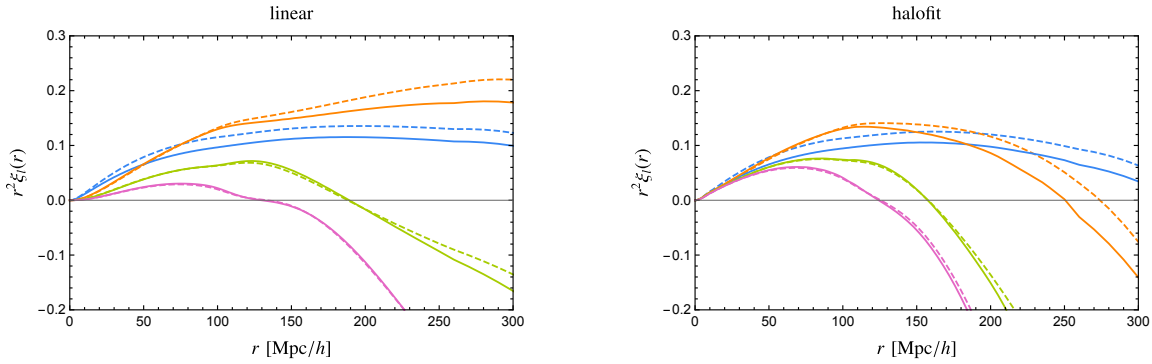

Figure 3.9: Multipoles of the lensing contribution (including its correlation with the standard term) at $\bar{z} = 1$. In the left panel we show the linear full-sky (solid) and linear flat-sky (dashed) result and in the right panel the non-linear full-sky (solid) and flat-sky (dashed) result. The monopole is shown in blue, the quadrupole in orange, the hexadecapole in green and the $\ell = 6$ in purple.

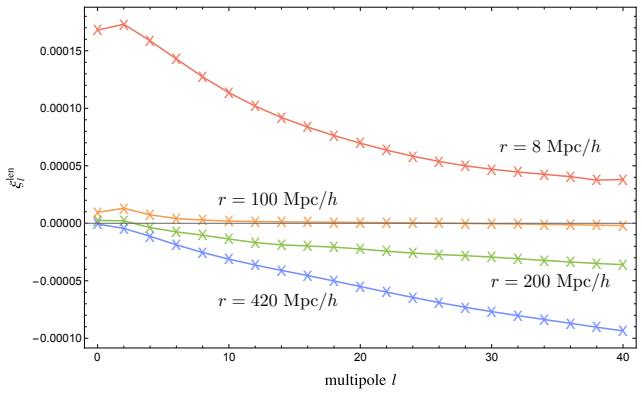

Figure 3.10: The full-sky non-linear lensing multipoles as a function of ℓ for different separations at $\bar{z} = 1$.

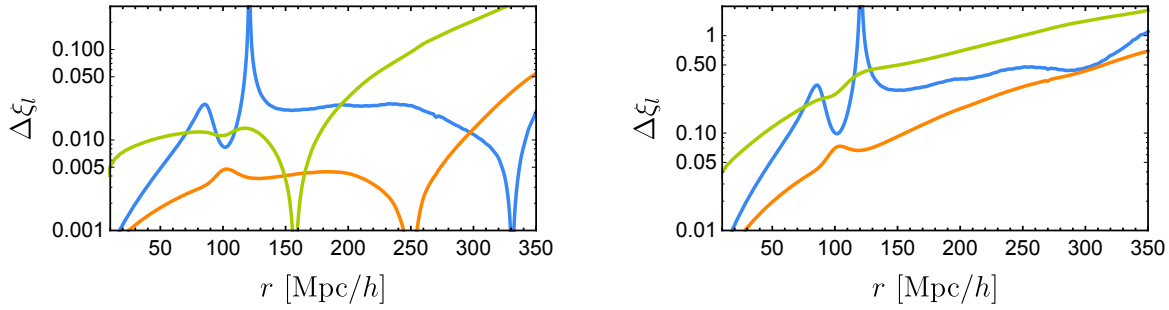

Figure 3.11: Fractional difference generated by lensing on the monopole (blue), quadrupole (orange) and hexadecapole (green). The lensing multipoles are calculated in the full-sky non-linear regime, whereas the standard multipoles are calculated in the flat-sky non-linear regime, to reproduce the theoretical prediction currently used. The left panel is for $\bar{z} = 1$ and the right panel for $\bar{z} = 2$.

In Fig. 3.9 we show the lensing contribution to the multipoles at $\bar{z} = 1$. In the left panel we show the linear result, using the flat-sky and Limber approximation (dashed) and the full-sky calculation (solid); and in the right panel we show the non-linear result. The flat-sky systematically overestimates the lensing contribution. As explained in Section 3.2.2 this is due to the fact that the Limber approximation underestimates the correlation between density and lensing, which is negative, and consequently it overestimates the total in most configurations. Above $r \sim 50h^{-1}$Mpc the lensing contribution is 10% and more. Hence it has to be included for an accurate estimation of the growth rate f. Contrary to the non-integrated relativistic effects, lensing generates non-negligible $\ell = 4$ and $\ell = 6$. Actually, as is shown in Fig. 3.10 the amplitude of the multipoles remains large for large values of ℓ. Measuring $\ell > 4$ will therefore provide a way of isolating the lensing contribution from the standard terms.

In Fig. 3.11 we show the fractional difference of the monopole, quadrupole and hexadecapole generated by lensing at $\bar{z} = 1$ and $\bar{z} = 2$. At $\bar{z} = 1$ we see that lensing

modifies the monopole by a few percent at intermediate scales. The quadrupole is less affected, apart from at very large scales $r \sim 350\,\mathrm{Mpc}/h$ where lensing contributes by 5%. The hexadecapole is the one that is the most affected by lensing, up to 10-20% above $250\,\mathrm{Mpc}/h$. At $\bar{z} = 2$ the lensing contribution is significant for all multipoles. The monopole is modified by 30% already at a $150\,\mathrm{Mpc}/h$ and this increases to 50% at $300\,\mathrm{Mpc}/h$. The contribution to the quadrupole is slightly smaller, but it still reaches 10% at $150\,\mathrm{Mpc}/h$ and 40% at $300\,\mathrm{Mpc}/h$. And the hexadecapole is strongly affected at all scales. Surveys like Euclid and the SKA, that will observe up to high redshift should therefore include lensing in their modelling of the multipoles of the correlation function.

In this Section we have only discussed the contribution from even multipoles to the correlation function. As stated before, in the flat-sky approximation only even multipoles exist, even in the presence of relativistic effects and lensing [11]. This follows directly from the fact that the correlation function is symmetric $\xi(\mathbf{r}) = \xi(-\mathbf{r})$ and that the flat-sky angle goes from μ to $-\mu$ when $\mathbf{r}$ goes to $-\mathbf{r}$. In the full-sky, the existence of odd multipoles depend on the choice of angle used to measure them. If the cosine of the angle simply changes sign when $\mathbf{r}$ goes to $-\mathbf{r}$, then odd multipoles exactly vanish also in the full-sky. This is the case for the angles β, γ and α defined in Fig. 3.1. However if one uses instead the angle α_1 (see Fig. 3.18) to measure the multipoles, then the correlation function contains odd multipoles in the full-sky because α_1 goes to $\pi + \alpha_1 - \theta$ when $\mathbf{r}$ goes to $-\mathbf{r}$. Hence even if the correlation function is symmetric, its expansion in terms of α_1 contains odd multipoles due to the fact that the angle itself breaks the symmetry of the configuration [252]. Note that the dipole of the correlation function using the angle α_1 has been measured in [112]. Finally let us stress that if we cross-correlate different populations of galaxies, then the correlation function is not symmetric anymore $\xi_{AB}(\mathbf{r}) \neq \xi_{BA}(-\mathbf{r})$ (where A and B denote the two populations under considerations) and it contains therefore odd multipoles already in the flat-sky approximation, as demonstrated in [48].

3.3 From the correlation function to the power spectrum

As discussed in the introduction, an alternative observable which is routinely used to analyse redshift surveys is the power spectrum. Here we discuss the impact of the large-scale relativistic effects and of the lensing on this observable.

Of course, since galaxies are seen on our background light-cone and not in 3D physical space, a galaxy position is fixed by a redshift z and a direction $\boldsymbol{n}$. But we can split the distance vector between two galaxies, $\mathbf{r}$ (which is the argument of the galaxy correlation function $\xi(\mathbf{r}, \bar{z})$) in a sufficiently small redshift bin into a radial, $r_\parallel$ and a transverse, $r_\perp$ component and express ξ in the variables $\xi(r_\parallel, r_\perp, \bar{z})$. We can then define the power spectrum simply as the Fourier transform of the correlation

[11] Note that this is not the case with the alternative definition of multipoles used in [248] which mixes different scales.

function,

$$P(k_\parallel, k_\perp, \bar{z}) = \int d^3r \xi(r_\parallel, r_\perp, \bar{z}) e^{i(r_\parallel k_\parallel + r_\perp k_\perp \cos\phi)} \tag{3.57}$$

$$= 2\pi \int_{-\infty}^{\infty} dr_\parallel \int_0^{\infty} dr_\perp \xi(r_\parallel, r_\perp, \bar{z}) e^{i(r_\parallel k_\parallel)} J_0(k_\perp r_\perp)\,. \tag{3.58}$$

In this expression $r_\parallel = r\sigma$ and $r_\perp = r\sqrt{1-\sigma^2}$ where

$$[-1,1] \ni \sigma = \begin{cases} \mu = \cos\alpha \\ \cos\beta \\ \cos\gamma \\ \cos\alpha_2 \end{cases} \tag{3.59}$$

depending on the angle used to split the survey into a radial and a transversal component. Note that $\mathbf{r}_\perp = r_\perp(\cos\phi, \sin\phi)$ is a 2D vector in the plane normal to the parallel direction and we have performed the ϕ integration choosing the x-axis in the $\mathbf{r}_\perp$ plane parallel to $\mathbf{k}_\perp$. For the case $\sigma = \mu$, $r_\parallel = \chi_2 - \chi_1$ the expression for the correlation function is given in Appendix 3.B and Section 3.2, (3.46). For the other angles, one has to use the relations given in Appendix 3.A.

However, we must consider that while the correlation function as given e.g. in Eq. (3.24) can be defined for all values $r_\parallel \in [0, \chi(\infty)] \simeq [0, 14h^{-1}\mathrm{Gpc}]$ and $r_\perp \in [0, 2\chi(\infty)]$, and is correct for $|r_\parallel H(\bar{z})| \ll 1$, this is no longer so for its Fourier transform[12]. To compute it we have to integrate the correlation function over all space, but as we just said, we cannot observe the correlation function outside of our horizon and the result is not reliable if $|r_\parallel H(\bar{z})| \gtrsim 1$. It is well defined only for a range of $(r_\parallel, r_\perp)$. This situation is further complicated by the fact that this range depends on redshift. Therefore, the simple Fourier transform given above gives a physically sensible result only for

$$k_\parallel \gg \frac{1}{\chi(\bar{z}+\Delta z) - \chi(\bar{z}-\Delta z)} \sim 2\Delta z H(\bar{z}) = \frac{1}{r_{\parallel\,\max}(\bar{z}, \Delta z)}\,, \qquad \Delta z \ll 1.$$

For these values of $k_\parallel$, contributions from radial distances such that the two galaxies are not in a thin shell around $\bar{\chi} = \chi(\bar{z})$ are cancelled by the rapid oscillations of the exponential in the Fourier transform.

With this word of caution we now simply Fourier transform the correlation function to obtain the power spectrum. We can either use the correlation function obtained via the $C_\ell(z_1, z_2)$'s or the one from the direct computation. Here we present the details for the latter.

As stated above, for the 'true' power spectrum, the integral over $r_\parallel$ should extend from $-\infty$ to $+\infty$ and the integral over $r_\perp$ should extend from 0 to $+\infty$. The correlation function is however not observable outside the horizon and the integral must therefore be truncated by a window function which removes these scales. In practice galaxy surveys do not observe the whole horizon but only part of it and

[12]Here $\chi(\infty) \simeq 14h^{-1}$Gpc represents the comoving size of our horizon today.

therefore the range of integration is even more reduced. The true window function of the observation patch leads to a convolution in the correlation function and therefore to a multiplication of the Fourier transform of the window in the power spectrum

From Eq. (3.58) we see that there is another reason to truncate the integral. The arguments $k_\parallel$ and $k_\perp$ (or equivalently k and $\nu = \hat{\mathbf{k}} \cdot \hat{\boldsymbol{n}}$) of the power spectrum are parallel to $r_\parallel$ and $r_\perp$ respectively. Now the direction of $r_\parallel$, for example, depends on the direction of the pair of galaxies we consider. If the domain of integration in (3.58) is sufficiently small, then a mean direction $\boldsymbol{n}$ can be introduced and this splitting is well defined: one can identify one line-of-sight for the whole patch of sky we are observing and split parallel and transverse directions with respect to this line-of-sight. If the patch is too large however, this procedure is no longer valid [13]. The integral (3.58) can still be done mathematically, but its physical interpretation becomes unclear. This illustrates the fact that the power spectrum is truly well defined only in the flat-sky. In practice this means that we can consider the Fourier transform of the correlation function in a sphere of radius $\Delta z/\mathcal{H}(\bar{z})$ for values $k \gg \mathcal{H}(\bar{z})/\Delta z$.

Similar to what is done for the correlation function, in the standard analysis, the ν dependence of $P(k, \nu, \bar{z})$ is used to extract the growth rate $f(\bar{z})$. Indeed as seen in Eq. (3.2), the standard power spectrum takes the simple form

$$P(k, \nu, \bar{z}) = p_0(k, \bar{z}) + p_2(k, \bar{z}) L_2(\nu) + p_4(k, \bar{z}) L_4(\nu) \,, \tag{3.60}$$

where the coefficients p_n are given by:

$$p_0(k, \bar{z}) = D_1^2(\bar{z}) P_m(k) \left[b^2 + \frac{2bf}{3} + \frac{f^2}{5} \right] , \tag{3.61}$$

$$p_2(k, \bar{z}) = D_1^2(\bar{z}) P_m(k) \left[\frac{4bf}{3} + \frac{4f^2}{7} \right] , \tag{3.62}$$

$$p_4(k, \bar{z}) = D_1^2(\bar{z}) P_m(k) \frac{8f^2}{35} \,. \tag{3.63}$$

The multipoles p_0 and p_2 contain different combinations of the bias and of the growth rate $f(\bar{z})$ and can be used to measure these two quantities. If p_4 can be measured as well it can be used as an additional consistency check. Furthermore, this quantity is independent of galaxy bias which renders it especially valuable.

The large-scale relativistic effects and the gravitational lensing are however expected to modify this simple multipole expansion. In principle to calculate the contribution of these effects to the multipoles, one would need to calculate Eq. (3.58) for all values of $k_\parallel$ and $k_\perp$ and then integrate over all directions, weighting by the appropriate Legendre polynomial

$$p_\ell(k, \bar{z}) = \frac{1}{2\ell + 1} \int_{-1}^{1} d\nu P(k, \nu, \bar{z}) L_\ell(\nu) \,. \tag{3.64}$$

As the correlation function is a symmetric function of μ, $\xi(\boldsymbol{x}_1, \boldsymbol{x}_2) = \xi(\boldsymbol{x}_2, \boldsymbol{x}_1)$, the power spectrum will be symmetric in ν so that only even ℓ's are non-zero. This

[13] Note however the work of [304] which proposes methods to account for different lines-of-sight in the measurement of the power spectrum.

is no longer the case when one correlates different tracers, e.g. bright and faint galaxies [214, 312].

The procedure to obtain the multipoles of the power spectrum can however be simplified by using directly the multipoles of the correlation function $\xi_\ell(r)$ (see Appendix 3.D for a proof of this relation)

$$p_\ell(k) = 4\pi i^\ell \int_0^\infty dr r^2 j_\ell(kr)\xi_n(r)\,. \tag{3.65}$$

As discussed before, the integral over r cannot run until infinity because the correlation function (and consequently its multipoles) is not observable over the whole space. For simplicity we assume that we observe galaxies within a sphere of radius $r_{\rm max}$, centred at redshift $\bar{z}$. This corresponds to introducing a window function in Eq. (3.65) which removes scales larger than $r_{\rm max}$. For the standard terms, the multipoles $p_\ell(k)$ are relatively insensitive to the choice of $r_{\rm max}$ since $r^2\xi^{\rm st} \to 0$ as $r \to \infty$. The large-scale relativistic effects scale however as $r^2\xi^{\rm rel} \to$ constant as $r \to \infty$ and consequently their multipoles depend on the choice of $r_{\rm max}$. This reflects the fact that these terms diverge when $k \to 0$ as we will see in section 3.3.1. The situation for the lensing term is even worse: the correlation function scales as $r^2\xi^{\rm len} \to \infty$ and the dependence in $r_{\rm max}$ is even stronger. The lensing power spectrum is therefore strongly dependent on the geometry of the survey, as already noticed in [200].

3.3.1 The flat-sky approximation

In the previous section we obtained the power spectrum by integrating over the full-sky correlation function, weighted by a window function to restrict the range of integration to the observed patch of the sky. Here we would like to compare this procedure with a flat-sky direct calculation of the power spectrum [14]. The power spectrum for the non-integrated terms has been derived previously in [165, 312]. It can be easily obtained by Fourier transforming the non-integrated relativistic contributions to the number counts, namely $\Delta^{\rm d1}, \Delta^{\rm d2}, \Delta^{\rm g1}, \Delta^{\rm g2}$ and $\Delta^{\rm g3}$ (see Eqs. (3.12) to (3.16)). Note that in principle this procedure does not generate an observable, because the Fourier transform of a function $f(\mathbf{k}, \eta)$ at a given conformal time η requires the knowledge of the function over the whole hypersurface of constant η [15]. An observer cannot observe this hypersurface, but only its intersection with her past light-cone. However, due to the statistical homogeneity and isotropy of our Universe, the properties of the function are the same everywhere, and the Fourier transform can be performed. We obtain (in agreement with [165] where only the non-integrated terms are considered)

$$P_\Delta^{\rm flat,\,non-int}(k,\nu,z) = \left| A + B\,\frac{\mathcal{H}}{k} + C\left(\frac{\mathcal{H}}{k}\right)^2 \right|^2 D_1^2(z) P_m(k)\,, \tag{3.66}$$

[14] Note that the relation between the flat-sky and full-sky power spectrum of density and RSD has been studied in detail in [252].

[15] In principle we do not observe at constant conformal time η but rather at constant redshift z. However the difference between η and z has been consistently included in the derivation of Δ so that a constant z can now be seen as a constant η.

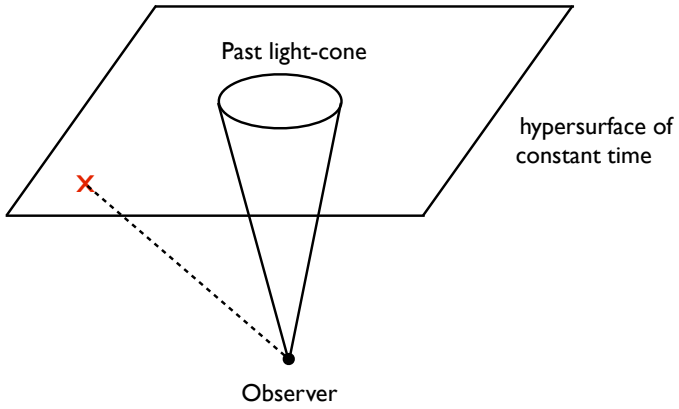

Figure 3.12: To calculate the Fourier transform of the lensing term $\Delta^{\rm lens}(\mathbf{k},\eta)$, one needs to know the value of $\Delta^{\rm lens}(\boldsymbol{x},\eta)$ for all $\boldsymbol{x}$ on the hypersurface of constant time η. However for a given observer, $\Delta^{\rm lens}(\boldsymbol{x},\eta)$ is well defined only on her past light-cone. Calculating $\Delta^{\rm lens}(\boldsymbol{x},\eta)$ outside of the past light-cone, like for example at the position of the cross would require to integrate the gravitational potential along the dashed trajectory, which is not physical, and would lead to wrong results.

where

$$A(\nu,z) = (b-\nu^2 f)\,, \tag{3.67}$$

$$B(\nu,z) = -i\nu\left(\frac{\dot{\mathcal{H}}}{\mathcal{H}^2}+\frac{2-5s}{\mathcal{H}\chi}+5s-f_{\rm evo}\right)\,, \tag{3.68}$$

$$C(z) = \left[3f+\frac{3}{2}\Omega_m(1+z)\frac{H_0^2}{\mathcal{H}^2}\left(1-5s-\frac{\dot{\mathcal{H}}}{\mathcal{H}^2}-\frac{2-5s}{\mathcal{H}\chi}-5s+f_{\rm evo}\right)\right] \tag{3.69}$$

A represents the standard terms, density and redshift space distortions. B is the Doppler term which is suppressed by a factor $\mathcal{H}/k$ and C represents the additional relativistic contributions which are suppressed by $(\mathcal{H}/k)^2$. To arrive at this result we have set $\Psi=\Phi$ and we have neglected the term containing the time derivative of the potential, since it is relevant only at late time and at very large angular scales where the flat sky approximation is not valid.

The contribution of the integrated terms to the flat-sky power spectrum are more complicated to calculate and have been neglected in [165, 312]. The reason is that integrated terms, like for example the lensing $\Delta^{\rm lens}(\boldsymbol{n},\eta)$, depend on the value of the gravitational potential along the photon trajectory in direction $\boldsymbol{n}$. As a consequence $\Delta^{\rm lens}(\boldsymbol{n},\eta)$ is well defined only on the past light-cone of the observer and not on the whole hypersurface of constant conformal time η. Calculating $\Delta^{\rm lens}(\boldsymbol{n},\eta)$ for a point which is not on the past light-cone of the observer would require to calculate the lensing signal along arbitrary trajectories that have nothing to do with the trajectories followed by photons, as depicted in Fig. 3.12.

To calculate the power spectrum of the integrated terms, we need therefore to go through the correlation function.

In Appendix 3.E we show how this can be done in the flat-sky approximation. To calculate the integrated terms in the flat sky approximation, we define a sky direction $\boldsymbol{n}_*$ and split the observation directions as $\boldsymbol{n}_1 = \boldsymbol{n}_* + \Delta\boldsymbol{n}/2$, $\boldsymbol{n}_2 = \boldsymbol{n}_* - \Delta\boldsymbol{n}/2$. We also split $\mathbf{r} = \mathbf{r}_\perp + \boldsymbol{n}_* r_\parallel$ with $\mathbf{r}_\perp = \chi(z)\Delta\boldsymbol{n}$. Representing the correlation function as the Fourier transform of the power spectrum, we can then perform the integral over $k_\parallel$ by neglecting the slow dependence of the power spectrum and taking into account only the fast oscillations of the exponential. This leads to the $\delta(k_\parallel)$ and $\delta^P(k_\parallel)$ defined below. All details are given in Appendix 3.E. We obtain

$$\begin{aligned}
&P_\Delta^{\rm flat,int}(k,\nu,z)\\
&= -3\pi\frac{\Omega_m H_0^2(1+z)D_1(z)(2-5s(z))}{\chi}P_m(k_\perp)\alpha(k_\perp,0,z)\left[\chi\delta^P(k_\parallel)+\frac{2}{k_\perp^2}\delta(k_\parallel)\right]\\
&+\frac{\pi}{2}\left(\frac{3\Omega_m H_0^2(2-5s(z))}{\chi}\right)^2\delta(k_\parallel)\int_0^\chi d\lambda P_m(k\chi/\lambda)\left[\frac{(\chi-\lambda)\chi^2}{\lambda}+\frac{2}{k^2}\right]^2 D_1^2(z(\lambda))(1+z(\lambda))^2\,.
\end{aligned} \tag{3.70}$$

The first line comes from the correlation of the integrated terms with density and the second line is the correlation of the integrated terms with themselves. The distribution δ^P is defined by (see Appendix 3.E for more detail)

$$\delta^P(k) = \frac{1}{2\pi}\int_{-\infty}^{\infty} dx|x|e^{ikx}\,. \tag{3.71}$$

The lensing terms are proportional to the distributions $\delta(k_\parallel)$ and $\delta^P(k_\parallel)$. They have to be understood as formal expressions. Physical power spectra are obtained by smoothing the signal with a longitudinal window function. Let us briefly explain this: we assume that our galaxies are all inside a radial window, $W(r_\parallel)$, with which the correlation function has to be convolved. Its Fourier transform, the power spectrum is then multiplied by the Fourier transform of the window, $\widehat{W}(k_\parallel)$. As an example, for the cross term involving $\delta^P(k_\parallel)$, denoting the pre-factor of $\delta^P(k_\parallel)$ by $P_\times$ and the result by $P_{\times\,\rm obs}$, we obtain an integral of the form

$$P_{\times\,\rm obs}(\mathbf{k},z) = P_\times(k_\perp,z)\frac{1}{2\pi}\int dr_\parallel dk_\parallel |r_\parallel| e^{ik_\parallel r_\parallel}|\widehat{W}(k_\parallel)|^2\,. \tag{3.72}$$

More details with examples of Gaussian and top hat windows can be found in [150].

3.3.2 Numerical results: comparison of the flat-sky and full-sky expressions

In Figs. 3.13 and 3.14 we show the multipoles of the power spectrum at $\bar{z} = 1$ as a function of k for all the non-integrated terms. We compare the results obtained from the full-sky correlation (3.65) (coloured lines) with the flat-sky results given in (3.66) (black lines). In principle, one could use a sharp cut-off in (3.65) to reflect the fact that the correlation function outside of the observed patch of the sky is zero. However, it is well-known that such a cut-off introduces spurious oscillations

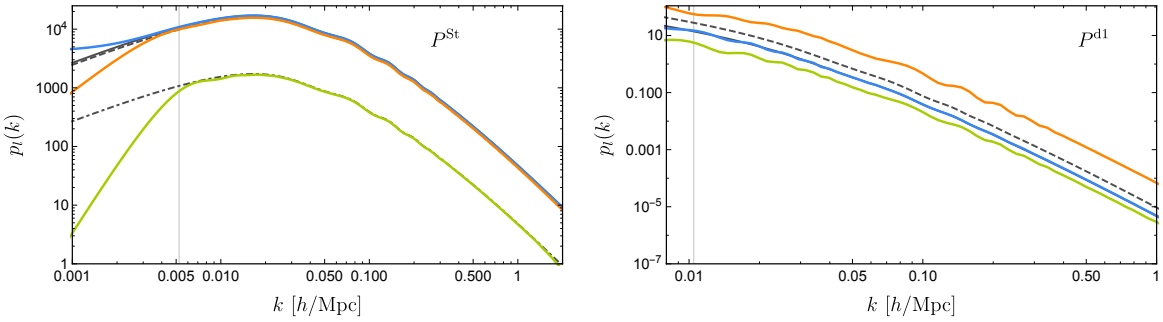

Figure 3.13: The multipoles of the power spectrum $p_\ell(k)$ at redshift $\bar{z} = 1$. The coloured lines show the multipoles obtained from Eq. (3.65): blue for the monopole ($\ell = 0$), orange for the quadrupole ($\ell = 2$) and green for the hexadecapole ($\ell = 4$). The black lines show the flat-sky result from Eqs. (3.61)-(3.63) and (3.66): solid for the monopole, dashed for the quadrupole and dot-dashed for the hexadecapole. The grey vertical line shows the smoothing scale of the window function. In the left panel we plot the well known density and redshift-space distortions, and in the right panel we plot the Doppler contribution d1.

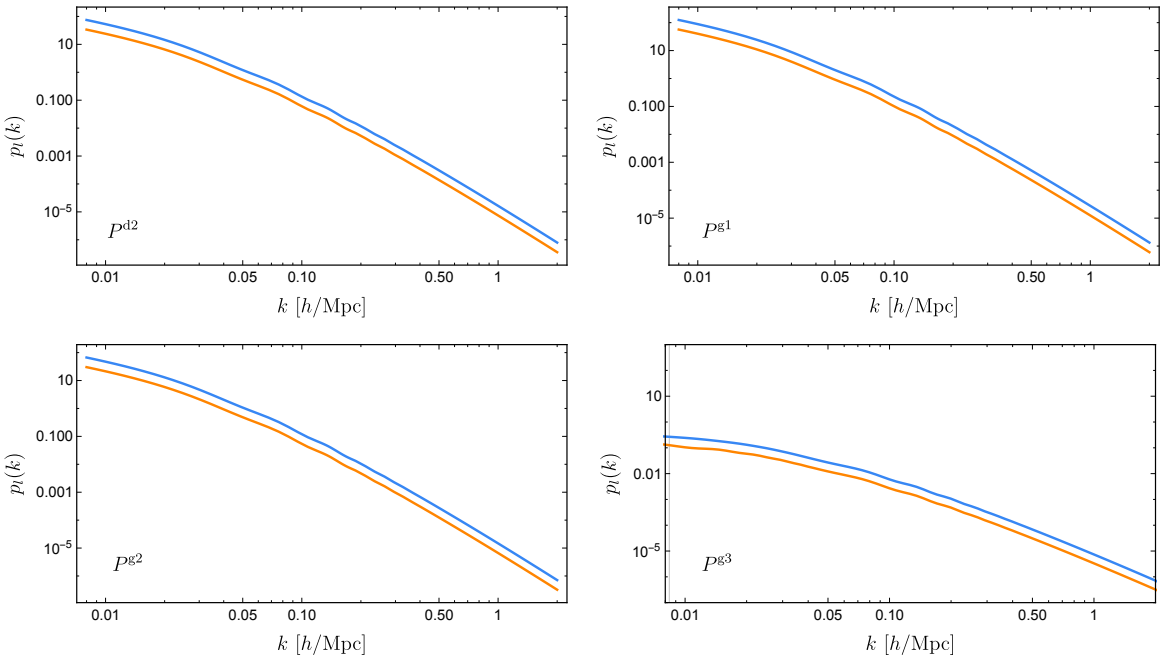

Figure 3.14: The monopole (blue) and quadrupole (orange) for the other non-integrated relativistic terms, d2 to g3 at $\bar{z} = 1$. The flat-sky results are indistinguishable from the full-sky ones and are therefore not indicated.

to the power spectrum. We therefore use the following window function to smoothly remove scales outside of the observed patch of the sky

$$W(r) = \frac{1}{2}\left(1 - \tanh\left[\frac{r - \lambda_1 + 3\lambda_2}{\lambda_2}\right]\right) \tag{3.73}$$

with $\lambda_1 = 1000\text{Mpc}/h$ and $\lambda_2 = 50\text{Mpc}/h$ which gives $\lambda_{\text{smooth}} \simeq 700\text{Mpc}/h$ or $k_{\text{smooth}} \simeq 0.005h/\text{Mpc}$.

The multipoles of the standard terms are shown in the left panel of Fig. 3.13. We see that for k larger than the smoothing scale (depicted by the grey vertical line), the full-sky multipoles agree extremely well with the flat-sky expression. For k smaller than the smoothing scale, the full-sky multipoles differ from the flat-sky ones, due to the presence of the window function which removes large scales.

The right panel of Fig. 3.13 shows the multipoles of the Doppler term d1. The full-sky quadrupole (orange) is significantly larger than the flat-sky quadrupole (black dashed). This is due to the fact that in the flat-sky, the contribution coming from the correlation of the Doppler term with the standard terms exactly vanishes, as it gives rise only to odd multipoles, which are exactly zero if one has only one population of galaxies. As a consequence the only contribution to the quadrupole comes from the correlation of the Doppler term with itself. In the full-sky, this is no longer the case. A quadrupole is induced from the correlation of the Doppler term with the density. This contribution is suppressed by a power $r/\chi \sim \mathcal{H}/k$ and becomes therefore of the same order of magnitude as the Doppler-Doppler correlation function. This situation again reflects the fact that to properly evaluate the impact of relativistic effects it is not consistent to use the flat-sky approximation, because full-sky corrections generate effects that are of the same order of magnitude as the relativistic terms.

In Fig. 3.14 we show the other non-integrated relativistic effects. In this case the full-sky and flat-sky multipoles agree very well. This is due to the fact in this case the difference between the flat-sky and full-sky result is of the order of $(r/\chi)^2$ and not r/χ and is therefore not visible at $\bar{z} = 1$ [16].

In Fig. 3.15 we show the multipoles of the lensing contribution. Here we only calculate the full-sky multipoles given by Eq. (3.65) since the flat-sky expression (3.70) is not well defined for $k_\parallel \neq 0$. As discussed before, the lensing power spectrum is extremely sensitive to the cut-off because the correlation function increases with r. As a consequence the window function defined in (3.73) and used for the non-integrated terms is too sharp and not well adapted for the lensing term. It gives rise to large unphysical oscillations in the power spectrum. We therefore use instead a Gaussian window function which is smoother

$$W(r) = \exp^{-r^2/a^2}\,, \tag{3.74}$$

[16] This can be understood by noting that full-sky corrections to the correlation function bring terms of the form $r/\chi \cdot \mu$. Since the cross-correlation between the standard terms and the Doppler term d1 contains a contribution proportional to μ in the flat-sky, the first non-zero even multipole in the full-sky will be given by $\mu \times r/\chi \cdot \mu$. On the other hand the flat-sky expression for the other relativistic effects contains even powers of μ and their full-sky correction must therefore contain at least two powers of μ, i.e. two powers of r/χ.

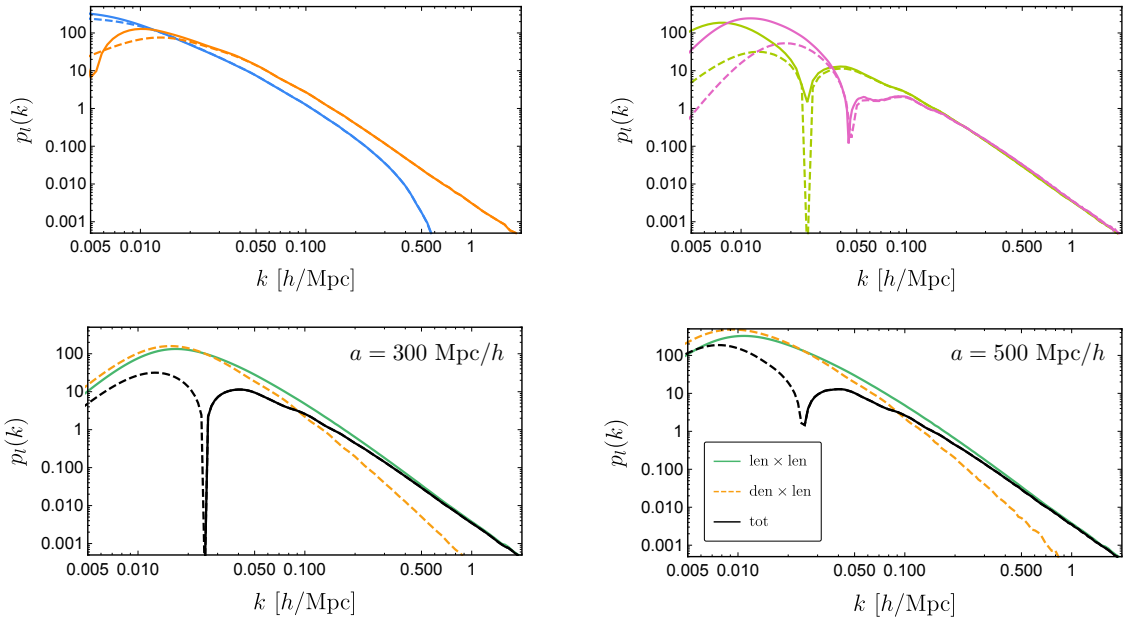

Figure 3.15: The lensing multipoles in the linear regime at $\bar{z} = 1$, calculated from Eq. (3.65) with the window function (3.74), with $a = 300\,\mathrm{Mpc}/h$ (dashed lines) and $a = 500\,\mathrm{Mpc}/h$ (solid lines). The left panel shows the monopole (blue) and quadrupole (orange). The right panel shows the hexadecapole (green) and the $\ell = 6$ multipole (purple). In the lower panels the hexadecapole contributions from density×lensing and lensing× lensing are shown separately for clarity.

where we consider two different values for a: $a = 300\,\mathrm{Mpc}/h$ (dashed lines) and $a = 500\,\mathrm{Mpc}/h$ (solid lines). All multipoles from the lensing term, monopole and quadrupole (left panel) as well as the hexadecapole and $\ell = 6$ multipole (right panel) are of the same order of magnitude. This is very different from the standard expression which is dominated by the monopole and quadrupole. The hexadecapole and the $\ell = 6$ multipole depend more strongly on the value of a than the monopole and quadrupole, which differ only for $k \leq 0.03h/\mathrm{Mpc}$. Nevertheless, the passage through zero is independent of the window size. This zero of the hexadecapole and of the $\ell = 6$ multipole is due to the competition between the positive lensing-lensing correlation which dominates at large k and the negative density-lensing correlation which dominates at small k, as can be seen from the bottom panels of Fig. 3.15.

The standard monopole, quadrupole and hexadecapole of the power spectrum are used to measure the growth rate and constrain cosmological parameters. Since large-scale relativistic effects and gravitational lensing contribute to these multipoles, they can in principle contaminate this estimation. In Fig. 3.16 we show the fractional difference between the full-sky non-integrated relativistic multipoles and the flat-sky standard multipoles at $\bar{z} = 1$

$$\Delta p_\ell^{\mathrm{rel}} = \frac{p_\ell^{\mathrm{rel}}}{p_\ell^{\mathrm{st}}}\,, \tag{3.75}$$

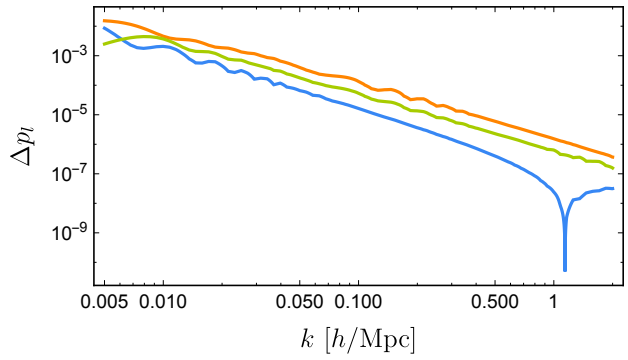

Figure 3.16: Fractional difference at $\bar{z} = 1$ generated by the large-scale relativistic effects on the monopole (blue), quadrupole (orange) and hexadecapole (green) of the power spectrum.

where $p_\ell^{\rm rel}$ denotes the multipoles from all the non-integrated relativistic effects and their correlation with the standard terms, similar to (3.56). We see that the correction generated by the relativistic effects is less than a percent at all scales and can therefore be neglected. At small redshift $\bar{z} = 0.1$ we expect a larger contribution, similar to the one that affects the multipoles of the correlation function, see Fig. 3.8. However we found that this contribution strongly depends on the window function and we defer therefore a careful study of this effect to a future publication [95].

In Fig. 3.17 we show the fractional difference between the lensing multipoles and the flat-sky standard multipoles at $\bar{z} = 1$ and $\bar{z} = 2$

$$\Delta p_\ell^{\rm lens} = \frac{p_\ell^{\rm lens}}{p_\ell^{\rm st}} \,, \tag{3.76}$$

where $p_\ell^{\rm lens}$ denotes the multipoles from the lensing and its correlation with the standard terms. We see that above $0.01\,h$/Mpc the lensing contribution to the monopole and quadrupole is less than a percent. Only on very small k does it reach a few percents. The hexadecapole is more strongly affected at all scales. At $\bar{z} = 2$, the monopole and quadrupole get corrections of 10-20% at small k and the corrections remain above 1% at all scales. These numbers seem to be in broad agreement with the flat-sky results of [150] [17]. Again the hexadecapole is strongly affected by lensing at all scales.

Note that as mentioned previously, the multipoles of the power spectrum strongly depend on the window function chosen to integrate (3.65), especially for the lensing contribution which grows with separation. In addition the multipoles of the power spectrum depend on the minimal separation we use in the integral (3.65), which in practice is given by the size of the pixels in which we measure the number counts. In particular, we have found that a window function which is too sharp leads to strong

[17] Note that the fractional differences in [150] are with respect to the BBKS power spectrum which contains no baryons and no redshift-space distortions and is linear, whereas our result is with respect to the non-linear standard power spectrum which contains density and redshift-space distortions. It is therefore expected that our fractional difference be smaller.

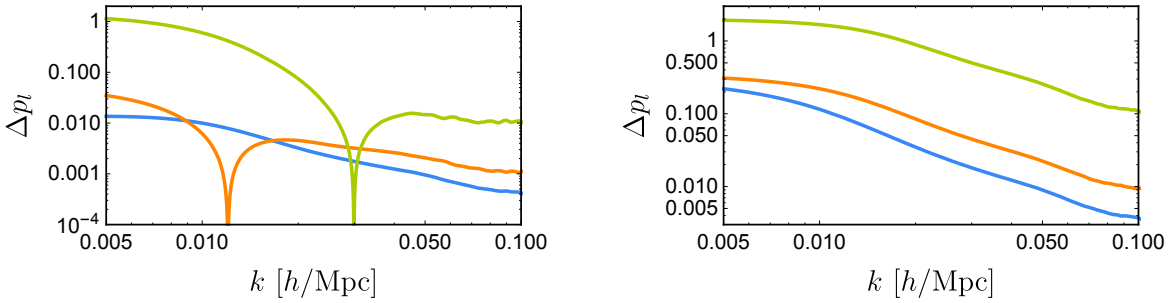

Figure 3.17: Fractional difference generated by the non-linear full-sky lensing on the monopole (blue), quadrupole (orange) and hexadecapole (green) of the power spectrum. Here a Gaussian window with $a = 300\,\mathrm{Mpc}/h$ has been used. The left panel is for $\bar{z} = 1$ and the right panel for $\bar{z} = 2$.

oscillations in the power spectrum. Similarly, the lower cutoff leads to oscillations for $k > \pi/r_{\mathrm{min}}$. In our case we choose $r_{\mathrm{min}} = 8\,\mathrm{Mpc}/h$ leading to oscillations around $k \sim 0.2\,h/\mathrm{Mpc}$. The results shown in Figs. 3.15, 3.16 and 3.17 should therefore be taken with some caution as they will depend on the form of the window, the smoothing scale and the minimum separation used in the Fourier transform. We defer a more detailed study of these parameters to a future publication, where we will also analyse the impact of the large-scale relativistic effects and of the lensing on the determination of cosmological parameters [95].

3.4 Discussion and Conclusions

In this paper we have studied the redshift-space correlation function and the power spectrum of galaxy number counts. Even though these functions depend on the cosmological model used to convert angles and redshifts into distances [18], they are useful for several reasons. First they are well adapted to describe the 3-dimensional information present in large-scale structure. This is not the case for the observable $C_\ell(z_1, z_2)$ angular-redshift power spectrum for which we cannot employ very fine redshift binning due to under-sampling. Second, the multipoles of the correlation function and of the power spectrum contain important information about the growth of perturbations which is difficult to isolate in the angular-redshift power spectrum. We therefore propose to use the redshift-space correlation function to analyse thin shells in redshift space, $\Delta z \sim 0.2$ and the power spectrum to analyse small (a few 100 Mpc) patches of sky.

Computing these quantities within linear perturbation theory and with the halofit approximation, we have shown how they are affected by large-scale relativistic effects and by lensing. The large-scale relativistic effects are important mainly at small redshifts. At $z = 0.1$ they introduce corrections to the monopole and quadrupole of

[18] Note that deviations from the fiducial model can be accounted for in a consistent way by introducing correction parameters that rescale the correlation function, see e.g. [303].

the correlation function of the order of 10% at a separation of $100\,\mathrm{Mpc}/h$ and they quickly increase with separation. The hexadecapole is less affected at intermediate scales, but at large scales the correction becomes similar to the other multipoles. We have seen that this large correction is due to the Doppler effect, which contains a term proportional to $1/(\mathcal{H}\chi)$ which is enhanced at small redshift. This term has previously been identified in [234, 245, 256]. At large redshift however, this Doppler term contributes to the multipoles at the same level as the other relativistic effects and generates corrections that are never larger than about 1%. We have also seen that full-sky corrections to the correlation function are of the same order as relativistic corrections. It is hence inconsistent to take onto account only one or the other. They have to be discussed together as we do it in this work.

At large redshift the lensing term becomes much more relevant than the large-scale relativistic contributions. Furthermore, the importance of lensing strongly depends on the orientation of the pair of galaxies. In particular it is most important along the line-of-sight, when $\mu \sim 1$. In this case on large scales, $r > 200\,\mathrm{Mpc}/h$, the lensing term even dominates over the standard terms (see Fig. 3.3). We have also studied the contribution of lensing to the multipoles of the correlation function and of the power spectrum and we have seen that at $z = 1$ lensing modifies the monopole and quadrupole of the correlation function and of the power spectrum by a few percents. At larger redshift $z = 2$ these corrections amount to 10-30% at intermediate scales and quickly increase with separation. This clearly shows that lensing cannot be neglected in the analysis of future galaxy surveys at high redshift. Moreover we have seen that the hexadecapole of the correlation function and of the power spectrum are strongly affected by lensing at $z = 1$ and $z = 2$. This comes from the fact that the hexadecapole from the standard terms is significantly smaller than the monopole and quadrupole, whereas the hexadecapole of lensing is of the same order as the monopole and quadrupole (as can be seen from Fig. 3.10). Measuring the hexadecapole is expected to provide a clean way of measuring the growth rate f since it is independent of bias. Here we see however that such a measurement would require a careful modelling of the lensing contribution. Furthermore, we have found that lensing generates significant higher multipoles $\ell > 4$ in the correlation function and in the power spectrum, see Figs. 3.9, 3.10, 3.11 and 3.15.

In our work, contrary to previous studies on the subject, we have derived an expression for the lensing correlation function which is exact, i.e. which does not rely on the flat-sky and Limber approximation. By comparing our result with the flat-sky result, we have found that the flat-sky approximation is only good in forward direction, $\mu = 1$, see Fig. 3.4. The full-sky lensing multipoles differ from the flat-sky one by 20-40%, see Fig. 3.9. Finally, we have seen that due to the mixing of scales, non-linearities in the matter power spectrum are relevant for lensing even for large separations out to $r > 200\,\mathrm{Mpc}/h$ for $\mu \sim 1$ where lensing is most relevant, see Fig. 3.5. A correct treatment of lensing requires therefore the use of the full-sky non-linear expressions.

The presence of higher multipoles in both, the correlation function and the power spectrum, might represent an ideal observational target to identify the lensing term. As it has been discussed previously [221], measuring the convergence κ via the

lensing of number counts is a promising alternative to shear measurements. On the other hand, it has been shown that neglecting lensing in the analysis of future surveys, at least for photometric surveys induces significant errors in parameter estimation [59]. It will be important to investigate whether this is also the case when precise spectroscopic redshifts are available. We shall study this in a forthcoming paper [95] using the methods outlined in this work.

APPENDIX

3.A Relations between the angles

In this appendix we derive in detail the relation between the angles θ, α, β and γ, see Fig. 3.18. More precisely, we give expressions for $\cos\alpha$, $\cos\beta$ and $\cos\gamma$ in terms of r, $\cos\theta$ and $\bar{z} = (z_1 + z_2)/2$ or rather $\bar{\chi} = \chi(\bar{z})$. Note that $(\chi_1 + \chi_2)/2$ and $\chi(\bar{z})$ differ by a term of order $(\Delta z)^2/H(\bar{z})$ which we neglect.

As defined in the main text, α is the angle between the line of length r connecting the two positions at redshifts z_1 and z_2 which span an angle θ at the observer and the line connecting z_2 and the intersection or the circle or radius $r_\parallel$ around z_2 with the Thales circle over $\mathbf{r}$ (see Fig. 3.1, left panel). Evidently α is given by

$$\cos\alpha \;=\; r_\parallel/r = \frac{2}{r}\sqrt{\bar{\chi}^2 - \frac{4\bar{\chi}^2 - r^2}{2(1+\cos\theta)}}\,. \tag{3.A77}$$

Here we have used eq. (3.31) to express $r_\parallel$ in terms of $(r, \bar{\chi}, \cos\theta)$.

The angle β is obtained as follows: We denote by s the length of the line from the observer O to the middle of r and by α_2 the angle of the triangle (O, z_2, z_1) at z_2, see Fig. 3.18. The cosine law gives the following relations

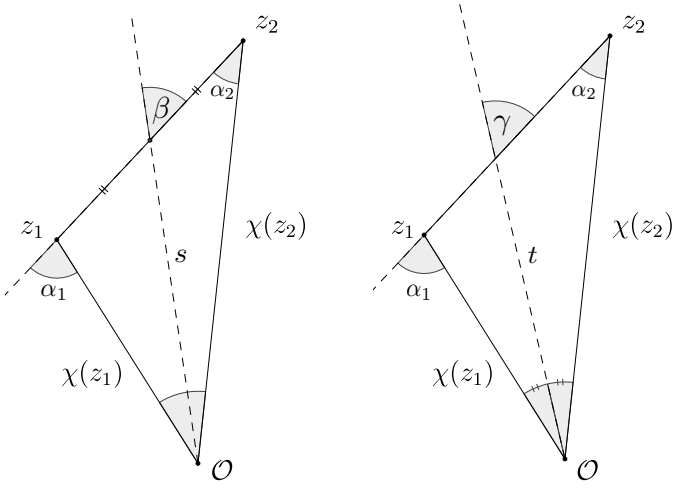

Figure 3.18: The angles α_1, α_2, β, γ and the lengths s and t used to determine respectively β and γ are indicated.

$$\chi_2^2 \;=\; s^2 + (r/2)^2 + rs\cos\beta\,, \qquad s^2 \;=\; (r/2)^2 + \chi_2^2 - r\chi_2\cos\alpha_2 \tag{3.A78}$$

Eliminating s and solving for $\cos\beta$ we find

$$\cos\beta = \frac{-r^2/2 + r\chi_2\cos\alpha_2}{r\sqrt{(r/2)^2 + \chi_2^2 - r\chi_2\cos\alpha_2}} \tag{3.A79}$$

Using furthermore

$$\cos\alpha_2 = \frac{\chi_2 - \chi_1\cos\theta}{r}$$

we obtain after some simplifications

$$\cos\beta = \frac{\chi_2^2 - \chi_1^2}{r\sqrt{\chi_1^2+\chi_2^2+2\chi_1\chi_2\cos\theta}} = \frac{2\bar{\chi}}{r}\sqrt{\frac{2r^2 - 4(1-\cos\theta)\bar{\chi}^2}{8\bar{\chi}^2\cos\theta^2 + (1\cos\theta)r^2}}\,. \tag{3.A80}$$

For the second line we used expressions (3.30) for $\chi_{1,2}$.

Considering the angle γ and using t as indicated in Fig. 3.18 and α_2 as before we see that $\gamma = \theta/2 + \alpha_2$ hence

$$\cos\gamma = \cos(\theta/2)\cos\alpha_2 - (1-\cos^2\theta/2)^{1/2}(1-\cos^2\alpha_2)^{1/2}$$

Inserting

$$\cos\theta/2 = \left(\frac{1+\cos\theta}{2}\right)^{1/2}$$

and the expressions for $\cos\alpha_2$ we obtain

$$\cos\gamma \;=\; \frac{(1+\cos\theta)^{1/2}(\chi_2-\chi_1)}{\sqrt{2}r} \;=\; \frac{\sqrt{r^2 - 2(1-\cos\theta)\bar{\chi}^2}}{r}\,. \tag{3.A81}$$

Again we have inserted the expressions (3.30) for $\chi_{1,2}$ in the last equal sign.

We shall also use the expressions for $\cos\alpha_i$ which are easily derived from the cosine theorem:

$$\cos\alpha_2 = \;\hat{\mathbf{r}}\cdot\boldsymbol{n}_2 \;=\; \frac{\chi_2 - \chi_1\cos\theta}{r}\,, \qquad \cos\alpha_1 = \;\hat{\mathbf{r}}\cdot\boldsymbol{n}_1 \;=\; -\,\frac{\chi_1 - \chi_2\cos\theta}{r} \tag{3.A82}$$

3.B The full angular–redshift correlation function

The 'full angular redshift correlation function' is $\xi(\theta, z_1, z_2)$ when we include all the relativistic terms. It can be computed as follows.

We first write down derivatives of Eq. (3.48) wrt χ_1 and χ_2 which are encoded in the functions $\zeta^{ij}(k\chi_1, k\chi_2)$. Using $r = \sqrt{\chi_1^2+\chi_2^2-2\chi_1\chi_2\cos\theta}$ and the recurrence relations for derivatives of spherical Bessel functions

$$j_\ell' = \frac{1}{2\ell+1}\left(\ell j_{\ell-1} - (\ell+1)j_\ell\right) \quad \text{and} \quad \frac{j_\ell(x)}{x} = \frac{1}{2\ell+1}\left(j_{\ell-1}+j_\ell\right)(x)$$

we find

$$\zeta^{00} \;=\; j_0(kr) \tag{3.B83}$$

$$\zeta^{01} \;=\; \frac{\chi_1\cos\theta - \chi_2}{r} j_1(kr) = -j_1(kr)\cos\alpha_2 \tag{3.B84}$$

$$
\begin{aligned}
\zeta^{11} &= \left(\frac{2}{kr}j_1(kr) - j_0(kr)\right)\left(\frac{\chi_1 - \chi_2\cos\theta}{r}\right)\left(\frac{\chi_2 - \chi_1\cos\theta}{r}\right) \\
&\quad + j_1(kr)\frac{\chi_1\chi_2\sin^2\theta}{kr^3} \\
&= -\frac{(\chi_2 - \chi_1\cos\theta)(\chi_1 - \chi_2\cos\theta)}{r^2}j_2(kr) + \frac{\cos\theta}{3}\left(j_0(kr) - j_2(kr)\right) \\
&= j_2(kr)\cos\alpha_2\cos\alpha_1 + \frac{\cos(\alpha_2 - \alpha_1)}{3}\left[j_0(kr) - j_2(kr)\right] \qquad (3.B85)
\end{aligned}
$$

$$
\begin{aligned}
\zeta^{02} &= \left(\frac{2}{kr}j_1(kr) - j_0(kr)\right)\left(\frac{\chi_2 - \chi_1\cos\theta}{r}\right)^2 - j_1(kr)\frac{\chi_1^2\sin^2\theta}{kr^3} \\
&= \left(\frac{2}{3} - (1 - \cos^2\theta)\frac{\chi_1^2}{r^2}\right)j_2(kr) - \frac{1}{3}j_0(kr) \\
&= \left(\frac{2}{3} - \sin^2\alpha_2\right)j_2(kr) - \frac{1}{3}j_0(kr) \qquad (3.B86)
\end{aligned}
$$

$$
\begin{aligned}
\zeta^{12} &= \frac{(1 + 2\cos^2\theta)\chi_1 - 3\chi_2\cos\theta}{5r}j_1(kr) + \\
&\quad \frac{(1 - 3\,\cos^2\theta)\chi_1^3 + \cos\theta(5 + \cos^2\theta)\chi_1^2\chi_2 - 2(2 + \cos\theta^2)\chi_1\chi_2^2 + 2\chi_2^3\cos\theta}{5r^3}j_3(kr) \\
&= -\frac{[2\cos(\alpha_2 - \alpha_1)\cos\alpha_2 + \cos\alpha_1]}{5}j_1(kr) \\
&\quad + \Big[\cos\alpha_1\sin^2\alpha_2 - \frac{2}{5}\cos\alpha_2\cos(\alpha_1 - \alpha_2)\Big]j_3(kr)
\end{aligned}
\qquad (3.B87)
$$

$$
\begin{aligned}
\zeta^{22} &= \frac{1 + 2\cos^2\theta}{15}j_0(kr) - \frac{1}{21}\left[1 + 11\cos^2\theta + \frac{18\cos\theta(\cos^2\theta - 1)\chi_1\chi_2}{r^2}\right]\, j_2(kr) + \\
&\quad \Bigg[\frac{4(3\cos^2\theta - 1)(\chi_1^4 + \chi_2^4)}{35r^4} \\
&\quad + \chi_1\chi_2(3 + \cos^2\theta)\frac{3(3 + \cos^2\theta)\chi_1\chi_2 - 8(\chi_1^2 + \chi_2^2)\cos\theta}{35r^4}\Bigg]\, j_4(kr) \\
&= \frac{1 + 2\cos^2(\alpha_1 - \alpha_2)}{15}j_0(kr) \\
&\quad - \frac{1}{42}\left[4 + 9\cos(2\alpha_1) + 9\cos(2\alpha_2) + 2\cos(2(\alpha_1 - \alpha_2))\right]j_2(kr) + \\
&\quad \frac{[3\cos(2(\alpha_1 - \alpha_2)) + 35\cos(2(\alpha_1 + \alpha_2)) + 10\cos(2\alpha_1) + 10\cos(2\alpha_2) + 6]}{280}j_4(kr)
\end{aligned}
\qquad (3.B88)
$$

The coefficients $\zeta^{21}(x_1, x_2)$ etc. are obtained from ζ^{12} etc. via the symmetry relation

$$\zeta^{ij}(x, y) = \zeta^{ji}(y, x)\,.$$

The flat sky limit of the above function is obtained by setting $\alpha_1 = \alpha_2 \equiv \alpha$. In this case all the terms in front of a j_ℓ are a multiple of the Legendre polynomial $L_\ell(\cos\alpha)$. More precisely, denoting the flat sky limit of ζ^{ij} by $\bar{\zeta}^{ij}$ we obtain

$$\bar{\zeta}^{00} = j_0(kr)\,, \qquad (3.B89)$$

$$\bar{\zeta}^{01} = -L_1(\cos\alpha)j_1(kr)\,, \qquad \bar{\zeta}^{11} = \frac{2}{3}L_2(\cos\alpha)j_2(kr) + \frac{1}{3}j_0(kr)\,, \tag{3.B90}$$

$$\bar{\zeta}^{02} = \frac{2}{3}L_2(\cos\alpha)j_2(kr) - \frac{1}{3}j_0(kr)\,, \tag{3.B91}$$

$$\bar{\zeta}^{12} = -3L_1(\cos\alpha)j_1(kr) - \frac{2}{5}L_3(\cos\alpha)\,, \tag{3.B92}$$

$$\bar{\zeta}^{22} = \frac{8}{35}L_4(\cos\alpha)j_4(kr) + \frac{4}{7}L_2(\cos\alpha)j_2(kr) + \frac{1}{5}j_0(kr)\,. \tag{3.B93}$$

The terms $\bar{\zeta}^{00}$, $\bar{\zeta}^{02}$ and $\bar{\zeta}^{22}$ give rise to the standard flat sky result (3.61) to (3.63). The flat sky results $\bar{\zeta}^{01}$ and $\bar{\zeta}^{12}$ are more subtle. Since we always have to add $\bar{\zeta}^{ij}+\bar{\zeta}^{ji}$ and $\bar{\zeta}^{ij}(\cos\alpha) = \bar{\zeta}^{ji}(\cos(\pi-\alpha)) = \bar{\zeta}^{ji}(-\cos\alpha)$ these odd terms actually cancel and do not contribute in the case of a single population of galaxies. They do contribute to a multi tracer signal, see [48].

The only coefficients that do not fall into this category, as explained in the main text, are the lensing terms which are computed using the identity

$$-\ell(\ell+1)L_\ell(\cos\theta) = \triangle_\Omega L_\ell(\cos\theta) = \frac{1}{\sin\theta}\partial_\theta\left(\sin\theta\partial_\theta L_\ell(\cos\theta)\right)\,.$$

They are given explicitly by

$$\begin{aligned}
\zeta^{0\mathrm{L}} &= 2\frac{k\chi_1\chi_2\cos\theta}{r}j_1(kr) - \left(k^2\frac{\chi_1^2\chi_2^2\sin^2\theta}{r^2}\right)j_2(kr) \\
&= k^2\left[\frac{2}{3}\chi_1\chi_2\cos\theta j_0(kr) + \frac{\chi_1\chi_2}{3}\left(2\cos\theta - 3\chi_1\chi_2\frac{\sin^2\theta}{r^2}\right)j_2(kr)\right] \qquad (3.B94)\\
&= \frac{(kr)^2}{3}\left[2\frac{\sin\alpha_1\sin\alpha_2\cos(\alpha_1-\alpha_2)}{\sin^2(\alpha_1-\alpha_2)}j_0(kr) + \frac{\sin\alpha_1\sin\alpha_2}{\sin^2(\alpha_1-\alpha_2)}\times\right. \\
&\quad \left.\left[\cos(\alpha_1-\alpha_2)+\cos\alpha_1\cos\alpha_2)\right]j_2(kr)\right] \qquad (3.B95)
\end{aligned}$$

$$\begin{aligned}
\zeta^{1\mathrm{L}} &= k^2\left[\frac{2}{3}\chi_2 r\cos\theta j_{-1}(kr) + \frac{2\chi_2(\chi_1\cos\theta-\chi_2)(\chi_1-2\chi_2\cos\theta)}{5r}j_1(kr) - \right. \\
&\quad \frac{1}{15r^3}\Big(\chi_2(4\chi_1^4\cos\theta - (9+\cos^2\theta)\chi_1^3\chi_2 + \cos\theta\left(\cos^2\theta+5\right)\chi_1^2\chi_2^2 + \\
&\quad \left.2(3-2\cos^2\theta)\chi_1\chi_2^3 - 2\chi_2^4\cos\theta\Big)j_3(kr)\right]\,, \qquad (3.B96)\\
&= (kr)^2\left[\frac{2}{3}\frac{\cos(\alpha_1-\alpha_2)\sin\alpha_1}{\sin(\alpha_1-\alpha_2)}j_{-1}(kr)\right. \\
&\quad -\frac{2}{5}\frac{(2\sin\alpha_1-\sin\alpha_2)(\sin\alpha_1-\cos(\alpha_1-\alpha_2)\sin\alpha_2)}{\sin^3(\alpha_1-\alpha_2)}\times \\
&\quad \left.j_1(kr) - \frac{1}{120}\frac{\sin\alpha_1\left[6\sin(2\alpha_1)+\sin(2(\alpha_1-\alpha_2))-15\sin(2(\alpha_1+\alpha_2))\right]}{\sin^2(\alpha_1-\alpha_2)}j_3(kr)\right] \qquad (3.B97)
\end{aligned}$$

$$\zeta^{2\mathrm{L}} = -k^2\Big\{\frac{2}{15}\chi_2\left(3\chi_1\cos\theta + (1-3\cos^2\theta)\chi_2\right)j_0(kr) +$$

$$\left[\frac{6\chi_1^3\chi_2\cos\theta-(9\cos^2\theta+11)\,\chi_1^2\chi_2^2}{21r^2}+\frac{2\cos\theta\,(3\cos^2\theta+8)\,\chi_1\chi_2^3+4\,(1-3\cos^2\theta)\,\chi_2^4}{21r^2}\right]j_2\,(kr)$$
$$+\left[\frac{\chi_2\,(2\,(1-3\cos^2\theta)\,\chi_2^5+6\cos\theta(3-\cos^2\theta)\chi_1\chi_2^4+(\cos^4\theta+12\cos^2\theta-21)\chi_1^2\chi_2^3)}{35r^4}\right.$$
$$\left.-\frac{\chi_2\,(2\cos\theta\,(\cos^2\theta+3)\,\chi_1^3\chi_2^2-12\chi_1^4\chi_2+4\chi_1^5\cos\theta)}{35r^4}\right]j_4(kr)\Bigg\} \tag{3.B98}$$

$$= -(kr)^2\Bigg\{\frac{1}{15}\frac{\sin\alpha_1(2\sin\alpha_1-3\sin(2(\alpha_1-\alpha_2))\cos\alpha_1)}{\sin^2(\alpha_1-\alpha_2)}j_0(kr)+\frac{\sin(\alpha_1)}{84\sin^4(\alpha_1-\alpha_2)}\times$$
$$\left[3\sin(3\alpha_1)(\cos(2\alpha_2)+3)-12\cos^3\alpha_1\sin(2\alpha_2)-\sin\alpha_1(3\cos(2\alpha_2)+1)\right]j_2(kr)$$
$$+\frac{\sin\alpha_1}{560\sin^2(\alpha_1-\alpha_2)}\Big[5\sin(\alpha_1+2\alpha_2)-35\sin(3\alpha_1+2\alpha_2)$$
$$+\sin(\alpha_1-2\alpha_2)+\sin(3\alpha_1-2\alpha_2)+2\sin\alpha_1+10\sin(3\alpha_1)\Big]j_4(kr)\Bigg\} \tag{3.B99}$$

$$\zeta^{\rm LL} = -\sin^2\theta(k^2\chi_1\chi_2)^2\left[\left(\frac{6(r^2+5\chi_1\chi_2\cos\theta)}{35r^2}-\frac{\chi_1^2\chi_2^2\sin^2\theta}{r^4}\right)j_4\,(kr)\right.$$
$$\left.+\frac{2\,(2r^2+3\chi_1\chi_2\cos\theta)}{7r^2}j_2(kr)\ +\frac{2}{5}j_0\,(kr)\right]$$
$$+4\cos\theta k^3\chi_1\chi_2\left[\left(\frac{r^2+6\chi_1\chi_2\cos\theta}{15r}-\frac{\chi_1^2\chi_2^2\sin^2\theta}{2r^3}\right)j_3\,(kr)\right.$$
$$\left.+\frac{2\,(r^2+\chi_1\chi_2\cos\theta)}{5r}j_1\,(kr)+\frac{r}{3}j_{-1}\,(kr)\right] \tag{3.B100}$$

$$= (kr)^3\Bigg\{\frac{4}{3}\frac{\sin\alpha_1\sin\alpha_2\cos(\alpha_1-\alpha_2)}{\sin^2(\alpha_1-\alpha_2)}j_{-1}(kr)$$
$$-\frac{2}{5}\frac{\sin\alpha_1\sin\alpha_2\cot(\alpha_1-\alpha_2)[\cos(2(\alpha_1-\alpha_2))+\cos(2\alpha_1)+\cos(2\alpha_2)-3]}{\sin^3(\alpha_1-\alpha_2)}j_1(kr)+$$
$$\frac{\sin\alpha_1\sin\alpha_2\cos(\alpha_1-\alpha_2)}{60\sin^4(\alpha_1-\alpha_2)}\left[2+6\cos(2\alpha_1)+\cos(2(\alpha_1-\alpha_2))+6\cos(2\alpha_2)\right.$$
$$\left.-15\cos(2(\alpha_1+\alpha_2))\right]j_3(kr)\Bigg\}+(kr)^4\Bigg\{-\frac{2}{5}\frac{\sin^2\alpha_1\sin^2\alpha_2}{\sin^2(\alpha_1-\alpha_2)}j_0(kr)-\frac{2\sin^2\alpha_1\sin^2\alpha_2}{7\sin^4(\alpha_1-\alpha_2)}\times$$
$$\left[2\sin^2(\alpha_1-\alpha_2)+3\cos(\alpha_1-\alpha_2)\sin\alpha_1\sin\alpha_2\right]j_2(kr)+\frac{\sin^2\alpha_1\sin^2\alpha_2}{280\sin^4(\alpha_1-\alpha_2)}\times$$
$$\Big[35\cos(2(\alpha_1+\alpha_2))-10\cos(2\alpha_2)-\cos(2(\alpha_1-\alpha_2))-10\cos(2\alpha_1)-14\Big]j_4(kr)\Bigg\}. \tag{3.B101}$$

For the lensing terms the flat sky limit cannot be obtained by setting $\alpha_1=\alpha_2$ since the terms ξ^{iL} diverge in this limit. We discuss the flat sky approximation of lensing in Appendix 3.E. We now give explicit expressions for the Q_k^{AB} in terms of the ζ^{ij}, to be inserted in eq. (3.46) to build the correlation function:

$$Q^{\rm den}(\theta,z_1,z_2) = b(z_1)b(z_2)S_D(z_1)S_D(z_2)\,\zeta^{00}(k\chi_1,k\chi_2,\theta)\,,$$

$$Q^{\rm rsd}(\theta,z_1,z_2) = \frac{k^2}{\mathcal{H}_1\mathcal{H}_2}S_V(z_1)S_V(z_2)\,\zeta^{22}(k\chi_1,k\chi_2,\theta)\,,$$

$$Q^{\rm len}(\theta,z_1,z_2) = \frac{(2-5s)^2}{4\chi_1\chi_2}\int_0^{\chi_1}\!\!\int_0^{\chi_2}\partial\lambda\partial\lambda'\frac{(\chi_1-\lambda)(\chi_2-\lambda')}{\lambda\lambda'}S_{\phi+\psi}(\lambda)S_{\phi+\psi}(\lambda')\zeta^{LL}(k\lambda,k\lambda',\theta)\,,$$

$$Q^{\text{den-rsd}}(\theta,z_1,z_2) = \frac{kb(z_1)}{\mathcal{H}_2}S_D(z_1)S_V(z_2)\,\zeta^{02}(k\chi_1,k\chi_2,\theta)\,,$$

$$Q^{\text{den-len}}(\theta,z_1,z_2) = b(z_1)S_D(z_1)\left(\frac{2-5s}{2\chi_2}\right)\int_0^{\chi_2}\partial\lambda\frac{\chi_2-\lambda}{\lambda}S_{\phi+\psi}(\lambda)\,\zeta^{0L}(k\chi_1,k\lambda,\theta)\,,$$

$$Q^{\text{rsd-len}}(\theta,z_1,z_2) = \frac{k}{\mathcal{H}_1}S_V(z_1)\left(\frac{2-5s}{2\chi_2}\right)\int_0^{\chi_2}\partial\lambda\frac{\chi_2-\lambda}{\lambda}S_{\phi+\psi}(\lambda)\,\zeta^{2L}(k\chi_1,k\lambda,\theta)\,,$$

$$\begin{aligned}Q^{\rm d1}(\theta,z_1,z_2) = &\left[\left(\frac{\dot{\mathcal{H}}}{\mathcal{H}^2}+\frac{2-5s}{\chi\mathcal{H}}+5s-f_{\rm evo}\right)S_V\right](z_1)\\ &\times\left[\left(\frac{\dot{\mathcal{H}}}{\mathcal{H}^2}+\frac{2-5s}{\chi\mathcal{H}}+5s-f_{\rm evo}\right)S_V\right](z_2)\,\zeta^{11}(k\chi_1,k\chi_2,\theta)\,,\end{aligned}$$

$$Q^{\rm X}(\theta,z_1,z_2) = \Delta^{\rm X}(z_1,k)\Delta^{\rm X}(z_2,k)\zeta^{00}(k\chi_1,k\chi_2,\theta) \qquad X\in\{\text{d2, g1, g2, g3}\}\,,$$

$$Q^{\rm g4}(\theta,z_1,z_2) = \frac{(2-5s)^2}{\chi_1\chi_2}\int_0^{\chi_1}\partial\lambda\int_0^{\chi_2}\partial\lambda' S_{\phi+\psi}(\lambda,k)S_{\phi+\psi}(\lambda',k)\zeta^{00}(k\lambda,k\lambda',\theta)\,,$$

$$\begin{aligned}Q^{\rm g5}(\theta,z_1,z_2) = &\left(\frac{\dot{\mathcal{H}}}{\mathcal{H}^2}+\frac{2-5s}{\chi\mathcal{H}}+5s-f_{\rm evo}\right)(z_1)\left(\frac{\dot{\mathcal{H}}}{\mathcal{H}^2}+\frac{2-5s}{\chi\mathcal{H}}+5s-f_{\rm evo}\right)(z_2)\\ &\times\int_0^{\chi_1}\partial\lambda\int_0^{\chi_2}\partial\lambda'\,\dot{S}_{\phi+\psi}(\lambda,k)\dot{S}_{\phi+\psi}(\lambda',k)\zeta^{00}(k\lambda,k\lambda',\theta)\,,\end{aligned}$$

$$Q^{\text{den-d1}}(\theta,z_1,z_2) = b(z_1)S_D(z_1)\left[\left(\frac{\dot{\mathcal{H}}}{\mathcal{H}^2}+\frac{2-5s}{\chi\mathcal{H}}+5s-f_{\rm evo}\right)S_V\right](z_2)\zeta^{01}(k\chi_1,k\chi_2,\theta)\,,$$

$$Q^{\text{den-X}}(\theta,z_1,z_2) = b(z_1)S_D(z_1)\Delta^{\rm X}(z_2,k)\zeta^{00}(k\chi_1,k\chi_2,\theta)\,,$$

$$Q^{\text{den-g4}}(\theta,z_1,z_2) = b(z_1)S_D(z_1)\frac{2-5s}{\chi_2}\int_0^{\chi_2}\partial\lambda S_{\phi+\psi}(\lambda,k)\zeta^{00}(k\chi_1,k\lambda,\theta)\,,$$

$$\begin{aligned}Q^{\text{den-g5}}(\theta,z_1,z_2) = &\,b(z_1)S_D(z_1)\left(\frac{\dot{\mathcal{H}}}{\mathcal{H}^2}+\frac{2-5s}{\chi\mathcal{H}}+5s-f_{\rm evo}\right)(z_2)\\ &\times\int_0^{\chi_2}\partial\lambda\dot{S}_{\phi+\psi}(\lambda,k)\zeta^{00}(k\chi_1,k\lambda,\theta)\,,\end{aligned}$$

$$Q^{\text{rsd-d1}}(\theta,z_1,z_2) = \frac{k}{\mathcal{H}_1}S_V(z_1)\left[\left(\frac{\dot{\mathcal{H}}}{\mathcal{H}^2}+\frac{2-5s}{\chi\mathcal{H}}+5s-f_{\rm evo}\right)S_V\right](z_2)\zeta^{21}(k\chi_1,k\chi_2,\theta)\,,$$

$$Q^{\text{rsd-X}}(\theta,z_1,z_2) = \frac{k}{\mathcal{H}_1}S_V(z_1)\Delta^{\rm X}(z_2,k)\zeta^{20}(k\chi_1,k\chi_2,\theta)\,,$$

$$Q^{\text{rsd-g4}}(\theta,z_1,z_2) = \frac{k}{\mathcal{H}_1}S_V(z_1)\frac{2-5s}{\chi_2}\int_0^{\chi_2}\partial\lambda S_{\phi+\psi}(\lambda,k)\zeta^{20}(k\chi_1,k\lambda,\theta)\,,$$

$$
\begin{aligned}
Q^{\text{rsd-g5}}(\theta,z_1,z_2) &= \frac{k}{\mathcal{H}_1}S_V(z_1)\left(\frac{\dot{\mathcal{H}}}{\mathcal{H}^2}+\frac{2-5s}{\chi\mathcal{H}}+5s-f_{\text{evo}}\right)(z_2)\\
&\quad\times\int_0^{\chi_2}\partial\lambda\dot{S}_{\phi+\psi}(\lambda,k)\zeta^{20}(k\chi_1,k\lambda,\theta)\,,\\
Q^{\text{len-d1}}(\theta,z_1,z_2) &= \left[\left(\frac{\dot{\mathcal{H}}}{\mathcal{H}^2}+\frac{2-5s}{\chi\mathcal{H}}+5s-f_{\text{evo}}\right)S_V\right](z_2)\\
&\quad\times\frac{2-5s}{2\chi_1}\int_0^{\chi_1}\partial\lambda\frac{\chi_1-\lambda}{\lambda}S_{\phi+\psi}(\lambda)\zeta^{L1}(k\lambda,k\chi_2,\theta)\,,\\
Q^{\text{len-X}}(\theta,z_1,z_2) &= \Delta^{\text{X}}(z_2,k)\frac{2-5s}{2\chi_1}\int_0^{\chi_1}\partial\lambda\frac{\chi_1-\lambda}{\lambda}S_{\phi+\psi}(\lambda)\zeta^{L0}(k\lambda,k\chi_2,\theta)\,,\\
Q^{\text{len-g4}}(\theta,z_1,z_2) &= \frac{(2-5s)^2}{2\chi_1\chi_2}\int_0^{\chi_1}\partial\lambda\frac{\chi_1-\lambda}{\lambda}\int_0^{\chi_2}\partial\lambda' S_{\phi+\psi}(\lambda,k)S_{\phi+\psi}(\lambda',k)\zeta^{L0}(k\lambda,k\lambda',\theta)\,,\\
Q^{\text{len-g5}}(\theta,z_1,z_2) &= \left(\frac{\dot{\mathcal{H}}}{\mathcal{H}^2}+\frac{2-5s}{\chi\mathcal{H}}+5s-f_{\text{evo}}\right)(z_2)\frac{2-5s}{2\chi_1}\\
&\quad\times\int_0^{\chi_1}\partial\lambda\int_0^{\chi_2}\partial\lambda'\frac{\chi_1-\lambda}{\lambda}S_{\phi+\psi}(\lambda)\dot{S}_{\phi+\psi}(\lambda',k)\zeta^{L0}(k\lambda,k\lambda',\theta)\,,\\
Q^{\text{d1-X}}(\theta,z_1,z_2) &= \left[\left(\frac{\dot{\mathcal{H}}}{\mathcal{H}^2}+\frac{2-5s}{\chi\mathcal{H}}+5s-f_{\text{evo}}\right)S_V\right](z_1)\Delta^{\text{X}}(z_2,k)\zeta^{10}(k\chi_1,k\chi_2,\theta)\,,\\
Q^{\text{d1-g4}}(\theta,z_1,z_2) &= \left[\left(\frac{\dot{\mathcal{H}}}{\mathcal{H}^2}+\frac{2-5s}{\chi\mathcal{H}}+5s-f_{\text{evo}}\right)S_V\right](z_1)\\
&\quad\times\frac{2-5s}{\chi_2}\int_0^{\chi_2}\partial\lambda S_{\phi+\psi}(\lambda,k)\zeta^{10}(k\chi_1,k\lambda,\theta)\,,\\
Q^{\text{d1-g5}}(\theta,z_1,z_2) &= \left[\left(\frac{\dot{\mathcal{H}}}{\mathcal{H}^2}+\frac{2-5s}{\chi\mathcal{H}}+5s-f_{\text{evo}}\right)S_V\right](z_1)\left(\frac{\dot{\mathcal{H}}}{\mathcal{H}^2}+\frac{2-5s}{\chi\mathcal{H}}+5s-f_{\text{evo}}\right)(z_2)\\
&\quad\times\int_0^{\chi_2}\partial\lambda\dot{S}_{\phi+\psi}(\lambda,k)\zeta^{20}(k\chi_1,k\lambda,\theta)\,,\\
Q^{\text{X-Y}}(\theta,z_1,z_2) &= \Delta^{\text{X}}(z_1,k)\Delta^{\text{Y}}(z_2,k)\zeta^{00}(k\chi_1,k\chi_2,\theta) \qquad X\,,\,Y\in\{\text{d2, g1, g2, g3}\}\,,\\
Q^{\text{X-g4}}(\theta,z_1,z_2) &= \Delta^{\text{X}}(z_1,k)\frac{2-5s}{\chi_2}\int_0^{\chi_2}\partial\lambda S_{\phi+\psi}(\lambda,k)\zeta^{00}(k\chi_1,k\lambda,\theta)\,,\\
Q^{\text{X-g5}}(\theta,z_1,z_2) &= \Delta^{\text{X}}(z_1,k)\left(\frac{\dot{\mathcal{H}}}{\mathcal{H}^2}+\frac{2-5s}{\chi\mathcal{H}}+5s-f_{\text{evo}}\right)(z_2)\\
&\quad\times\int_0^{\chi_2}\partial\lambda\dot{S}_{\phi+\psi}(\lambda,k)\zeta^{10}(k\chi_1,k\lambda,\theta)\,,\\
Q^{\text{g4-g5}}(\theta,z_1,z_2) &= \left(\frac{\dot{\mathcal{H}}}{\mathcal{H}^2}+\frac{2-5s}{\chi\mathcal{H}}+5s-f_{\text{evo}}\right)(z_2)\frac{2-5s}{\chi_1}\\
&\quad\times\int_0^{\chi_1}\partial\lambda\int_0^{\chi_2}\partial\lambda' S_{\phi+\psi}(\lambda,k)\dot{S}_{\phi+\psi}(\lambda,k)\zeta^{00}(k\lambda,k\lambda',\theta)\,.
\end{aligned}
$$

The correlators $Q^{BA}(z_1, z_2)$ are obtained from $Q^{AB}(z_1, z_2)$ using the identity $Q^{BA}(z_1, z_2) = Q^{AB}(z_2, z_1)$. The functions S_X and Δ^X are given in terms of the transfer function $T(k)$ and the density growth function $D_1(a)$ as

$$S_D = -\frac{3}{5}\frac{k^2}{\Omega_m \mathcal{H}_0^2}\frac{D_1(a)}{a}T(k)\,, \tag{3.B102}$$

$$S_V = \frac{3}{5}\frac{k\mathcal{H}}{\Omega_m \mathcal{H}_0^2}\frac{dD_1(a)}{da}T(k) = -f\frac{\mathcal{H}}{k}S_D\,, \tag{3.B103}$$

$$S_\phi = \frac{9}{10}\frac{D_1(a)}{a}T(k)\,, \qquad S_{\phi+\psi} = 2S_\phi\,, \tag{3.B104}$$

$$\Delta^{\mathrm{d2}} = -\frac{9}{5}\frac{\mathcal{H}^2}{\Omega_m \mathcal{H}_0^2}\frac{dD_1(a)}{da}T(k)\,, \tag{3.B105}$$

$$\Delta^{\mathrm{g1}} = \left(\frac{\dot{\mathcal{H}}}{\mathcal{H}^2} + \frac{2-5s}{\chi\mathcal{H}} + 5s - f_{\mathrm{evo}}\right)S_\phi\,, \tag{3.B106}$$

$$\Delta^{\mathrm{g2}} = -(2-5s)S_\phi\,, \qquad \Delta^{\mathrm{g3}} = \mathcal{H}^{-1}\dot{S}_\phi\,. \tag{3.B107}$$

Here we have set $\Phi = \Psi$ and the transfer function $T(k)$ as well as the growth function $D_1(a)$ have to be determined either with a Boltzmann solver like CLASS or using an analytic approximation like the one derived in Ref. [100]. We have normalized the growth function as well as the scale factor to unity today, $D_1(1) = 1$. For the numerical results shown in our figures we used the Boltzmann solver CLASS. We have checked analytically and numerically that our correlation functions for the standard and (d1)-terms agrees with the full sky results of [48].

3.C Approximation for the non-linear full-sky lensing

As discussed in Section 3.2.2, to calculate the non-linear full-sky lensing we calculate the halo-fit power spectrum at a fixed redshift z_* and then evolve it along the line-of-sight using the linear growth rate. To choose z_* we use the flat-sky non-linear result, that we calculate first without approximation and second with the same approximation as in the full-sky. We find that when $z_* = 0.42$ the approximate solution is in extremely good agreement with the correct solution. We use therefore the same z_* to calculate the full-sky result, for which it is not possible to do an exact integration (see discussion in Section 3.2.2).

In Fig. 3.19 we compare the non-linear full-sky lensing calculated with different values for z_*. In red we show the result for $z_* = 0.42$ (best fit from the flat-sky), and in black and blue we show the two extreme cases: $z_* = 1$ (black) and $z_* = 0$ (blue). We see that the lensing terms behave as expected: a smaller z_* gives rise to a larger result, since in this case we overestimate the power spectrum along the line-of-sight. The curve $z_* = 0.42$ is well situated between the two extreme cases, as was the case in the flat-sky. This gives us confidence that the approximation works well also for the full-sky lensing.

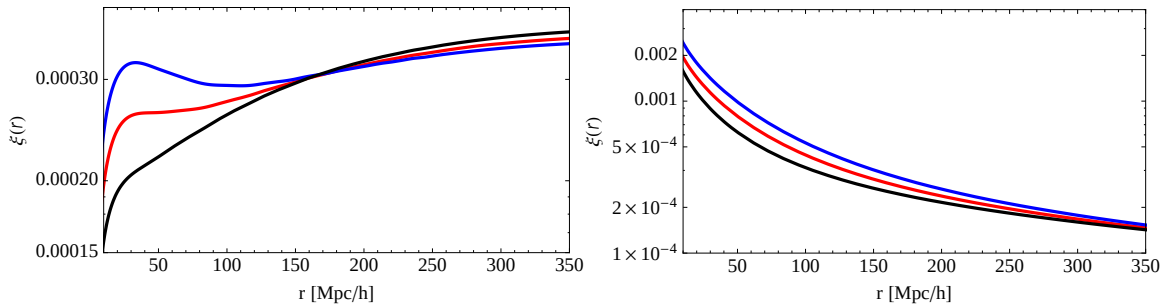

Figure 3.19: We show the full-sky non-linear density-lensing correlation function (left) and lensing-lensing correlation function (right) at $\bar{z} = 1$ as a function of separation, for $\mu = 1$. The black solid line shows the calculation with $z_* = 1$, the blue line with $z_* = 0$ and the red line with $z_* = 0.42$.

3.D Direction dependent power spectra

In this appendix we prove a simple property of direction dependent power spectra which is often used. This result is of course not new but it is usually used without derivation and mainly in special cases. Here we prove it in full generality.

Theorem *$\xi(\mathbf{r})$ is a correlation function which depends on the orientation of $\mathbf{r}$ only via its scalar product with one fixed given direction $\boldsymbol{n}$ (e.g. the line of sight). Denoting the corresponding direction cosine by μ and expanding ξ in Legendre polynomials, we have*

$$\xi(\mathbf{r}) = \sum_n \xi_n(r) L_n(\mu)\,, \qquad \mu = \hat{\mathbf{r}} \cdot \boldsymbol{n}\,. \tag{3.D108}$$

In this situation the Fourier transform of ξ, the power spectrum, is of the form

$$P(\mathbf{k}) = \sum_n p_n(k) L_n(\nu)\,, \quad \nu = \hat{\mathbf{k}} \cdot \boldsymbol{n} \quad \textit{where} \tag{3.D109}$$

$$p_n(k) = 4\pi i^n \int_0^\infty dr r^2 j_n(kr)\xi_n(r)\,, \quad \textit{and} \tag{3.D110}$$

$$\xi_n(r) = \frac{(-i)^n}{2\pi^2} \int_0^\infty dk k^2 j_n(kr) p_n(k)\,. \tag{3.D111}$$

Proof The Fourier transform of ξ is defined as

$$P(\mathbf{k}) = \int d^3 r e^{i\mathbf{r}\cdot\mathbf{k}} \xi(\mathbf{r})\,. \tag{3.D112}$$

We use that

$$e^{i\mathbf{r}\cdot\mathbf{k}} = \sum_\ell i^\ell (2\ell+1) j_\ell(kr) L_\ell(\hat{\mathbf{k}} \cdot \hat{\mathbf{r}})$$

and

$$L_\ell(\hat{\mathbf{k}} \cdot \hat{\mathbf{r}}) = \frac{4\pi}{2\ell+1} \sum_{m=-\ell}^{\ell} Y_{\ell m}(\hat{\mathbf{k}}) Y^*_{\ell m}(\hat{\mathbf{r}}) = \frac{4\pi}{2\ell+1} \sum_{m=-\ell}^{\ell} Y_{\ell m}(\hat{\mathbf{r}}) Y^*_{\ell m}(\hat{\mathbf{k}})\,.$$

Here $Y_{\ell m}$ are the spherical harmonics as given e.g. in [94]. Inserting these identities in (3.D112) using the ansatz (3.D108) for the correlation function, we obtain

$$P(\mathbf{k}) = \sum_{\ell m}\sum_{nm'} \frac{(4\pi)^2 i^\ell}{2\ell+1} \int d^3r \xi_n(r) j_\ell(kr) Y_{\ell m}(\hat{\mathbf{k}}) Y^*_{\ell m}(\hat{\mathbf{r}}) Y_{nm'}(\hat{\mathbf{r}}) Y^*_{nm'}(\boldsymbol{n}) \quad . \tag{3.D113}$$

Using the orthogonality relation of spherical harmonics, the integration over directions gives

$$P(\mathbf{k}) = 4\pi \sum_n i^n \int_0^\infty dr r^2 \xi_n(r) j_n(kr) L_n(\nu)\,. \tag{3.D114}$$

Identification of the expansion coefficients yields (3.D110). Eq. (3.D111) is obtained in the same way using the inverse Fourier transform,

$$\xi(\mathbf{r}) = \frac{1}{(2\pi)^3} \int d^3k e^{-i\mathbf{k}\cdot\mathbf{r}} P(\mathbf{k})\,. \qquad \blacksquare$$

Clearly, if $\xi(\mathbf{r}) = \langle \Delta(\boldsymbol{x})\Delta(\boldsymbol{x}+\mathbf{r})\rangle$ is independent of $\boldsymbol{x}$ (Δ is statistically homogeneous), ξ does not depend on the sign of $\mathbf{r}$ and in the sum above only ξ_n with even n's can contribute so that $P(\mathbf{k})$ is real.

Inserting the expressions for the $Q^{\rm AB}$ in (3.46) to obtain the correlation function, we realize that in the flat sky limit ($\boldsymbol{n}_1 \to \boldsymbol{n}_2$), all our terms ξ^{AB} where the corresponding Q^{AB} do not contain integrated terms, are actually of this form. This also shows that in this limit $\zeta^{01}+\zeta^{10}$ and $\zeta^{12}+\zeta^{21}$ must vanish since they contain $j_1(kr)$ and $j_3(kr)$ and would yield imaginary contributions to the power spectrum.

For wide angles $\boldsymbol{n}_1 \neq \boldsymbol{n}_2$ the correlation function depends on two directions. Furthermore, for large $\mathbf{r}$ it is not translation invariant as it depends on the redshift on our background light-cone at which $\mathbf{r}$ is placed. In this case, the Fourier transform of the correlation function is no longer simply given by the power spectrum of the fluctuations.

The theorem proven above has a simple but useful corollary which is sometimes called the *closure relation* of spherical Bessel functions [21]. Inserting the expression (3.D110) into (3.D111) and using that it holds for arbitrary functions $p_n(k)$, we find

$$\frac{2}{\pi}\int_0^\infty j_n(rk) j_n(rk') r^2 dr = \delta(k-k') k^{-2}\,, \tag{3.D115}$$

for positive k and k'. Using

$$j_n(x) = \sqrt{\frac{\pi}{2x}} J_{n+1/2}(x)$$

we can convert (3.D115) into an equation for ordinary Bessel functions J_m:

$$\int_0^\infty J_{n+1/2}(rk) J_{n+1/2}(rk') r dr = k^{-1}\delta(k-k')\,, \tag{3.D116}$$

This identity also holds for J_m with integer m, see [122], No 6.512-8.

3.E The flat sky approximation

To derive expression (3.70) we consider the observed galaxy density fluctuation in real space given in Eq. (3.8). We neglect the integrated Sachs Wolfe term and the $\dot{\Phi}$ term in the first line; they are very small and relevant mainly on very large angular scales where the flat sky approximation breaks down. The remaining integrated term is then only the lensing term and the subdominant Shapiro time delay. Furthermore, we set $\Psi = \Phi$ which is a very good approximation in ΛCDM at late times. Denoting the power spectrum of the comoving density contrast δ_c at redshift $z = 0$ by P_δ and using the perturbed Einstein and continuity equations we find

$$\Phi = \Psi = -\frac{3}{2}\frac{\Omega_m H_0^2 (1+z) D_1(z)}{k^2}\delta_c \tag{3.E117}$$

$$V = -\frac{\mathcal{H}}{k} f(z) D_1(z) \delta_c \,, \tag{3.E118}$$

where $f(z)$ is the growth rate as given in (4.2), $D_1(z)$ is the growth function such that $\delta_c(k,z) = D_1(z)\delta_c(k) \equiv D_1(z)\delta_c(k,0)$ and Ω_m is the matter density parameter today.

Neglecting first the integrated terms we can simply Fourier transform this expression from $\chi(z)\boldsymbol{n} \equiv \boldsymbol{x}$ to $\mathbf{k}$ and use that the power spectrum is the square of the Fourier transform amplitude. This yields

$$P_{n.i} = \left| A + B/(k\mathcal{H}) + C/(k\mathcal{H})^2 \right|^2 P_\delta(k) \,, \tag{3.E119}$$

where A, B and C are given in (3.67) and (3.69).

To derive the cross term of the non-integrated with the integrated terms, it is more useful to start with the correlation function. Let us denote $A + B/(k\mathcal{H}) + C/(k\mathcal{H})^2 = \alpha(k,\nu,z)$ and $\hat{F}(k,\nu,z) = \alpha(k,\nu,z)\delta_c(k)$ with Fourier transform $F(\boldsymbol{x},z)$. Denoting

$$I(\chi(z)\boldsymbol{n},z) = \frac{2}{\chi(z)}\int_0^{\chi(z)} d\lambda \left[2 - \frac{\chi(z)-\lambda}{\lambda}\Delta_\Omega\right]\Phi \,, \tag{3.E120}$$

we have

$$\begin{aligned}\xi_{\Delta\Delta}(\mathbf{r},z) &= \langle F(\chi_1\boldsymbol{n}_1,z_1)F(\chi_2\boldsymbol{n}_2,z_2)\rangle + \langle I(\chi_1\boldsymbol{n}_1,z_1)F(\chi_2\boldsymbol{n}_2,z_2)\rangle \\ &\quad + \langle F(\chi_1\boldsymbol{n}_1,z_1)I(\chi_2\boldsymbol{n}_2,z_2)\rangle + \langle I(\chi_1\boldsymbol{n}_1,z_1)I(\chi_2\boldsymbol{n}_2,z_2)\rangle\end{aligned} \tag{3.E121}$$

where $\chi_i = \chi(z_i)$ and $\mathbf{r} = \chi_2\boldsymbol{n}_2 - \chi_1\boldsymbol{n}_1$, $z = (z_1+z_2)/2$ and we assume both $\chi_i \gg r$ and the z_i should not be very different. Using the relation between Φ and δ_c, the contribution of the cross term to the correlation function is then given by

$$\begin{aligned}\xi_{IF}(\mathbf{r},z) &= -\frac{3}{(2\pi)^3}\frac{\Omega_m H_0^2 (2-5s(z))}{2\chi_1}\int \frac{d^3k}{k^2} P_\delta(k) e^{-i\mathbf{k}\boldsymbol{n}_2\chi_2}\alpha(k,\nu,z_2)\times \\ &\quad \int_0^{\chi_1} d\lambda \left[\lambda(\chi_1-\lambda)k_\perp^2 + 2\right] D_1(z(\lambda))(1+z(\lambda)) e^{i\mathbf{k}\boldsymbol{n}_1\lambda}\end{aligned} \tag{3.E122}$$

In the spirit of the flat sky approximation we now set $\boldsymbol{n}_1 = \boldsymbol{n}_* + \Delta\boldsymbol{n}/2$ and $\boldsymbol{n}_2 = \boldsymbol{n}_* - \Delta\boldsymbol{n}/2$ assuming that $\Delta\boldsymbol{n}$ is very small. Splitting $\mathbf{r} = \mathbf{r}_\perp + \boldsymbol{n}_* r_\parallel$ with $\mathbf{r}_\perp = \chi(z)\Delta\boldsymbol{n}$ and $r_\parallel = r\cos\alpha_2$, see Fig. 3.18, we then perform the k-integral in the direction parallel to $\boldsymbol{n}_*$, $dk_\parallel \exp(-ik_\parallel(\chi_2 - \lambda))$. We neglect the slow dependence of the power spectrum on $k_\parallel$ and only consider the rapidly oscillating exponential which gives $2\pi\delta(\chi_2 - \lambda)$. Hence the integral over λ does not contribute if $\chi_2 > \chi_1$, otherwise it reduces to the integrand at χ_2,

$$\begin{aligned}\xi_{IF}(\mathbf{r}, z) &= -\frac{3}{(2\pi)^2}\frac{\Omega_m H_0^2(2 - 5s(z))\Theta(\chi_1 - \chi_2)}{2\chi_1} D_1(z_2)(1 + z_2) \\ &\quad \int \frac{d^2k_\perp}{k_\perp^2} P_\delta(k_\perp) e^{-i\mathbf{k}_\perp\cdot\mathbf{r}_\perp} \alpha(k_\perp, 0, z_2) \left[\chi_2(\chi_1 - \chi_2)k_\perp^2 + 2\right] ,\end{aligned} \tag{3.E123}$$

where Θ is the Heaviside Θ-function.

Using polar coordinates, $d^2\mathbf{k}_\perp = dk_\perp k_\perp d\varphi$ we can perform the φ integration which yields a Bessel function, $2\pi J_0(k_\perp r_\perp) = 2\pi J_0(k_\perp r\sin\alpha_2)$. The term $\xi_{FI}(\mathbf{r}, \bar{z})$ contributes in the same way with z_1 and z_2 exchanged. Setting $\chi_1 - \chi_2 = r_\parallel = r\mu$ and neglecting the difference of χ_1 and χ_2 (z_1 and z_2) in all other places, we find for the sum of both mixed terms

$$\begin{aligned}\xi_{IF+FI}(\mathbf{r}, z) &= -\frac{3}{2\pi}\frac{\Omega_m H_0^2(2 - 5s(z))}{2\chi} D_1(z)(1 + z) \\ &\quad \int \frac{dk_\perp}{k_\perp} P_\delta(k_\perp) J_0(k_\perp r\sqrt{1 - \mu^2}) \alpha(k_\perp, 0, z) \left[\chi|\mu| r k_\perp^2 + 2\right] .\end{aligned} \tag{3.E124}$$

Here we have also neglected the difference between $\cos\alpha_2$ and μ. In the flat sky approximation all these angles are equal. (If we would want to be precise, actually in the case $z_1 \equiv z_2$, hence $\mu = 0$ the Shapiro time delay would obtain a factor 4, not 2, but we neglect this in the flat sky approximation.)

To obtain the Fourier transform of (3.E124) which is the contribution n.i.-I to the power spectrum we first multiply the equation with $\int dk_\parallel \exp(-ik_\parallel r_\parallel)\delta(k_\parallel) = 1$. We then write the factor $|\chi_2 - \chi_1| = |r_\parallel| = |\mu| r$ inside the integral,

$$\int dk_\parallel \exp(-ik_\parallel r_\parallel)|r_\parallel|\delta(k_\parallel) = |r_\parallel|$$

is the Fourier transform of

$$\delta^P(k_\parallel) \equiv \frac{1}{2\pi}\int dr_\parallel \exp(ik_\parallel r_\parallel)|r_\parallel| . \tag{3.E125}$$

Note that without the absolute value δ^P would become $-i\delta'$. This distribution is purely imaginary while δ^P is real. However, like δ or δ' its support is on $k_\parallel = 0$, i.e. for a function f which vanishes in a small neighborhood around $k_\parallel = 0$ we have $\delta^P \cdot f \equiv 0$.

Inserting (3.E125), we can write the correlation function ξ_{IF+FI} as the Fourier transform of

$$P_{\rm n.i.-I}(\mathbf{k},z) = -3\pi\frac{\Omega_m H_0^2(2-5s(z))}{\chi}D_1(z)(1+z)P_\delta(k_\perp)\alpha(k_\perp,0,z)\left[\delta^P(k_\parallel)+\frac{2}{k_\perp^2}\delta(k_\parallel)\right]. \tag{3.E126}$$

Note also that since $k_\parallel = 0$, in the flat sky limit, the integrated term is not correlated with redshift space distortions.

Let us finally compute the double integrated term,

$$\xi_{II}(\mathbf{r},z) = \frac{(3\Omega_m H_0^2(2-5s(z)))^2}{(2\pi)^3 4\chi^2}\int\frac{d^3k}{k^4}P_\delta(k)\int_0^{\chi_1}d\lambda\int_0^{\chi_2}d\lambda'\left[\lambda(\chi_1-\lambda)k_\perp^2+2\right]\times \left[\lambda'(\chi_2-\lambda')k_\perp^2+2\right]D_1(z(\lambda))(1+z(\lambda))D_1(z(\lambda'))(1+z(\lambda'))e^{-i\mathbf{k}(\boldsymbol{n}_1\lambda-\boldsymbol{n}_2\lambda')} \tag{3.E127}$$

Via the same procedure as above, the integration over $k_\parallel$ leads to $2\pi\delta(\lambda-\lambda')$ and we find

$$\xi_{II}(\mathbf{r},z) = \frac{(3\Omega_m H_0^2(2-5s(z)))^2}{(2\pi)^2 4\chi^2}\int\frac{d^2k_\perp}{k_\perp^4}P_\delta(k_\perp) \int_0^{\chi}d\lambda\left[\lambda(\chi-\lambda)k_\perp^2+2\right]^2 D^2(z(\lambda))(1+z(\lambda))^2 e^{-i\mathbf{k}_\perp\mathbf{r}_\perp(\lambda/\chi))}. \tag{3.E128}$$

We now perform a change of variables, $\mathbf{k}_\perp \mapsto (\lambda/\chi)\mathbf{k}_\perp$. In terms of this new variable, the integral contribution to the correlation function becomes

$$\xi_{II}(\mathbf{r},z) = \frac{(3\Omega_m H_0^2(2-5s(z)))^2}{(2\pi)^2 4\chi^2}\int_0^{\chi}d\lambda\int\frac{d^2k_\perp}{k_\perp^4}P_\delta(k_\perp\chi/\lambda)e^{-i\mathbf{k}_\perp\mathbf{r}_\perp}\times \left(\frac{\lambda}{\chi}\right)^2\left[\frac{(\chi-\lambda)\chi^2}{\lambda}k_\perp^2+2\right]^2 D^2(z(\lambda))(1+z(\lambda))^2. \tag{3.E129}$$

Again, performing the φ integration we end up with

$$\xi_{II}(\mathbf{r},z) = \frac{(3\Omega_m H_0^2(2-5s(z)))^2}{8\pi\chi^2}\int_0^{\chi}d\lambda\int dk_\perp k_\perp P_\delta(k_\perp\chi/\lambda)J_0(k_\perp r\sqrt{1-\mu^2})\times \left(\frac{\lambda}{\chi}\right)^2\left[\frac{(\chi-\lambda)\chi^2}{\lambda}+\frac{2}{k_\perp^2}\right]^2 D^2(z(\lambda))(1+z(\lambda))^2. \tag{3.E130}$$

Inserting the same factor 1 as for the mixed term above, we can read off the flat sky power spectrum of the integrated contribution,

$$P_{II}(\mathbf{k},z) = \frac{\pi(3\Omega_m H_0^2(2-5s(z)))^2}{2\chi^2} \int_0^{\chi}d\lambda P_\delta(k\chi/\lambda)\delta(k_\parallel)\left(\frac{\lambda}{\chi}\right)^2\left[\frac{(\chi-\lambda)\chi^2}{\lambda}+\frac{2}{k^2}\right]^2 D^2(z(\lambda))(1+z(\lambda))^2.$$

(3.E131)

Adding (3.E119, 3.E126, 3.E131) we obtain the result (3.70). For completeness, and since we use it for some of our results, we also write down the flat sky correlation function,

$$\begin{aligned}\xi_\Delta(\mathbf{r},z) &= \int dk_\perp k k_\perp P_\delta(k) J_0(k_\perp r\sqrt{1-\mu^2}) \int_{-1}^{1} d\nu |\alpha(k,\nu,z)|^2 e^{-ik\nu\mu r} \\ &\quad -\frac{3\Omega_m H_0^2(2-5s(z))}{4\pi\chi} D_1(z)(1+z) \\ &\qquad \int \frac{dk_\perp}{k_\perp} P_\delta(k_\perp) J_0(k_\perp r\sqrt{1-\mu^2}) \alpha(k_\perp,0,z) \left[\chi|\mu| r k_\perp^2 + 2\right] + \\ &\quad \frac{(3\Omega_m H_0^2(2-5s(z)))^2}{8\pi\chi^2} \int_0^\chi d\lambda \int \frac{dk_\perp}{k_\perp^3} P_\delta(k_\perp\chi/\lambda) J_0(k_\perp r\sqrt{1-\mu^2}) \times \\ &\quad \left(\frac{\lambda}{\chi}\right)^2 \left[\frac{(\chi-\lambda)\chi^2}{\lambda} k_\perp^2 + 2\right]^2 D^2(z(\lambda))(1+z(\lambda))^2 \,. \end{aligned} \tag{3.E132}$$

Since α only contains terms which are constant, linear or quadratic in ν, the ν-integration is easily performed analytically.

4

Nonlinear contributions to angular power spectra

Based on:
[163] M. Jalilvand, B. Ghosh, E. Majerotto, B. Bose, R. Durrer,& M. Kunz, *Nonlinear contributions to angular power spectra*, **Phys.Rev.D** 101 (2020), [arXiv: 1907.13109]

From the previous chapter, we got an idea of the limitations of working with the angular power spectra C_ℓ's, but it still remains very significant as an observational tool for incorporating the relativistic contributions. Here we take an initiative to model the nonlinear C_ℓ's for studying cosmological structure formation in intermediate to small scales. We find that using a clever flat-sky approximation that agrees very well with a full-sky treatment done in CAMB [196], we can perform fast computations to obtain these nonlinear C_ℓ's. The novelty of this work lies in the fact that we have computed the C_ℓ's in the redshift space, and not merely in the real space, where the overdensity that we theoretically consider is definitely not an observable one. We provide the first step for analysing nonlinearities, which does not yet include lensing contributions, but should indeed be extended to do that in the near future. We first compute the one-loop corrections to the redshift-space power spectrum from the standard perturbation theory, which is eventually used to compute the redshift-space power spectrum from the Lagrangian perturbation theory (LPT), effective field theory (EFT) and Taruya-Nishimichi-Saito (TNS) model as well. Using the above-mentioned flat-sky approximation, we then calculate the nonlinear C_ℓ's in redshift-space. In order to gauge the accuracy of our results, we compare them with the COLA simulations that provide the first three even multipoles from which we can construct the full anisotropic power spectrum. It is to be noted that at much smaller scales it is more sensible to use a full N-body simulation approach. We find that the most reliable way to model the redshift-space nonlinearities is via the TNS model, which performs very well in case of narrow redshift bins which enhance the impact of nonlinear RSD. However, for larger bin widths, where RSD effects are much less prominent, we observe that the most accurate approach is that using Halofit combined with the Kaiser factor.

Abstract: Future galaxy clustering surveys will probe small scales where nonlinearities become important. Since the number of modes accessible on intermediate to small scales is very high, having a precise model at these scales is important especially in the context of discriminating alternative cosmological models from the standard one. In the mildly nonlinear regime, such models typically differ from each other, and galaxy clustering data will become very precise on these scales in the near future. As the observable quantity is the angular power spectrum in redshift space, it is important to study the effects of nonlinear density and redshift space distortion (RSD) in the angular power spectrum. We compute nonlinear contributions to the angular power spectrum using a flat-sky approximation, and compare the results of different perturbative and nonperturbative approaches. We find that the Taruya-Nishimichi-Saito (TNS) perturbative approach is significantly closer to the comoving Lagrangian acceleration (COLA) approximation than Eulerian or partially resummed-Lagrangian one-loop approximations, effective field theory of large scale structure or a halofit-inspired model. However, none of these prescriptions agree with each other in the nonlinear regime. A surprising and new result of the present analysis is that for narrow redshift bins, $\Delta z \lesssim 0.01$, the angular power spectrum acquires nonlinear contributions on all scales, right down to $\ell = 2$, and is hence not a reliable tool at this time. To overcome this problem, we need to model nonlinear RSD terms, for example as TNS does, but for a matter power spectrum that remains reasonably accurate well into the deeply nonlinear regime, such as halofit.

4.1 Introduction

After the tremendous success of Cosmic Microwave Background (CMB) observations [12], presently major efforts in cosmology are going into the observation and modelling of the distribution of galaxies [20, 272, 35, 39, 251, 204, 36, 119, 271]. As this data set is three dimensional, it is potentially much richer and may allow us to study the evolution of cosmic structure formation.

However, on small scales the fluctuations in the matter density can become large at the present time. Therefore, first order cosmological perturbation theory is not sufficient to describe structure formation on these scales and numerical N-body simulations, in principle including also hydrodynamic effects, are needed. This is a very complicated process and usually many phenomenological parameters have to be used to describe the highly nonlinear hydrodynamic processes which are affected by star formation, AGN (active galactic nuclei) feedback and more [244, 262, 229].

On intermediate scales, higher order perturbation theory and phenomenological modelling of the galaxy power spectrum can be used [175, 265, 283, 231, 50]. This is the topic of the present work. In the past, people have mainly looked at the power spectrum in Fourier space [36, 35]. Within linear perturbation theory this is approximated by the so-called Kaiser formula [175], which includes redshift space distortions (RSD) i.e. the fact that the observed redshift is affected by peculiar velocities which are in turn correlated with matter overdensities,

$$P(k,\mu,\bar{z}) \;=\; D_1^2(\bar{z})\left[b(\bar{z}) + f(\bar{z})\mu^2\right]^2 P_m(k), \tag{4.1}$$

where $\mu = \hat{\mathbf{k}} \cdot \boldsymbol{n}$ is the cosine of the angle between the unit vector in direction $\mathbf{k}$, $\hat{\mathbf{k}}$, and the observation direction $\boldsymbol{n}$, which is a unit vector. Here $\bar{z}$ is a mean redshift of the survey under consideration, $P_m(k)$ is the linear matter density power spectrum today, $D_1(\bar{z})$ is the linear growth factor normalized to $D_1(0) = 1$, $b(\bar{z})$ is the galaxy bias and

$$f(\bar{z}) = -\frac{D_1'}{D_1}(1+\bar{z}) = \frac{d\ln D_1}{d\ln(a)}\,, \tag{4.2}$$

is the growth rate, where the prime denotes the derivative with respect to the redshift $\bar{z}$. This formula has been generalized in the literature to include nonlinearities in the matter power spectrum, usually by replacing $D_1^2(\bar{z})P_m(k)$ by a one-loop or two-loop power spectrum [265] or by a phenomenological approximation like halofit [280, 283]. Workers in the field have also corrected the 'Kaiser relation' $f(\bar{z})(\hat{\mathbf{k}}\cdot\boldsymbol{n})^2$ for the peculiar velocity with a nonlinear and phenomenological description [208]. With the increasing precision of the data available from galaxy surveys such as Euclid[1] [189, 19], WFIRST [2] [274], 4MOST [299] and (DESI)[3][13], and with the upcoming HI surveys (e.g. [24, 227, 22]) that have a very high redshift resolution, it is important to model the theoretical galaxy power spectrum as accurately as possible. Even at scales as large as those of baryon acoustic oscillations, we need to go beyond linear perturbation theory [36, 52].

Eq. (4.1) is a good approximation to cosmological observations only if we have a small, far away galaxy survey in a fixed direction $\boldsymbol{n}$ at nearly fixed redshift $\bar{z}$. A true galaxy survey lives on our background lightcone and the radial distance between galaxies is related to their redshift difference. The correlation function therefore is truly a function of two directions, $\boldsymbol{n}_1$, $\boldsymbol{n}_2$ and two redshifts, z_1, z_2. Assuming statistical isotropy it depends only on $\cos\theta = \boldsymbol{n}_1 \cdot \boldsymbol{n}_2$, z_1 and z_2. A harmonic transform in $\cos\theta$ yields the spherical power spectrum $C_\ell(z_1, z_2)$. This has been derived at first order in perturbation theory in [46, 67]. Apart from density and RSD, the complete formula includes several relativistic effects like the integrated Sachs Wolfe effect, the Shapiro time delay, the gravitational potential at the source and gravitational lensing convergence (also termed 'magnification bias'). Apart from the last term, all relativistic contributions are relevant only on very large scales corresponding to $\ell \lesssim 10$. The gravitational lensing contribution is relevant in wide redshift bins, at relatively high redshifts, $z \gtrsim 1$, or in widely separated redshift bins [46, 221, 59]. For the redshift bin widths used in this work, we discuss briefly in Appendix 4.D the importance of lensing in angular power spectra, relative to the RSD contribution.

Here, we consider spectroscopic surveys which have a very precise redshift distribution and we shall neglect lensing. We want to determine the effect of loop corrections in Eulerian and Lagrangian perturbation theory as well as other phenomenological approaches to the nonlinear matter power spectrum. We study how these corrections affect the observable angular power spectrum, C_ℓ, when considering density and redshift space distortions, and we compare them with results from

[1] `www.euclid-ec.org`
[2] `https://wfirst.gsfc.nasa.gov/`
[3] `www.desi.lbl.gov`

the more accurate COmoving Lagrangian Acceleration (COLA)[285, 143, 295, 302] simulations. The density and RSD contributions are dominant at relatively low redshifts and for spectroscopic surveys like Euclid; furthermore, it is these terms which are most affected by nonlinearities. The main point of this paper is not to make precise forecasts for which certainly the lensing term should not be neglected, but to study the effect of nonlinear corrections in the C_ℓ's coming from clustering and RSD.

In the next section, we derive a 'flat sky approximation' for density and RSD which is surprisingly accurate even at low ℓ. In section 4.3 we describe and compare four different nonlinear prescriptions for the power spectrum in redshift space, which can be found in the literature. This section is not new but we spell out these approximations for completeness. In Section 4.4 we compute the C_ℓ's from the different approximations and compare them with the linear and halofit results. This section contains our main findings. We also compare our theoretical predictions to measurements made from a set of COLA N-body simulations. In Section 4.5 we discuss our findings and conclude.

4.2 The flat sky approximation

In this section, we discuss a flat-sky approximation [37, 81, 64] using which we want to compute the angular power spectrum $C_\ell(z_1, z_2)$ for galaxy number counts from the 3-dimensional power spectrum, where z_1 and z_2 are two (relatively close) redshifts. We start from the correlation function in configuration space which in principle depends on two spatial positions and two redshifts, $\xi(\boldsymbol{x}_1, z_1; \boldsymbol{x}_2, z_2)$ where $(\boldsymbol{x}_1, z_1)$ and $(\boldsymbol{x}_2, z_2)$ are constrained to lie on our background lightcone. We assume that the redshifts are relatively close so that the time evolution between z_1 and z_2 can be neglected. Then the correlation function depends only on $\mathbf{r} = \boldsymbol{x}_2 - \boldsymbol{x}_1$ and $\bar{z} = (z_1 + z_2)/2$ (see Fig. 4.1). This correlation function in real space, $\xi(\mathbf{r}, \bar{z})$, is the Fourier transform of the power spectrum

$$\xi(\mathbf{r}, \bar{z}) = \frac{1}{(2\pi)^3} \int d^3\mathbf{k} P(\mathbf{k}, \bar{z}) e^{-i\mathbf{k}\cdot\mathbf{r}}. \tag{4.3}$$

Let us now consider the flat sky approximation, which amounts to assuming that the direction from the observer to the points $\boldsymbol{x}_1$ and $\boldsymbol{x}_2$ are nearly equal, $\mathbf{n}_1 \simeq \mathbf{n}_2 = \mathbf{n}$, i.e. the survey covers a relatively small patch of the sky in a fixed direction $\boldsymbol{n}$. This is the situation Eq. (4.1) can be used as an approximation for the power spectrum. In this case we can also decompose the separation vector $\mathbf{r}$ into components perpendicular and parallel to the line of sight direction $\mathbf{n}$, as shown in Fig. 4.1, so we have:

$$\begin{aligned} \mathbf{r} &= \mathbf{r}_\perp + r_\parallel \mathbf{n}, \\ r_\parallel &= r\nu \simeq \chi(z_2) - \chi(z_1) \simeq \tfrac{\Delta z}{H(\bar{z})}\,, \end{aligned} \tag{4.4}$$

where $\chi(z)$ is the comoving distance to redshift z, $\nu = \hat{\mathbf{r}} \cdot \hat{\mathbf{n}}$ as shown in Fig. 4.1. Similarly in k-space we define

$$\mathbf{k} = \mathbf{k}_\perp + k_\parallel \mathbf{n},$$

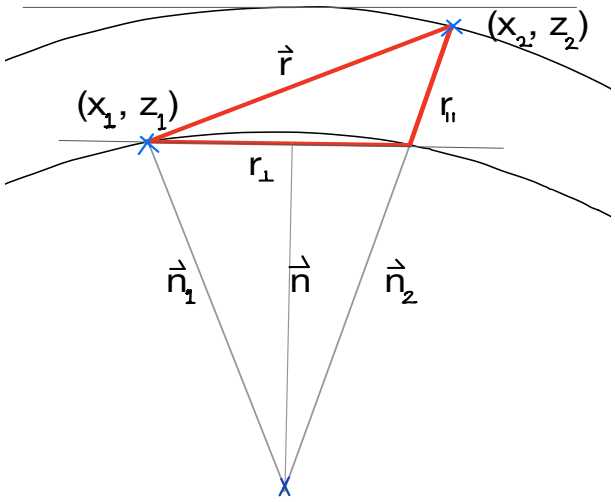

Figure 4.1: We show the positions $(\boldsymbol{x}_1, z_1)$ and $(\boldsymbol{x}_2, z_2)$ on the background lightcone of an observer situated at X and their flat sky approximations.

$$k_{\parallel} = k\mu = k\,\hat{\mathbf{k}}\cdot\mathbf{n}\,. \tag{4.5}$$

We now introduce the dimensionless two dimensional vector $\boldsymbol{\ell}$ by $\mathbf{k}_{\perp} \equiv \boldsymbol{\ell}/\chi(\bar{z})$. Therefore by using Eqs. (4.4) and (4.5) we can rewrite Eq. (4.3) as:

$$\xi(\mathbf{r},\bar{z}) = \frac{1}{(2\pi)^3}\int \frac{d^2\boldsymbol{\ell}}{\chi^2(\bar{z})} dk_{\parallel} P(\mathbf{k},\bar{z}) e^{-i\left(\frac{\boldsymbol{\ell}\cdot\mathbf{r}_{\perp}}{\chi(\bar{z})}+k_{\parallel}\frac{(z_2-z_1)}{H(\bar{z})}\right)}. \tag{4.6}$$

On the other hand, we know how to compute $\xi(\mathbf{r}, z)$ from the angular power spectrum. In the flat-sky approximation this yields (see e.g. [94])

$$\xi(\mathbf{r}_{\perp}, z_1, z_2) = \frac{1}{(2\pi)^2}\int d^2\boldsymbol{\ell}\, C_{\ell}(z_1,z_2) e^{-i\boldsymbol{\ell}\cdot\mathbf{r}_{\perp}/\chi(\bar{z})}. \tag{4.7}$$

By comparing Eqs. (4.6) and (4.7), we find the relation between the angular power spectrum and the three dimensional power spectrum in Fourier space as

$$C_{\ell}(z_1,z_2) = \frac{1}{2\pi\chi^2(\bar{z})}\int_{-\infty}^{+\infty} dk_{\parallel} P\left(k,\bar{z}\right) e^{-ik_{\parallel}(z_2-z_1)/H(\bar{z})}\,, \tag{4.8}$$

for $k = \sqrt{k_{\parallel}^2 + (\ell/\chi)^2}$. Note that this approximation is not equivalent to the Limber approximation [198] which is often used for weak lensing calculations where $k \simeq (\ell+1/2)/\chi(z)$ is used instead of an integration of the power spectrum times the Bessel function. In this flat sky approximation we identify the flat sky vectors

$$\mathbf{k}_{\perp} \equiv \boldsymbol{\ell}/\chi(\bar{z}), \tag{4.9}$$

and integrate over $k_{\parallel}$. More details about this approximation are discussed in a forthcoming paper [213]. Contrary to Limber's approximation, which is bad for the

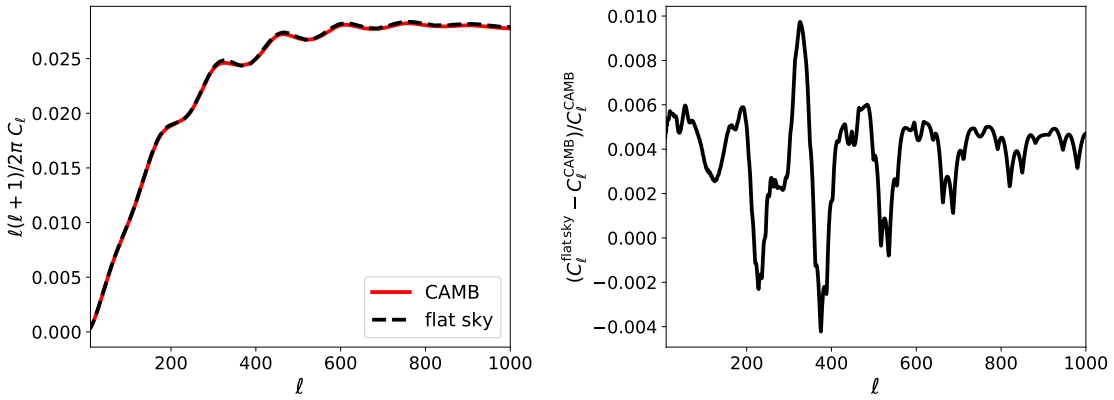

Figure 4.2: The left panel shows the comparison between the flat-sky approximation of Eq. (4.8) and the angular power spectrum computed by CAMB that uses Eq. (4.10) at $z = 1$, using a top hat window function with $\Delta z = 0.1$. The right panel shows the relative difference between the two.

density and RSD contributions to number counts (see, e.g. [89]), this approximation turns out to be excellent for close redshifts $z_1 \simeq z_2$, when compared to the exact definition of $C_\ell(z_1, z_2)$ which, at low ℓ, is given by (see Appendix B of [46], where we have added the bias dependence)

$$\begin{aligned} C_\ell(z_1,z_2) \;=\; & \frac{2}{\pi} b(z_1) b(z_2) \int dk\, k^2 P_m(k,z_1,z_2) \Big[j_\ell(k\,\chi(z_1)) j_\ell(k\,\chi(z_2)) \\ & - \frac{f(z_2)}{b(z_2)} j_\ell(k\,\chi(z_1)) j_\ell''(k\,\chi(z_2)) - \frac{f(z_1)}{b(z_1)} j_\ell''(k\,\chi(z_1)) j_\ell(k\,\chi(z_2)) + \\ & + \frac{f(z_1)}{b(z_1)} \frac{f(z_2)}{b(z_2)} j_\ell''(k\,\chi(z_1)) j_\ell''(k\,\chi(z_2)) \Big]. \end{aligned} \tag{4.10}$$

Here $P_m(k, z_1, z_2)$ is the matter power spectrum and $b(z_1)$, $b(z_2)$ are the linear tracer biases at z_1 and z_2. For large redshift separations the flat sky approximation gets worse. This is because this approximation corresponds to replacing the spherical Bessel function by their lowest frequency modes, assuming that $|\chi(z_1) - \chi(z_2)| \ll \chi(z_1),\ \chi(z_2)$ which is no longer valid when the redshift difference becomes large (see [213] for a detailed derivation – for large redshift differences we additionally need to model the decoherence in $P(k, z_1, z_2)$ correctly, e.g. with the fitting function of [71]). In Fig. 4.2 we compare the angular power spectrum for $z_1 = z_2 = 1$ computed in the flat sky approximation Eq. (4.8) with the one computed with the exact formula of Eq. (4.10). The differences are at most 1%.

4.3 Nonlinear corrections to the power spectrum in redshift space

In this section we give a summary of different nonlinear corrections to the power spectrum that can be found in the literature. More precisely we consider four different

approaches: one-loop corrections from standard Newtonian (Eulerian) perturbation theory which we shall term SPT, one-loop partially resummed Lagrangian perturbation theory (pr-LPT) , corrections from effective field theory of large scale structure (EFT) and the Taruya-Nishimichi-Saito (TNS) model. Some important references for each of these approaches are [129, 212, 29, 283] respectively. We perform all perturbative calculations at the one-loop level (see Appendix 4.A for details). We also make use of a set of measurements of the redshift power spectrum from COLA simulations. These represent our most accurate prediction, with which we can compare the perturbative approaches. These simulations are described briefly below. At the end of this section we compare the different approximations to these simulations.

4.3.1 COLA

We have run a set of 10 Parallel COmoving Lagrangian Acceleration (PICOLA) simulations [143, 302] of box size $1024\,\mathrm{Mpc}/h$ with 1024^3 dark matter particles and a starting redshift $z_{\rm ini} = 49$. These are all run under a similar ΛCDM cosmology with Planck parameters [12]: $\Omega_m = 0.315$, $\Omega_b = 0.0493$, $h = 0.674$, $n_s = 0.965$ and $\sigma_8(z = 0) = 0.811$. The simulation redshift space power spectrum multipoles are measured using the distant-observer (or flat sky) approximation[4] and are then averaged over three line-of-sight directions. We further average over the 10 PICOLA simulations. We measure the first three even multipoles, the monopole, quadrupole and hexadecapole. Using these we can then construct the full anisotropic power spectrum, $P(k, \mu)$[5]

$$\begin{aligned} P_{\rm tot}^{\rm sCOLA}(\mathbf{k}, z) &= 2P_0(k, z) + \frac{2}{5}\mathcal{L}_2(\mu)P_2(k, z) \\ &+ \frac{2}{9}\mathcal{L}_4(\mu)P_4(k, z) + [\text{higher order multipoles}], \end{aligned} \tag{4.11}$$

where $\mathcal{L}_i$ is the Legendre polynomial of order 'i' and P_i is the $i^{\rm th}$ multipole which is an average over the measurements made from the COLA simulations. Finally, we note that the COLA method is an approximate method and has been shown to deviate from the full N-body approach at smaller scales [158, 51, 44]. This issue can be ignored as we simply use these simulations as a benchmark in accuracy with which to compare the less accurate perturbative predictions outlined next. For example, the redshift space monopole for lowly biased halos was shown to be accurate to full N-body to within a few percent at $z \leq 1$ up to $k = 0.7h/\mathrm{Mpc}$ in [158]. On the other hand, the quadrupole deviates by up to 10% at $z = 1$ at $k = 0.7h/\mathrm{Mpc}$ in the same paper. Regarding this issue, we expect the dark matter monopole and quadrupole to perform better than the halo multipoles, and for their accuracy to improve at

[4]That is, we assume the observer is located at a distance much greater then the box size ($r \gg 1024\,\mathrm{Mpc}/h$), and so all lines of sight are treated as being parallel to the chosen Cartesian axes of the simulation box. Next, we disturb the position of the matter particles using their velocity components (v_x, v_y or v_z).

[5]Note that the hexadecapole at the redshifts considered here is already very small in magnitude and so the exclusion of higher order multipoles will only negligibly affect the form of $P(k, \mu)$.

higher redshifts. Furthermore, we expect the theoretical models discussed in this section to perform significantly worse at these scales.

4.3.2 SPT

One-loop contributions to the power spectrum in redshift space (denoted by superscript s) in the context of SPT are already well-established and have previously been calculated in the literature (for a review see e.g. [30]). Here as a reference we point to Eq. (15) of [129]:

$$\begin{aligned} P_{\rm tot}^{\rm sSPT}(\mathbf{k},z) &\equiv P_{\rm lin}^{s} + P_{\rm one-loop}^{\rm sSPT} = P_{\rm lin}^{s} + P_{22}^{s} + P_{13}^{s} \\ &= (1+\beta\mu^2)^2 b^2 P_{\rm lin}(k,z) + 2\int \frac{d^3\mathbf{q}}{(2\pi)^3} P_{\rm lin}(q,z) P_{\rm lin}(|\mathbf{k}\text{-}\mathbf{q}|,z)[F_2^S(\mathbf{q},\mathbf{k}\text{-}\mathbf{q})]^2 \\ &\quad + 6(1+\beta\mu^2) b P_{\rm lin}(k,z) \int \frac{d^3\mathbf{q}}{(2\pi)^3} P_{\rm lin}(q,z) F_3^S(\mathbf{q},\text{-}\mathbf{q},\mathbf{k})\,, \end{aligned} \tag{4.12}$$

where $P_{\rm lin}(k,z)$ is the linear power spectrum in real space, $\beta \equiv f/b$, f being the linear growth rate and b being the linear bias, $\mu = \hat{\mathbf{k}}\cdot\mathbf{n}$, and $F_2^S(\mathbf{q},\mathbf{k}\text{-}\mathbf{q})$ and $F_3^S(\mathbf{q},\text{-}\mathbf{q},\mathbf{k})$ are the kernels of higher order perturbations. Their expressions are computed from Eq. (13) of Ref. [129] by neglecting higher order biases. The details of the integrations that appear in Eq. (4.12) are given in Appendix 4.A for completeness. Further, since we only consider dark matter we set $b = 1$.

4.3.3 pr-LPT

Here we consider a specific case of partially resummed-LPT (pr-LPT) introduced in [212]. The power spectrum using pr-LPT is given in Eq. (63) of Ref. [212],

$$\begin{aligned} P_{\rm tot}^{\rm sLPT}(\mathbf{k},z) &= \exp\left\{-k^2[1+f(f+2)\mu^2]A\right\} \\ &\quad \times \left\{P_{\rm tot}^{\rm sSPT}(\mathbf{k},z) + (1+f\mu^2)^2[1+f(f+2)\mu^2]k^2 P_{\rm lin}(k,z)A\right\}, \end{aligned} \tag{4.13}$$

where

$$A = \frac{1}{6\pi^2}\int dq P_{\rm lin}(q,z). \tag{4.14}$$

The prefactor encodes a damping on small scales from velocity dispersion.

4.3.4 EFT

We also consider effective field theory of large scale structure [28, 62, 268, 195, 238, 107] where counter terms are added to the SPT power spectrum, for which we refer to Eq. (3.8) of Ref. [29]

$$P_{\rm tot}^{\rm sEFT}(\mathbf{k},z) = P_{\rm tot}^{\rm sSPT}(\mathbf{k},z) - 2\sum_{n=0}^{3} c_{2|\delta_s,2n}\mu^{2n}\frac{k^2}{k_{\rm nl}^2}P_{\rm lin}(k,z), \tag{4.15}$$

where

$$c_{2|\delta_s,6} = f^3 c_{2|\delta_s,0} - f^2 c_{2|\delta_s,2} + f c_{2|\delta_s,4}. \tag{4.16}$$

$$\tag{4.17}$$

We do not apply a resummation scheme as is commonly done in the literature. The effect of resummation has been shown to have a low impact on the fitting to COLA data conducted in [29]. The values of the counter term coefficients are determined by fitting to the COLA simulations. This follows a similar procedure to [52]. We refer the reader to this work for justifications and details of this procedure. This is briefly described in Appendix 4.C where also the numerical values of the fitting parameters are given.

4.3.5 TNS

The last model we consider is the one-loop TNS model. This model was introduced in [283] and is one of the best approaches to perturbation theory known at present, having been applied in the recent BOSS galaxy clustering analysis [36, 35]. It has also been thoroughly validated against simulations and has stood up to other perturbative models [228, 282, 157, 314, 119, 120, 53, 50, 208, 51, 52]. The model is given by [283]

$$P_{\rm tot}^{sTNS}(k,z) = \frac{1}{1+(k^2\mu^2\sigma_v^2)/2}\Big[P_{\rm one-loop}^{\delta\delta}(k,z) + 2\mu^2 P_{\rm one-loop}^{\delta\theta}(k,z) + \mu^4 P_{\rm one-loop}^{\theta\theta}(k,z) + A(k,\mu,z) + B(k,\mu,z) + C(k,\mu,z)\Big]. \tag{4.18}$$

The terms in brackets are all constructed within SPT, with $\delta\delta$, $\delta\theta$ and $\theta\theta$ denoting density-density, density-velocity and velocity-velocity one-loop power spectra. The perturbative correction terms A, B and C are nonlinear corrections coming from the RSD modelling while the prefactor is added for phenomenological modeling of the Fingers of God effect. Within this prefactor, σ_v, is a free parameter that is fit to the COLA simulations (see Appendix 4.C). We refer the reader to [283, 52] for a detailed description of the components A, B and C of the model but we give some basic expressions in Appendix 4.B. We stick to one-loop TNS in this study, the reason is that although the two-loop version is shown to do marginally better than the one-loop at higher redshifts (look at [40] for example), the addition of loops in standard PT is not guaranteed to improve predictions and our aim is to quantify how nonlinearities (here expressed through the one-loop and fingers-of-god damping) translate to the angular spectra, and in particular, how redshift bin-width acts as a 'filter' for these redshift anisotropy nonlinearities, highlighted in Fig. 4.5.

4.3.6 Comparisons

In this section we compare Eq. (4.12) (SPT - blue), Eq. (4.13) (pr-LPT - green), Eq. (4.15) (EFT - magenta) and Eq. (4.18) (TNS - orange) with Eq. (4.11) (COLA reconstructed 2d spectrum - grey dots). We also compare Eq. (4.1) with $P_m(k)$ given

by linear theory (linear Kaiser - dashed black), nonlinear halofit power spectrum [280] (halofit - red) and the matter power spectrum as measured from the simulations (black dots). These comparisons are done at $z = 0.5$ and are shown in Fig. 4.3 and Fig. 4.4 for $\mu = 0$ (transversal direction) and $\mu = 1$ (radial direction) respectively. We expect that the grey dots marking the reconstructed COLA 2D spectrum of Eq. (4.11) provide the most accurate modeling for the full spectrum. This is our benchmark for accuracy.

We also show the one-loop contributions to $P_{\rm lin}$, P_{13} and P_{22}, of Eq. (4.12) in the upper panels of Fig. 4.3 and Fig. 4.4. They start to become important at $k \sim 0.1h/\mathrm{Mpc}$ for $\mu = 0$, which is well known from the literature, and on smaller scales for $\mu = 1$ as we can see in Fig. 4.4 and as we will also discuss later. Furthermore, P_{13} and P_{22} have opposite signs and their amplitudes are individually much larger than their sum, which is an indication for the well known bad convergence properties of SPT [61].

The one-loop SPT power spectrum (blue line) at $z = 0.5$ is shown in the middle panel of Fig. 4.4 for $\mu = 1$ and in Fig. 4.3 for $\mu = 0$ (in this plot the blue line is covered by the orange line). One sees clearly that SPT has too much power at small scales and fits the COLA simulations (grey dots) in a satisfactory way only for $k \lesssim 0.1h/\mathrm{Mpc}$.

The black dots are the COLA matter power spectrum multiplied by the 'Kaiser factor' $(1 + \beta\mu^2)^2$. They are accurate until about $k = 0.13h/\mathrm{Mpc}$. The keen reader may ask why the grey dots and black dots do not overlap in Fig. 4.3 at small scales. This could be due to inaccuracies in the COLA velocities used in computing the multipoles as well as the exclusion of higher order multipoles in Eq. (4.11).

Next we consider pr-LPT (green curves). It is clear from Fig. 4.3 and Fig. 4.4, that the damping introduced in the pr-LPT model is much too strong. Nevertheless, this correction can fit the power spectrum roughly until $k < 0.13h/\mathrm{Mpc}$ which is already better than the SPT fit.

The EFT power spectrum is plotted as the magenta line (in Fig. 4.3 this line is covered by the orange line). Somewhat surprisingly, this fit is only a little but not significantly better than pr-LPT for the angular scales considered. It represents a reasonable approximation until $k \simeq 0.15h/\mathrm{Mpc}$. One key reason for the poor fit at $\mu = 1$ is the lack of damping within the SPT spectrum which the EFT counter terms cannot suppress efficiently. The inclusion of resummation is expected to improve the fit (see for example [52]) but we leave this to future work.

Lastly, the TNS model is shown in orange. Clearly, this model represents the best fit to the full reconstructed simulated power spectrum for $\mu = 1$ (compare the orange line and the grey dots in Fig. 4.4, lower panel). It can be used roughly until $k \simeq 0.2h/\mathrm{Mpc}$. This is somewhat disappointing, as we aspire to achieve a good fit until $k \simeq 1h/\mathrm{Mpc}$ – to reach convergence in the C_ℓ integral for narrow redshift bins we find that we need to go even to $2h/\mathrm{Mpc}$. On even smaller scales, corrections from baryonic physics, that are not present in the simulations used here, can at any rate no longer be ignored.

We also note that for $\mu = 0$ the SPT, EFT and TNS power spectra are identical, i.e. in Fig. 4.3 the blue, magenta and orange lines overlay. These spectra only differ

in their treatment of redshift space distortions which are absent in the transversal direction, $\mu = 0$.

In Fig. 4.3 and 4.4 we also show the comparison of the COLA measurements with the halofit model multiplied by the Kaiser factor given in Eq. (4.1) (red curve). While this approximation is excellent when fitted to the COLA matter power spectrum, see Fig. 4.3, it does not correctly model the redshift space distortions. Hence, the higher order RSD and the nonlinearity in the continuity equation which is not taken into account in this formula is very relevant. This is also clear from comparing the black dots, obtained from the matter power spectrum of the COLA simulations by multiplication with the Kaiser term, and the grey dots which represent the full sum of the simulated multipoles. It is also interesting to note that while the matter power spectrum of the simulations on small scales is larger than the linear power spectrum, adding all the multipoles actually reduces the power spectrum in redshift space on small scales when compared to the linear power spectrum. While the pr-LPT approximation exaggerates this reduction of power, all other approximations either cannot model it at all or (in the case of TNS) underestimate this effect. This is most visible in radial direction, $\mu = 1$. In the transversal direction, $\mu = 0$, the nonlinear corrections from SPT, EFT and TNS all overshoot significantly while pr-LPT is still too small. Here halofit provides the best approximation, see Fig. 4.3. In the radial direction, $\mu = 1$, only TNS manages to provide a reasonable fit for $k \gtrsim 0.1h/\text{Mpc}$, but for $k \gtrsim 0.2h/\text{Mpc}$ it also starts to over-estimate the power significantly so that there is effectively no good analytical prescription available to model the redshift space power spectrum into the nonlinear regime.

4.4 Nonlinear correction to the angular power spectrum

To profit optimally from future galaxy redshift surveys (Euclid, DESI, 4MOST, SKA, ...) [19, 299, 13, 257] we must also be able to model scales where nonlinearities become relevant. Since the angular power spectrum is the true observable quantity, it is important to study the effects of nonlinearities directly on this quantity. In this section, we discuss the effect of nonlinearities on the angular power spectrum using the different approaches discussed in the previous section to model them, and we study their effects at different redshifts and for different widths of the redshift bins considered.

Although the power spectrum $P^s(k, \mu, z)$ in Fourier space, and its counterpart, the correlation function $\xi(r, \mu, z)$, provide some insight into galaxy observations on small scales, here we want to investigate how these nonlinearities project onto the sky, i.e. onto the directly observable angular power spectrum.

In the top panel of Fig. 4.5 we compare the C_ℓ's from the different nonlinear approximations discussed in the previous section at redshift $z = 0.5$ and using bin width $\Delta z = 0.1$. For $\ell \lesssim 150$, which corresponds roughly to the nonlinearity scale at $z = 0.5$, the spectra agree relatively well. Beyond that scale they become very different, and even though in k-space TNS is a better approximation to the numerical

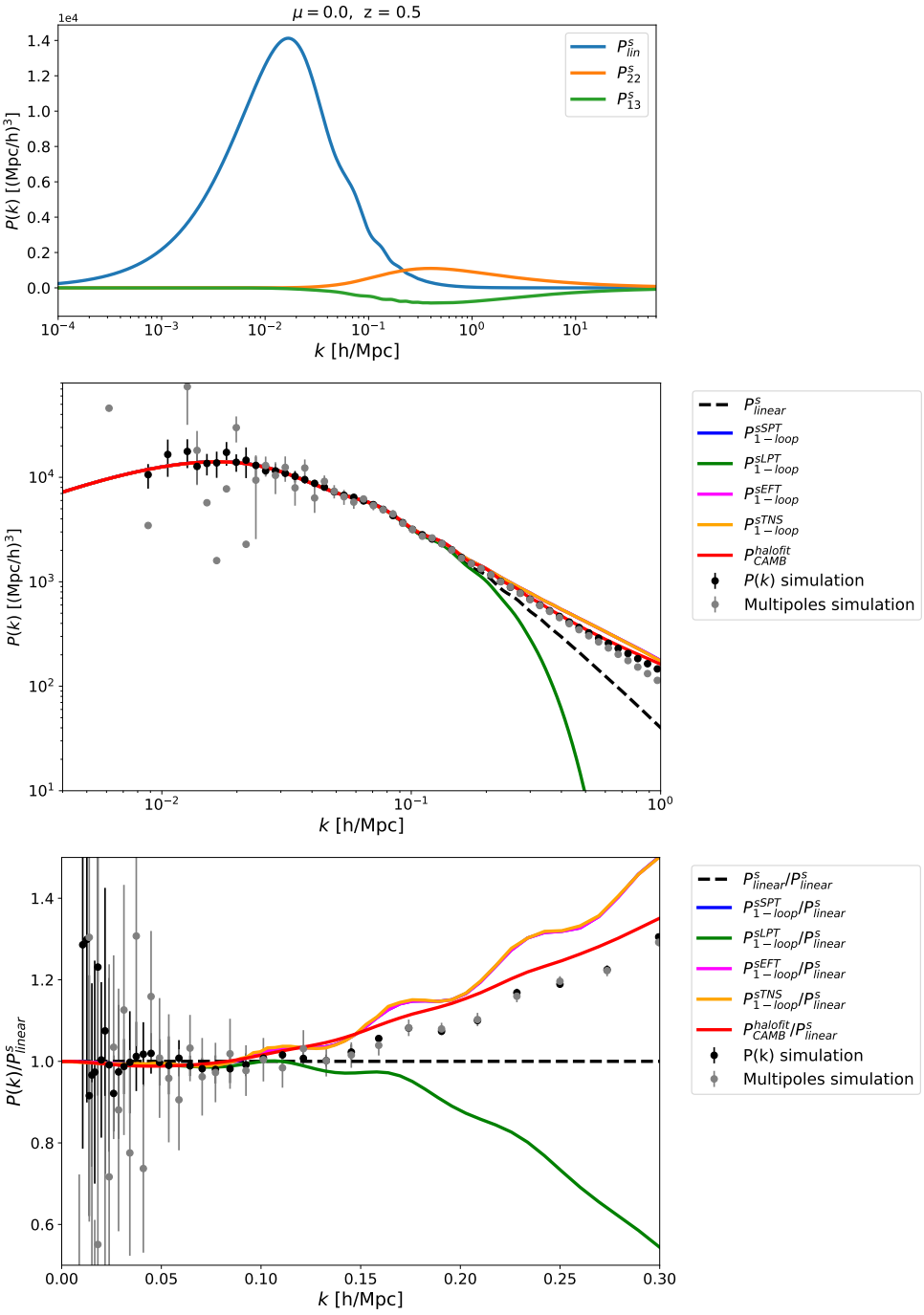

Figure 4.3: The power spectrum $P^s(k,\mu)$ in redshift space in the transversal direction, $\mu = 0$ (effectively the density power spectrum), with $b = 1$ and $z = 0.5$. The upper panel shows the linear spectrum P^s_{11} (blue) along with the one-loop contributions P^s_{22} (orange) and P^s_{13} (green). The middle panel shows the comparison between $P^{\rm sSPT}_{\rm one-loop}$, $P^{\rm sLPT}_{\rm one-loop}$, and $P^{\rm sEFT}_{\rm one-loop}$ and $P^{\rm sTNS}_{\rm one-loop}$ defined respectively in Eq. (4.12), Eq. (4.13), Eq. (4.15) and Eq. (4.18). In the lower panel the ratios of the corresponding nonlinear spectra and the linear one are shown. The black dots show the monopole of the N-body simulations while the grey dots also include the quadrupole and the hexadecapole available from COLA.

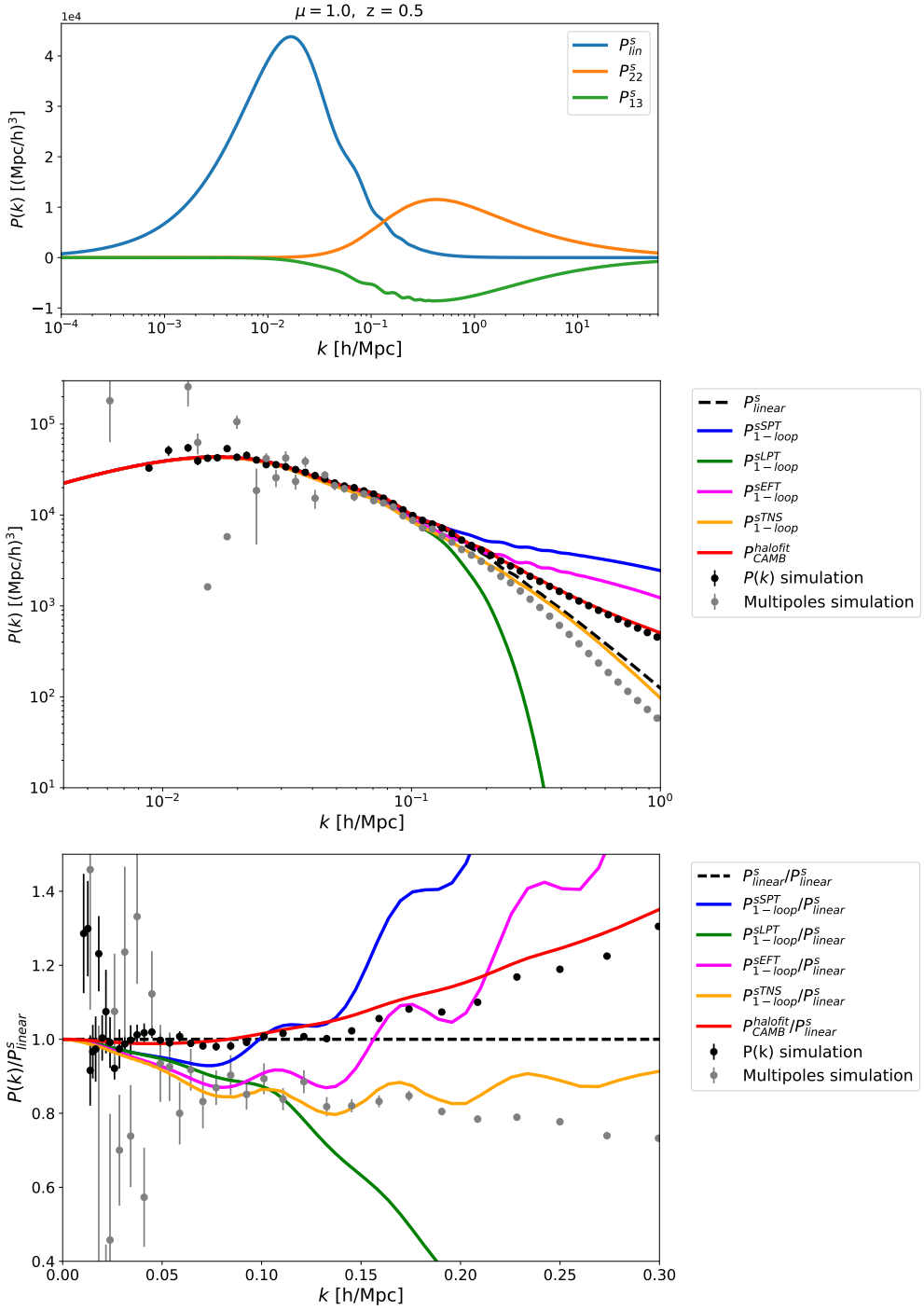

Figure 4.4: The same as Fig. 4.3 but in the radial direction, $\mu = 1$, where redshift space distortions are important. We see that the Kaiser formula used for halofit and for the black COLA points does not provide a good fit to the RSD even at mildly nonlinear scales.

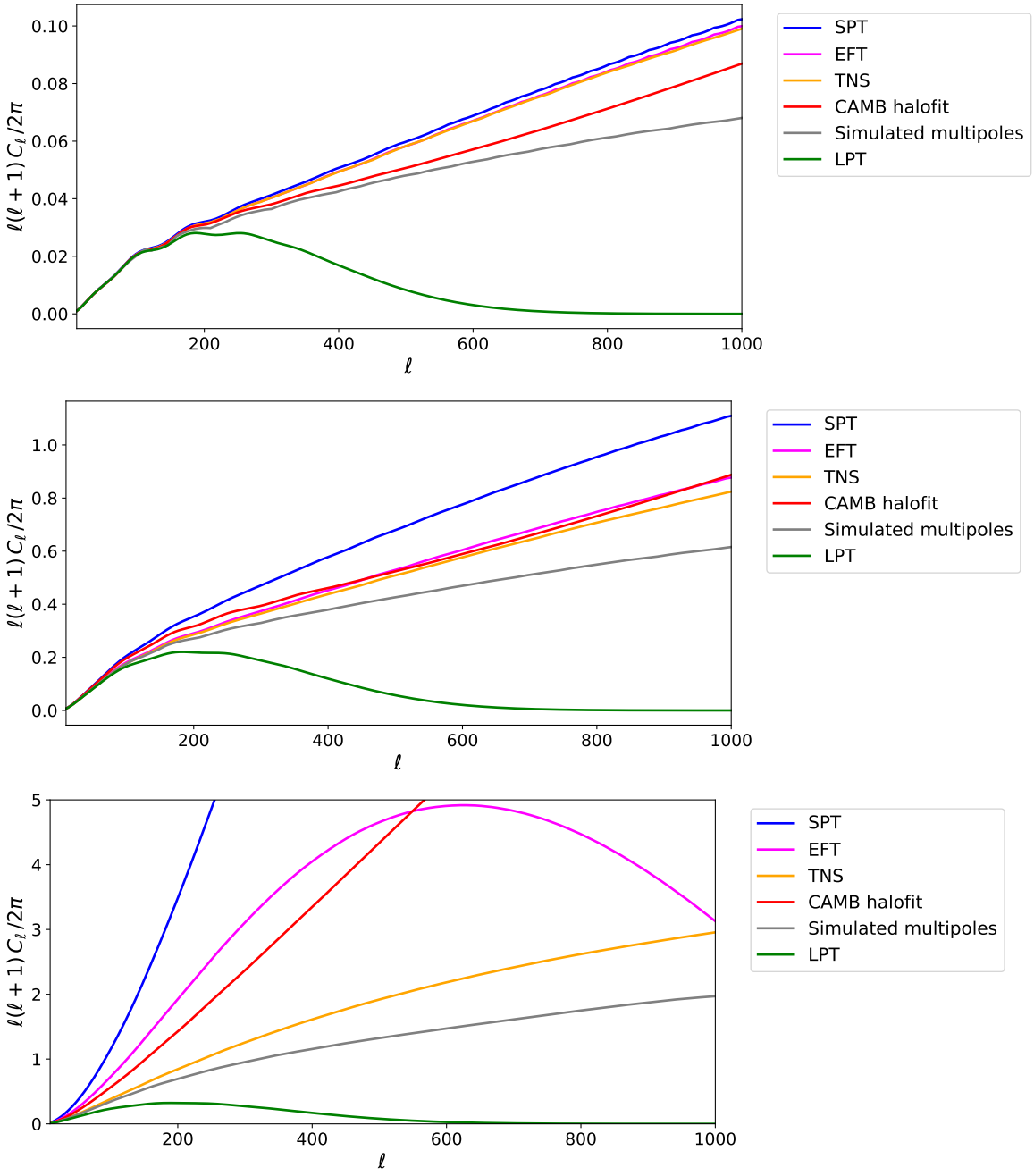

Figure 4.5: The plot shows the C_ℓ's from density and RSD at $z = 0.5$ computed using the different approaches discussed in the text: $P^{\mathrm{sSPT}}_{\mathrm{one-loop}}$, Eq. (4.12), $P^{\mathrm{sLPT}}_{\mathrm{one-loop}}$, Eq. (4.13), $P^{\mathrm{sEFT}}_{\mathrm{one-loop}}$, Eq. (4.15), and $P^{\mathrm{sTNS}}_{\mathrm{one-loop}}$, Eq. (4.18), as well as the nonlinear C_ℓ computed by CAMB using the halofit model, and the simulated multipoles from COLA. The redshift bin width is $\Delta z = 0.1$ for the top panel, $\Delta z = 0.01$ for the middle panel and $\Delta z = 0.001$ for the bottom panel. None of the models shown here manages to agree with the numerical simulations except on the largest scales and for wide redshift bins.

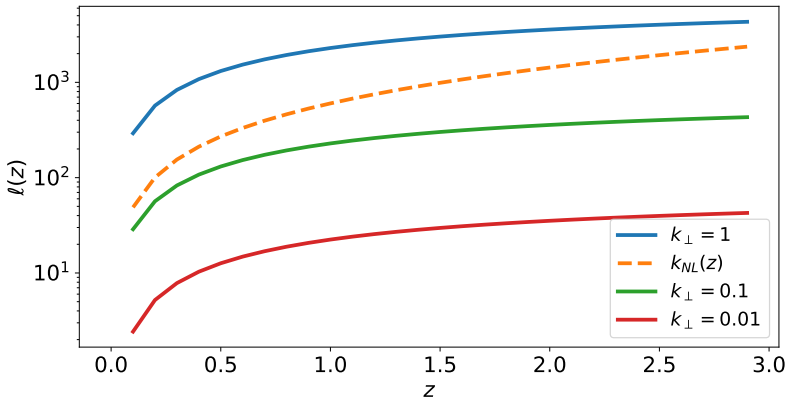

Figure 4.6: We show $\ell(k_\perp, z)$ for $k_\perp = (0.01\,,\ 0.1\,,\ 1)h/\mathrm{Mpc}$ as well as $\ell_{\rm NL}(z) = \ell(k_{\rm NL}(z), z)$ as a function of redshift z.

results this is no longer true in ℓ space where the CAMB halofit (red line) seems to best mimic the COLA result (grey line), but also this result is more than 20% off at $\ell = 1000$ from the COLA simulation and a better approximation is certainly needed.

When smaller bin widths are chosen, $\Delta z = 0.01$ for the middle panel and $\Delta z = 0.001$ for the lower panel, the difference between the approximations and the COLA simulations becomes even worse. For these bin widths more small scale power enters the C_ℓ's which not only increases their amplitude but also makes them more sensitive to the treatment of nonlinearities. This important new finding is discussed in more detail around Fig. 4.8.

We define the nonlinearity scale through the condition

$$\sigma(R_{\rm NL}) = 0.2 \tag{4.19}$$

that was also used by Euclid [189, 250]. Here $\sigma^2(R)$ is the usual variance of the mass fluctuation in a sphere of radius R,

$$\sigma^2(R, z) \equiv \frac{1}{2\pi^2}\int_0^\infty \frac{dk}{k}\left(\frac{3j_1(kR)}{kR}\right)^2 k^3\delta^2(k, z)\,, \tag{4.20}$$

so that $\sigma(R = 8h/\mathrm{Mpc}) = \sigma_8$. We then associate a nonlinearity scale in Fourier space through

$$k_{\rm NL}(z) = \frac{2\pi}{R_{\rm NL}(z)}\,. \tag{4.21}$$

A given transversal wave number $k_\perp$ at redshift z roughly corresponds to a multipole

$$\ell(k, z) \simeq k_\perp \chi(z)\,. \tag{4.22}$$

In Fig. 4.6 we show $\ell(k_\perp, z)$ for three different values of $k_\perp$ as well as $\ell_{\rm NL}(z) = \ell(k_{\rm NL}(z), z)$.

In Fig. 4.7 we compare linear and nonlinear spectra for different redshifts for the TNS model in Fourier space. For $k < 0.15h/\mathrm{Mpc}$ the density only spectra (dashed

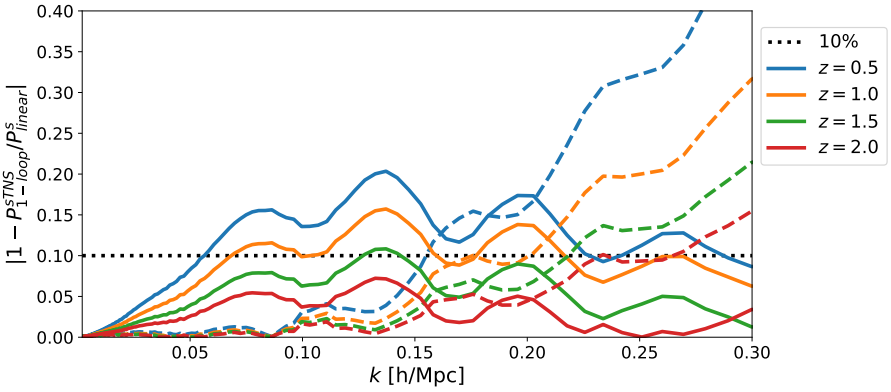

Figure 4.7: Relative differences between $P^s(k,\mu)^{\rm NL}$ and $P^s(k,\mu)^{\rm lin}$ for the TNS model for different redshifts. The dashed lines represent the density only ($\mu = 0$), and the solid ones represent density plus RSD ($\mu = 1$). The horizontal dotted black line is the 10% line. For the density-only spectrum nonlinearities become important around $k = 0.1h/\text{Mpc}$, while in the $\mu = 1$ spectrum with RSD the nonlinearities appear on much larger scales.

lines) are closer to the linear result than the spectra including RSD with $\mu = 1$ (solid lines). This indicates that velocities exhibit nonlinearities already on larger scales than the density. Roughly at $k = 0.15h/\text{Mpc}$ this trend is reversed. When we enter a more nonlinear regime (after shell crossing), the velocities tend to damp the power in redshift space, so the density + RSD spectra are less nonlinear than the density only spectra on these scales. Interestingly, the 'cross-over' scale of $k = 0.15h/\text{Mpc}$ seems to be nearly redshift independent.

In Fig. 4.8 we compare linear and nonlinear angular spectra for different redshifts using the TNS model for the nonlinear case. As we explain later in Fig. 4.12 and 4.13, for the smaller redshift bins which are sensitive to RSD, TNS follows the simulation results better than CAMB halofit. For $\Delta z = 0.1$, the higher the redshift the higher the value of ℓ below which our model deviates by less than 10% (black dotted line) from the linear result. Furthermore, redshift space distortions are not very visible in ℓ space for $\Delta z = 0.1$ (see top panel of Fig. 4.8).

For $\Delta z = 0.01$ and $\Delta z = 0.001$ (middle and low panels of Fig. 4.8), RSDs are very prominent but now, even for very low ℓ, the linear approximation is no longer sufficient. This is due to the fact that a very precise redshift resolution in the spectrum is sensitive to very small radial modes, hence to very high values of $k_\parallel$ which are affected by nonlinearities. Physically this just means that we are sensitive to nonlinearities if we want high resolution in any direction, radial or transversal. This shift of the nonlinearity scale to lower ℓ's for narrow redshift bins is also visible in the lower panels of Fig. 4.5.

This is a very important result of the present paper: if we want to resolve RSD in the angular power spectrum we must have sufficiently precise redshift measurements, in which case the C_ℓ's are sensitive to nonlinearities in the radial power spectrum for virtually all ℓ's.

At the highest redshift, $z = 2$ and for the most narrow redshift bin, $\Delta z = 0.001$

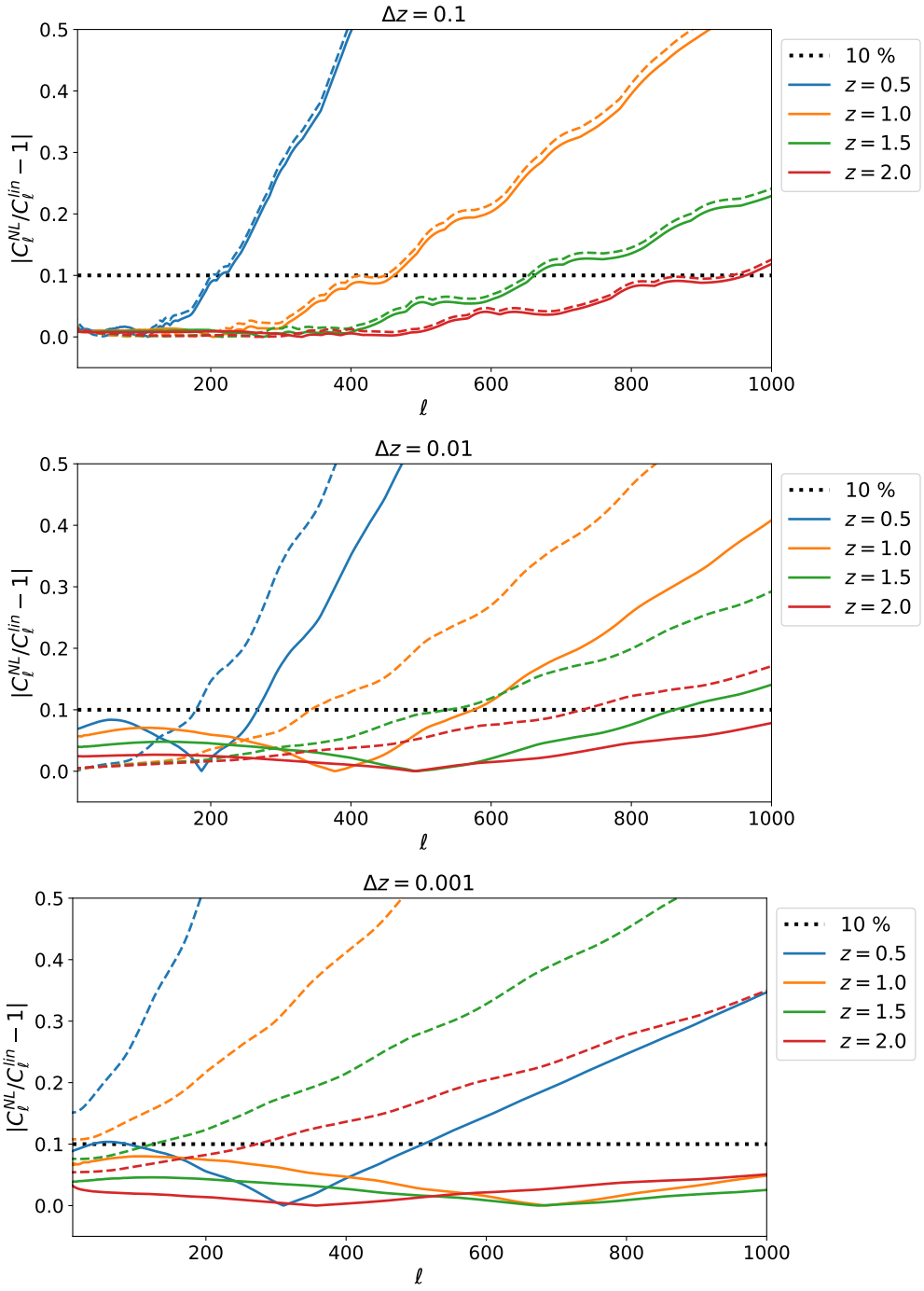

Figure 4.8: Relative difference between $C_\ell^{\rm NL}$ and $C_\ell^{\rm lin}$ for the TNS model for different redshifts. The dashed lines represent the density only (neglecting any RSD terms in the power spectrum) , and the solid ones represent density plus RSD. The horizontal dotted black line is the 10% line.

this yields simply a nearly constant offset from the linear results by about 5%. For lower redshifts and/or larger bin widths the difference from the linear result grows with ℓ as one naively expects. It is also interesting to note that for the smallest bin width (bottom panel of Fig. 4.8), the deviation never exceeds 10% for $z \geq 1$ or $z = 0.5$ and $\ell \lesssim 500$. This can be understood by noting that RSDs which are most significant for the smallest bin width damp the nonlinearities.

Mathematically, the fact that nonlinearities at small Δz enter already at low ℓ can be understood very nicely from the flat sky approximation. Convolving Eq. (4.8) with a tophat window function of width Δz we find for a mean redshift denoted by $\bar{z}$

$$C_\ell(\bar{z}, \Delta z) = \frac{1}{\pi\chi^2} \int dk_\parallel j_0^2 \left(\frac{k_\parallel \Delta z}{2H(\bar{z})}\right) P\left(k_\parallel, \frac{\ell}{\chi}\right) . \tag{4.23}$$

Here the spherical Bessel function, $j_0^2(k_\parallel \Delta z/2H)$ acts as a 'low pass filter' which filters out modes with $k_\parallel \gg 2H(z)/\Delta z$. For very small Δz the integral therefore extends to high values of $k = \sqrt{k_\parallel^2 + (\ell/\chi)^2}$ for any ℓ, and these modes can become large and nonlinear. In this case nonlinearities affect the result even at the lowest ℓ values. In other words, for linear perturbation theory to apply it is not sufficient that the relevant transverse modes, $k_\perp = \ell/\chi(z)$ are well in the linear regime, but also the relevant radial modes, $k_\parallel \leq 2H(z)/\Delta z$ must be in the linear regime. A crude approximation yields

$$k_{\parallel,\max} \simeq \frac{2\pi H(\bar{z})}{\Delta z} < k_{\rm NL}(\bar{z}) \quad \text{or} \quad \Delta z \gtrsim (\Delta z)_{\min} = \frac{2\pi H(\bar{z})}{k_{\rm NL}(\bar{z})} . \tag{4.24}$$

We show $(\Delta z)_{\min}$ as a function of $\bar{z}$ in Fig. 4.9. The critical width is therefore of the order of $\Delta z \approx 0.01$ to 0.02, for narrower redshift bins (higher redshift resolution) we have to expect that (radial) nonlinearities affect the C_ℓ for all values of ℓ, not only for $\ell > \ell_{\rm NL}$.

The radial cutoff scale $k_{\parallel,\max}$, also shown in Fig. 4.9, lies well below the nonlinear scale for $\Delta z = 0.1$, while for $\Delta z = 0.01$ it is in the range of $k \approx 0.3h$/Mpc to $0.8h$/Mpc, depending on redshift, already in the nonlinear regime. For narrow redshift bins, $\Delta z = 0.001$, it becomes larger than the 'absolute' convergence scale of $k \approx 2h$/Mpc, for which the C_ℓ integral (4.23) converges without any damping from the Bessel function, i.e. also for $\Delta z \to 0$ (except for very high ℓ where the effective starting value of the integration, ℓ/χ, is pushed to higher k).

To illustrate clearly the relevance of RSDs we show the difference between the density only (dashed) and density plus RSD (solid) in the nonlinear predictions in Fig. 4.10 using the TNS approximation. For the widest redshift bin, $\Delta z = 0.1$, redshift space distortions are not very relevant. For small Δz, however, they significantly reduce the C_ℓ spectrum at high ℓ. As for the power spectrum, on linear scales RSD enhances the power spectrum via the Kaiser effect while on nonlinear scales it reduces it due to the velocity overshoot which damps the density power spectrum in redshift space. The crossover between the dashed and the solid line roughly corresponds to the nonlinearity scale at a given redshift. This explains also why the crossover location is nearly independent of the bin width Δz.

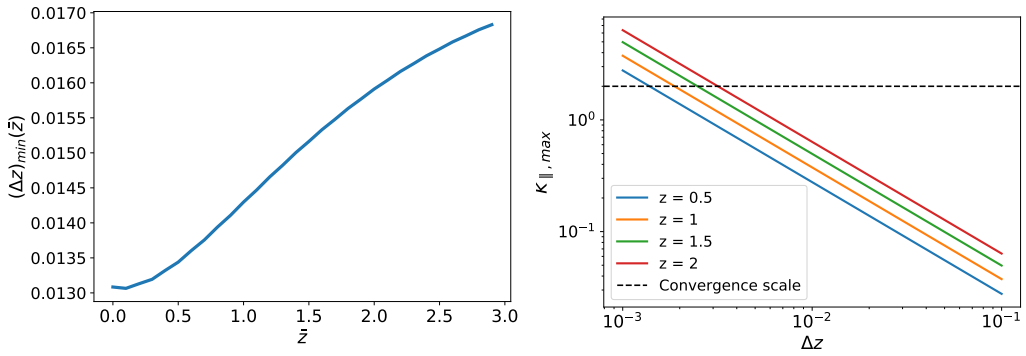

Figure 4.9: Left: $(\Delta z)_{\rm min}$ defined in Eq. (4.24) as a function of $\bar{z}$. For redshift bins narrower than $(\Delta z)_{\rm min}$ we expect radial nonlinearities to affect the C_ℓ's also for low values of ℓ. Right: The radial scale $k_{\parallel,\rm max}$ for which the integrand of the C_ℓ integral is damped by the Bessel function, as function of bin width Δz, for different redshifts. We also show as a dashed line the convergence scale of the integral in the case $\Delta z \to 0$.

To quantify the importance of RSD terms, we have performed a simple Fisher forecast for several bin widths. We modeled the RSDs with the Kaiser formula applied to halofit, and only kept the cosmic variance contribution to the noise (neglecting survey-dependent contributions like shot noise and sky fraction). More details about the Fisher analysis are given in Appendix 4.E. The signal-to-noise ratio (SNR) is shown in Fig. 4.11 as a function of redshift bin width, Δz, for three different redshifts. As we see, the RSD signal drops by an order of magnitude when going from $\Delta z = 0.01$ to $\Delta z = 0.1$, highlighting the importance of using narrow redshift bins for measuring RSD. The RSD signal is however still detectable even for wide bins, and it should therefore be included in the C_ℓ also for $\Delta z = 0.1$.

In Fig. 4.12 we compare also the result of halofit from CAMB (dashed) with the one from the COLA simulations (solid) for density plus RSD angular power spectra. For the bin width $\Delta z = 0.1$ we only have a slight overshoot of the CAMB spectrum at $\ell > 400$ for $z = 0.5$, all other spectra are in good agreement. However, for small bin widths $\Delta z \leq 0.01$, and especially for $\Delta z = 0.001$, the insufficient treatment of the RSD in the halofit model where they are taken into account simply by the linear Kaiser formula, leads to a significant spurious amplification of the power spectrum already at low values of ℓ. This overshoot is more significant at lower redshifts, where nonlinearities are more relevant, but it is already visible at $z = 2$.

In Fig. 4.13 we compare the results using the TNS approximation (dashed) with the ones from the COLA simulations (solid) for density plus RSD angular power spectra. Clearly, the TNS approximation handles redshift space distortions much better that halofit and the spurious excess is reduced and no longer visible for $z = 1.5$ and 2.0. However, we have checked that the relative difference between the simulation result and TNS is larger than cosmic variance for $z = 2$ and $\ell > 200$ as well as $z \leq 1.5$ and $\ell = 100$ for narrow bins, $\Delta z = 0.001$. It becomes larger than cosmic variance at $\ell = 700$, 350 and 200 for $\bar{z} = 1.5$, 1 and 0.5 respectively,

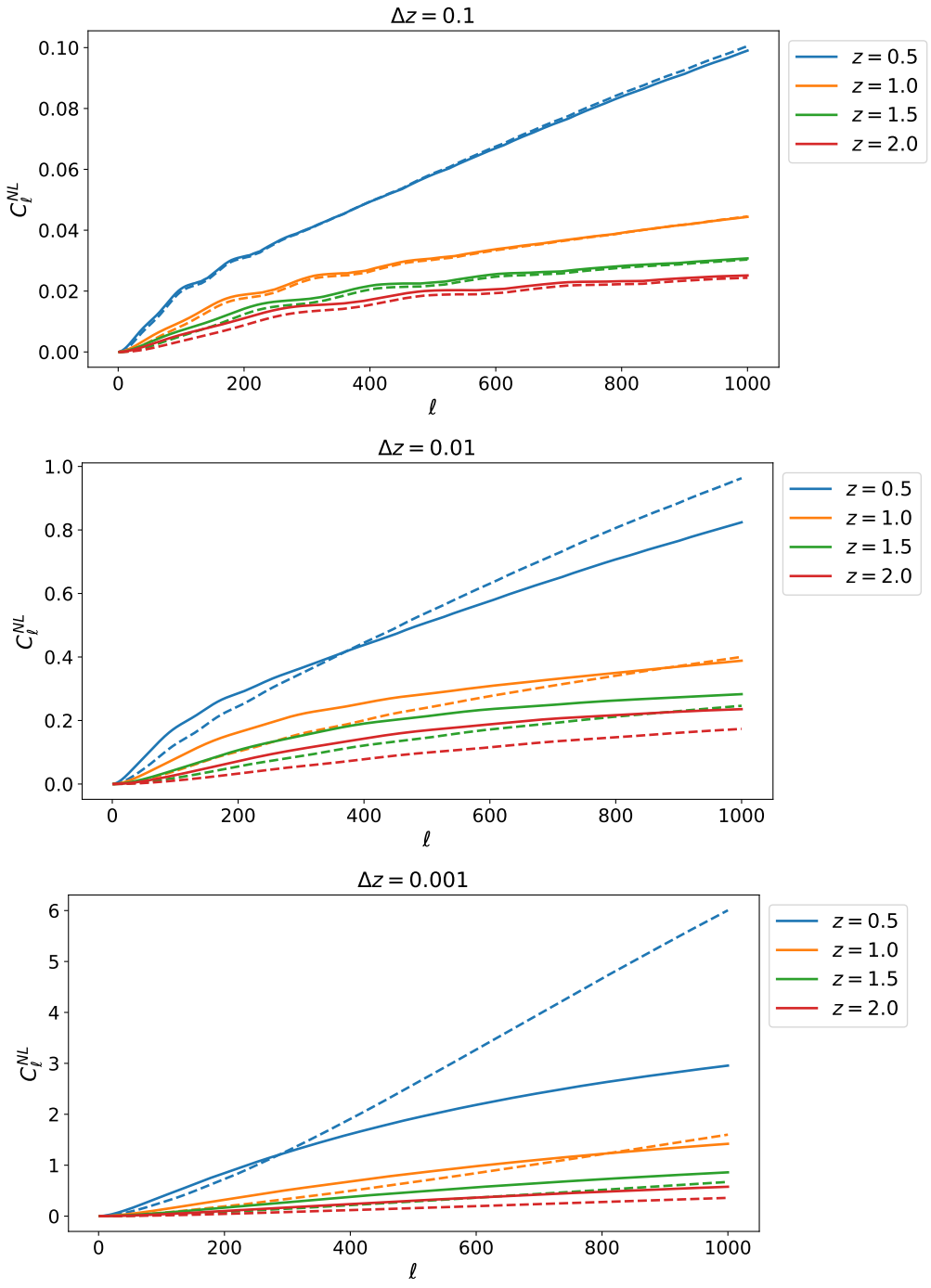

Figure 4.10: The comparison between $C_\ell^{\rm NL}$ for density and density + RSD, for different mean redshifts and with width $\Delta z = 0.1$, 0.01, 0.001 from top to bottom. NL stands for nonlinear, and in this plot we show the case of TNS model. The dashed lines contain density only while in the the solid lines both, density and RSD are included.

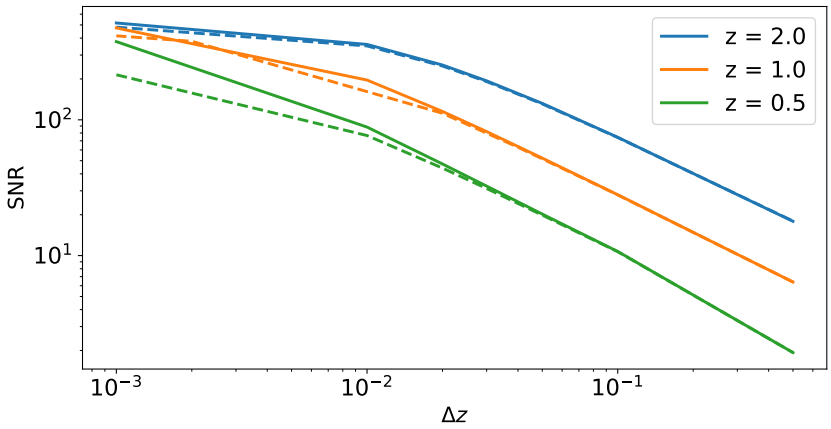

Figure 4.11: Signal-to-noise ratio for detecting RSD as a function of Δz for different redshifts. Dashed lines represent SNR using linear C_ℓ's and solid lines represent SNR using nonlinear C_ℓ's. For $z = 1$ and $z = 2$ we sum up to $\ell_{\rm max} = 1000$ and for $z = 0.5$, we sum up to $\ell_{\rm max} = 600$ which is $2\ell_{\rm NL}$.

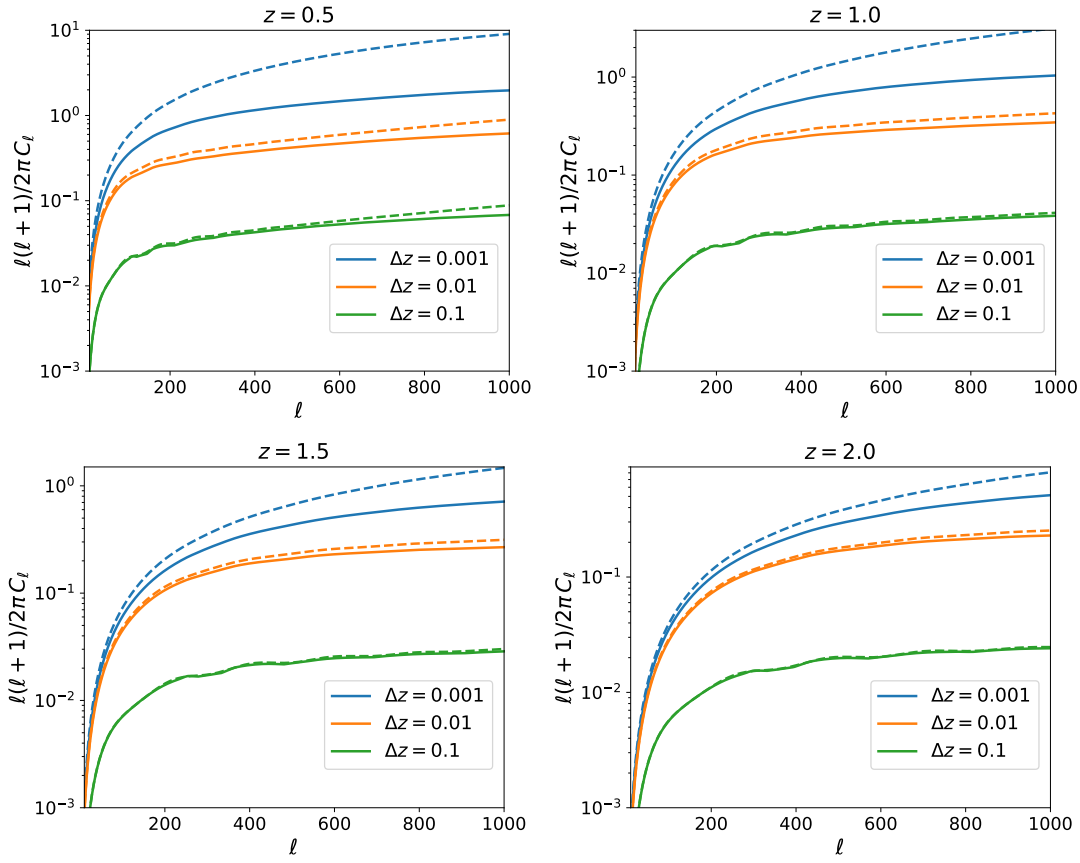

Figure 4.12: Comparison between CAMB halofit (dashed) and the COLA simulations (solid) for the redshifts $z = 0.5$, 1.0, 1.5, 2.0 and for different redshift bin widths.

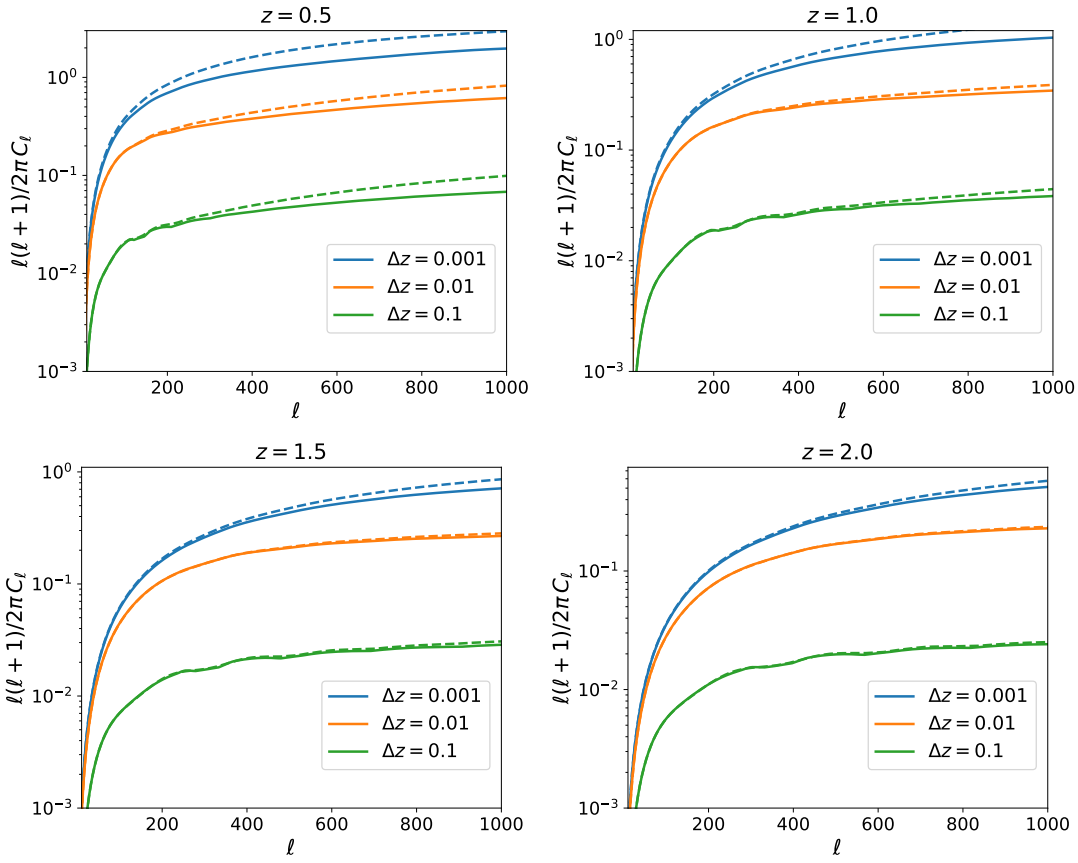

Figure 4.13: Comparison between TNS (dashed) and COLA simulations (solid) for the redshifts $z = 0.5$, 1.0, 1.5, 2.0 and for different redshift bin widths.

for both bin widths, $\Delta z = 0.01$ and $\Delta z = 0.1$. This indicates again that for slim redshift bins, $\Delta z = 0.001$, nonlinearities are relevant already at low ℓ (where however cosmic variance is very large). For wide redshift bins, $\Delta z = 0.1$, where RSD are not significant, the halofit model from CAMB is actually a better approximation than TNS. We have already seen this in Fig. 4.5.

4.5 Discussion and conclusion

In this paper we have compared different perturbation theory-based schemes, standard perturbation theory (SPT), partially resummed Lagrangian perturbation theory (pr-LPT), the effective field theory of large scale structure (EFT), the TNS model, and halofit to treat nonlinearities in the angular power spectrum. We also compare these predictions with COLA simulations. These simulations are percent level accurate within $k \lesssim 1h/\mathrm{Mpc}$ when compared to full N-body measurements of the matter power spectrum [302]. At the level of the redshift space multipoles, the simulations still provide fair accuracy up to $k \sim 0.3h/\mathrm{Mpc}$ [52]. All other models considered here are less accurate in the modeling of RSD and so we use the COLA simulations as our benchmark in accuracy.

For these approaches, we provide two bases of comparisons. The first is at the level of the two dimensional redshift space power spectrum $P(k, \mu)$. Even though this comparison is not new, it is useful to understand the results for the angular power spectrum. For $P(k, \mu)$ we draw the following conclusions:

- Using the COLA simulations as a reference, the TNS model offers the best modelling of the RSD anisotropy, being comparable to the COLA measurements into the quasi linear regime, $k \lesssim 0.2h/\mathrm{Mpc}$, at $z = 0.5$, for all μ. nonlinear RSD modelling is essential in modelling the 2D power spectrum. This has been checked by comparing the Kaiser formula combined with the halofit nonlinear matter power spectrum to the COLA measurements. Despite being a good approximation at $\mu \sim 0$, halofit performs the worst out of all models at $\mu \sim 1$ and $k \gtrsim 0.1h/\mathrm{Mpc}$.

The main and new basis for comparison is at the level of the angular power spectrum. We note that this quantity is more directly related to observations. Our main conclusions are summarized as follows:

- We find that the flat sky approximation is valid at percent level accuracy and so adopt this for all our comparisons of C_ℓ.

- For large bin widths ($\Delta z \sim 0.1$), RSD is much less important and the main contributor to nonlinear information is within the matter power spectrum. At this bin width halofit combined with the Kaiser factor agrees within a few percent with our benchmark model, the COLA simulation up to $\ell \lesssim 400$ at $z = 0.5$ and higher for higher z.

- Small bin widths greatly enhance the impact of nonlinear RSD. Because of this, the TNS model out-performs all other models for $\Delta z = 0.01$ and $\Delta z = 0.001$.

Despite this, it is still a poor approximation, being accurate to within a few percent only for $\ell \lesssim 150$ at $z = 0.5$.

- The most surprising result is that for small bin widths, nonlinear RSD information becomes important also for very low ℓ, with significant nonlinear effects ($\sim 10\%$) being found at $\ell \leq 50$ at $z = 0.5$ for the TNS model.
- For large bin widths, the effect of lensing, which is not easy to incorporate in $P(k, \mu)$, but is straightforwardly included in the C_ℓ's, cannot be ignored, and at $z = 0.5$ with $\Delta z = 0.1$, it is already equal in magnitude to the RSD signal at $\ell \leq 150$, This is discussed in Appendix 4.D.

In conclusion, at the level of the angular power spectrum, it becomes very difficult to disentangle nonlinearities and various contributions to the signal. In particular, at low redshift, nonlinear RSD can play a large role at $\ell \leq 150$ for small bin width, while for large bin widths lensing begins to affect the signal. At high redshift ($z > 1$) nonlinear RSD is better controlled but lensing becomes more important for large bin widths. At $z = 1$ lensing is subdominant to RSD up to $\ell \lesssim 500$ for small and large bin width choices. The TNS model offers a relatively good prescription to model the nonlinear effects of RSD in the angular power spectrum, but is still very limited, especially at low redshift where nonlinearities are enhanced.

While this can be circumvented for wide redshift bins by only considering spectra for 'linear' ℓ's, this becomes impossible for narrow redshift bins. In fact, for $\Delta z \lesssim 0.001$, we need to accurately model the nonlinear spectrum to high k for all values of ℓ, no prescription is currently accurate enough to do this. It appears therefore that, at least for now, the angular spectrum is less well suited to measure RSDs than the correlation function.

We have found that while the TNS approximation is the only one with a reasonably good treatment of velocities, it does not reproduce well the COLA angular power spectra for wide redshift bins, $\Delta z \geq 0.1$. For such wide-bin spectra, RSDs are not important and halofit, which gives the better fit to the density only power spectrum than TNS, is actually preferable. On the other hand, for slim redshift bins, $\Delta z \leq 0.01$ TNS is a much better approximation. For such bin widths, radial nonlinearities are already relevant for very low ℓ's which renders halofit, or even more so the linear power spectrum, simply useless. On the other hand, on scales $\ell > \ell_{\rm NL}(z)$, where also the transverse wave number enters the nonlinear regime, also the TNS approximation which models the pure matter density power spectrum becomes insufficient, especially at low redshift, $z \simeq 0.5$.

From this work it is clear that we are still far away from modelling the angular power spectrum at 1% precision over a reasonable range of ℓ. But we now know better in which direction we have to make progress. We need to model the density power spectrum similar to halofit but then correct for nonlinear RSD like in the TNS model. Especially, if we want to model the C_ℓ's in narrow redshift bins where they are sensitive to redshift space distortions. This is essential if we wish to safely extract very important cosmological information. We must make sure to model RSD very precisely, as they can enter the C_ℓ's at small $\ell \ll \ell_{\rm NL}(z)$ depending on the bin width.

APPENDIX

4.A Derivation of the one-loop terms

Following the notations and conventions in [129] for Eq. (4.12), we have:

$$\begin{aligned} P^s_{tot}(\mathbf{k}) &\equiv P^s_{11} + P^s_{22} + P^s_{13} \\ &= (1+\beta\mu^2)^2 b_1^2 P_{11}(k) + 2\int \frac{d^3\mathbf{q}}{(2\pi)^3} P_{11}(q) P_{11}(|\mathbf{k}\text{-}\mathbf{q}|)[F_2^S(\mathbf{q}, \mathbf{k}\text{-}\mathbf{q})]^2 \\ &\quad +6(1+\beta\mu^2) b_1 P_{11}(k) \int \frac{d^3\mathbf{q}}{(2\pi)^3} P_{11}(q) F_3^S(\mathbf{q}, \text{-}\mathbf{q}, \mathbf{k}) \end{aligned} \tag{4.A25}$$

where $\beta \equiv f/b_1$ and b_1 denotes the linear bias. The symmetrised expression for $F_2^S(\mathbf{k}_1, \mathbf{k}_2)$ and the unsymmetrised one for $F_3(\mathbf{k}_1, \mathbf{k}_2, \mathbf{k}_3)$ are shown in Eq. (13) of [129]. We symmetrise $F_3(\mathbf{k}_1, \mathbf{k}_2, \mathbf{k}_3)$ and find $F_3^S(\mathbf{q}, \text{-}\mathbf{q}, \mathbf{k})$, neglecting higher order biases.

As can be seen in Eq. (13) of [129], the expressions for F_2^S and F_3^S are given in terms of J_2^S, J_3^S, K_2^S and K_3^S, which can be computed from the general nth order expression as found in literature (see for example Eq. (10a) and (10b) of [159]). While Eq. (4.A26) and Eq. (4.A27) given below are easily available in literature, for obtaining Eq. (4.A28) and Eq. (4.A29), we have used the expression for $n = 3$ and symmetrised it. However, our results did not match very accurately with the symmetrised expression obtained from Eq. (11) of [129], and therefore we explicitly write them below in Eq. (4.A28) and Eq. (4.A29). We find these relations to be as follows:

$$J_2^S(\mathbf{q}_1, \mathbf{q}_2) = \frac{5}{7} + \frac{1}{2}\frac{\mathbf{q}_1.\mathbf{q}_2}{q_1 q_2}\left(\frac{q_1}{q_2} + \frac{q_2}{q_1}\right) + \frac{2}{7}\frac{(\mathbf{q}_1.\mathbf{q}_2)^2}{q_1^2 q_2^2} \tag{4.A26}$$

$$K_2^S(\mathbf{q}_1, \mathbf{q}_2) = \frac{3}{7} + \frac{1}{2}\frac{\mathbf{q}_1.\mathbf{q}_2}{q_1 q_2}\left(\frac{q_1}{q_2} + \frac{q_2}{q_1}\right) + \frac{4}{7}\frac{(\mathbf{q}_1.\mathbf{q}_2)^2}{q_1^2 q_2^2} \tag{4.A27}$$

$$\begin{aligned} J_3^S(\mathbf{q}_1, \mathbf{q}_2, \mathbf{q}_3) = \frac{1}{3}\text{Sym}\Bigg[& 7\frac{\mathbf{q}.\mathbf{q}_1}{q_1^2} J_2^S(\mathbf{q}_2, \mathbf{q}_3) + \frac{q^2 \mathbf{q}_1.(\mathbf{q}_2+\mathbf{q}_3)}{q_1^2 |\mathbf{q}_2+\mathbf{q}_3|2} K_2^S(\mathbf{q}_2, \mathbf{q}_3) \\ & + \left(7\frac{\mathbf{q}.(\mathbf{q}_1+\mathbf{q}_2)}{|\mathbf{q}_1+\mathbf{q}_2|^2} + \frac{q^2(\mathbf{q}_1+\mathbf{q}_2).\mathbf{q}_3}{|\mathbf{q}_1+\mathbf{q}_2|^2 q_3^2}\right) K_2^S(\mathbf{q}_1, \mathbf{q}_2))\Bigg] \end{aligned} \tag{4.A28}$$

$$\begin{aligned} K_3^S(\mathbf{q}_1, \mathbf{q}_2, \mathbf{q}_3) = \frac{1}{3}\text{Sym}\Bigg[& \frac{\mathbf{q}_1.\mathbf{q}}{q_1^2} J_2^S(\mathbf{q}_2, \mathbf{q}_3) + \frac{q^2 \mathbf{q}_1.(\mathbf{q}_2+\mathbf{q}_3)}{q_1^2 |\mathbf{q}_2+\mathbf{q}_3|2} K_2^S(\mathbf{q}_2, \mathbf{q}_3) \\ & + \left(\frac{\mathbf{q}.(\mathbf{q}_1+\mathbf{q}_2)}{|\mathbf{q}_1+\mathbf{q}_2|^2} + \frac{q^2(\mathbf{q}_1+\mathbf{q}_2).\mathbf{q}_3}{|\mathbf{q}_1+\mathbf{q}_2|^2 q_3^2}\right) K_2^S(\mathbf{q}_1, \mathbf{q}_2)\Bigg] \end{aligned} \tag{4.A29}$$

Here 'Sym' indicates symmetrisation in $\mathbf{q}_1$, $\mathbf{q}_2$ and $\mathbf{q}_3$.

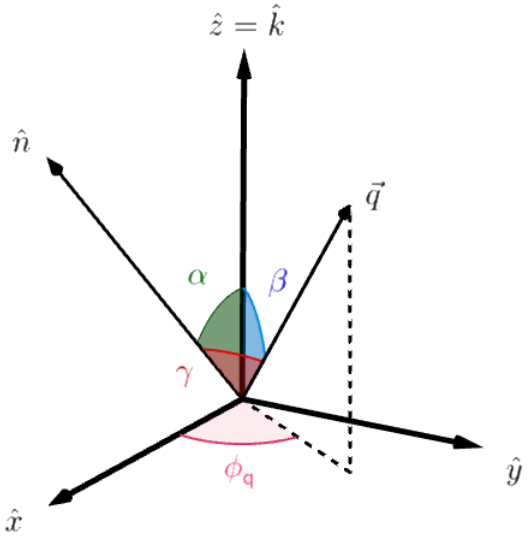

Figure 4.14: Vectors and angles involved in the calculations of P_{13} and P_{22}: $\hat{\mathbf{k}}$ is the direction of the wave vector $\mathbf{k}$ of Eq. (4.12) and $\mathbf{q}$ is also given in Eq. (4.12). $\mathbf{n}$ is the line-of-sight direction.

One can replace $\mathbf{q}_1$, $\mathbf{q}_2$, $\mathbf{q}_3$ and $\mathbf{k} = \mathbf{q}_1 + \mathbf{q}_2 + \mathbf{q}_3$ as required and effectively calculate these kernels.
The final expressions for $F_2^S(\mathbf{q},\mathbf{k}\text{-}\mathbf{q})$ and $F_3^S(\mathbf{q},\text{-}\mathbf{q},\mathbf{k})$ along with subsequent calculations can be found in a Mathematica notebook [116].
In the kernels F_2^S and F_3^S we encounter the scalar products $\hat{\mathbf{q}} \cdot \boldsymbol{n} \equiv \mu_q = \cos(\gamma)$, $\hat{\mathbf{k}} \cdot \boldsymbol{n} \equiv \mu = \cos(\alpha)$, and $\hat{\mathbf{k}} \cdot \mathbf{q} \equiv x = \cos(\beta)$. We also define $r = |\mathbf{q}|/|\mathbf{k}|$. We can write μ_q in terms of μ, x, and ϕ_q, where ϕ_q is the angle between the projection of $\mathbf{q}$ and $\mathbf{n}$ onto the plane perpendicular to $\hat{\mathbf{k}}$ (see Fig. 4.14)

$$\mu_q = x\,\mu + \sqrt{(1-x^2)(1-\mu^2)}\cos(\phi_q) \tag{4.A30}$$

For an arbitrary function $\psi(\mathbf{k},\mathbf{q})$, we can write:

$$\int \psi(\mathbf{k},\mathbf{q}) d^3q = \int_0^\infty q^2 dq \int_{-1}^1 dx \int_0^{2\pi} d\phi_q \psi(\mathbf{k},\mathbf{q})\,. \tag{4.A31}$$

Therefore the integration corresponding to $P_{22}^s(k,\mu)$ in Eq. (4.A25) reduces to

$$P_{22}^s = \frac{2k^3}{(2\pi)^3}\int_0^\infty dr r^2 P_{11}(r) \int_{-1}^1 dx P_{11}(k\sqrt{1+r^2-2r\,x}) \int_0^{2\pi} d\phi_q [F_2^S(r,\phi_q,x,\mu,b_1,f)]^2\,, \tag{4.A32}$$

where we take the integral over ϕ_q analytically, and the result can be found in our Mathematica notebook [116]. We write P_{22}^s as a sum over powers of μ, b_1 and f as

$$P_{22}^s = \sum_{\ell=0}^{\ell=4}\sum_{m=0}^{m=2}\sum_{n=0}^{n=4} \mu^{2\ell} b_1^m f^n A_{\ell mn}(k)\,, \tag{4.A33}$$

and finally by integrating over r and x we find the coefficients $A_{\ell mn}(k)$ numerically. Next, we explain the computation of $P^s_{13}(k,\mu)$, where the integration is as follows:

$$P^s_{13} = 6(1+\beta\mu^2)b_1 P_{11}(k)\frac{1}{(2\pi)^3}\int_0^\infty dr r^2 P_{11}(r)\int_{-1}^1 d\mu_q \int_0^{2\pi} d\phi_q F_3^S(r,\phi_q,x,\mu,b_1,f)\,, \tag{4.A34}$$

We integrate over ϕ_q and μ_q analytically, the result of which is contained in our Mathematica notebook [116]. Then similar to P^s_{22}, we write P^s_{13} as a sum over powers of μ, b_1 and f as

$$P^s_{13} = \sum_{\ell=0}^{\ell=2}\sum_{m=0}^{m=1}\sum_{n=0}^{n=3}\mu^{2\ell}b_1^m f^n B_{\ell mn}(k)\,, \tag{4.A35}$$

and by integrating over r numerically, we find the coefficients $B_{\ell mn}(k)$ which are given in our Mathematica notebook [116]. We use the minimum and maximum values of wave number that we have from our CLASS output, $k_{\rm min}$, $k_{\rm max}$, for the limits of q.

In order to avoid numerical problems, we employ the following algorithm for computing the integrals in case of P_{13}:
We divide the integration range in two large parts.

- For $k_{\rm min} < q < k$:
  If $k < 1000\,k_{\rm min}$, we integrate the original term(s) from $q_{\rm min} = k_{\rm min}$ to k. Else, we take the sum of the integration of the series expansion around $q = 0$ from $q_{\rm min}$ to $q < k/1000$ and integration of the original term(s) from $k/1000$ to $q < k$.

- For $k < q < k_{\rm max}$:
  If $10\,k > k_{\rm max}$, we integrate the original term(s) (with the signs corrected for argument of Logarithm) from k to $k_{\rm max}$. Else, we take the sum of the integration of the original term(s) from k to $10\,k$ and the integration of the series expansion around $q = \infty$ from $10\,k$ to $k_{\rm max}$.

4.B TNS model A, B and C correction terms

In this appendix we present the basic forms of the RSD correction terms appearing in Eq. (4.18). These terms are given as

$$\begin{aligned} A(k,\mu) = &\sum_{m,n=1}^{3}\mu^{2m}f^n\frac{k^3}{(2\pi)^2} \\ &\times\Bigg[\int dr\int dx\Big(A_{mn}(r,x)P_{\rm lin}(k)+\tilde{A}_{mn}(r,x)P_{\rm lin}(kr,z)\Big) \\ &\times\frac{P_{\rm lin}(k\sqrt{1+r^2-2rx},z)}{(1+r^2-2rx)}+P_{\rm lin}(k,z)\int dr a_{mn}(r)P_{\rm lin}(kr,z)\Bigg], \end{aligned} \tag{4.B36}$$

$$B(k,\mu) = \sum_{n=1}^{4}\sum_{a,b=1}^{2}\mu^{2n}(-f)^{a+b}\frac{k^3}{(2\pi)^2} \times \int dr \int dx B^n_{ab}(r,x)\frac{P_{a2}(k\sqrt{1+r^2-2rx},z)P_{b2}(kr,z)}{(1+r^2-2rx)^a}, \tag{4.B37}$$

$$C(k,\mu) = (k\mu f)^2 \times \int \frac{d^3p d^3q}{(2\pi)^3}\delta_D(\boldsymbol{k}-\boldsymbol{q}-\boldsymbol{p})\frac{\mu_p^2}{p^2}(1+fx^2)^2 P_{\rm lin}(p,z)P_{\rm lin}(q,z), \tag{4.B38}$$

where $\mu_p = \hat{\boldsymbol{k}}\cdot\hat{\boldsymbol{p}}$, $r = k/q$ and $x = \hat{\boldsymbol{k}}\cdot\hat{\boldsymbol{q}}$. Explicit expressions for $A_{mn}, \tilde{A}_{mn}, a_{mn}$ and B^n_{ab} can be found in the Appendices of [283]. The $C(k,\mu)$ term is known to have small oscillatory features and thus it is usually omitted in the literature. We choose to include it in our work.

4.C Fitting Procedure for EFT and TNS model

To fit the RSD free parameters of the EFT (Eq. 4.15) and TNS (Eq. 4.18) models to the simulation data we simply minimize the $\chi^2_{\rm red}$

$$\chi^2_{\rm red}(k_{\rm max}) = \frac{1}{N_{\rm dof}}\sum_{k=k_{\rm min}}^{k_{\rm max}}\sum_{\ell,\ell'=0,2}\left[P^S_{\ell,\rm data}(k) - P^S_{\ell,\rm model}(k)\right] \times {\rm Cov}^{-1}_{\ell,\ell'}(k)\left[P^S_{\ell',\rm data}(k) - P^S_{\ell',\rm model}(k)\right], \tag{4.C39}$$

where ${\rm Cov}_{\ell,\ell'}$ is the Gaussian covariance matrix between the different multipoles, and $k_{\rm min} = 0.006\,h/{\rm Mpc}$. The number of degrees of freedom $N_{\rm dof}$ is given by $N_{\rm dof} = 2\times N_{\rm bins} - N_{\rm params}$, where $N_{\rm bins}$ is the number of $k-$bins used in the summation and $N_{\rm params}$ is the number of free parameters in the theoretical model. Here, $N_{\rm params} = 2$ for EFT and not 3 because we only fit the first two multipoles[6], and $N_{\rm params} = 1$ for the TNS model.

We increase $k_{\rm max}$ until $\chi^2_{\rm red}(k_{\rm max}) \geq 1$. This gives a good indication of where the model doesn't fit the data so well anymore. In the fit we keep cosmology fixed to the COLA simulation's fiducial values and only vary the counter term coefficients and σ_v.

We use linear theory to model the covariance between the multipoles (see Appendix C of [283] for details). This has been shown to reproduce N-body results up to $k \leq 0.300h/{\rm Mpc}$ at $z = 1$. In the covariance matrix we assume a number density of $n = 1\times10^{-3}\,h^3/{\rm Mpc}^3$ and a survey volume of $V_s = 4\,{\rm Gpc}^3/h^3$ which are similar specifications for a Euclid like survey [19]. The best fit parameters as well as $k_{\rm max}$ are shown in Table 4.1.

[6]The inclusion of the hexadecapole would restrict the determined range we can safely fit to. Further, the monopole and quadrupole contain most of the RSD information so we can omit the hexadecapole from these fits.

Table 4.1: Table showing the maximum $k_{\rm max}[h/{\rm Mpc}]$ used in Eq. (4.C39) and best fit model parameters for TNS and EFT models found by a least χ^2 fit to the COLA data.

Model	TNS				EFT			
z	0.5	1	1.5	2	0.5	1	1.5	2
$k_{\rm max}$	0.16	0.21	0.27	0.35	0.16	0.21	0.27	0.311
σ_v	7.35	6.26	5.12	4.19	-	-	-	-
$c_{2\|\delta_s,0}/k_{\rm nl}^2$	-	-	-	-	0.05	0.00	0.00	0.13
$c_{2\|\delta_s,2}/k_{\rm nl}^2$	-	-	-	-	13.57	8.96	5.66	1.52
$c_{2\|\delta_s,4}/k_{\rm nl}^2$	-	-	-	-	7.34	8.03	6.86	5.73

4.D Neglecting the lensing term

Throughout the paper, we have neglected the lensing contribution to the angular power spectrum. In this appendix, we show that among the three different redshift bins that we used, namely, $\Delta z = 0.1$, $\Delta z = 0.01$, and $\Delta z = 0.001$, lensing is of the same order as the RSD contribution only for $\Delta z = 0.1$ while for the other two redshift bins, it is negligible.

In Fig. 4.15, we show the ratio of lensing to the RSD term for different redshifts with $\Delta z = 0.01$ (left panel) and $\Delta z = 0.1$ (right panel). For $\Delta z = 0.1$, lensing is not negligible when compared to RSD, however, we have shown that for this window width, RSD is also not very significant. For $\Delta z = 0.001$ (left panel), the lensing terms are at most 1% of the RSD terms. It is also interesting to note that for $\Delta z = 0.1$ the lensing signal is very small at $\ell < 400$. This comes from the fact that the lensing signal is the sum of the always negative lensing-density correlation and the positive lensing-lensing term. As the density term is larger than lensing, at low redshift the signal is dominated by the first term and is therefore negative. At sufficiently high redshift when enough lensing has accumulated, the lensing-lensing term starts to dominate and the signal becomes positive. For $\Delta z = 0.1$ this happens roughly at $z = 1$. For $\Delta z = 0.01$ this happens roughly at $z \sim 0.5$ for the low multipoles, $\ell < 200$ while for higher multipoles the positive lensing-lensing signal dominates. Since the cross correlation lensing(z_2)-density(z_1) is significant only for density fluctuations at redshift over which the lensing term is integrated, $z_1 < z_2$, this contribution is smaller for smaller redshift bins.

4.E Fisher forecast

In this appendix, we explain in more details the Fisher forecast we have performed for RSD detection. We replace each μ^2 term with $A\mu^2$, where A is an artificial amplitude with fiducial value of 1, and our aim is to forecast how precisely we can measure this amplitude. For nonlinear RSD, we simply use the Kaiser formula applied to halofit model, basically replacing $P(k_\parallel, \frac{\ell}{\chi}, \bar{z})$ in Eq. (4.8) with the Kaiser

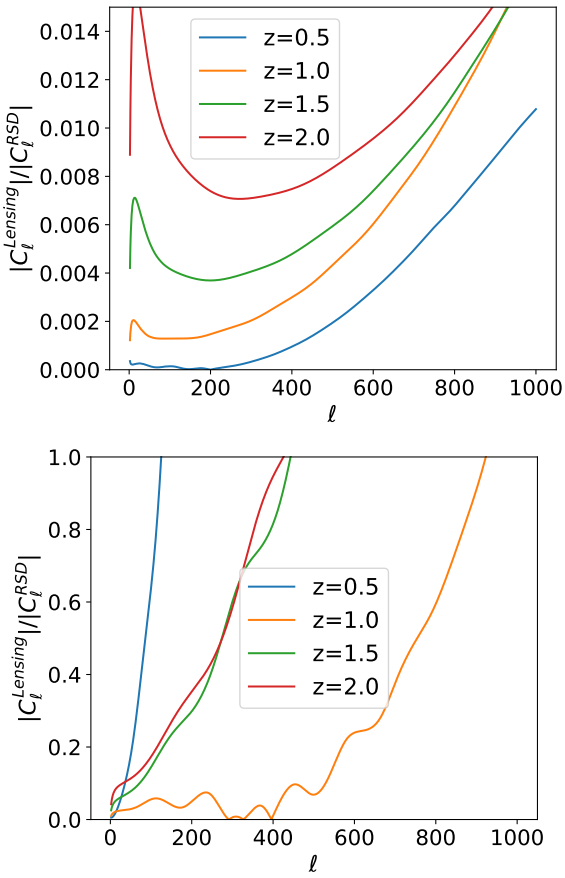

Figure 4.15: Ratio of lensing terms to RSD tems for different redshifts with $\Delta z = 0.01$ (left panel) and $\Delta z = 0.1$ (right panel).

formula given in Eq. (4.1), we have

$$C_\ell^{\Delta\Delta}(z,z) = \frac{1}{2\pi\chi^2(\bar{z})}\left[\int_{-\infty}^{+\infty} dk_\parallel (1 + 2Af\mu^2 + A^2 f^2\mu^4) P(k_\parallel, \ell/\chi, z)\right] \equiv C_\ell^{\delta\delta} + 2AC_\ell^{\delta\theta} + A^2 C_\ell^{\theta\theta}\,, \tag{4.E40}$$

where Δ is the density perturbations in redshift space

$$\Delta(\boldsymbol{n}, z) = \delta(\boldsymbol{n}, \mathbf{r}) - \frac{\nabla_z v_z(\mathbf{r})}{aH(z)}\,, \tag{4.E41}$$

and $\theta = \nabla_z v_z(\mathbf{r})/aH(z)$, where z is the line of sight direction. For the Fisher forecast, we follow a similar approach as the one used in Section 4 of [162]. The Fisher matrix for parameters α and β with covariance matrix, $\mathcal{C}$, follows the formula

$$F_{\alpha\beta} = \sum_\ell \frac{2\ell+1}{2}\left[(\partial_\alpha \mathcal{C})\left(\mathcal{C}^{-1}\right)(\partial_\beta \mathcal{C})\left(\mathcal{C}^{-1}\right)\right] \tag{4.E42}$$

which for our case with one parameter, A and covariance matrix being the C_ℓ's, reduces to

$$F_{AA} = \sum_{\ell=2}^{\ell_{\rm max}} \frac{2\ell+1}{2} \left[\frac{\partial_A C_\ell^{\Delta\Delta}}{C_\ell^{\Delta\Delta}} \right]^2 . \tag{4.E43}$$

5

General Relativistic corrections in density-shear correlations

Based on:
[115] B. Ghosh, R. Durrer, & E. Sellentin, *General Relativistic corrections in density-shear correlations*, **JCAP 1806** (2018) 008, [arXiv: 1801.02518]

From the discussions in Section 1.2, we know that gravitational lensing is arguably the most important relativistic effect that has a direct consequence on the observed signal. There are mainly three kinds of lensing probes - the *galaxy clustering*, which statistically estimates overdensities by counting galaxies at a particular random separation (δ correlated with δ); the *cosmic shear measurements*, which provide information about the shapes of galaxies (γ correlated with γ); and the *galaxy-galaxy lensing*, which correlates the shape of the background galaxies with the position of the foreground ones that act as lenses to the background (γ correlated with δ). The distortion due to the third kind is called a tangential shear, where the source galaxy ellipticities get oriented perpendicular to the line connecting the foreground and the background galaxies. The primary message this work intends to convey is that similar to the number counts, there are relativistic effects in galaxy-galaxy lensing probes which should not be ignored. These effects arise due to the presence of matter distributions between the foreground and the observer, which contribute as well to the distortion of the background galaxy shapes. Current analyses of galaxy survey observations neglect such effects by including them either in the error budget, or marginalising over them. We suggest that the relativistic corrections, especially lensing, should rather be directly included in the main signal, since they have a significant contribution to it. On carrying out a mock survey analysis of the Dark Energy Survey (DES), we find that for the most strongly correlated foreground and background redshifts, the $\gamma - \gamma$ correlation term contributes almost 50% to the total signal, although at low foreground redshifts this is merely 1.5% (for a complete survey with zero magnification bias). We carry out the same analysis using higher redshifts that are expected to be probed by Euclid, and find the lensing correction to be even higher, suggesting that the deeper the survey, the more significant it is to take these corrections into account.

Abstract: We investigate the corrections which relativistic light-cone computations induce on the correlation of the tangential shear with galaxy number counts, also known as galaxy-galaxy lensing. The standard-approach to galaxy-galaxy lensing treats the number density of sources in a foreground bin as observable, whereas it is in reality unobservable due to the presence of relativistic corrections. We find that already in the redshift range covered by the DES first year data, these currently neglected relativistic terms lead to a systematic correction of up to 30% in the density-shear correlation function for the highest redshift bins. This correction is dominated by the the fact that a redshift bin of number counts does not only lens sources in a background bin, but is itself again lensed by all masses between the observer and the counted source population. Relativistic corrections are currently ignored in the standard galaxy-galaxy analyses, and the additional lensing of a counted source populations is only included in the error budget (via the covariance matrix). At increasingly higher redshifts and larger scales, these relativistic and lensing corrections become however increasingly more important, and we here argue that it is then more efficient, and also cleaner, to account for these corrections in the density-shear correlations.

5.1 Introduction

Currently one of the most impressive success stories in cosmology is the highly accurate observation and our detailed understanding of the cosmic microwave background (CMB), its anisotropies and its polarisation, see e.g. [11, 12, 10, 97, 96]. As a cosmological community, we would now like to repeat this success story at lower redshifts by using present and future galaxy surveys. Contrary to the CMB which primarily comes from the two-dimensional surface of last scattering, galaxy surveys are three-dimensional and therefore contain more, potentially richer information. Especially by using tomography, i.e., by splitting a source population into different redshift bins, we can study how cosmic structure formation proceeds and thereby directly test the gravitational instability picture.

To repeat the CMB success story, it is important that we make optimal use of the low-redshift data. Of course, the fact that clustering becomes non-linear on smaller scales and late time as well as the influence of non-gravitational hydrodynamical effects and more, render the interpretation of the data more difficult. The current standard-approach to model these non-linearities is to translate a linear power spectrum to a non-linear power spectrum by using 'Halofit' [280], and in this paper we shall adhere to this approach, noting however that it only refers to the non-linear growth of scalar perturbations in Newtonian gravity. General Relativistic N-body codes do exist and the agreement of the matter power spectrum from relativistic simulations with Halofit is excellent [7].

The problem of galaxy formation depending on its environment is on an observational level modeled by 'biasing': the observed galaxy density distribution δ_g is assumed to be related to the underlying matter density distribution, $\delta_g = b(z)\delta$ via some biasing function b. When cosmological parameters are inferred, this bias function is treated as nuisance parameters, and marginalized over. Another nuisance

parameter in shear correlations is the intrinsic alignment contribution to the shear signal. Also this is marginalized over. The free parameters of these bias functions are likely to mimic, to some extent, the contribution from relativistic effects which we study in this paper. However, since these effects are signals of theoretical interest which can be calculated, marginalizing over them is suboptimal.

In this paper we investigate the impact of general relativistic corrections on the correlation between number counts in a foreground bin, and lensing in a background bin. Our starting point is that it has lately been shown [310, 309, 46, 67] that counting galaxies in a fixed solid angle and redshift bin does not directly measure the galaxy over-density. The resulting count is not only affected by redshift space distortions [175], but also enhanced or decreased by lensing and magnification bias [211] and by large-scale relativistic effects. The relativistic effects other than lensing are mainly relevant on very large scales where they can mimic a primordial non-Gaussianity [56, 246]. Redshift space distortions are well known and are routinely used to constrain the cosmic growth factor [219, 239].

In recent years it has been shown that also the lensing and magnification bias term is considerable and will be measured in future galaxy clustering analyses [221]. Furthermore, neglecting it can lead to misinterpretation of results from galaxy surveys, see, e.g. [59, 222, 297]. Also in this paper we investigate the effects of the lensing term. More precisely, we focus on galaxy-galaxy lensing, where the tangential shear of background sources is correlated with number counts in the foreground. We study how relativistic effects, and especially the lensing term from projection, affect the correlation of galaxy density fluctuations with the tangential shear. We find, that already in present surveys the effect can contribute up to 50% at high redshift. That this term has to be included in the galaxy-galaxy lensing cross correlation is of course not new. It has already been discussed ten years ago in Ref. [315] and subsequently in several other papers. Nevertheless it is not included in present analyses. Here we present a concrete case study to estimate the maximum size of the effect in recent surveys.

This paper is structured as follows: In the next section we derive the theoretical expressions for the cross-correlation function between relativistically correct number counts and the tangential shear, and its corresponding angular power spectrum in redshift space. In Section 5.3 we present some numerical examples and discuss them. We show especially how the recently published DES (Dark Energy Survey) first year results [1] could gain in precision by including the lensing term directly into the signal of the number counts. In Section 5.4 we conclude. We present a comprehensive derivation of the density-shear correlation function in the full and flat sky in Appendix 5.A.

5.2 Correlating number counts with shear measurements

Here we present the first order expression for the correlation between galaxy number counts and the tangential shear. For completeness, a detailed derivation is presented

in Appendix 5.A, where we also make the connection to results known from the literature.

In first order perturbation theory, the number of galaxies within a redshift bin dz and a solid angle $d\Omega$ at observed redshift z, in observed direction $\boldsymbol{n} = \boldsymbol{n}(\vartheta, \varphi)$ is given by

$$N(z, \boldsymbol{n}) = \bar{N}(z)[1 + \Delta(z, \boldsymbol{n}, m_{\rm lim})] \tag{5.1}$$

where $\bar{N}(z)$ is the average spatial number density at redshift z, and where the observable over-density is [46, 67, 86, 56]

$$\begin{aligned}\Delta(\boldsymbol{n}, z, m_{\rm lim}) &= b(z)\delta + \frac{1}{\mathcal{H}}\left[\dot{\Phi} + \partial_r^2 V\right] + (2 - 5s)\left[\int_0^r \frac{d\tilde{r}}{r}(\Phi + \Psi) - \kappa\right] \\ &\quad + (f_{\rm evo} - 3)\mathcal{H}V + (5s - 2)\Phi + \Psi \\ &\quad + \left(\frac{\dot{\mathcal{H}}}{\mathcal{H}^2} + \frac{2 - 5s}{r\mathcal{H}} + 5s - f_{\rm evo}\right)\left(\Psi + \partial_r V + \int_0^r d\tilde{r}(\dot{\Phi} + \dot{\Psi})\right) .\end{aligned} \tag{5.2}$$

Here an overdot denotes a derivative with respect to conformal time, $\mathcal{H}$ is the conformal Hubble parameter and $r = r(z)$ is the comoving distance to redshift z. The peculiar velocity is given by V, the velocity potential in longitudinal gauge, such that velocity components are given by $v_i = -\partial_i V$. The term δ is the matter density fluctuation in comoving gauge: on small scales it reduces to the Newtonian density contrast, but it is by itself not observable, even if the galaxy bias function $b(z)$ were known. The quantities Φ and Ψ are the Bardeen potentials. More details on Eq. (5.2) are given in [86] and [88].

Furthermore, denoting the angular Laplacian as Δ_Ω, the convergence κ is given by the angular Laplacian of the lensing potential, ϕ,

$$\kappa = -\frac{1}{2}\Delta_\Omega \phi\,, \tag{5.3}$$

$$\phi(\boldsymbol{n}, z) = -\int_0^{r(z)} d\tilde{r}\frac{r(z) - \tilde{r}}{r(z)\tilde{r}}(\Phi + \Psi)(\tilde{r}\boldsymbol{n}, \tau_0 - \tilde{r})\,. \tag{5.4}$$

We denote the limiting luminosity by $L_{\rm lim}$. The evolution bias, $f_{\rm evo}$, captures the fact that new galaxies form and galaxies merge as the Universe expands and hence their number density evolves not simply as $(1+z)^3$; $f_{\rm evo}$ depends on redshift and on $L_{\rm lim}$ and is defined as

$$f_{\rm evo}(z, L_{\rm lim}) \equiv \frac{\partial \ln\langle a^3 \bar{N}(z, L > L_{\rm lim})}{\partial \ln a}\,. \tag{5.5}$$

Here $\bar{N}(z, L > L_{\rm lim})$ is the background number density of galaxies with luminosity above $L_{\rm lim}$ and $a = 1/(z+1)$ is the cosmic scale factor. Finally, we introduce magnification bias: due to magnification, less luminous galaxies still make it into our survey if they are in a region of high magnification and vice versa. Denoting the limiting magnitude of the survey $m_{\rm lim}$, the magnification bias is given by

$$s(z, m_{\rm lim}) \equiv \left.\frac{\partial \log_{10} \bar{N}(z, L > L_{\rm lim})}{\partial m}\right|_{m_{\rm lim}}\,. \tag{5.6}$$

The redshift dependence of this quantity depends on the specific survey. Only if we see all galaxies of a considered type, i.e. if the survey is complete, we have $s = 0$. Note that s nearly always enters in the combination $5s - 2$. This is the factor which multiplies the fluctuations of the angular diameter (area) distance [47], $\delta D_A(z)$ which contributes twofold: it leads to an increase in the transversal volume (area) and hence to a decrease in the density; this is the term -2. But it also increases the observed brightness in sources of a given luminosity and can bring them into an incomplete survey, enhancing the density; this is the term $+5s$ which is also called magnification bias. In the combination $(5s - 2)\kappa$ we shall call them here the "lensing contribution" to the actually observable $\Delta(\boldsymbol{n}, z)$.

In Appendix 5.A we derive the following expression for the correlation function between the observable galaxy number count Δ and the tangential shear γ_t

$$\langle \Delta(\boldsymbol{n}, z)\gamma_t(\boldsymbol{n}', z')\rangle = \frac{-1}{4\pi}\sum_\ell \frac{2\ell+1}{\ell(\ell+1)} P_{\ell 2}(\boldsymbol{n}\cdot\boldsymbol{n}')C_\ell^{\Delta,\kappa}(z, z')\,. \tag{5.7}$$

Here, $P_{\ell m}(\mu)$ is the Legendre polynomial of degree ℓ and order m, and $C_\ell^{\Delta,\kappa}(z, z')$ is the angular power spectrum of the correlation between Δ and κ. We split it into its correlation with the not-directly observable density contrast ('δ'), augmented by redshift space distortions ('rsd'), by the convergence κ and by large scale relativistic effects ('ls')

$$C_\ell^{\Delta,\kappa}(z, z') = b(z)C_\ell^{\delta,\kappa}(z, z') + C_\ell^{\mathrm{rsd},\,\kappa}(z, z') - (2-5s(z))C_\ell^{\kappa,\kappa}(z, z') + C_\ell^{\mathrm{ls},\,\kappa}(z, z')\,. \tag{5.8}$$

Here, $C_\ell^{\mathrm{rsd},\kappa}$ denotes the correlation of κ with the redshift space distortion (rsd) term caused by $\partial_r^2 V$, while $C_\ell^{\mathrm{ls},\kappa}$ denotes its correlation with all the remaining relativistic terms which are relevant mainly on very large scales. They also include the so-called Doppler term $\propto \partial_r V$ which is strictly speaking not relativistic but also only relevant on large scales. The lensing term $-(2 - 5s(z))C_\ell^{\kappa,\kappa}$ and the large scale corrections, $C_\ell^{\mathrm{ls},\,\kappa}$, apart from the Doppler term are due to General Relativity and we call them 'General Relativistic corrections'. We shall see that on intermediate and small scales, $\ell > 20$, the lensing term by far dominates these corrections to the number density.

In standard analyses, which includes the DES analysis, only the term $C_\ell^{\delta,\kappa}(z, z')$ is considered. The main point of this paper is to show that this introduces systematic deviations in the signal and that in particular the lensing of the number densities in the foreground bin cannot be neglected. In the next section we compute all the terms for several examples and we show that only the $C_\ell^{\kappa,\kappa}(z, z')$ term is a relevant correction for present and near future galaxy clustering surveys. Redshift space distortions are always much smaller and the relativistic terms contribute only on very large scales, $\ell < 10$, where cosmic variance is significant and which are not accessed in the DES survey.

5.3 Numerical Examples

In this section we present changes in the signal for numerical evaluations of the above relativistic contributions for the standard ΛCDM cosmology. We use the

public code CLASS [194, 41] which has been expanded to include the relativistic contributions to galaxy number counts [88]. We assume purely scalar perturbations with cosmological parameters of the Planck-2015 results [12]. More precisely, we set the Hubble parameter $H_0 = 67.556$ km s^{-1} Mpc^{-1}, the baryon density parameter $\Omega_b h^2 = 0.022032$, the cold dark matter density parameter $\Omega_{\rm cdm} h^2 = 0.12038$, the curvature $K = 0$, the number of neutrino species $N_\nu = 3.046$ and the neutrino masses are neglected. We set the galaxy bias to unity, $b(z) = 1$, and assume a complete survey, $s = 0$, for our analysis.

We first present results for a mock survey which mimics the redshift binning of the first year DES observations. A similar analysis with somewhat smaller sky coverage has also been published by KiDS (Kilo Degree survey) [294]. In contrast to DES, we assume however full-sky coverage since our interest also includes the very low multipoles where relativistic effects leave noticeable traces.

In this paper we do not want to exactly determine the contribution to the DES correlation functions and error budget from our terms, we just want to give the correct order of magnitude. Clearly, since this is a systematic effect which is easy to model, it would be more useful to add it to the data than to just include it in the error budget.

Furthermore, if $2 - 5s(z) > 0$, which is true in observed volumes where a survey reaches near completeness, then the $C_\ell^{\kappa,\kappa}$ contribution is negative as is $C_\ell^{\delta,\kappa}$ so that $|C_\ell^{\delta,\kappa} - 2C_\ell^{\kappa,\kappa}| > |C_\ell^{\delta,\kappa}|$.

5.3.1 A generic survey with DES-like redshift binning

The DES collaboration has presented first year data on the cross-correlation of galaxy clustering and lensing [1]. This analysis uses five galaxy redshift bins in the foreground (abbreviated by 'f') with width $\Delta z = 0.15$. These foreground populations are correlated with four tangential shear redshift bins in the background, (abbreviated by 'b') with widths $\Delta z = 0.23,\ 0.2,\ 0.27$ and 0.23 respectively. The mean redshifts of these bins are given by

$$z_{f1} = 0.225 \quad z_{f2} = 0.375 \quad z_{f3} = 0.525 \quad z_{f4} = 0.675 \quad z_{f5} = 0.825 \tag{5.9}$$

$$z_{b1} = 0.315 \quad z_{b2} = 0.53 \quad z_{b3} = 0.765 \quad z_{b4} = 1.1 \tag{5.10}$$

In order to establish whether relativistic corrections have a noticeable impact on current surveys, we model a generic DES-like survey by using the above redshifts for centers of Gaussian redshift bins with the corresponding widths. If relativistic effects have a noticeable impact, then the correlations $C_\ell^{\delta,\kappa}(z_{fi}, z_{bj})$, where only δ-terms are included, deviate from the correlations $C_\ell^{\Delta,\kappa}(z_{fi}, z_{bj})$, where also the relativistic terms are included.

We have thus calculated the contribution of $C_\ell^{\delta,\kappa}(z_{fi}, z_{bj})$ in $C_\ell^{\Delta,\kappa}(z_{fi}, z_{bj})$ for all $z_{fi} < z_{bj}$. In Fig. 5.1 we show the full relative difference $(C_\ell^{\Delta,\kappa} - C_\ell^{\delta,\kappa})/C_\ell^{\Delta,\kappa}$, whereas in Fig. 5.2 we show the relative contribution $2C_\ell^{\kappa,\kappa}/C_\ell^{\Delta,\kappa}$ from the convergence κ alone.

As it can be seen in the top panel of Fig. 5.1, for the lowest foreground bin, the subdominant terms apart from δ (as seen in Eq. 5.8) contribute up to 1.5%

to the total on large scales ($\ell > 20$). The scales accessible to the DES 1st year survey correspond to $\ell > 50$, where the contribution of the subdominant terms is small, around 1-1.5%. For $\ell \gtrsim 40$, lower redshift lensing bins which are closer to the foreground source always dominate while for $\ell < 40$ this is no longer so. For very wide angles the relativistic effects which increase for larger redshifts contribute significantly.

In the bottom panel we show the relative contribution from the 'subdominant' terms for the highest background bin and all foreground bins. Of course this is a monotonically increasing function of the foreground redshift. It rises up to 50% for $\ell > 50$ which contribute to the DES results. Clearly, these contributions cannot be neglected. Note that the results obtained in the top and bottom panel of Fig. 5.1 have been obtained using 'Halofit' [280] for the density power spectrum. This is relevant above $\ell \sim 50$ as is shown in the middle panel where the results with (dashed) and without (solid) Halofit are compared for two redshift bin combinations. In Fig. 5.2 we now show simply $-2C_\ell^{\kappa,\kappa}/C_\ell^{\Delta,\kappa}$. We have verified that for $\ell \gtrsim 50$ this is virtually identical to $(C_\ell^{\Delta,\kappa} - C_\ell^{\delta,\kappa})/C_\ell^{\Delta,\kappa}$, hence all the difference is actually due to lensing. It ranges from a mere 1% for the lowest foreground bin to more than 50% for the highest one, which assures us that the contribution will increase further with the higher redshift bins of future surveys (see also Fig. 5.4). At low ℓ the lensing contribution alone does not explain all the signal and redshift space distortions and relativistic effects can become significant. In Fig. 5.3, we show and compare the different contributions, with the total galaxy number count signal shown in black. This is done only for the highest redshift bins, z_{f5} and z_{b4}, since the differences are most prominent in this case. While we see that the redshift space distortions and other relativistic effects have comparatively small contributions, the one due to lensing is definitely important, it is in fact larger than the density term at very large scales, $\ell < 10$. For lower redshifts, the lensing term is smaller and we have found that at low ℓ redshift space distortions and relativistic effects cannot be neglected. For a comparison with the DES first year results only the C_ℓ's with $\ell > 50$ are relevant, since the sky coverage of the DES first year is about 1/30th of the full sky.

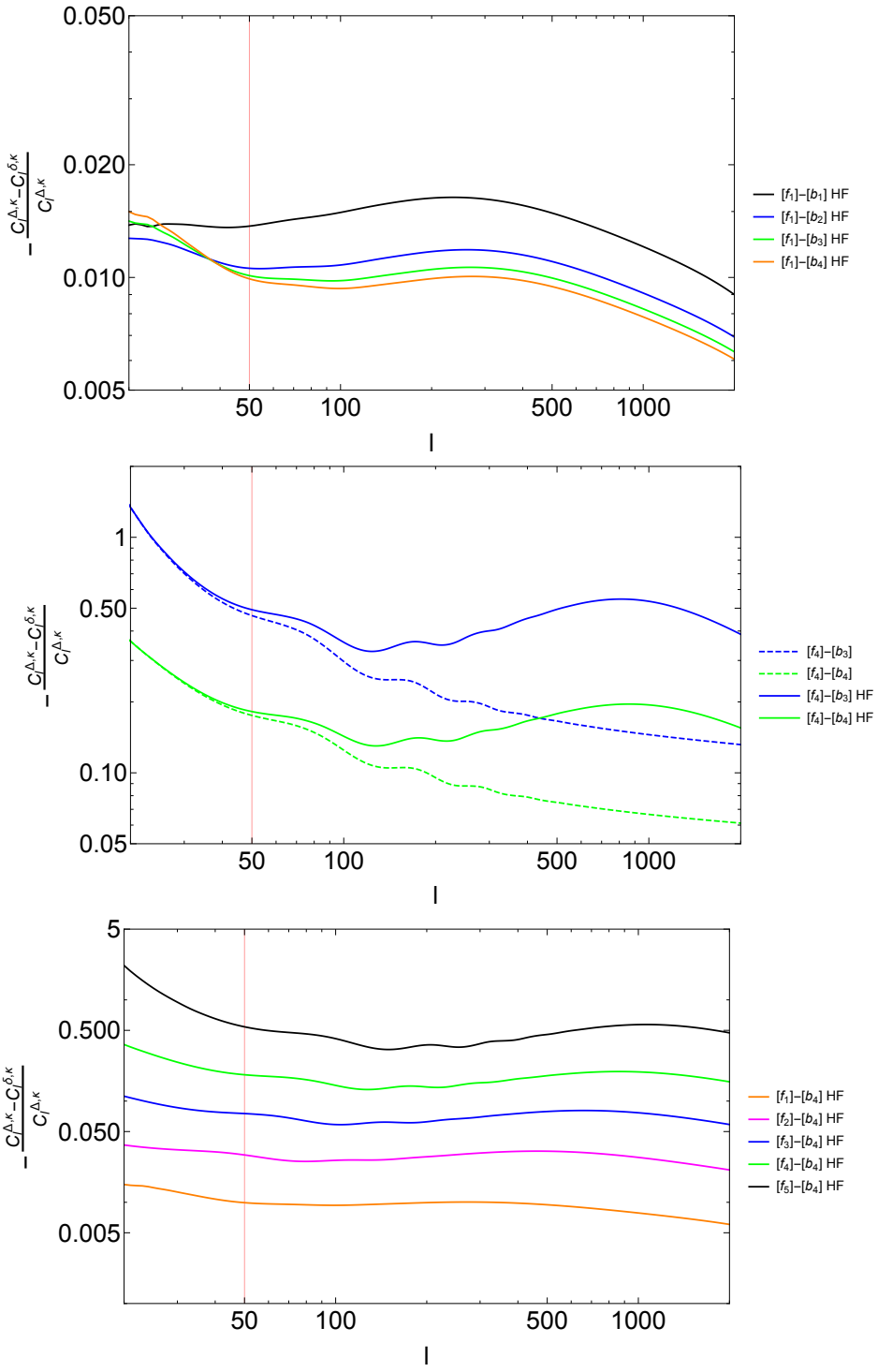

Figure 5.1: The top and middle panels show the relative contribution of all terms apart from δ for the cross-correlations between the lowest foreground bin and second highest foreground bin denoted here by $[f_1]$ and $[f_4]$ respectively, with the higher background bins. This is expressed in terms of the relative difference in angular power spectra of the mentioned contributions. The bottom one is for all foreground bins correlated with the highest background $[b_4]$. HF stands for Halofit. DES results are only sensitive to the values of ℓ above the vertical red line at $\ell = 50$. The signals are all negative, and hence the vertical axis is written with a negative sign.

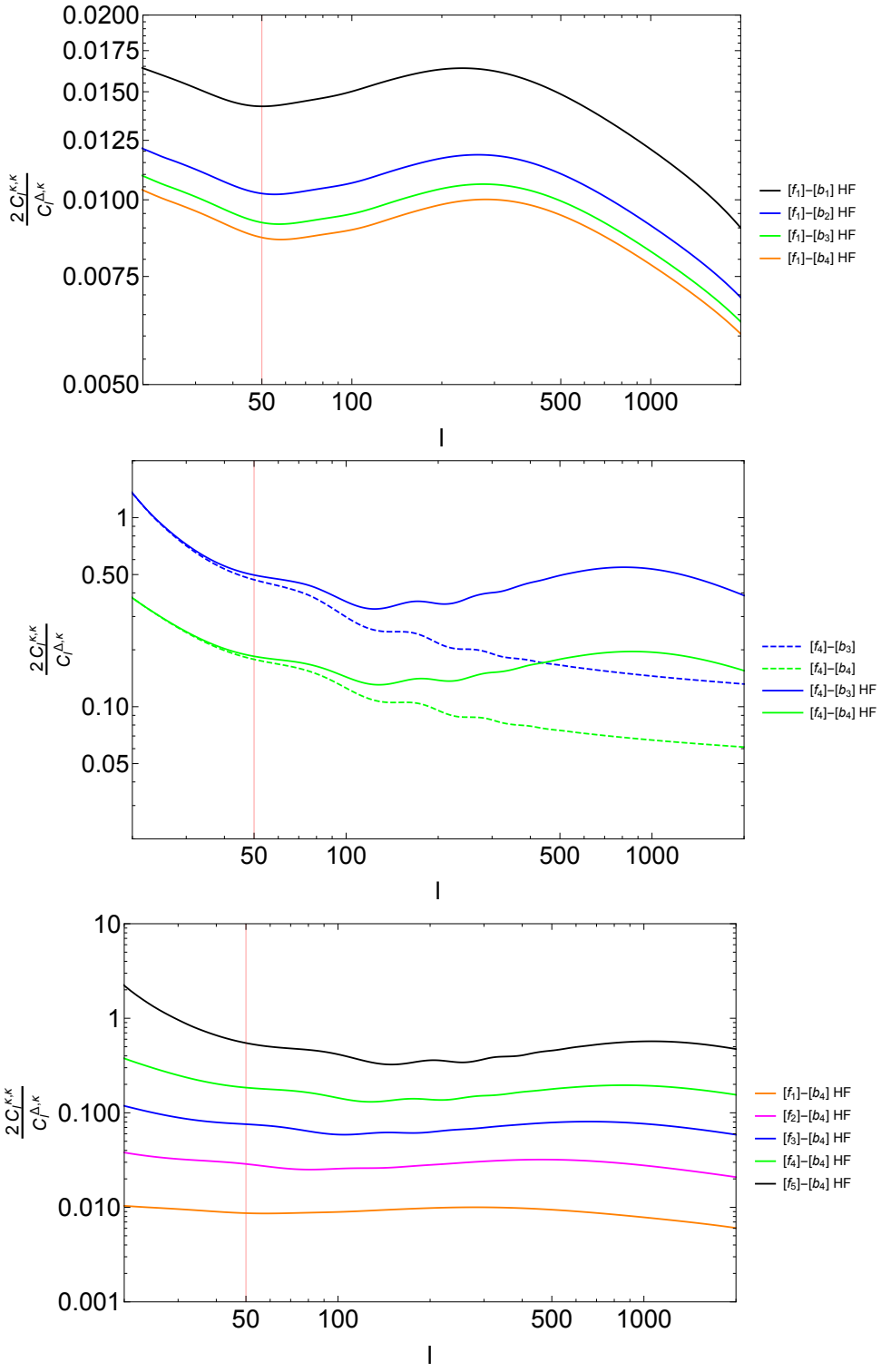

Figure 5.2: The same as in Fig. 5.1 but here $C_\ell^{\Delta,\kappa} - C_\ell^{\delta,\kappa}$ is replaced by $-2C_\ell^{\kappa,\kappa}$.

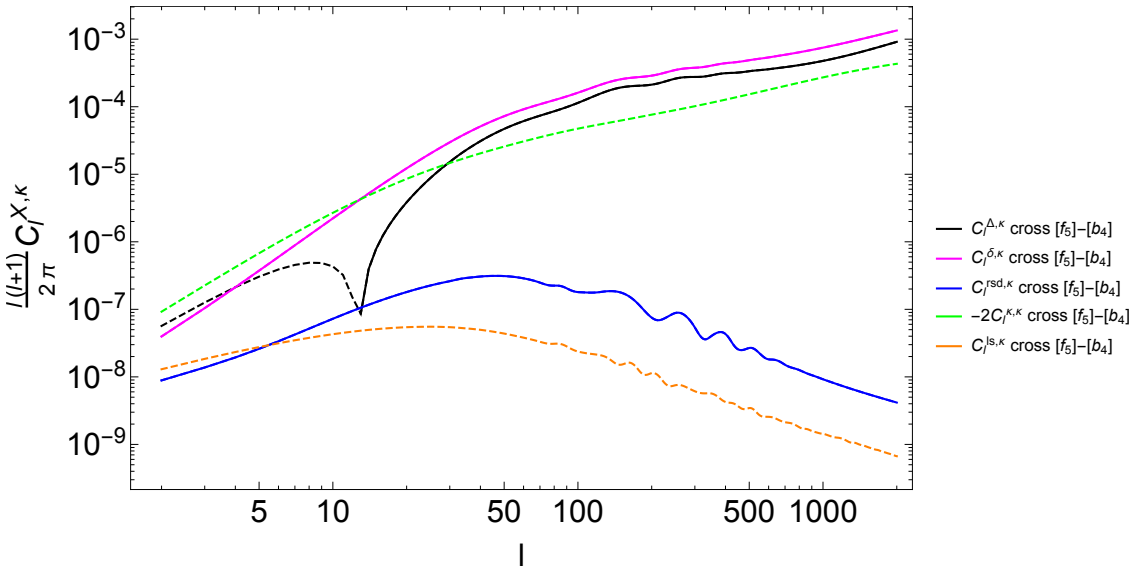

Figure 5.3: This figure compares the different contributions to the number count shear cross-correlation, always using Halofit. The black line represents the total galaxy number counts–tangential shear correlation, the magenta, green, blue and orange ones are for the density, κ, redshift space distortion and large scale relativistic effects respectively. The dashed lines indicate negative signals.

5.3.2 Future surveys and higher redshifts

As our numerical examples illustrate, the impact of especially lensing on the number counts increases with redshift. Future surveys like Euclid [19, 190, 103], LSST (Large Synoptic Survey Telescope) [3, 202] or SKA (Square Kilometer Array) [2, 203] will go to higher redshifts than the here modeled DES-like redshift binning, and it will be even more important to take lensing effects on the number counts into consideration. In the case of SKA, the lensing term is of course absent for intensity maps [126] but present for number counts. As an example, in Fig. 5.4, we show the situation for two cases: $z_f = 1.0$, $z_b = 1.5$ and $z_f = 1.5$, $z_b = 2.0$. In both cases, the $\kappa-\kappa$ contribution is seen to be identical to the full difference $(C_\ell^{\Delta,\kappa} - C_\ell^{\delta,\kappa})$, and is therefore evidently the most significant effect.

5.4 Conclusion

Galaxy surveys are these days analyzed via mainly two approaches, one of which is to investigate galaxy clustering and one is to detect gravitational shear, also known as gravitational lensing. It has recently become popular to cross-correlate these two observations, such that the correlations between the number density in a foreground bin, and the shear in a background bin are measured. In a relativistic framework, galaxy catalogues do however not measure purely the density δ but the combination Δ of density, redshift space distortions, lensing and large scale relativistic terms as

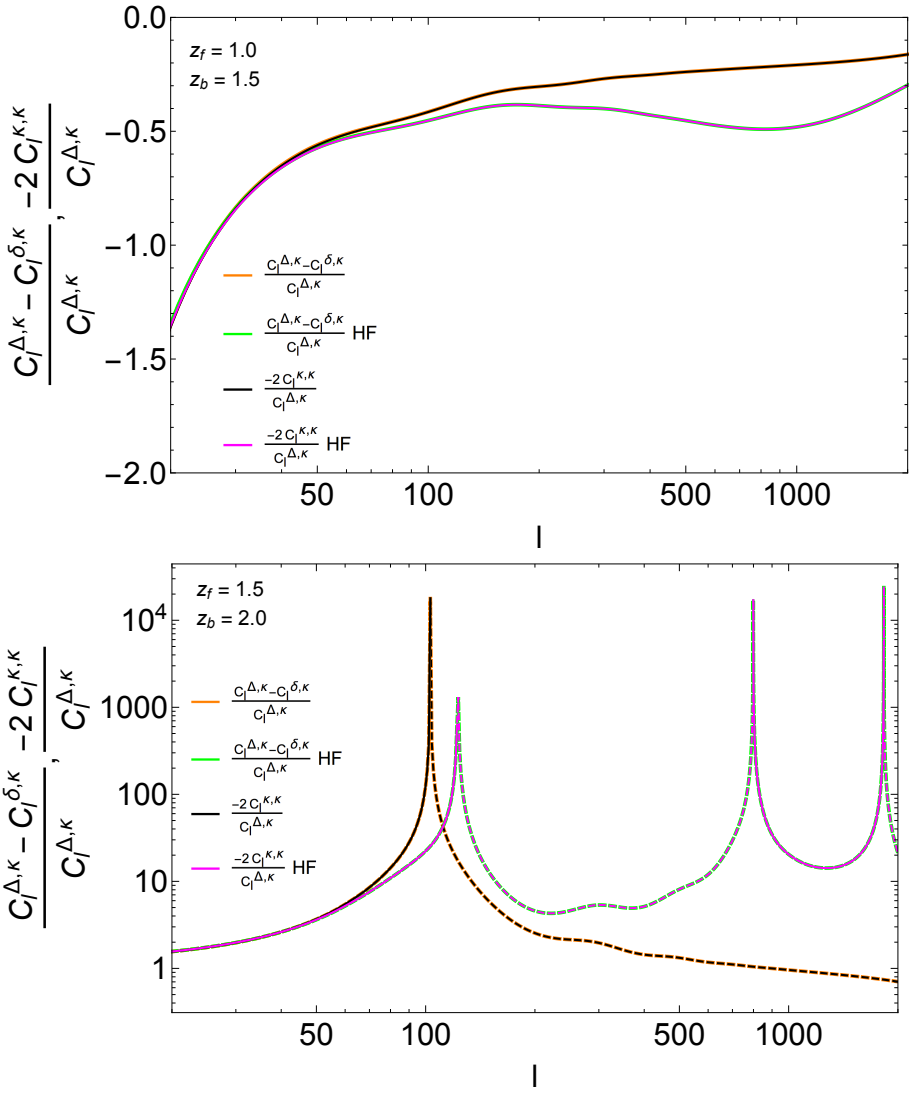

Figure 5.4: The top and bottom panels show the relative difference of the full number counts which include relativistic corrections, and the contribution from only δ to the number count-tangential shear correlation (orange for linear and green for Halofit). The contribution of lensing κ alone is also shown (black for linear and magenta for Halofit). For large ℓ the full difference and the $\kappa - \kappa$ term are identical while at low ℓ there is no difference between the linear perturbation theory result and Halofit. We consider the cases $z_f = 1.0$ and $z_b = 1.5$, and $z_f = 1.5$ and $z_b = 2.0$ respectively. The dashed lines in the bottom panel indicate negative signals. The spikes are due to sign changes.

given in Eq. (5.2). We have investigated this issue in this paper.

The number density of sources in a foreground bin is, in a relativistic setting, not a direct observable. Most prominently, the number density is affected by redshift space distortions and by lensing itself, but also by the large scale relativistic effects and the Doppler term. These introduce additional correlations with a lensing bin in the background. Owing to these extra-correlations, it is not ideal to simply 'combine

probes' as is frequently done, and to compute a joint covariance matrix for lensing, galaxy counts and galaxy-galaxy lensing. Rather, the relativistic corrections in the number counts should be directly accounted for as signal. In this paper we have shown that for a DES-like redshift binning, this can lead to a 50% correction of the signal in the density-tangential shear correlation function of the highest redshift bin. For the lowest redshift bin, the correction due to relativistic effects is 1.5%. This contribution systematically enhances the correlation Δ-κ. In our treatment we have set $s = 0$ which is probably not a very good approximation especially for the highest redshift bins. Including the correct value for $s(z)$ (which we do not know) will reduce the correction somewhat.

Not including the relativistic effects in the signal, but computing a joint covariance matrix and marginalizing over galaxy bias parameters, will hide the relativistic corrections in the error bars and in the marginalized biases. This is a sub-optimal procedure from a theoretical perspective, as galaxy clustering already occurs in Newtonian gravity, but the here discussed relativistic effects are a signal of General Relativity, and hence contribute to our physical understanding of the Universe. For future surveys with decreasing errors and higher redshifts, not hiding these effects in the error bars will also be important in order to reach the targeted percent accuracy on cosmological parameters. With increasing sky coverage and redshift, the relativistic effects can even dominate the cross-correlation on large angular scales.

Note also, that the claim that lensing be relevant only on very small scales is simply not correct. Its relative contribution to the the total number-count-tangential shear power spectrum is nearly constant from $\ell \sim 50$ to $\ell = 2000$ with a wide hump around $\ell \sim 700$. The increase of lensing at smaller scales is therefore similar to the one of density fluctuations.

The goal of this brief and simple study is not a detailed signal to noise analysis of the effect in the DES data. It is possible that in the highest redshift bin the density-tangential shear cross correlation in the first-year analysis of the DES data is systematically biased by a factor of more than 50% so that our correction would be smaller than the error. We also have not analysed how neglecting lensing in these cross-correlations propagates into the parameter estimation from DES. This would require a more detailed study taking into account also the number count spectra where lensing also is not considered in the present DES data analysis. Nevertheless, we think such a large effect has to be at least discussed and, as we show here, it is relatively easy to include it. A more detailed signal to noise analysis of the effect in the DES data is left for a future work, maybe in collaboration with DES.

Finally, we want to stress that including the $\kappa-\kappa$ term in the analysis is not only necessary but also very fruitful. This term is sensitive to the lensing potential and it contains additional information which we can use, e.g., to test modified gravity models, see [220].

APPENDIX

5.A Deriving the correlation function for number counts and tangential shear

In this appendix we derive the correlation between density number counts and the tangential shear and we make contact with the formulas usually found in the literature.

5.A.1 Full Sky

We consider the correlation between the galaxy number density in direction $\mathbf{n}$ at redshift z, $\Delta(\mathbf{n}, z)$ and the tangential shear at $(\mathbf{n}', z')$ perpendicular to $\mathbf{n}'$ in direction $\mathbf{e}$ which points from $\mathbf{n}'$ towards $\mathbf{n}$, see Fig. 5.5. The 2×2 shear tensor γ_{ab} is given

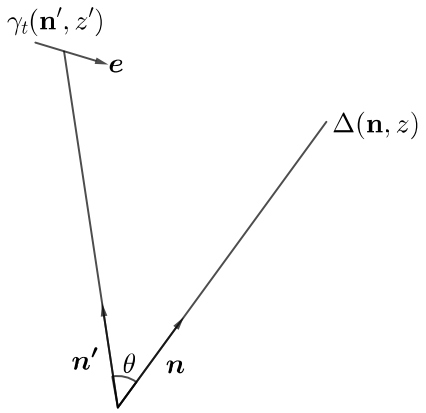

Figure 5.5: Notation for the correlation between the galaxy number density fluctuation $\Delta(\mathbf{n}, z)$ and the tangential shear $\gamma_t(\mathbf{n}', z')$ in direction $\mathbf{e}$.

in terms of the lensing potential ϕ by

$$\gamma_{ab}(\boldsymbol{n}', z') = -(\nabla_a \nabla_b - \frac{1}{2}\delta_{ab}\Delta_\Omega)\phi \tag{5.A11}$$

$$\gamma_t(\boldsymbol{n}', z') = \gamma_{ab}(\boldsymbol{n}', z') e^a e^b \,, \tag{5.A12}$$

where δ_{ab} is the 2×2 identity matrix, ∇_a is the covariant derivative on the sphere and $\mathbf{e}$ is the tangent vector on the sphere pointing from $\mathbf{n}'$ to $\mathbf{n}$. We expand the

fields Δ and ϕ in spherical harmonics,

$$\phi(\boldsymbol{n}', z') = \sum_{\ell,m} a^{\phi}_{\ell m}(z') Y_{\ell m}(\boldsymbol{n}') \tag{5.A13}$$

$$\Delta(\boldsymbol{n}, z) = \sum_{\ell,m} a^{\Delta}_{\ell m}(z) Y_{\ell m}(\boldsymbol{n})\,. \tag{5.A14}$$

Without loss of generality we may choose $\mathbf{n} = \mathbf{e}_z$ in $z-$direction and $\mathbf{e} = -\mathbf{e}_\vartheta$ in $-\vartheta$-direction. Using that $Y_{\ell m}(\mathbf{e}_z) = \delta_{m0}\sqrt{\frac{2\ell+1}{4\pi}}$ we then obtain

$$\begin{aligned}\langle \Delta(\boldsymbol{n}, z)\gamma_t(\boldsymbol{n}', z')\rangle &= -\sum_{\ell,m,\ell',m'} \langle a^{\Delta\,*}_{\ell m}(z) a^{\phi}_{\ell' m'}(z')\rangle Y^*_{\ell m}(\mathbf{e}_z)\left(\nabla_\vartheta\nabla_\vartheta - \frac{1}{2}\Delta_\Omega\right) Y_{\ell' m'}(\boldsymbol{n}') \\ &= -\sum_{\ell} C^{\Delta,\phi}_\ell(z, z')\sqrt{\frac{2\ell+1}{4\pi}}\left(\nabla_\vartheta\nabla_\vartheta - \frac{1}{2}\Delta_\Omega\right) Y_{\ell 0}(\boldsymbol{n}')\,. \end{aligned} \tag{5.A15}$$

Here we assumed that the fluctuations Δ and ϕ are statistically isotropic such that

$$\langle a^{\Delta\,*}_{\ell m}(z) a^{\phi}_{\ell' m'}(z')\rangle = C^{\Delta,\phi}_\ell(z, z')\delta_{\ell,\ell'}\delta_{m,m'}\,. \tag{5.A16}$$

Next we use the spin raising and spin lowering operators (see [96], Appendix 4 for details) to write the covariant derivative $\nabla_\vartheta = \frac{1}{2}(\,\eth + \eth^*)$ and $\Delta_\Omega = \frac{1}{2}(\,\eth\,\eth^* + \eth^*\,\eth)$ so that

$$\nabla_\vartheta\nabla_\vartheta - \frac{1}{2}\Delta_\Omega = \frac{1}{4}\left(\,\eth^2 + \,\eth^{*\,2}\right)$$

Now in terms of $\mu = \cos\vartheta'$ for a function (spin $s = 0$) which does not depend on φ we find (again, details are found in [96], Appendix 4)

$$\eth^2 f(\mu) \;=\; \eth^{*\,2} f(\mu) \;=\; (1-\mu^2) f''(\mu)\,.$$

Inserting this in $Y_{\ell 0}(\boldsymbol{n}') = \sqrt{\frac{2\ell+1}{4\pi}} P_\ell(\mu)$ we obtain

$$\begin{aligned}\frac{1}{4}\left(\,\eth^2 + \,\eth^{*\,2}\right) Y_{\ell 0}(\boldsymbol{n}') &= \frac{1}{2}\sqrt{\frac{2\ell+1}{4\pi}}(1-\mu^2) P''_\ell(\mu) \\ &= \frac{1}{2}\sqrt{\frac{2\ell+1}{4\pi}} P_{\ell\,2}(\mu)\,.\end{aligned}$$

Here $P_{\ell\,2}$ is the associated Legendre function of order 2 (see [5] and [96], Appendix 4 for details). Inserting this in (5.A16) we obtain

$$\langle \Delta(\boldsymbol{n}, z)\gamma_t(\boldsymbol{n}', z')\rangle = \frac{-1}{8\pi}\sum_\ell C^{\Delta,\phi}_\ell(z, z')(2\ell+1) P_{\ell\,2}(\cos\vartheta') \tag{5.A17}$$

$$= \frac{-1}{4\pi}\sum_\ell C^{\Delta,\kappa}_\ell(z, z')\frac{2\ell+1}{\ell(\ell+1)} P_{\ell\,2}(\boldsymbol{n}\cdot\boldsymbol{n}')\,, \tag{5.A18}$$

where we have used that $a^\kappa_{\ell m} = (\ell+1)\ell a^\phi_{\ell m}/2$. This result implies that the corresponding correlation spectrum is

$$C^{\Delta,\gamma_t}_\ell(z, z') = -C^{\Delta,\kappa}_\ell(z, z')\,. \tag{5.A19}$$

The angular dependence via $P_{\ell 2}(\boldsymbol{n}\cdot\boldsymbol{n}')$, is a consequence of the fact that we are correlating the 2-tensor γ_{ab} with a scalar quantity, hence the corresponding correlation function $\langle\Delta(\boldsymbol{n},z)\gamma_t(\boldsymbol{n}',z')\rangle$ transforms like a tensor under rotations around $\boldsymbol{n}'$.

This remains true for the correlation of an arbitrary scalar quantity A with the tangential shear which is therefore given by (5.A18) replacing $C_\ell^{\Delta,\kappa}(z,z')$ by $C_\ell^{A,\kappa}(z,z')$. Note also that the normalisation scales with ℓ as expected since

$$\int_{-1}^{1} P_{\ell\, s}(\mu)P_{\ell' s}(\mu)d\mu = \frac{2}{2\ell+1}\frac{(\ell+s)!}{(\ell-s)!}\delta_{\ell,\ell'}\,.$$

5.A.2 Flat sky

Usually the above equation is derived somewhat differently in the flat sky approximation. This is largely sufficient if one considers relatively small sky patches as e.g. the DES year-1 data with their ≈1300 square degrees. In flat sky $\boldsymbol{\ell}$ is a 2d vector, the Fourier transform variable of the sky position $\mathbf{x}$ which is dimensionless. The spherical harmonics are then replaced by $Y_{\ell m}\to\frac{1}{2\pi}\exp(i\boldsymbol{\ell}\cdot\mathbf{x})$, $\eth = -\partial_1 + i\partial_2$ and $\eth^* = -\partial_1 - i\partial_2$. One can obtain the flat sky result of the above equation directly by using the flat sky versions of $\eth$ and $\eth^*$. This yields

$$\frac{1}{2}(\eth^2 + \eth^{*\,2})Y_{\ell m} \;\to\; -\frac{\ell^2}{4\pi}\left(\cos^2\varphi - \sin^2\varphi\right)e^{i\boldsymbol{\ell}\cdot\mathbf{x}} = \frac{\ell^2}{2\pi}\left(\frac{1}{2}-\cos^2\varphi\right)e^{i\boldsymbol{\ell}\cdot\mathbf{x}} \quad (5.A20)$$

Statistical isotropy in the flat sky yields

$$\langle\Delta^*(\boldsymbol{\ell},z)\phi(\boldsymbol{\ell}',z')\rangle = \delta^2(\boldsymbol{\ell}-\mathbf{x}\ell')C_\ell^{\Delta,\phi}(z,z'),$$

and the convergence is given by $\kappa(\boldsymbol{\ell}) = \frac{\ell^2}{2}\phi(\boldsymbol{\ell})$. Note that correctly speaking we consider two flat skies, one at redshift z where the foreground galaxies lie and one at redshift z' where we measure the shear of the background galaxies.

Using $\cos\varphi = \boldsymbol{\ell}'\cdot\mathbf{e}/\ell'$, (5.A20) leads to

$$\gamma_t(\boldsymbol{x},z') = \frac{1}{2\pi}\int d^2\boldsymbol{\ell}'\left((\boldsymbol{\ell}'\cdot\mathbf{e})^2 - \frac{1}{2}\ell'^2\right)e^{-i\boldsymbol{\ell}'\cdot\boldsymbol{x}}\phi(\boldsymbol{\ell}',z'), \quad (5.A21)$$

so that we obtain for the correlation function

$$\langle\Delta(\mathbf{y},z)\gamma_t(\boldsymbol{x},z')\rangle \;=\; \frac{2}{(2\pi)^2}\int d^2\ell\left((\hat{\boldsymbol{\ell}}\cdot\mathbf{e})^2-\frac{1}{2}\right)e^{ir\boldsymbol{\ell}\cdot\mathbf{e}}C_\ell^{\Delta,\kappa}(z,z')\,. \quad (5.A22)$$

In the last line we set $\hat{\boldsymbol{\ell}} = \boldsymbol{\ell}/\ell$ and we have used statistical isotropy and $\kappa(\boldsymbol{\ell}) = \ell^2\phi(\boldsymbol{\ell})/2$. The angular integration gives

$$\int_0^{2\pi}\left(\cos^2\varphi-\frac{1}{2}\right)e^{ir\ell\cos(\varphi)}d\varphi = -\pi J_2(r\ell)\,, \quad (5.A23)$$

where J_2 is the Bessel function [5] of order 2. With this we find

$$\langle\Delta(\boldsymbol{x},z)\gamma_t(\boldsymbol{x}+\mathbf{r},z')\rangle = -\frac{1}{2\pi}\int_0^\infty \ell d\ell J_2(\ell r)C_\ell^{\Delta,\kappa}(z,z')\,. \quad (5.A24)$$

To make contact with the formulas found in the literature, e.g. in [1], we consider a distribution $n_f(z)$ of foreground galaxies and a distribution $n_b(z')$ of background shear measurements. Integrating over these distributions and using that a foreground galaxy at z only shears a background one at z' for $z < z'$, we obtain

$$\langle \Delta^{(f)}(\boldsymbol{x}) \gamma_t^{(b)}(\boldsymbol{x}+\mathbf{r}) \rangle = \frac{-1}{2\pi} \int_0^\infty dz n_f(z) \int_z^\infty dz' n_b(z') \int_0^\infty \ell d\ell J_2(\ell r) C_\ell^{\Delta,\kappa}(z,z') \,. \tag{5.A25}$$

The difference of this expression from the one usually used in the literature is that there the approximation $C_\ell^{\Delta,\kappa}(z,z') \sim C_\ell^{\delta,\kappa}(z,z')$ is used, i.e. it is assumed the number density of foreground objects is (modulo a bias factor) given by the underlying density δ. One can then express the shear power spectrum as an integral over the gravitational potential which is related to the density by the Poisson equation. Using the Limber approximation one can write the result as an integral over the dimensionless power spectrum in k-space. This leads after some standard manipulations to

$$\begin{aligned} \langle \delta\gamma_t \rangle(\theta) = \frac{3\Omega_m H_0^2}{2} \int_0^\infty \frac{\ell d\ell}{2\pi} J_2(\ell\theta) \int_0^\infty dz n_f(z) \\ \int_z^\infty dz' n_b(z') \frac{r(z)(r(z')-r(z))}{r(z')H(z)} P\left(\frac{\ell+1/2}{r(z)}, z\right) \,. \end{aligned} \tag{5.A26}$$

This is the expression found, e.g., in [1] where for $n_f(z)$ and $n_b(z')$ we have to consider the distribution of foreground respectively background galaxies in the different redshift bins. Here, P is the (dimensionless) Fourier space density fluctuations spectrum, and in our numerical applications we have used Halofit [280] to model its non-linearities.

6

The observable E_g statistics

Based on:
[113] B. Ghosh, & R. Durrer, *The observable E_g statistics*, **JCAP 1906** (2019) 010, [arXiv: 1812.09546]

We have already touched upon the topic of alternate theories of gravity in Section 1.3 and Chapter 2, and now we are going to discuss a simple test of gravity at cosmological scales, known as E_g statistics. To be more accurate, E_g is actually a test of ΛCDM and the regimes in which it fails to work. This observable, despite having the limitation of being valid only within linear perturbation theory, has the advantage of providing a bias independent insight in case measurements are made using the same galaxy population. It is based upon the fact that the well-known equality of the Bardeen potentials in the general relativistic regime where anisotropic stress is zero, in general breaks down when a modification of the theory of gravity is considered. In such cases, one can measure the velocity field at a given redshift, extract the matter overdensity from there, and then extract the lensing signal at this redshift by cross-correlating these galaxies and the background lensing maps. The ratio between the lensing-galaxy cross-correlation and the galaxy-galaxy cross-correlation acts as a direct probe of the deviation from ΛCDM cosmology. Similar to Chapter 5, we want to include lensing corrections in E_g measurements as well. The importance of this has already been established in [222], but it was also demonstrated that trying to include lensing corrections compromises the most positive feature of E_g statistics, that is the bias independence. A solution that is applicable for intensity mapping surveys was proposed. However, we understand that it is of absolute importance to take the lensing corrections into account so that we can construct an "observable" E_g measurement. This is what we attempt to do in this work using CMB lensing, and we find that the relative error in the E_g values is only around 4% for the highest foreground redshift of DES (for zero magnification bias), whereas it goes up to 40% if we look at redshift of $z = 2$ for Euclid (considering realistic magnification biases), indicative of the fact that lensing corrections are relevant for E_g measurements as well.

Abstract: Recently Dizgah & Durrer have shown that the E_g statistics, useful to test theories of modified gravity, is plagued by additional scale and bias dependent lensing contributions. In this work we develop and illustrate a method to remove these lensing terms by using in addition to the galaxy clustering data also shear data and the correlations of shear and galaxy clustering. We introduce a truly observable statistics termed $\tilde{E}_g$ which conserves the properties of scale and bias independence on linear scales. The method discussed here is best adapted to photometric surveys. It is found that the corrections to the original E_g statistics are small for the present DES data, but for future surveys of the quality of Euclid they are very substantial.

6.1 Introduction

Over the past few decades, our understanding of the observable Universe has undergone a rapid development, and especially observations of the cosmic microwave background (CMB) have led to a cosmological standard model, ΛCDM, with parameters which are determined at a few percent precision or better. Lately, the inclusion of observations from the cosmological large scale structure (LSS), especially the baryon acoustic oscillations, has become more and more relevant. The observed accelerated expansion of the Universe is compatible with General Relativity (GR) only when including a cosmological constant Λ. Such a constant cannot be distinguished by any experiment from the effect of quantum vacuum energy, but its value, corresponding to an energy scale of about 10^{-3}eV, is very discrepant with all expectations from particle physics. This unsatisfactory situation has motivated the development of modified theories of gravity, which challenge GR on very large scales, allowing for accelerated expansion without a cosmological constant. Thus, even though GR and modified gravity provide similar expansion laws at the background level, they usually exhibit differences when the evolution of perturbations are taken into account. This is something that can be effectively probed with current and upcoming cosmological LSS surveys.

A recently proposed observable which aims to distinguish between ΛCDM and modified gravity theories by providing a test for gravity at large scales, is the so-called E_g statistics introduced by Zhang et al. in 2007 [313]. The E_g statistics is defined as the ratio of galaxy-lensing cross-correlations to the galaxy-velocity cross-correlation, and is expected to provide a bias independent insight if both measurements are made using the same galaxy population. There have been different measurements of E_g using different data sets since then [254, 38, 243]. In this paper, we will follow the approach used by Pullen et al. [243], where instead of the galaxy-lensing cross correlations, the CMB lensing cross correlations are used. The reason for this is that CMB lensing is very accurate and enables surveys to probe at earlier times and even larger scales compared to galaxy surveys. Also, it is not plagued by the systematics of shear measurements such as intrinsic alignment.

A previous study [222] has shown, however, that neglecting the lensing contribution to galaxy number counts at high redshifts can give rise to large errors (up to 25-40 % for $z = 1.5$), and is hence indispensable for correct number count measurements. However, if the definition of E_g includes these corrections, the scale and bias

independence of the E_g statistics is compromised, which refutes its original purpose. As a result, one needs to develop a method which will enable the desired use of this quantity without posing a threat to its special, positive features.

In this paper, we explore how lensing corrections can be incorporated in standard E_g measurements. However, while [222] suggest to use 21 cm intensity mapping which is not affected by lensing and which has been explored in [242], we propose a different method which can be implemented in galaxy number count surveys. Although intensity mapping measurements have a promising future with surveys like the Square Kilometer Array (SKA) [203] , we should also be able to carry out studies regarding E_g statistics with the ongoing galaxy surveys.

A correction similar to the one proposed in the present work has also been suggested in Ref. [305]. In this paper, however the lensing contribution was estimated by rescaling the CMB lensing term. Here we propose to use in addition to the number counts also shear data which directly measure the lensing power spectrum and the galaxy–lensing cross correlation spectrum at the redshift of the galaxy survey. This avoids the uncertain, and most probably bias dependent scaling proposed in [305], but requests more observational data. For our method to work we need therefore both, number count and shear power spectra at a given redshift z as well as the number count–CMB lensing correlation spectrum and the CMB lensing power spectrum.

According to [243], E_g in case of CMB lensing can be estimated as,

$$E_g(\ell, z) = \Gamma(z) \frac{C_\ell^{\kappa g}(z_*, z)}{\beta C_\ell^{gg}(z, z)} \tag{6.1}$$

where z_* denotes the CMB redshift and z is the redshift of the galaxy survey. $\Gamma(z)$ is a pre-factor depending on Hubble parameter $H(z)$, the lensing kernel $W(z_*, z)$, and the galaxy redshift distribution denoted by $f_g(z)$. The pre-factor $\Gamma(z)$ is not very relevant for this work as we simply wish to provide a method of measuring E_g without going into the technicalities, and hence we do not discuss it in detail here. More about this pre-factor can be found in literature [243, 305]. $C_\ell^{\kappa g}$ is the lensing convergence–galaxy angular cross-power spectrum, C_ℓ^{gg} is the galaxy angular auto-power spectrum, and β is the redshift space distortion parameter. Within linear perturbation theory, $\beta = f/b_g$, where f is the linear growth rate and b_g is the galaxy bias.

The remainder of this paper is structured as follows: In Section 6.2 we briefly outline the theory leading to E_g, and explain how lensing corrections can be effectively incorporated in our measurements. In Section 6.3 we present numerical results for CMB lensing of foreground galaxies with redshift bins corresponding to the Dark Energy Survey (DES) Year 1 results [1] and for some redshifts of the Euclid collaboration [19]. Our numerical results are obtained from linear perturbation theory and are therefore only valid on sufficiently large scales. In Section 6.4 we discuss our findings and conclude.

6.2 Theory

As mentioned above, E_g statistics is aimed at distinguishing between GR and modified gravity theories. The fundamental parameters that come to mind when we wish to make this distinction are the gravitational Bardeen potentials Φ and Ψ which appear in the perturbed Friedman-Robertson-Walker metric in longitudinal gauge,

$$ds^2 = a^2(t)[-(1+2\Psi)dt^2 + (1-2\Phi)\delta_{ij}x^i dx^j]\,. \tag{6.2}$$

In the case of GR, $\Phi = \Psi$ in the absence of anisotropic stress. However, for modified theories of gravity, a valid way to check the relation between these two potentials is to measure the ratio between the lensing effect that is proportional to the quantity $\nabla^2(\Phi+\Psi)$ and the peculiar velocity field of non-relativistic particles that is related to the time component of the metric, Ψ. Following Zhang [313], we define in Fourier space,

$$E_g(z,k) = \frac{k^2(\Phi+\Psi)}{3H_0^2(1+z)\theta(k)}\,, \tag{6.3}$$

where $\theta = \nabla\cdot\mathbf{v}/H(z)$, $\mathbf{v}$ being the peculiar velocity field and $H(z)$ the Hubble parameter at a redshift z. The quantity $\theta(k)$ in ΛCDM cosmology becomes $\theta(k) = f(z)\delta_m(k,z)$, where $f(z) \simeq [\Omega_m(z)]^{0.55}$ within GR. $\Omega_m(z)$ denotes the matter density parameter at redshift z. According to Poisson's equation,

$$k^2\Phi = \frac{3}{2}H_0^2\Omega_{m,0}(1+z)\delta_m\,, \tag{6.4}$$

where $\Omega_{m,0} = \Omega_m(0)$. Thus, within GR, E_g reduces to $E_g(z,k) = \Omega_{m,0}/f(z)$, simplifying eq.(6.3) with the help of eq.(6.4) and the relation $\Phi = \Psi$. In particular, E_g depends neither on scale nor on galaxy bias.

This reduced version of E_g can be given a more general form in order to cater to modified gravity by incorporating two arbitrary functions $\mu(k,z)$ and $\gamma(k,z)$ such that

$$k^2\Phi = 4\pi G a^2\bar{\rho}\mu(k,z)\delta_m(k,z), \quad \Psi = \gamma(k,z)\Phi\,. \tag{6.5}$$

In a theory where the modification of gravity can be cast in this way, we have,

$$E_g(k,z) = \frac{\Omega_{m,0}\mu(k,z)[\gamma(k,z)+1]}{2f} \tag{6.6}$$

which reduces to the GR form for $\mu(k,z) = \gamma(k,z) = 1$. For a generic modified theory of gravity, however, we expect this quantity to depend on scale in a non-trivial way.

Having discussed the basic idea behind the E_g statistics approach, it is important to understand why lensing corrections are inevitable as well as a threat to the very foundation of E_g statistics, and how we can deal with them. In Section 6.3, we show some numerical examples to support our claim, but in this section, we wish to assert its importance theoretically.

For our current interests, we will be focussing only on the over-density and lensing term (for the full expression, see [46]). We can neglect the redshift space distortion for wide redshift bins having $\Delta z \gtrsim 0.1$, and we may also ignore large-scale effects involving the Bardeen potentials for subhorizon scales ($\ell > 20$). Thus we can approximate the galaxy fluctuations in direction $\mathbf{n}$ and at redshift z by:

$$\begin{aligned}\Delta^g(\mathbf{n}, z) &= b(z)\delta_m(\chi(z)\mathbf{n}, z) + \left(1 - \frac{5}{2}s(z)\right)\int_0^{\chi(z)} d\chi \frac{\chi(z)-\chi}{\chi(z)\chi}\nabla^2_\Omega(\Phi+\Psi)(\chi\mathbf{n}, t_0-\chi) \\ &= b\delta_m - 2\left(1-\frac{5}{2}s\right)\kappa \end{aligned} \tag{6.7}$$

where $\chi(z)$ is the comoving distance to redshift z, $b(z)$ is the galaxy bias and $s(z)$ is the magnification bias. δ_m is the matter over-density and κ is the convergence.

The magnification bias is the logarithmic derivative of the galaxy number count at the limiting magnitude,

$$s(z, m_{\rm lim}) \equiv \left.\frac{\partial \log_{10}\bar{N}(z, L > L_{\rm lim})}{\partial m}\right|_{m_{\rm lim}} . \tag{6.8}$$

Here $m_{\rm lim} = 5\log L_{\rm lim}$+const. is the limiting magnitude of the survey. The magnification bias accounts for the fact that highly magnified galaxies, even if they are intrinsically not luminous enough can get included in the survey. Only if the survey is sensitive enough to include all galaxies (of a given type) down to the lowest luminosities, we have $s = 0$.

Since we truly observe Δ^g and not δ_m, if we have to take along the additional lensing term, κ , with the overdensity δ when correlating number counts with lensing data. For any two redshifts z_1 and z_2 we then find

$$C_\ell^{\kappa g}(z_1, z_2) = b(z_2)C_\ell^{\kappa\delta}(z_1, z_2) - (2 - 5s(z_2))C_\ell^{\kappa\kappa}(z_1, z_2) \tag{6.9}$$

and correspondingly, the auto-correlation of number counts gives

$$\begin{aligned} C_\ell^{gg}(z_1, z_2) &= b(z_1)b(z_2)C_\ell^{\delta\delta}(z_1, z_2) + (2-5s(z_1))(2-5s(z_2))C_\ell^{\kappa\kappa}(z_1, z_2) \\ &\quad -b(z_2)(2-5s(z_1))C_\ell^{\kappa\delta}(z_1, z_2) - b(z_1)(2-5s(z_2))C_\ell^{\kappa\delta}(z_2, z_1) \end{aligned} \tag{6.10}$$

Now, in case of CMB lensing, the scale independent and bias independent quantity actually is not the one given in eq.(6.1) but

$$\tilde{E}_g(\ell, z) = \Gamma(z)\frac{C_\ell^{\kappa\delta}(z_*, z)}{\beta(z)C_\ell^{\delta\delta}(z, z)} , \tag{6.11}$$

while what we naively measure is

$$E_g(\ell, z) = \Gamma(z)\frac{C_\ell^{\kappa g}(z_*, z)}{\beta(z)C_\ell^{gg}(z, z)} . \tag{6.12}$$

Here, E_g is the statistics that galaxy surveys actually measure, while $\tilde{E}_g$ is the one excluding lensing corrections. Inserting (6.9) and (6.10) above we have

$$E_g \propto \frac{C_\ell^{\kappa g}(z_*,z)}{\beta(z)C_\ell^{gg}(z,z)} = \frac{1}{\beta(z)}\frac{bC_\ell^{\kappa\delta}(z_*,z)-(2-5s)C_\ell^{\kappa\kappa}(z_*,z)}{b^2C_\ell^{\delta\delta}(z,z)+(2-5s)^2C_\ell^{\kappa\kappa}(z,z)-2b(2-5s)C_\ell^{\kappa\delta}(z,z)}\,, \tag{6.13}$$

where b and s are to be evaluated at redshift z at all instances. It is clear from eq. (6.13) that a straightforward way to remove the difference between the scale independent quantity $\tilde{E}_g$ and the measured quantity E_g would be to have a galaxy population with $(2-5s)=0$, i.e., $s=2/5$ which corresponds to intensity mapping. This is the idea suggested in [222, 242], but here we want to explore a different method that can be implemented in galaxy surveys, without depending on upcoming intensity mapping surveys. The idea is to obtain the E_g statistics for the density power spectra in terms of the galaxy number counts, the lensing power spectrum (obtained by shear measurements) and their correlation, that is, in terms of the observable spectra, namely, $C_\ell^{\kappa g}(z_1,z_2)$, $C_\ell^{gg}(z_1,z_2)$ and $C_\ell^{\kappa\kappa}(z_1,z_2)$ which appear in eq. (6.9) and eq. (6.10).

Using (6.9) we first find

$$b(z)C_\ell^{\kappa\delta}(z_*,z) = C_\ell^{\kappa g}(z_*,z)+(2-5s(z))C_\ell^{\kappa\kappa}(z_*,z)\,. \tag{6.14}$$

From (6.10) we obtain

$$\begin{aligned} b^2(z)C_\ell^{\delta\delta}(z,z) &= C_\ell^{gg}(z,z)-(2-5s(z))^2C_\ell^{\kappa\kappa}(z,z)+2b(z)(2-5s(z))C_\ell^{\kappa\delta}(z,z)\,, \\ &= C_\ell^{gg}(z,z)+(2-5s(z))^2C_\ell^{\kappa\kappa}(z,z)+2b(z)(2-5s(z))C_\ell^{\kappa g}(z,z)\,. \end{aligned} \tag{6.15}$$

Inserting this in eq. (6.11) we obtain

$$\tilde{E}_g(\ell,z) = \Gamma(z)\frac{bC_\ell^{\kappa\delta}(z_*,z)}{\beta(z)b^2C_\ell^{\delta\delta}(z,z)} = \frac{1}{\beta(z)}\frac{C_\ell^{\kappa g}(z_*,z)+(2-5s)C_\ell^{\kappa\kappa}(z_*,z)}{C_\ell^{gg}(z,z)+(2-5s)^2C_\ell^{\kappa\kappa}(z,z)+2(2-5s)C_\ell^{\kappa g}(z,z)}\,, \tag{6.16}$$

where b and s are to be evaluated at redshift z. In the next section we want to study in which cases the difference between $\tilde{E}_g$ and E_g is relevant. For this we introduce the relative difference defined as,

$$\frac{\Delta E_g}{\tilde{E}_g} = \frac{\tilde{E}_g - E_g}{\tilde{E}_g}\,. \tag{6.17}$$

6.3 Numerical Results

In order to illustrate our method proposed in Section 6.2, we show some examples using the specifications from the Dark Energy Survey (DES) Year 1 and for a Euclid-like survey [190, 19]. For the numerical calculation we use the public code CLASS [194, 41] in which relativistic contributions to galaxy number counts

are included [88]. We assume purely scalar perturbations, and consider the cosmological parameters of the Planck 2015 results [12]. Thus in our evaluations, the Hubble parameter is $H_0 = 67.556$ km s^{-1} Mpc^{-1} $= 100h$ km s^{-1} Mpc^{-1}, the baryon density parameter is $\Omega_b h^2 = 0.022032$, the cold dark matter density parameter is $\Omega_{\rm cdm} h^2 = 0.12038$, the curvature is $K = 0$, the number of neutrino species is $N_\nu = 3.046$ and the neutrino masses are neglected.

6.3.1 E_g statistics for DES-like redshift binning

From the specifications of the first year results of the DES collaboration [1, 290, 92, 144, 101] which has measured all - the galaxy number counts, lensing and the cross-correlation of galaxy clustering and lensing, we consider five galaxy redshift bins in the foreground having a width $\Delta z = 0.15$. The mean redshifts of these bins are,

$$z_1 = 0.225 \quad z_2 = 0.375 \quad z_3 = 0.525 \quad z_4 = 0.675 \quad z_4 = 0.825\,. \tag{6.18}$$

In this section, we numerically compute the required angular power spectra for the purpose of E_g measurement, in case of CMB lensing for the above mentioned DES foreground redshifts. For our purpose, we assume a complete survey setting[1]

In fig. 6.1 we show the behaviour of $\tilde{E}_g(\ell, z)$ against ℓ for different values of DES foreground redshifts, which have been obtained from the observable angular power spectra using eq. (6.16). $\tilde{E}_g$ is clearly scale independent for $\ell \gtrsim 100$. We also find that the uncorrected E_g has an error of about 4% compared to the corrected one $\tilde{E}_g$ for the highest foreground redshift of DES. This error is much smaller than the ratio $C_\ell^{\kappa\kappa}/C_\ell^{\delta\kappa}$ which can become as large as 0.3, see Ref. [115]. We suggest that the additional terms in the numerator and the denominator partially cancel in the correction. As we shall see in Section 6.3.2, for much higher redshifts like that of Euclid, this error will increase by about a factor of ten.

[1]The DES collaboration has not published any value for $s(z)$, the true value is most probably different from zero and depends on z. However it is not available to us as the DES collaboration has neglected convergence in its analysis.

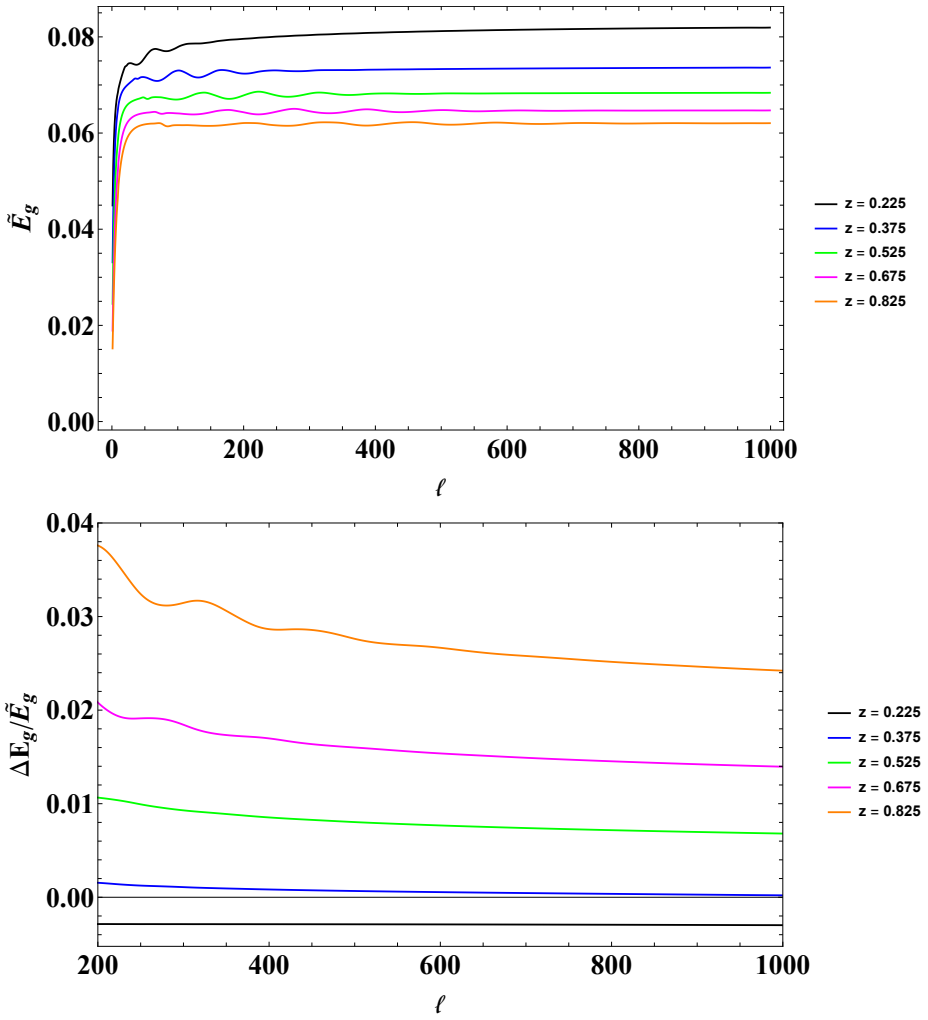

Figure 6.1: The upper panel shows E_g as a function of ℓ for different values of z corresponding to foreground bins of DES Year 1 results. The lower panel shows the correction on E_g value due to lensing effects for each redshift bin.

6.3.2 E_g statistics for Euclid-like redshift binning

Now we repeat the same analysis as in Section 6.3.1 for few redshifts probed by the Euclid satellite [19]. According to Euclid photometric specifications, the galaxy bias and magnification bias are given as a function of the redshift as[2],

$$b(z) = b_0\sqrt{1+z} \tag{6.19}$$

$$s(z) = s_0 + s_1 z + s_2 z^2 + s_3 z^3 \tag{6.20}$$

Here we set $b_0 = 1$ and the magnification bias coefficients are $s_0 = 0.1194$, $s_1 = 0.2122$, $s_2 = -0.0671$ and $s_3 = 0.1031$. The window function is taken to be Gaussian

[2]In Ref. [305] Euclid is also considered with a similar galaxy bias, but the luminosity bias is set to the constant values $s = 0.48$ for the spectroscopic survey and $s = 0.326$ for the photometric survey. These values are close to the point $s = 0.4$ where the correction vanishes, artificially reducing the lensing correction.

with a standard deviation of $\Delta z_i/2$, where $\Delta z_i \gtrsim 2\delta_z$ is the width of the i-th bin, δ_z being the photometric redshift error given by $\delta_z = 0.05(1+z)$. For more details about Euclid specifications, we also refer to Appendices A.1 and B of [221].

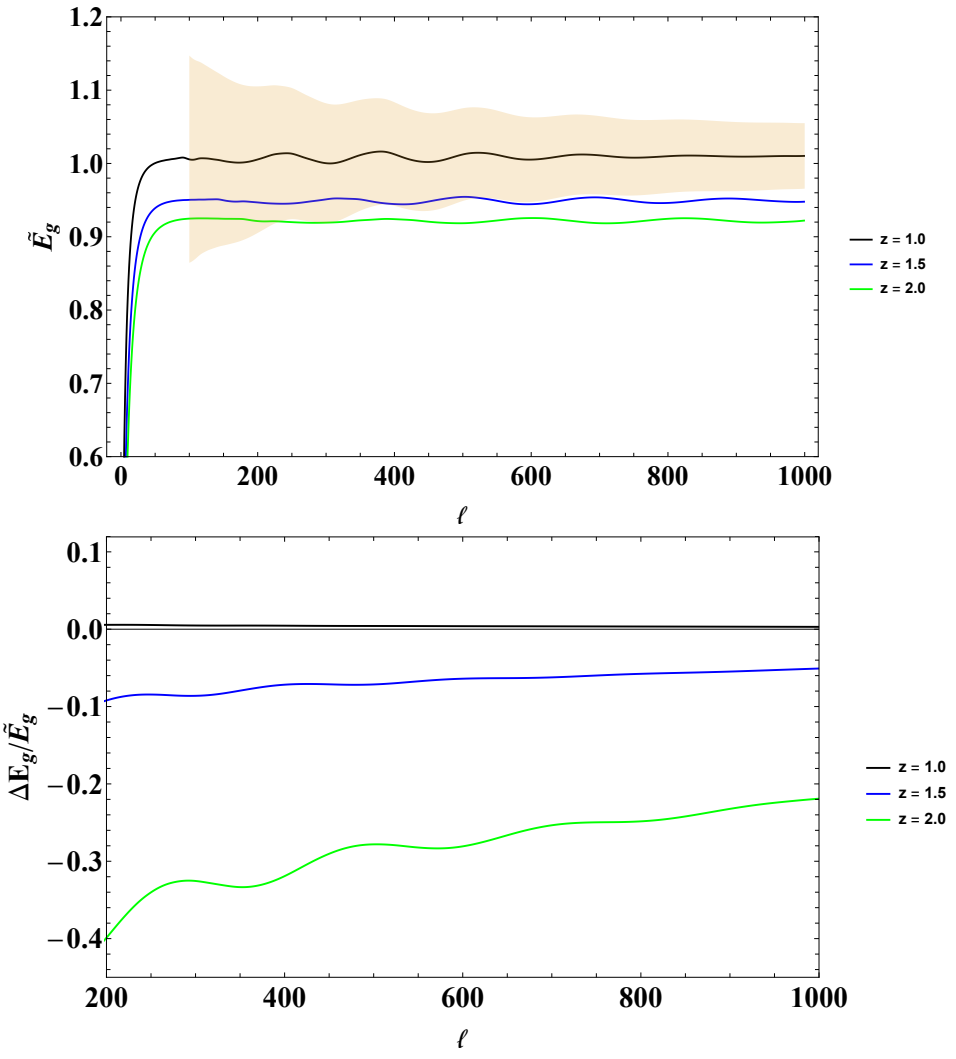

Figure 6.2: Same as Fig. 6.1 but for the case of Euclid. At $z = 1$ we have $s(z) = 0.37$ which renders the correction terms very small, while at $z = 2$ we find $s(z) = 1.1$. The shaded area represents the cosmic variance error as a function of ℓ for $\ell > 100$.

As seen in fig. 6.2, now the uncorrected E_g has an error of about 40% compared to the corrected E_g for the highest redshift of Euclid, that is, $z = 2$. The error is significantly scale dependent which comes from the fact that the uncorrected signal is scale dependent. As one can see from the top panel, the corrected statistics, $\tilde{E}_g(\ell, z)$ is again scale independent for $\ell \gtrsim 50$.

As for the absolute value of the result we have found that our normalization $\Gamma(z)$ has to be multiplied by an overall factor which amounts to 6 for DES and 0.35 for

Euclid. The ratio,

$$\frac{E_g(\ell, z_2)}{E_g(\ell, z_1)} = \left(\frac{\Omega_m(z_1)}{\Omega_m(z_2)}\right)^{0.55} \tag{6.21}$$

which we expect in a ΛCDM cosmology is very well realized in our findings (fig. 6.3).

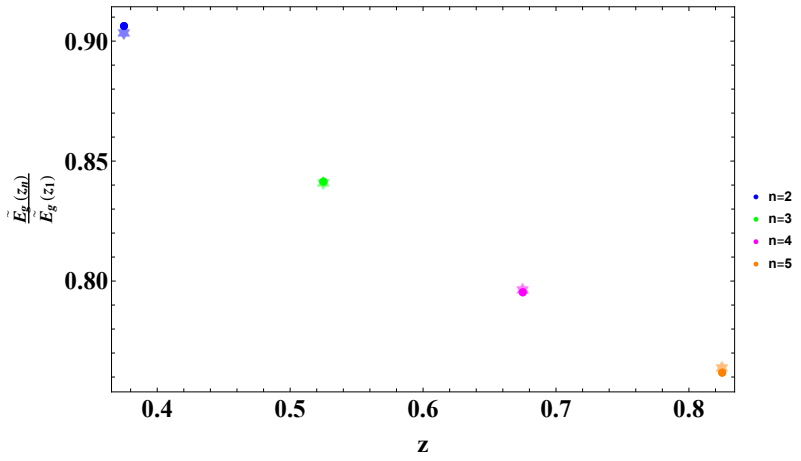

Figure 6.3: The ratio as defined in eq.(6.21), here shown for the DES redshift bins. The circular dots represent the theoretically expected values as in the right hand side of eq. (6.21), and the stars represent our numerical results.

6.4 Discussion and Conclusion

With upcoming surveys aiming for high redshift probes and increasing precision, the utility of the E_g statistics in measuring deviations from general relativity is very promising. It is however important to include lensing and magnification bias effects in these measurements to reach the best possible accuracy. In this paper we have shown how this can be achieved in a photometric survey where we dispose of galaxy number counts, shear measurements and their correlation so that all three observable spectra C_ℓ^{gg}, $C_\ell^{\kappa g}$ and $C_\ell^{\kappa\kappa}$ are available. Our method constructs the corrected E_g statistics termed $\tilde{E}_g(\ell, z)$ from these observables. This quantity is independent of scale (for sufficiently large ℓ) and bias (in the linear regime). We have found that the lensing contributions are small for low redshift surveys like DES (up to $\sim 4\%$), but they are very significant in case of higher redshift surveys like Euclid (up to $\sim 40\%$). Our work is based purely on theoretical calculations using linear perturbation theory and has to be taken with a grain of salt. From the DES survey we simply assume the same foreground redshifts and galaxy bias and galaxy distribution in redshift, while for Euclid we use the galaxy distribution in redshift as well as the galaxy and magnification biases. Nevertheless, it is safe to assume that Euclid will be able to measure the needed C_ℓ's with cosmic variance limited accuracy out to $\ell \sim 1000$. For $z = 2$ this corresponds to a linear scale of about $14h^{-1}$Mpc which is still well in the linear regime at $z = 2$. The relative error from cosmic variance [96] of a C_ℓ observable is $\sqrt{2/(2\ell+1)}$ so that $\tilde{E}_g$ which is a ratio of C_ℓ's is expected to have a

cosmic variance error of

$$\frac{\delta^{cv}\tilde{E}_g(\ell)}{\tilde{E}_g(\ell)} = \frac{2}{\sqrt{2\ell+1}} \simeq \sqrt{\frac{2}{\ell}}\,, \tag{6.22}$$

which amounts to 14% for $\ell = 100$ and 4.5% for $\ell = 1000$. This is the cosmic variance indicated as shaded region in fig. 6.2. When summing all available multipoles ℓ (assumed to be independent) from some value $\ell_{\rm min}$ to $\ell_{\rm max}$, the cosmic variance error can be further reduced to

$$\frac{\delta^{cv}\tilde{E}_g}{\tilde{E}_g} \simeq \frac{\sqrt{2\log\left(\ell_{\rm max}/\ell_{\rm min}\right)}}{\ell_{\rm max}-\ell_{\rm min}}\,, \tag{6.23}$$

which is about 0.003, significantly less than 1%, for the values $\ell_{\rm max} = 1000$ and $\ell_{\rm min} = 100$ (see fig. 6.4 below).

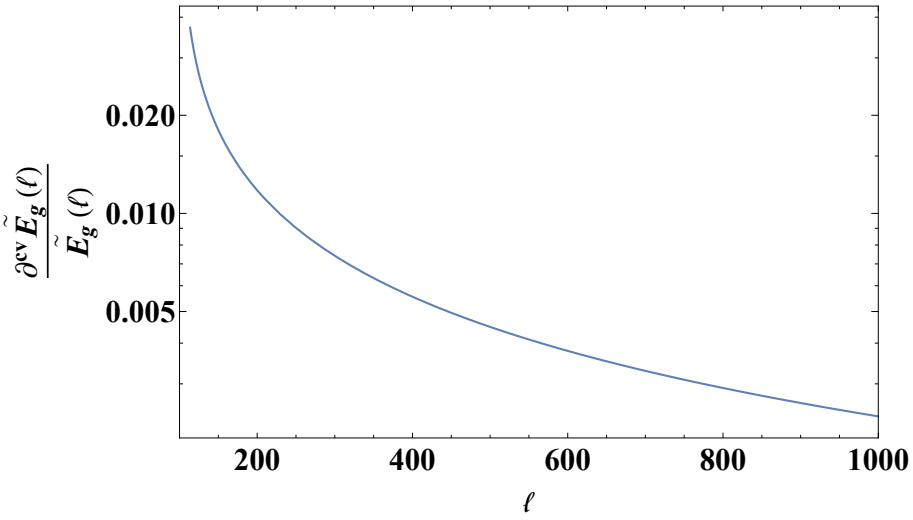

Figure 6.4: The cumulative cosmic variance error as a function of ℓ as given in eq.(6.23).

This shows that the corrections discussed in this work, even if probably not yet relevant for the present DES data, certainly have to be taken into account to optimize our analysis of future data of the quality of Euclid. The strength of the E_g statistics is its scale invariance which allows a simple combination of the result from different scales. In addition, its bias independence renders it independent of the galaxies considered as long as their bias is linear, even if it is not scale independent. However, at second order we in general expect non-linear bias which will affect the E_g statistics which renders it less attractive at small, non-linear scales.

7

Intrinsic and extrinsic shape and size correlations of galaxies in weak lensing data

Based on:
[114] B. Ghosh, R. Durrer and B.M. Schäfer, *Intrinsic and extrinsic shape and size correlations of galaxies in weak lensing data*, [arXiv: 2005.04604]

After we have had a look at weak gravitational lensing and agreed upon the importance of lensing corrections in galaxy survey observations, we need to go one step further and acknowledge the presence of effects that manifest in addition to lensing. One such important effect is the astrophysical contribution of intrinsic alignments, which is the subject of this work. This kind of effects arise due to the fact that nearby galaxies are subjected to a local tidal gravitational field that influences the process of their formation, and also their shapes and sizes. This tidal shear is basically expressed as the second derivative of the gravitational potential Φ. The shape and size correlation of galaxies can be studied in the light of both weak lensing and the tidal interaction which can be described via a linear alignment model for elliptical galaxies. Interestingly, these two effects are analogous as far as the reaction of the galaxy is concerned. While a galaxy changes its physical appearance in response to intrinsic alignment, there is a deformation in the shape of its light bundle as a result of lensing. Mathematically speaking, in case of intrinsic alignments, the quantity giving rise to the deformation is proportional to the inverse of the velocity dispersion $1/\sigma^2$, while for lensing, the gravitational potential is expressed in units of c^2. In this work, we attempt to parametrise how elliptical galaxies react to such external tidal gravitational fields and use a Fisher forecast to predict the intrinsic as well as extrinsic correlations of their shape and size with weak lensing. For this we first study the tidal interaction of galaxies using the Jeans equation for stationary and static systems and then go on to compute the angular spectra for shapes and sized from the source terms that are expressed in terms of Φ. This eventually helps us quantify the information content of shape and size correlations using a Fisher-matrix formalism, where we find that the size measurements have larger Poissonian errors than the shape measurements, and combining shape and size is not expected to improve the results significantly.

Abstract: The subject of this paper are shape and size correlations of galaxies due to weak gravitational lensing and due to direct tidal interaction of elliptical galaxies with gravitational fields sourced by the cosmic large-scale structure. Setting up a linear intrinsic alignment model for elliptical galaxies which parameterises the reaction of the galaxy to an external tidal shear field through the velocity dispersion, we predict intrinsic correlations and cross-correlations with weak lensing for both shapes and sizes, juxtaposing both types of spectra with lensing. We quantify the observability of the intrinsic shape and size correlations and estimate with the Fisher-formalism how well the alignment parameter can be determined from the Euclid weak lensing survey. Specifically, we find a contamination of the weak lensing convergence spectra with an intrinsic size correlation amounting to up to 10% over a wide multipole range $\ell = 100 \ldots 300$, with a corresponding cross-correlation exhibiting a sign change, similar to the cross-correlation between weak lensing shear and intrinsic shapes. A determination of the alignment parameter yields a precision of a few percent forecasted for Euclid, and we show that all shape and many size correlations should be measurable with Euclid.

7.1 Introduction

Weak lensing has emerged as a powerful probe for investigating the cosmic large-scale structure [215, 26, 18, 25, 181], for testing gravitational theories and for constraining cosmological parameters. As gravitational lensing probes fluctuations in the gravitational potential directly [176, 147, 146, 145, 33, 133, 132, 224, 124], it depends on minimal assumptions and is fixed for a given gravitational theory. Correlations in the shapes of galaxies induced by weak lensing [31, 32] have been detected almost two decades ago, and by now lensing is recognised as a tool for investigating cosmological theories alongside the cosmic microwave background and galaxy clustering [296, 153, 154, 223]. The last generation of surveys, most notably KiDS and DES [1] have provided independent confirmation for the ΛCDM-model and support parameter determinations from the CMB, even though tensions between the two probes, most notably in the matter density Ω_m and σ_8 remain [205, 91]. The next generation of surveys, in particular Euclid [19] and LSST will probe cosmological models to almost fundamental limits of cosmic variance, but with decreasing statistical errors the control of systematical errors will become one of the central questions for data analysis, along with higher-order effects in the lensing signal related to evaluating the tidal shear fields along a geodesic, effects of lensing on galaxy number counts [115, 289] in galaxy-galaxy lensing correlation, as well as non-Gaussian statistics of the lensing signal due to nonlinear structure formation and non-Gaussian contributions to the covariance [160, 177, 178, 225].

Among astrophysical contaminants of the weak lensing signal, intrinsic alignments [166, 206, 138, 17, 185, 209, 187] are perhaps the most dramatic, leading to significant biases in the estimation of cosmological parameters, surpassing most likely baryonic corrections [301, 267]. There are two primary models for the two dominant galaxy types for linking the apparent shapes to tidal gravitational fields in the large-scale structure [93], which acts, due to long-ranged correlations, as the medium to

reduce randomness and to correlate the measured ellipticities. The shapes of spiral galaxies are thought to be determined by the orientation of the angular momentum of the stellar disc [65, 80, 23], and ultimately of the dark matter halo harbouring the stellar component. With this idea in mind, shape correlations are traced back to angular momentum correlations, which in turn would depend through tidal torquing as the angular momentum generated mechanism on the tidal shear fields. Tidal torquing models commonly predict ellipticity correlations on small scales at a level of at most 10% of the weak lensing signal on multipoles above $\ell \simeq 300$ for a survey like Euclid, many physical assumptions have been challenged, most notably the orientation of the disc relative to the host halo angular momentum, as well as an over-prediction of the correlation inherent to the torquing mechanism.

Elliptical galaxies, on the other hand, are thought to acquire shape correlations through direct interaction with the tidal shear field [264, 43, 217, 42, 293]: Second derivatives of the gravitational potential would give rise to an anisotropic deformation of the galaxy, in the principal directions of the tidal shear tensor. Interestingly, the reaction of a galaxy to the tidal shear field is determined by the inverse velocity dispersion $1/\sigma^2$ similar to lensing, where the relevant quantity is the gravitational potential in units of c^2. Tidal alignments of elliptical galaxies are thought to be present at intermediate angular scales of a few hundred in multipole ℓ for a survey like Euclid, with amplitudes being typically an order of magnitude smaller than that of the weak lensing effect. In parallel, alignment models using ideas from effective field theories provide parameterised relationships between tensors constructed from the cosmic density and velocity fields and can capture a wider range of alignment mechanisms and track them into the nonlinear regime [298], but perhaps with a less clear physical picture. There are indications that this in fact takes place in Nature, for instance in measurements of shape correlations in the local Universe [55], in shallow surveys [191, 70, 232], using stacking techniques or correlation techniques in deeper surveys [140, 207, 74] and correlation techniques in weak lensing surveys [135, 137, 180, 170, 136, 173, 164, 182, 263, 183, 174, 172]. Likewise, intrinsic alignment effects have been investigated in fluid-mechanical simulations of galaxy formation [for instance 286, 287, 73, 84, 75, 139, 27].

While intrinsic alignments refer to a physical change of the appearance of the galaxies [for reviews, see 179, 171, 184, 292], there is an analogous deformation effect on the shape of the light bundle emanating from a galaxy by gravitational lensing. To lowest order, both effects depend on tidal gravitational field which suggests that the effects must be correlated. The main difference is that while lensing shear comes from the gravitational tidal field integrated along the line of sight, intrinsic alignment is due to the local gravitational tidal field. Nevertheless, cross-correlations between the physical change in shape and the apparent change in shape are predicted to be nonzero for elliptical galaxies, and to be more exact, should in fact be negative as galaxies align themselves radially with a large structure while lensing generates a tangential alignment. As a result, ellipticity correlations of galaxies is a sum of the conventional weak lensing (often referred to as GG), the intrinsic alignment (or II) and the cross-correlation between the two (called GI). Parameter estimation from weak lensing [63, 58, 42] as well as weak lensing mass reconstructions [104,

68] would be affected by these intrinsic contributions, and can be taken care of by direct modelling or by self-calibration [291, 307, 306, 308, 236]. In addition, intrinsic alignments can show up in cross correlation with the reconstructed CMB-lensing deflection field [141, 127, 72, 188, 218], and they might be usable as cosmological probes in their own right [233, 284].

There should be analogous effects of the size of an elliptical galaxy due to tidal gravitational fields: In gravitational lensing the light bundle can be isotropically enlarged, i.e. changed in size while the shape is conserved: This nonzero convergence is caused by the trace of the tidal field, and determines to lowest order magnification as well, adding cosmological information [149, 279]. Similarly, the size of an elliptical galaxy would physically change for a fixed velocity dispersion if the trace of the tidal field is nonzero,[1] or equivalently, if it resides in an overdense or underdense region. An underdense region with density contrast $\delta < 0$ would source a gravitational potential Φ through the Poisson-equation $\Delta\Phi/c^2 = 3\Omega_m/(2\chi_H^2)\delta$, with the Hubble-distance $\chi_H = c/H_0$, such that the eigenvalues of $\partial_i\partial_j\Phi$ would be negative, stretching the galaxy to a physically larger size. Alternatively, one can argue that the change of volume (or area) is given by the Jacobian of the differential acceleration, i.e. of the tidal field, such that the perturbed volume is $V/V_0 = \det(\delta_{ab} + \partial_a\partial_b\Phi)$, implying that $\ln V - \ln V_0 = \ln\det(\delta_{ab} + \partial_a\partial_b\Phi) = \mathrm{tr}\ln(\delta_{ab} + \partial_a\partial_b\Phi) \simeq \mathrm{tr}(\partial_a\partial_b\Phi) = \Delta\Phi$ and consequently $V/V_0 = \exp(\Delta\Phi)$ and $(V - V_0)/V \simeq \Delta\Phi$. To what extent extrinsic and intrinsic size correlations can add to our understanding of cosmology has been investigated by [134].

The motivation of our paper are exactly these correlations between the sizes of elliptical galaxies as they would be predicted by a linear alignment model as a consequence of the trace $\Delta\Phi$ of the tidal shear tensor $\partial_a\partial_b\Phi$ being nonzero, as proposed by [140]. These intrinsic size correlations would be generated in complete analogy to intrinsic shape correlations caused by the traceless part of the tidal shear, and would contaminate measurements of weak lensing convergence correlations [16] in the same way as intrinsic shape correlations are a nuisance to the weak lensing shear. Alternatively, one can imagine these as a manifestation of ellipticity-density correlations [152], only that density is mapped out by the galaxy size. After introducing tidal interactions of elliptical galaxies with their surrounding large-scale structure in Section 7.2, we compute shape correlations from direct tidal interaction and through gravitational lensing in Section 7.3. We quantify the information content of each of the correlations and the amount of covariance in Section 7.4, before discussing our results in Section 7.5. In general we work in the context of a wCDM-cosmology with a constant equation of state value of w close to -1, and standard values for the cosmological parameters, i.e. $\Omega_m = 0.3$, $\sigma_8 = 0.8$, $h = 0.7$ and $n_s = 0.96$, and a parameterised spectrum for nonlinearly evolving scales. We compute numerical results on the information content of size-correlations for the case of a tomographic weak lensing survey like Euclid's [19]. Throughout the paper, summation convention is implied.

[1] While in certain definitions the trace is subtracted in the tidal field, here the tidal field is simply $\partial_a\partial_b\Phi$ including the trace which is important as is it responsible for size changes.

7.2 Tidal interactions of galaxies and gravitational lensing

In a simplified way one can imagine elliptical galaxies as a stellar component in virial equilibrium with a velocity dispersion σ^2, filling the gravitational potential. [241] then argue that if the velocity dispersion is isotropic, one can invoke the Jeans-equation for stationary and static systems in order to relate density $\rho(r)$ and potential $\Phi(r)$,

$$\sigma^2 \partial_r \ln \rho(r) = -\partial_r \Phi \quad \rightarrow \quad \rho(r) \propto \exp\left(-\frac{\Phi(r)}{\sigma^2}\right), \tag{7.1}$$

reminiscent of the barometric formula. Here, $r = 0$ is the centre of our galaxy where ρ is maximal and Φ has a minimum. If the gravitational potential is distorted by external fields as the galaxy is not an isolated object, the equipotential contours get distorted correspondingly and the stellar component reacts and galaxy assumes a different shape. We still assume that Φ has a minimum at the center of the galaxy, $r = 0$. To lowest order, the change in shape takes place along the principal axes of the tidal tensor $\partial_a \partial_b \Phi$, which is defined as the tensor of second derivatives of the gravitational potential Φ.

$$\Phi(r) \rightarrow \Phi(r) + \frac{1}{2} \partial_a \partial_b \Phi \; r_a r_b, \tag{7.2}$$

leading to a distortion of the density of the stellar component. For weak tidal fields, the exponential can be Taylor-expanded to yield

$$\rho \propto \exp\left(-\frac{\Phi(r)}{\sigma^2}\right) \left[1 - \frac{\partial_a \partial_b \Phi}{2\sigma^2} r_a r_b\right]. \tag{7.3}$$

For this perturbed stellar component one can compute the change of the second moments of the brightness distribution, where we ignore projection effects for a moment and use $\rho(r)$ for projected quantities,

$$\Delta q_{cd} = \int \partial^2 r \; \rho(r) \; r_c r_d \; r_a r_b \times \frac{\partial_a \partial_b \Phi}{2\sigma^2} = S_{abcd} \; \Phi_{ab}, \qquad \Phi_{ab} \equiv \partial_a \partial_b \Phi \,, \tag{7.4}$$

which bears a resemblance to the generalised Hooke-law $\Delta q_{cd} = S_{abcd} \, \Phi_{ab}$, relating the stresses Φ_{ab} to the observable strains Δq_{cd}, which suggests to think of S_{abcd} as the susceptibility of a galaxy to change its shape or size under the influence of tidal gravitational fields. In the theory of elastic media one would then in fact use index symmetries to derive that there must be two material constants, similarly, in the theory of viscous fluids one defines two Lamé-viscosity coefficients (bulk and shear viscosity), so naturally the question arises whether the same constant of proportionality determines the size and the shape deformation as in the case of lensing.

In our model we assume that the reaction of the galaxy to the tidal shear is instantaneous, which is an assumption that can be challenged: Adjustment to a new tidal field should take place on the free-fall time scale $t_{\rm ff} = 1/\sqrt{G\rho}$ with the total matter density ρ, that is typically a factor of $\Delta = 200$ higher than the background

density $\Omega_m \rho_{\rm crit}$ with $\rho_{\rm crit} = 3H_0^2/(8\pi G)$. Substitution shows that the free fall time scale is only $\sqrt{8\pi/(3\Omega_m\Delta)} \simeq 0.37$ times shorter than the age of the Universe $1/H_0$, but because at least in linear structure formation tidal gravitational fields are close to constant in dark energy-cosmologies, the approximation might not be too bad. Of course in nonlinear structure formation, the time-scale of evolution would be much shorter and could give rise to an interesting time evolution of intrinsic alignments even for elliptical galaxies [192, 260, 261]

After introducing polar coordinates, assuming spherical symmetry for the unperturbed galaxy and writing $r_0 = r\cos\phi$ and $r_1 = r\sin\phi$ for the vector components, the elasticity tensor is in our case given by

$$S_{abcd} = \frac{1}{2\sigma^2}\int \partial r\, r^5 \rho(r) \int \partial\phi\, \cos^{4-(a+b+c+d)}\phi \sin^{a+b+c+d}\phi, \tag{7.5}$$

has 16 entries and is fully symmetric under index exchange. Absorbing the prefactor $\int \partial r\, r^5\rho(r)/(2\sigma^2)$ into an alignment parameter D, S_{abcd} can only assume three different values, namely $S_{0000} = \int \partial\phi\, \cos^4\phi = S_{1111} = \int \partial\phi\, \sin^4\phi = 3\pi/4$, $S_{0001} = \int \partial\phi\, \cos^3\phi\sin\phi = S_{1110} = \int \partial\phi\, \cos\phi\sin^3\phi = 0$ and $S_{0011} = \int \partial\phi\, \cos^2\phi\sin^2\phi = \pi/4$.

Introducing the four Pauli-matrices $\sigma^{(n)}_{ab}$ as the basis for the tidal shear $\partial_a\partial_b\Phi$,

$$\begin{aligned}
\sigma^{(0)} &= \begin{pmatrix} +1 & 0 \\ 0 & +1 \end{pmatrix},\ \sigma^{(1)} = \begin{pmatrix} +1 & 0 \\ 0 & -1 \end{pmatrix}, \\
\sigma^{(2)} &= \begin{pmatrix} 0 & +1 \\ -1 & 0 \end{pmatrix},\ \text{and}\ \sigma^{(3)} = \begin{pmatrix} 0 & +1 \\ +1 & 0 \end{pmatrix},
\end{aligned} \tag{7.6}$$

Since $\sigma^{(2)}$ is anti-symmetric while the tidal tensor is symmetric as partial differentiations interchange, the component of Φ_{ab} in direction $\sigma^{(2)}$ vanishes. We now determine the change in size s that is introduced by a tidal field $\Phi_{ab} \propto \sigma^{(0)}_{ab}$,

$$s = \frac{1}{2}\Delta q_{cd}\sigma^{(0)}_{cd} = \frac{1}{2}S_{abij}\sigma^{(0)}_{cd}\sigma^{(0)}_{ab} = \frac{1}{2}\left(S_{0000} + S_{0011} + S_{1100} + S_{1111}\right) = \pi, \tag{7.7}$$

whereas the change in shape ϵ_+ introduced by a tidal field $\Phi_{ab} \propto \sigma^{(1)}_{ab}$ would be

$$\epsilon_+ = \frac{1}{2}\Delta q_{cd}\sigma^{(1)}_{cd} = \frac{1}{2}S_{abij}\sigma^{(1)}_{cd}\sigma^{(1)}_{ab} = \frac{1}{2}\left(S_{0000} - S_{0011} - S_{1100} + S_{1111}\right) = \frac{\pi}{2}, \tag{7.8}$$

or the change in shape $\epsilon_\times$ generated by the tidal field $\Phi_{ab} \propto \sigma^{(3)}_{ab}$,

$$\epsilon_\times = \frac{1}{2}\Delta q_{cd}\sigma^{(3)}_{cd} = \frac{1}{2}S_{abij}\sigma^{(3)}_{cd}\sigma^{(3)}_{ab} = \frac{1}{2}\left(S_{0101} + S_{0110} + S_{1001} + S_{1010}\right) = \frac{\pi}{2}, \tag{7.9}$$

i.e. the changes in shape are only half as large as the change in size, analogously to the weak lensing convergence with $\Delta\psi = 2\kappa$, which implies as well that the same alignment parameter governs the shape and size distortions. With an assumption on the shape of the projected stellar density $\rho(r)$, for instance a Sérsic-profile [269, 123],

$$\rho(r) \propto \exp\left(-b(n)\left[\left(\frac{r}{r_0}\right)^{1/n} + 1\right]\right), \tag{7.10}$$

it is possible to derive the scaling of ellipticity induced by the action of a tidal gravitational field, dominantly with the size of the galaxy but also with the Sérsic-index n. In eqn. (7.10), r_0 is the scale radius of the stellar component, and $b(n) \simeq 2n - 1/3$, approximatively [83]. Computing the relevant integral $\int \partial r\, r^5 \rho(r)$ for a properly normalised density distribution $\int \partial^2 r\, \rho(r) = 2\pi \int \partial r\, r\rho(r) = 1$ and using the definition of ellipticity ϵ as it would result from the second moments q_{ab} of the normalised brightness distribution $I(r)$ which we equate to the stellar density $\rho(r)$,

$$\epsilon = \frac{q_{xx} - q_{yy}}{q_{xx} + q_{yy}} + 2\mathrm{i}\frac{q_{xy}}{q_{xx} + q_{yy}}, \quad \text{with} \quad q_{ab} = \int \partial^2 r\, \rho(r)\, r_a r_b, \tag{7.11}$$

where one recognises the size of the image in the denominator, $q_{xx}+q_{yy} = \int \partial^2 r \rho(r)(x^2+y^2) = 2\pi \int \partial r\, r^3 \rho(r)$, it is possible to show the scaling of the ellipticity to be

$$\begin{aligned}\epsilon &\propto \left(\int_0^\infty \partial r\, r^5 \rho(r)\right) \Big/ \left(\int_0^\infty \partial r\, r^3 \rho(r)\right) \\ &= r_0^2 \times \int_{-b}^\infty \partial x\, \left(\frac{x}{b} + 1\right)^{6n-1} \exp(-x) \Big/ \int_{-b}^\infty \partial x\, \left(\frac{x}{b} + 1\right)^{4n-1} \exp(-x). \end{aligned} \tag{7.12}$$

Technically, we obtained this result after substitution $x = b\left[(r/r_0)^{1/n} - 1\right]$, where the ratio of integrals has in general only a numerical solution and shows the dependence of the susceptibility to shape change due to tidal forces caused by the distribution of the stars inside the galaxy. The dominant scaling of ellipticity with the size r_0^2 of the galaxy is dimensionally consistent with the linear tidal shear model $q_{ab} = S_{abcd}\, \Phi_{cd}$. The results are shown in Fig. 7.1, which indicates a strong scaling of the alignment parameter with increasing Sérsic-index n, where we should note that we consider the Sérsic-profile as a reasonably simple model for the stellar distribution, which is not consistent with a constant velocity dispersion σ^2, and neither a gravitating self-consistent solution. Rather, it is supposed to illustrate that the internal dynamics of an elliptical galaxy can impact on the magnitude of tidal alignment and that not all elliptical galaxies should have the same alignment parameter if their Sérsic-index varies.

It is straightforward to show that the distortion modes are all independent for the linear model, i.e. tidal fields $\propto \sigma_{ab}^{(m)}$ will never source distortion modes $\propto \sigma_{cd}^{(n)}$ with $m \neq n$. For making the influence of the tidal field on the galaxy size more specific, we compute the change in size s explicitly as the second moment of the brightness distribution for the isotropic case,

$$\begin{aligned} s &= \frac{1}{2\sigma^2} \int \partial^2 r\, r^2 \rho(r) \left[\frac{1}{2}\partial_a \partial_b \Phi\, r_a r_b\right] = \frac{1}{2\sigma^2} \int \partial^2 r\, r^2 \rho(r) \left[\frac{1}{4}\Delta\Phi\, r^2\right] \\ &= \frac{\pi}{\sigma^2} \int r^5 \partial r\, \rho(r) \frac{\Delta\Phi}{4} \propto \frac{\pi}{2}\Delta\Phi \end{aligned} \tag{7.13}$$

such that the change in size comes out proportional to the trace $\Delta\Phi$ of the tidal field and consistent with the above argumentation with the same definition of the alignment parameter D.

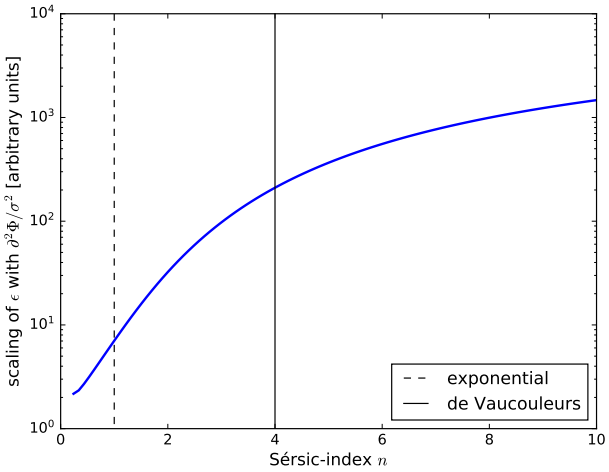

Figure 7.1: Scaling of the relation between ellipticity ϵ and Sérsic-index n, for a given tidal gravitational field and a given velocity dispersion σ^2. As particular cases, the exponential profile for $n = 1$ and the de Vaucouleurs-profile for $n = 4$ are indicated by vertical lines.

With many galaxies in a tomographic bin A with a suitable, normalised redshift distribution $p_A(z)\partial z$ one can define the line of sight-averaged ellipticity from second angular derivatives of the weighted projection of the potential Φ:

$$\varphi_{A,ab} = \partial_a\partial_b\varphi_A \quad \text{with} \quad \varphi_A = D\int \partial\chi\, p_A(z(\chi))\frac{\partial z}{\partial\chi}\frac{D_+}{a}\frac{\Phi}{\chi^2} = \int \partial\chi\, W_{\varphi,A}(\chi)\,\Phi, \tag{7.14}$$

with the Hubble-function $H(\chi)/c = \partial z/\partial\chi$ which originates from the transformation of the redshift distribution, and the growth rate D_+/a of gravitational potentials, and the alignment parameter D, which encapsulates the proportionality between tidal field and physical shape and size change. The line of sight-weighting function $W_{\varphi,A}$ of bin A is defined by the last equals sign. The parameter D reflects the brightness distribution of a galaxy through its fourth moments and scale inversely with the velocity dispersion σ^2. Because linear intrinsic alignments have the opposite sign compared to gravitational lensing in the same gravitational potential, we choose a negative value for the alignment parameter D in order to not having to carry through minus-signs explicitly. This is due to the fact that an overdense region enlarges the image of a galaxy in lensing but compresses a galaxy physically.

Equation (7.14) can be amended to include a bias model, as the galaxy density traces the dark matter density not perfectly. As the intrinsic shape and size-spectra correspond to ellipticity- and diameter-weighted galaxy correlation functions, a biasing model would in fact matter and can change the dependence between the observables and the tidal field as a function of scale or redshift. For simplicity, we work with a bias of unity without any dependence on mass or redshift, which is reasonable for low-mass galaxies in the relevant redshift range [270]. Modelling the statistics of the intrinsic alignment effects from a Gaussian random field as we do

subsequently ignores that the galaxy shapes and sizes provide a measurement of the tidal field restricted to peak regions of the large-scale structure, which influences the statistics of tidal fields [235, 260], while the dependence of tidal shears on the environment should be reproduced [108, 253].

The angular derivatives ∂_a are related to the spatial derivatives ∂_x through $\partial_a = \chi\partial_x$, with $x = \theta\chi$ in the small-angle approximation. From that, one can recover the ellipticity components $\epsilon_{+,A}$ and $\epsilon_{\times,A}$ as well as the size s_A from a decomposition of the tensor $\varphi_{A,ab}$ with the Pauli-matrices $\sigma^{(n)}_{ab}$,

$$\varphi_{A,ab} = s_A\sigma^{(0)}_{ab} + \epsilon_{+,A}\sigma^{(1)}_{ab} + \epsilon_{\times,A}\sigma^{(3)}_{ab}, \tag{7.15}$$

where three components are sufficient because of the symmetry $\varphi_{A,ab} = \varphi_{A,ba}$. Using two properties of the Pauli-matrices $\sigma^{(n)}_{ab}$, namely $\sigma^{(l)}_{ab}\sigma^{(m)}_{bc} = \delta_{lm}\sigma^{(0)}_{ac} + \epsilon_{lmn}\sigma^{(n)}_{ac}$, and their tracelessness $\sigma^{(m)}_{aa} = 0$, it is possible to invert the last relation and to obtain the expansion coefficients,

$$s_A = \frac{1}{2}\varphi_{A,ab}\sigma^{(0)}_{ab}, \quad \epsilon_{+,A} = \frac{1}{2}\varphi_{A,ab}\sigma^{(1)}_{ab}, \text{ and } \quad \epsilon_{\times,A} = \frac{1}{2}\varphi_{A,ab}\sigma^{(3)}_{ab}. \tag{7.16}$$

The approach above is motivated by the weak lensing shear γ, which results from the tensor $\psi_{B,ij}$ containing the second derivatives of the weak lensing potential ψ_B,

$$\psi_{B,ij} = \partial_i\partial_j\psi_B \quad \text{with} \quad \psi_B = 2\int \partial\chi\, \frac{G_B(\chi)}{\chi}\frac{D_+}{a}\Phi = \int \partial\chi\, W_{\psi,B}(\chi)\Phi, \tag{7.17}$$

with the lensing efficiency

$$G_B(\chi) = \int_{\max(\chi,\chi_B)}^{\chi_{B+1}} \partial\chi'\, p(\chi')\frac{\partial z}{\partial\chi'}\left(1 - \frac{\chi}{\chi'}\right). \tag{7.18}$$

It is interesting to note that the effect of convergence and shear are fully analogous to the changes in size and shape due to direct tidal interaction, up to some interesting details: A light bundle, consisting of photons as relativistic test particles for the gravitational potential, is deflected twice as strongly compared to non-relativistic test particles such as the stars inside an elliptical galaxy, and the constant of proportionality that makes the gravitational potential dimensionless is c^2 in lensing instead of σ^2 for the intrinsic alignments. Finally, the lensing kernel G_B/χ is non-zero not only inside the bin B under consideration but the integral extends from $\chi = 0$ to the outer rim of bin B, χ_{B+1}. We compute both lensing and intrinsic alignments from the dimensionless potential Φ give in units of c^2 and use a numerical value for the alignment parameter scaled by c^2/σ^2. Again, there is an analogous decomposition

$$\psi_{B,ij} = \kappa_B\sigma^{(0)}_{ij} + \gamma_{+,B}\sigma^{(1)}_{ij} + \gamma_{\times,B}\sigma^{(3)}_{ij} \tag{7.19}$$

with the analogous inversion,

$$\kappa_B = \frac{1}{2}\psi_{B,ij}\sigma^{(0)}_{ij}, \quad \gamma_{+,B} = \frac{1}{2}\psi_{B,ij}\sigma^{(1)}_{ij}, \text{ and } \quad \gamma_{\times,B} = \frac{1}{2}\psi_{B,ij}\sigma^{(3)}_{ij}. \tag{7.20}$$

The intrinsic size field provides a measure of the projected density in the same way as the weak lensing convergence κ, but with a different weighting function:

$$\begin{aligned} s &= \frac{1}{2}\varphi_{ab}\sigma_{ab}^{(0)} = \frac{D}{2}\sigma_{ab}^{(0)}\partial_a\partial_b \int \partial\chi\, p(\chi)\frac{D_+}{a}\frac{\Phi}{\chi^2} \\ &= \frac{D}{2}\int \partial\chi\, p(\chi)\frac{D_+}{a}\Delta\Phi = \frac{3\Omega_m}{4\chi_H^2}D\int \partial\chi\, p(\chi)\frac{D_+}{a}\delta, \end{aligned} \tag{7.21}$$

by substituting the Poisson-equation $\Delta\Phi = 3\Omega_m/(2\chi_H^2)\delta$, using $\partial_a = \chi\partial_x$ for the derivatives, and approximating the full Laplacian by the one containing the derivatives perpendicular to the line of sight. Again, one recognises a factor of two between the gravitational acceleration of photons in gravitational lensing and non-relativistic particles as in our case of stars inside an elliptical galaxy. As discussed before, an actual measurement of the mean size s of the galaxies into a certain direction would in addition be weighted with a biasing factor because the tidal field is only measurable at positions where galaxies exist: While the inclusion of a reasonably simple linear and deterministic biasing model is certainly possible and straightforward, we ignore this out of simplicity.

This implies that the statistics of all modes of the shape and size field can be described by spectra of the source fields, which in turn are given by a Limber-projection. Specifically, the spectrum of $\varphi_{A,ab}$ reads

$$\begin{aligned} &\langle\varphi_{A,ab}(\ell)\varphi^*_{B,ij}(\ell')\rangle = (2\pi)^2\delta_D(\ell-\ell')\, C^{\varphi_A\varphi_B}_{abij}(\ell) \\ &\text{with}\quad C^{\varphi_A\varphi_B}_{abij}(\ell) = \ell_a\ell_b\ell_i\ell_j \int \frac{\partial\chi}{\chi^2}\, W_{\varphi,A}(\chi)W_{\varphi,B}(\chi)\, P_{\Phi\Phi}(k=\ell/\chi), \end{aligned} \tag{7.22}$$

similarly, one obtains for the field $\psi_{B,ij}$,

$$\begin{aligned} &\langle\psi_{A,ab}(\ell)\psi^*_{B,ij}(\ell')\rangle = (2\pi)^2\delta_D(\ell-\ell')\, C^{\psi_A\psi_B}_{abij}(\ell) \\ &\text{with}\quad C^{\psi_A\psi_B}_{abij}(\ell) = \ell_a\ell_b\ell_i\ell_j \int \frac{\partial\chi}{\chi^2}\, W_{\psi,A}(\chi)W_{\psi,B}(\chi)\, P_{\Phi\Phi}(k=\ell/\chi), \end{aligned} \tag{7.23}$$

and finally for their cross-correlation,

$$\begin{aligned} &\langle\varphi_{A,ab}(\ell)\psi^*_{B,ij}(\ell')\rangle = (2\pi)^2\delta_D(\ell-\ell')\, C^{\varphi_A\psi_B}_{abij}(\ell) \\ &\text{with}\quad C^{\varphi_A\psi_B}_{abij}(\ell) = \ell_a\ell_b\ell_i\ell_j \int \frac{\partial\chi}{\chi^2}\, W_{\varphi,A}(\chi)W_{\psi,B}(\chi)\, P_{\Phi\Phi}(k=\ell/\chi). \end{aligned} \tag{7.24}$$

In general, all lensing effects originating from a tidal gravitational field will have the opposite sign than the intrinsic tidal alignment, which causes the cross-correlation between lensing and intrinsic alignments to have a negative sign. This is taken care of numerically by choosing a negative value for the alignment parameter D, which does not affect the auto-correlations: Those are proportional to D^2 and therefore positive. In analogy we define the angular spectra $C^{\varphi_A\varphi_B}(\ell)$, $C^{\psi_A\psi_B}(\ell)$ and $C^{\varphi_A\psi_B}(\ell)$ of the potentials φ_A and ψ_B. For the spectrum of the gravitational potential we use a linear spectrum of the form $P_{\Phi\Phi}(k) \propto k^{n_s-4}T^2(k)$ with a transfer function $T(k)$ and a nonlinear extension on small scales [78, 155], normalised to σ_8, but assume

Gaussian statistics throughout. We apply a smoothing on a scale defined through $M = 4\pi/3\,\Omega_m\rho_{\rm crit}R^3$, $\rho_{\rm crit} = 3H_0^2/(8\pi G)$,

$$\Phi(k) \to \Phi(k)\exp\left(-\frac{(kR)^2}{2}\right), \tag{7.25}$$

to the potential used for intrinsic alignments, where we set the mass scale to be $M = 10^{12}M_\odot/h$: In doing this we can control how close size- and shape-correlations trace the tidal shear field, and select the relevant long-wavelength modes.

7.3 Angular spectra of galaxy shapes and sizes

The prefactors $\ell_a\ell_b$ appearing in the expressions for the spectra of the projected tidal shears can be compactly written by introducing polar coordinates, $\ell_0 = \ell\cos\phi$ and $\ell_1 = \ell\sin\phi$. Then,

$$\begin{aligned}\ell_a\ell_b &= \frac{\ell^2}{2}\left(\sigma^{(0)}_{ab} + (\cos^2\phi - \sin^2\phi)\sigma^{(1)}_{ab} + 2\sin\phi\cos\phi\sigma^{(3)}_{ab}\right)\\ &= \frac{\ell^2}{2}\left(\sigma^{(0)}_{ab} + \cos(2\phi)\sigma^{(1)}_{ab} + \sin(2\phi)\sigma^{(3)}_{ab}\right),\end{aligned} \tag{7.26}$$

recovering the fact that the phase angle rotates twice as fast as the coordinate system. We are going to make the choice $\phi = 0$ by a suitable rotation of the coordinate frame, such that there are no contractions with $\sigma^{(3)}_{ab}$, and correspondingly vanishing $\gamma_\times$ or $\epsilon_\times$. This corresponds effectively to the computation of E- and B-modes of the shear field and of the ellipticity field, with

$$e(\ell) = \quad \cos(2\phi)\gamma_+(\ell) + \sin(2\phi)\gamma_\times(\ell), \tag{7.27}$$

$$b(\ell) = -\sin(2\phi)\gamma_+(\ell) + \cos(2\phi)\gamma_\times(\ell), \tag{7.28}$$

where in our model there are no B-modes due to the index exchange symmetry. Now, the decomposition with Pauli-matrices makes it possible to write down all ellipticity spectra as contractions of the possible spectra of the source terms, for lensing,

$$C^{\gamma\gamma}_{AB}(\ell) = \frac{1}{4}\sigma^{(1)}_{ab}\sigma^{(1)}_{ij}C^{\psi_A\psi_B}_{abij}(\ell) = \frac{\ell^4}{4}C^{\psi_A\psi_B}(\ell), \tag{7.29}$$

for intrinsic alignments,

$$C^{\epsilon\epsilon}_{AB}(\ell) = \frac{1}{4}\sigma^{(1)}_{ab}\sigma^{(1)}_{ij}C^{\varphi_A\varphi_B}_{abij}(\ell) = \frac{\ell^4}{4}C^{\varphi_A\varphi_B}(\ell), \tag{7.30}$$

and for the cross-correlation between the two,

$$C^{\epsilon\gamma}_{AB}(\ell) = \frac{1}{4}\sigma^{(1)}_{ab}\sigma^{(1)}_{ij}C^{\varphi_A\psi_B}_{abij}(\ell) = \frac{\ell^4}{4}C^{\varphi_A\psi_B}(\ell). \tag{7.31}$$

A measurement of the shape correlations is limited by a Poissonian shape noise contribution,

$$N^{\rm shape}_{AB}(\ell) = \sigma^2_{\rm shape}\frac{n_{\rm tomo}}{\bar{n}}\delta_{AB}, \tag{7.32}$$

with a value of $\sigma_{\rm shape} = 0.4$ and the number density $\bar{n} = 4.727 \times 10^8$ galaxies per steradian typical for Euclid-studies. It is straightforward to show that of the 20 possible spectra 10 are in fact nonzero, and that certain consistency relations hold, for instance $\langle\kappa\kappa'\rangle = \langle\gamma_+\gamma'_+\rangle + \langle\gamma_\times\gamma'_\times\rangle$ as well as $\langle ss'\rangle = \langle\epsilon_+\epsilon'_+\rangle + \langle\epsilon_\times\epsilon'_\times\rangle$, in any coordinate frame.

The resulting extrinsic and intrinsic shape spectra are shown for a tomographic survey in Fig. 7.2: Intrinsic shape correlations are relevant at intermediate multipoles, but are surpassed by one to two orders of magnitude by weak lensing-induced shape correlations, for realistic values of the alignment parameter D. Intrinsic and extrinsic shapes are anti-correlated, and the cross-correlation is modulating the spectra over much wider multipole ranges. In fulfilment of the Cauchy-Schwarz-inequality, the cross-correlation has values between the pure lensing and intrinsic alignment effect. The alignment parameter D was chosen to be 10^{-5}, and scales proportional to $(c/\sigma)^2$, where $\sigma = 10^5$m/s would be a typical value for a Milky Way-sized object with $10^{12}M_\odot/h$: Increasing the velocity dispersion (where $\sigma \propto M^{1/3}$ due to the viral law) requires a larger alignment parameter D. This value of the alignment parameter is chosen lower than the value measured by [293] in CFHTLenS-data, even though details of the models differ from a technical point of view [293, who compute the correlations in real-space before Fourier-transforming into Fourier-space, whereas our model is set up entirely in Fourier-space], the models themselves should be compatible. Compared to the IllustrisTNG-simulation [316], where the alignment parameter as a constant of proportionality is measured directly in the relation between ellipticity and tidal shear, our value for D is higher, because the measurement of the ambient tidal shear field contains a contribution from the local matter density and disregards biasing effects. Currently, there are still large uncertainties concerning the value and its dependence on galaxy mass as well as a possible evolution in redshift and galaxy biasing, such that we decided to use an intermediate value.

In a similar manner as in the previous section, one obtains the size spectra from contracting the possible spectra of the source terms, for lensing,

$$C^{\kappa\kappa}_{AB}(\ell) = \frac{1}{4}\sigma^{(0)}_{ab}\sigma^{(0)}_{ij}C^{\psi_A\psi_B}_{abij}(\ell) = \frac{\ell^4}{4}C^{\psi_A\psi_B}(\ell), \tag{7.33}$$

for intrinsic alignments,

$$C^{ss}_{AB}(\ell) = \frac{1}{4}\sigma^{(0)}_{ab}\sigma^{(0)}_{ij}C^{\varphi_A\varphi_B}_{abij}(\ell) = \frac{\ell^4}{4}C^{\varphi_A\varphi_B}(\ell), \tag{7.34}$$

and again, for the cross-correlation between the two,

$$C^{s\kappa}_{AB}(\ell) = \frac{1}{4}\sigma^{(0)}_{ab}\sigma^{(0)}_{ij}C^{\varphi_A\psi_B}_{abij}(\ell) = \frac{\ell^4}{4}C^{\varphi_A\psi_B}(\ell), \tag{7.35}$$

i.e. all size-spectra are equal to their shape-counterparts. In the estimation process, there is a constant, diagonal noise contribution

$$N^{\rm size}_{AB}(\ell) = \sigma^2_{\rm size}\frac{n_{\rm tomo}}{\bar{n}}\delta_{AB}, \tag{7.36}$$

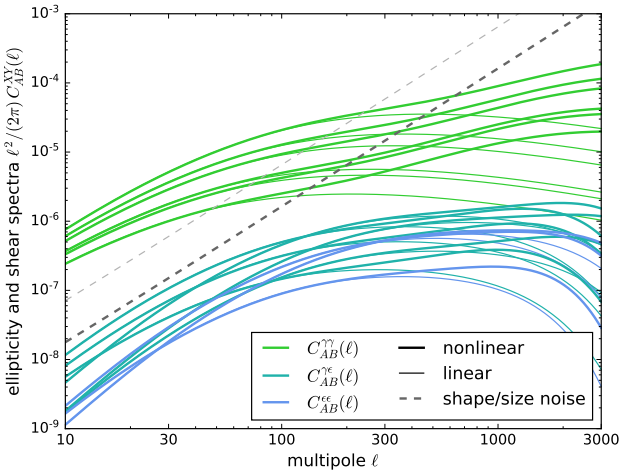

Figure 7.2: Shape-shape correlations as a function of multipole order ℓ, separated by gravitational lensing $C^{\gamma\gamma}_{AB}(\ell)$, intrinsic size correlations $C^{\epsilon\epsilon}_{AB}(\ell)$ and the cross-correlation $C^{\gamma\epsilon}_{AB}(\ell)$ (of which we show the absolute value), with the Poissonian noise contributions $N^{\rm shape}_{AB}(\ell)$ (dark grey) and $N^{\rm size}_{AB}(\ell)$ (light grey, a factor of 4 higher) in comparison, for Euclid's redshift distribution and tomography with 3 bins, for a ΛCDM-cosmology with an alignment parameter $D = -10^{-5}$ on a mass scale $M = 10^{12} M_\odot/h$, corresponding to a virial velocity of $\sigma \simeq 10^5$m/s. Thick and thin lines indicate a nonlinear and linear spectrum, respectively.

with the size noise $\sigma_{\rm size} = 0.8$.

Fig. 7.2 shows at the same time the intrinsic and extrinsic size-spectra, as they would result from a tomographic survey. In fact, as a consequence of the linear alignment model and the linearity of weak lensing the size-correlations are identical to the shape correlations, including the anti-correlation between intrinsic and extrinsic size. Given the fact that there is a slightly higher uncertainty in the measurement of angular size in comparison to shape one can already now expect that the corresponding signal to noise-ratios for size-correlations are slightly inferior to shapes. These statements rely on the fact that the same alignment parameter D is relevant for both shapes and sizes, as the linear alignment model would suggest. Similarly, we show in Fig. 7.3 the Pearson correlation coefficient $r_{\gamma\epsilon}$ as a function of multipole ℓ,

$$r_{\gamma\epsilon} = \frac{C^{\gamma\epsilon}_{AA}(\ell)}{\sqrt{C^{\gamma\gamma}_{AA}(\ell)\, C^{\epsilon\epsilon}_{AA}(\ell)}}, \tag{7.37}$$

where we would like to emphasise that the Pearson-coefficients for shapes and sizes are identical, $r_{\gamma\epsilon} = r_{\kappa s}$. We set the bin-indices equal, $A = B$, because only in this case $C^{\epsilon\epsilon}_{AB}(\ell)$ and $C^{ss}_{AB}(\ell)$ are unequal to zero. The values for $r_{\gamma\epsilon}$ suggest that there is in fact redundancy in the spectra.

Finally, we compute the cross-correlations between galaxy shapes and sizes, for lensing

$$C^{\kappa\gamma}_{AB}(\ell) = \frac{1}{4}\sigma^{(0)}_{ab}\sigma^{(1)}_{ij} C^{\psi_A\psi_B}_{abij}(\ell) = \frac{\ell^4}{4} C^{\psi_A\psi_B}(\ell) \tag{7.38}$$

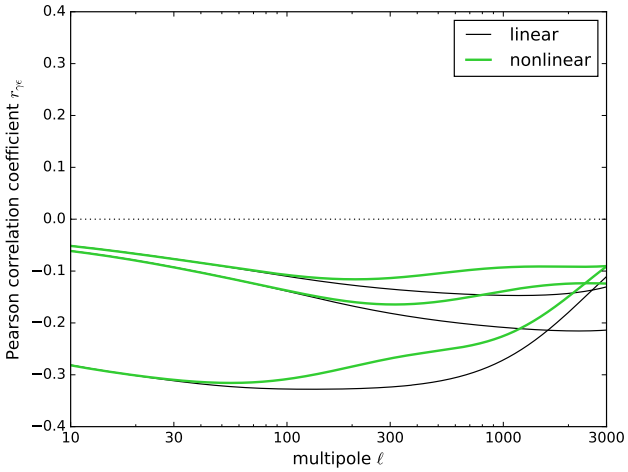

Figure 7.3: Pearson correlation coefficients $r_{\gamma\epsilon}$ as a function of multipole order ℓ.

for intrinsic alignments,

$$C^{s\epsilon}_{AB}(\ell) = \frac{1}{4}\sigma^{(0)}_{ab}\sigma^{(1)}_{ij}C^{\varphi_A\varphi_B}_{abij}(\ell) = \frac{\ell^4}{4}C^{\varphi_A\varphi_B}(\ell) \tag{7.39}$$

and for the cross-correlation between lensing and alignments,

$$C^{\kappa\epsilon}_{AB}(\ell) = \frac{1}{4}\sigma^{(0)}_{ab}\sigma^{(1)}_{ij}C^{\psi_A\varphi_B}_{abij}(\ell) = \frac{\ell^4}{4}C^{\psi_A\varphi_B}(\ell) \tag{7.40}$$

$$C^{s\gamma}_{AB}(\ell) = \frac{1}{4}\sigma^{(0)}_{ab}\sigma^{(1)}_{ij}C^{\psi_A\varphi_B}_{abij}(\ell) = \frac{\ell^4}{4}C^{\varphi_A\psi_B}(\ell), \tag{7.41}$$

where due to the independence of the errors in the shape and size correlations one does not have to deal with a noise contribution when estimating spectra. Effectively, the cross-correlations between shape and size look identical to the autocorrelations, but in their estimation process there is no noise term, if statistical independence of the two measurement processes for shape and size is given.

7.4 Information content of shape and size correlations

For quantifying the information content of intrinsic size and shape correlations in comparison to weak lensing convergence and shear we use the Fisher-matrix formalism. Arranging the measurements of galaxy shapes and sizes into a data vector yields the data covariance matrix,

$$C = \begin{pmatrix} C^{\epsilon\epsilon}_{AB}(\ell) + 2C^{\epsilon\gamma}_{AB}(\ell) & C^{s\epsilon}_{AB'}(\ell) + C^{s\gamma}_{AB'}(\ell) \\ + C^{\gamma\gamma}_{AB}(\ell) + N^{\text{shape}}_{AB} & + C^{\kappa\epsilon}_{AB'}(\ell) + C^{\kappa\gamma}_{AB'}(\ell) \\ C^{s\epsilon}_{A'B}(\ell) + C^{s\gamma}_{A'B}(\ell) & C^{ss}_{A'B'}(\ell) + 2C^{s\kappa}_{A'B'}(\ell) \\ + C^{\kappa\epsilon}_{A'B}(\ell) + C^{\kappa\gamma}_{A'B}(\ell) & + C^{\kappa\kappa}_{A'B'}(\ell) + N^{\text{size}}_{A'B'} \end{pmatrix} \tag{7.42}$$

Given the similarities between the shape and size correlations allows to rewrite the covariance matrix as

$$C = \begin{pmatrix} \frac{\ell^4}{4}\left(C^{\varphi_A\varphi_B}(\ell) + 2C^{\varphi_A\psi_B}(\ell) + C^{\psi_A\psi_B}(\ell)\right) + N_{AB}^{\rm shape} & \frac{\ell^4}{4}\left(C^{\varphi_A\varphi_{B'}}(\ell) + 2C^{\varphi_A\psi_{B'}}(\ell) + C^{\psi_A\psi_{B'}}(\ell)\right) \\ \frac{\ell^4}{4}\left(C^{\varphi_{A'}\varphi_B}(\ell) + 2C^{\varphi_{A'}\psi_B}(\ell) + C^{\psi_{A'}\psi_B}(\ell)\right) & \frac{\ell^4}{4}\left(C^{\varphi_{A'}\varphi_{B'}}(\ell) + 2C^{\varphi_{A'}\psi_{B'}}(\ell) + C^{\psi_{A'}\psi_{B'}}(\ell)\right) + N_{A'B'}^{\rm size} \end{pmatrix}, \tag{7.43}$$

which is dangerously close to being singular, underlining the degeneracy between the shape- and size measurements. Already at this stage one should expect that a combined measurement of shear and size does not yield strong improvements of the signal to noise-ratio alone, and given the fact that the same potentials are involved with identical physical dependences on cosmology, resulting Fisher-matrices will be very similar. We use the Fisher-matrix formalism as a quick way to quantify the fundamental sensitivities and degeneracies, while noting that the non-Gaussian shape of the likelihood matters in most cases and that tools for dealing with non-Gaussian likelihoods analytically exist [277, 266].

The Fisher-matrix $F_{\mu\nu}$ for a tomographic survey assumes the generic form

$$F_{\mu\nu} = f_{\rm sky}\sum_\ell \frac{2\ell+1}{2}{\rm tr}\left(C^{-1}\partial_\mu S\, C^{-1}\partial_\nu S\right) \tag{7.44}$$

where we implicitly assume a full sky coverage by having independent Fourier-modes. Similarly, we define the signal to noise ratio Σ,

$$\Sigma^2 = f_{\rm sky}\sum_\ell \frac{2\ell+1}{2}{\rm tr}\left(C^{-1}S\, C^{-1}S\right), \tag{7.45}$$

with the noiseless spectrum $S(\ell)$ of which the signal strength is sought. For the case of Euclid, we extend the summation over the multipoles from $\ell = 10$ to $\ell = 3000$, and we are assuming for simplicity a full-sky coverage with no correlations between different multipoles but scale down the signal subsequently with a sky coverage of $f_{\rm sky}$, which would be justified because most of the signal originates at small angular scales. We set the number of tomographic bins to $n_{\rm tomo} = 5$.

Clearly, not all galaxies are ellipticals for which the tidal alignment model would apply, but only a fraction of $q \simeq 1/3$ of them. Therefore, we compute two values for the signal to noise-ratio Σ: First, we weight the GI-type spectra by a factor q, and the II-type spectra by a factor q^2 relative to the GG-term, as lensing operates on all galaxies identically irrespective of their type. These numbers for Σ would correspond estimates of the spectra from the full data set and indicate the level of significance by which the shape or size correlations are incompatible with a pure gravitational lensing model. Fig. 7.4 quantifies the signal to noise-ratio Σ for measuring intrinsic shape and intrinsic size correlations: We compute the signal to noise-ratio for a measurement of the II and GI-terms in both shape- and size correlations in the presence of the full cosmic variance, which is dominated by gravitational lensing, i.e. by the GG-terms. As expected, lensing-induced shape correlations are measurable

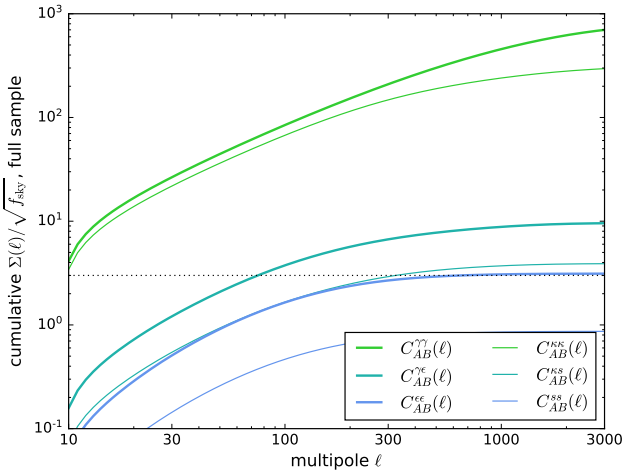

Figure 7.4: Cumulative signal to noise-ratio $\Sigma(\ell)/\sqrt{f_{\rm sky}}$ for Euclid 5-bin tomography for measuring shape correlations and intrinsic size correlations, for the full galaxy sample.

at a higher signal to noise-ratio compared to size correlations, but both are easily within the reach of Euclid. The signal to noise ratio suggests that GI-type terms are detectable in shape correlations and perhaps marginally in size correlations, and II-terms are marginally detectable, with intrinsic shape correlations being the least disappointing.

The inverse Σ^{-1} of the signal to noise-ratio is at the same time the relative error D/σ_D on the alignment parameter D, which suggests that measurements of the alignment parameter can be carried out the level of a few ten percent, so the investigation of trends with galaxy mass, type or redshift seem feasible. We have chosen a rather conservative value for D, nothing precludes the usage of a strategy to boost intrinsic alignments relative to lensing. As for the morphological mix of spiral and elliptical galaxies we conclude that the signal to noise ratios are likewise proportional to q for the GI-terms and to q^2 for the II-terms, such that effectively the combined parameter $q \times D$ is determined through a measurement. In the same way as adopting higher values for the alignment parameter D, a higher fraction of elliptical galaxies q would be reflected in the signal to noise-ratio Σ.

On the other hand one could pursue the strategy to pre-select elliptical galaxies on the basis of their colours or morphologies and to measure the shape- and size correlations on the resulting, reduced data set. In this case, effectively, the total number of galaxies $\bar{n}$ is reduced by q and the number of galaxy pairs by q^2, leading to an increased Poissonian noise term, which becomes larger by a factor of q. Consequently, the signal strength for weak lensing is much weaker, as it is estimated from a much smaller number of galaxies, but the relative amplitudes between lensing and the intrinsic alignment spectra are smaller. The resulting numbers are shown in Fig. 7.5, where the overall higher shape and size noise terms decrease the significance, but vice versa, the amplitude of the intrinsic correlations relative to those of lensing are higher, such that a feasible strategy for measuring intrinsic shape corre-

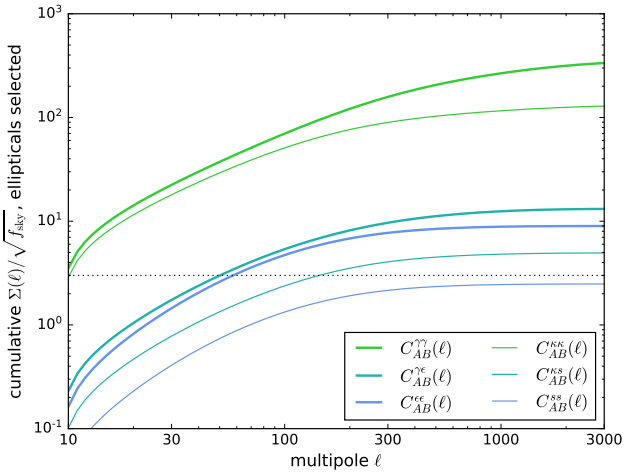

Figure 7.5: Cumulative signal to noise-ratio $\Sigma(\ell)/\sqrt{f_{\rm sky}}$ for Euclid 5-bin tomography for measuring shape correlations and size correlations, for a case when elliptical galaxies are selected for the estimation of correlations.

lations could be to measure the GI-terms and the II-terms with a selected sample of elliptical galaxies. The intrinsic size correlations, however, seem to be out of reach with Euclid, no matter the strategy. The attainable signal to noise ratio depends not only on the alignment parameter D but also on the mass-scale on which the spectra are smoothed: The two are not independent and should be related through a virial relationship linking velocity dispersion σ^2 and mass M, $\sigma^2 \propto M^{2/3}$, but choosing a smaller mass scale has the consequence that higher multipoles contribute to the signal an increase $\Sigma(\ell)$.

Fig. 7.6 shows constraints on a wCDM-cosmology from galaxy shapes and galaxy sizes: As both observables are probing tidal gravitational fields with identical physical dependences there can not be any fundamental difference in the degeneracies, with the only exception that the noise in the size-measurement is typically larger compared to the shape-measurement, which effectively cuts off high multipoles from contributing to the signal. And we would like to emphasise that the two measurements are highly correlated such that one does not gain an advantage from combining the two. We would argue, however, that there is potential to use shape and size-correlations to investigate deviations from the Newtonian form of the Poisson equation due to modified theories of gravity. For this, one needs a very good understanding of the detailed mechanisms of alignment with possibly nonlinear corrections to the tidal alignment model, as well as the scaling behaviour of the alignment parameter with redshift and galaxy mass [142], and possibly different alignment parameters for subpopulations of elliptical galaxies, as the strong dependence on the Sérsic-index suggests. Fundamental degeneracies in the spectra are present between the alignment parameter D and σ_8, which are perfectly degenerate in the linear regime, but the degeneracy is broken by combining GG, GI and II-terms in the measurement, as they are proportional to σ_8^2, $\sigma_8^2 D$ and $\sigma_8^2 D^2$, respectively. In a very similar way, the proportionality of the lensing spectrum to Ω_m^2 to first order

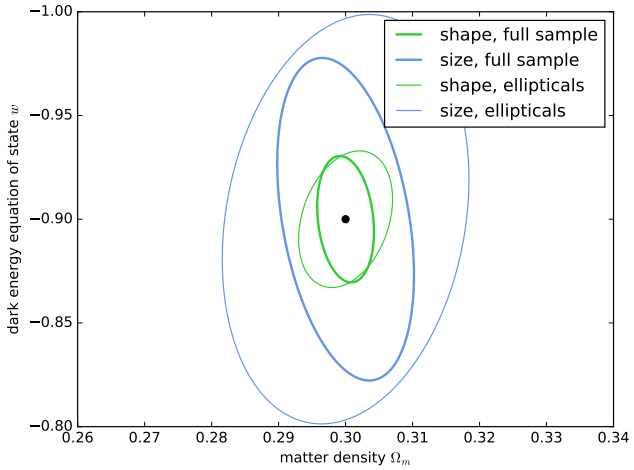

Figure 7.6: Marginalised 1σ-contours from the Fisher-matrix analysis on a standard wCDM-cosmology (with $w = -0.9$) for a fixed value $D = -10^{-5}$ for the alignment parameter and a smoothing scale of $10^{12} M_{\odot}/h$: We give contours separated by shape and size correlations, and for the full galaxy sample versus a sample containing only elliptical galaxies.

translates to the GI-term, which is proportional to Ω_m. The influence of the particular dark energy model by mapping the redshift distribution of the galaxies onto a distribution in comoving distance, is identical for all correlations. Pursuing the two strategies of either keeping the full galaxy sample and downweighting GI-spectra by $q = 1/3$ and II-terms by q^2 yields smaller errors than pre-selecting elliptical galaxies first, because the smaller Poisson-noise, but the second strategy has a higher relative contribution from intrinsic alignments, which start to matter in deriving constraints, as they provide cosmological information.

7.5 Summary and Conclusion

The subject of our investigation were extrinsic and intrinsic shape and size correlations of elliptical galaxies due to weak gravitational lensing and intrinsic alignments. Our starting point was the description of the stellar density of a virialised system through the Jeans-equation, in which we perturb the gravitational potential with an external tidal shear field. Under the condition that this field is reasonably weak and the galaxy compact enough, one can compute the response in shape and size of a galaxy in linear approximation in the tidal field, controlled by the galaxy's velocity dispersion σ^2. The susceptibility of a galaxy to tidal distortion is highly dependent on the stellar profile: A toy model using the Sérsic profile family showed a strong increase in the response from exponential profiles to de Vaucouleurs-profiles.

These are our main findings:

- Assuming a weakly perturbed Jeans-equilibrium for elliptical galaxies naturally reproduces a linear response of the shape and the size of a galaxy to

external tidal gravitational fields, and suggests that the same alignment parameter is responsible for the change in shape and in size. Nominally, the velocity dispersion σ of the galaxy sets the scale for the gravitational field, which is remarkably similar to the quantity Φ/c^2 in gravitational lensing. With virial equilibrium on can continue to argue that σ^2 is proportional to M/R with the mass M and the size R, such that the ratio $(R/\sigma)^2$, which controls the perturbation of the stellar component, is in fact constant [compare 241]. Therefore, alignments should not strongly depend on the mass scale under consideration, which would however enter through a convolution of the tidal shear spectrum with a filter function. Galaxy biasing would introduce an additional modulation of the intrinsic alignment effect and should be included in particular when comparing intrinsic alignment spectra with the straightforward galaxy clustering; in this sense the intrinsic shapes and sizes become weighted clustering spectra.

- Using the standard Poisson-equation, the galaxy sizes provide a direct mapping of the ambient matter density, and that the intrinsic and extrinsic shapes and sizes are consistent to each other. To which extend this can be used to probe deviations from Newtonian gravity is largely unclear and depends on a detailed understanding of the astrophysics of the objects. When using shape- and size-correlations as cosmological probes, the Poisson equation causes them to contain only degenerate information, and there is a direct mapping between GG, GI and II-type terms. In addition, the shape and size-correlations are highly degenerate to the point where size correlations become redundant in comparison to the stronger and more sensitive shape correlations. We would like to make a point, however, that size correlations can provide an alternative method for mapping out the matter distribution.

- Similar to the case of shape correlations, one obtains a completely diagonal autocorrelation for the intrinsic sizes, $C^{ss}_{AB}(\ell) \propto \delta_{AB}$ and a non-diagonal cross-correlation between size and convergence, $C^{s\kappa}_{AB}(\ell)$, so the non-diagonal part of the lensing signal only contains GG and GI, but never II-terms [161, 278, 156], and in principle nulling- and boosting techniques [169, 167, 168] are applicable to size-correlations as well.

- Computing a forecast for Euclid we obtain the result that intrinsic shape- and size-correlations as well as their cross-correlations with lensing are measurable. Typical signal to noise-ratios obtained for 5-bin tomography are with Euclid range around 10 for $C^{\gamma\epsilon}_{AB}(\ell)$- and $C^{\epsilon\epsilon}_{AB}(\ell)$-correlations, while size correlations are more difficult to detect. Simulating two strategies, measuring correlations in the full galaxy sample or pre-selecting elliptical galaxies first, showed that the latter could be able to make $C^{\epsilon\epsilon}_{AB}(\ell)$-correlations detectable. Our forecasts used a conservative value for the alignment parameter, $D \simeq -10^{-5}$, which should strongly depend on the mass scale [241] and potentially on the profile shape as well. With this value of D, among the size correlations, only $C^{\kappa s}_{AB}(\ell)$ could yield a marginal detection. But since the intrinsic signal is directly proportional to D, increasing D by a factor 3-4 would change this result.

- Investigating the dependence of the spectra on the fundamental parameters of the cosmological model with a standard Fisher-matrix analysis showed that intrinsic shape and size-correlations have essentially identical parameter dependences, irrespective of whether the mechanism is gravitational lensing or intrinsic alignments. Typically, the shape-measurement yields smaller Poissonian errors compared to the size estimation, such that the value of the errors is smaller in a size measurement. A combination of the two measurements would not yield significant improvements due to the large covariance between the two measurements. Nevertheless, since they are complementary, the two measurements can provide a consistency test for General Relativity on cosmological scales. We pursued two strategies, which consist in pre-selecting the elliptical galaxies, which increases the noise due to reducing the data, or keeping the full galaxy sample and downweighting the GI- and II-terms with the fraction of elliptical galaxies. The first strategy yielded tighter errors, but in the second strategy one picks up stronger contributions from the GI- and II-terms to the Fisher-matrix, which in turn are very similar to galaxy clustering correlations.

In the future, we would like to investigate the usability of both types of shape and size spectra for designing specific tests of gravity, for instance for Vainshtein-type screening mechanisms [186, 288], which would manifest themselves in differences between the intrinsic and extrinsic shape and size spectra. Likewise, there is the question whether measurements of the velocity dispersion could help to disentangle intrinsic size from lensing shear, as the size effect would cause galaxies with the same velocity dispersion to appear systematically larger in underdense regions, and through velocity dispersion a common baseline could be established. In addition, we would like to point out that the susceptibility $\int \partial r\, r^5 \rho(r)$ of a stellar system with density ρ could differ for subclasses of elliptical galaxies giving rise to different effective alignment parameters D. Lastly, we would like to comment on possible intrinsic-size and shape effects arising at second order: Similar to lens-lens coupling one could expect a B-mode generation if lensing shear acts on a correlated intrinsic ellipticity field [similar to 79], and if lensing deflection shifts the galaxies to new positions [117, 118]. To what extent spiral galaxies would exhibit similar intrinsic size correlations is unclear, and possibly much more dependent on the astrophysics of galaxy formation, beyond models of tidal torquing [259]. Lastly we would argue that intrinsic size correlations are straightforward to be implemented in effective field theories of structure formation [105, 298], as they only require the computation of $\Delta\Phi$ on a smoothed field.

8

Summary and Conclusions

In this thesis, we highlighted the importance of reconciling theory with observations, when it comes to analysing the results of galaxy survey data. We emphasised on the fact that the observable galaxy number counts are not merely an estimate of the overdensity that we would naively expect, but a combination of different contributions that arise due to density and volume perturbations of the observed light cone along the way as photons propagate from the galaxies to the observer on earth. We established that the only way we can truly observe galaxies in the sky is via an approach that is dependent on their redshift and angular position. In more details, we addressed the corrections due to redshift-space distortion (RSD) and weak gravitational lensing, and especially for the latter, we came to the conclusion that the inclusion of these effects for upcoming surveys probing higher redshifts is indispensable. For this, we studied the two-point statistics of galaxy observables, namely the correlation function, power spectrum and angular power spectrum, and which of these suit our requirements the best. We also discussed the treatment of these statistics in the non-linear regime, which will be useful for a more enriched understanding of cosmological structure formation.

In Chapter 2 we mathematically proved that the intuitive expectation of the frame-independence of observable galaxy number counts is true. This work is based upon the importance of studying theories of gravity beyond general relativity, the scalar-tensor theory in this case, where we showed that by a simple conformal transformation we can go from the usual Einstein frame to the Jordan frame. We computed the behaviour of the background as well as perturbation quantities in both these frames and found that while many of them are either gauge-invariant or frame-invariant, the truly observable galaxy number counts are both, re-establishing them as good physical observables.

In Chapter 3, we computed the full-sky relativistic correlation function and power spectrum including all relativistic effects, in an attempt to go beyond the usually adopted flat-sky approximation approach. We did this via two approaches - one involving the direct computation of the correlation function, and the other via the angular power spectra. We conclude that the contribution of lensing multipoles at higher redshifts is highly significant, while the other large-scale relativistic effects

are more prominent at smaller redshifts. We also found that the corrections due to large-scale effects and wide angle corrections are of the same order of magnitude.

In Chapter 4, we tried to find a way to model the angular power spectra C_ℓ's in the nonlinear regime but in the redshift-space. This is a challenging task because the existing analytical prescriptions do not agree very well with numerical simulations, which have so far been considered the best approach in dealing with nonlinearities. Although we specified the reason for using C_ℓ's as the ability to incorporate relativistic effects, for the current work we went only up to including redshift space distortions as a first step towards more complicated computations in the near future. We adopted a flat-sky approximation for faster computations, which we confirm to be agreeing up to 1% with results obtained from a full-sky code such as CAMB. We studied different perturbation methods, including one-loop corrections to SPT, LPT, EFT and TNS, and compared them with a partial N-body simulation like COLA. We concluded that we need to model the density power spectrum similar to halofit but then correct for non-linear RSD like in the TNS model, especially for narrow redshift bins which are sensitive to RSD.

In Chapter 5, we shifted our focus to lensing, and stressed on the importance of lensing corrections in galaxy-galaxy lensing probes. We talked about additional lensing contributions in the observed signal that arise due to the presence of matter distribution between the foreground galaxies and the observer, which we suggested to include in the main signal and not just in the error budget. To demonstrate this, we used a mock survey where we use the DES redshift bins with Gaussian distribution, and found that the contribution due to lensing-lensing correlation is only around 1.5% for the weakest correlation, but up to 50% for the strongest. Also, when we repeated the same exercise for higher redshifts intended to be probed by Euclid, we find that this contribution goes up even further, up to 70%. This proves the fact that the higher in redshifts we go, the more significant the lensing corrections become.

In Chapter 6, we studied lensing corrections again, but in the case of E_g statistics which is a test of gravity at large cosmological scales. E_g statistics work in the linear perturbation theory regime only, but are useful because of their positive feature of giving a bias-independent measurement, provided we use the same galaxy population. Following our discussions in Chapter 5, it is only natural to expect that lensing corrections will have a strong effect in E_g statistics as well. However, if we try to incorporate these corrections, the bias-independence of the measurements are compromised, which can be tackled in case of intensity mapping surveys where lensing doesn't come into the picture. Our work here was to try to implement a method by which lensing can be incorporated even in the usual galaxy surveys, for which we use the observable spectra. We found that the errors that arise due to non-inclusion of lensing increase significantly from 4% to 40% with higher foreground redshifts, as expected.

In Chapter 7, we went one step ahead and analysed additional astrophysical effects on weak lensing, namely the intrinsic alignment effects. These effects, that arise out of the interaction of galaxies with their tidal shear fields, are in some ways analogous to lensing itself, and by studying their contribution to the total lensing

signal in terms of shape and size correlations, we can obtain information about how convenient it is to measure either shape, size or both and how much error is incurred in these measurements. We find that these intrinsic correlations have the same parameter dependences, whether the underlying mechanism is lensing or intrinsic alignment. We also found that shape estimation has a better cumulative signal-to-noise ratio than size estimation, although a combination of the two may not cause a dramatic improvement in the measurements.

The work that has been discussed in this thesis can be extended to answer more unsolved questions on relativistic contributions in galaxy observations. As mentioned, the E_g statistics as a test of gravity has the shortcoming of being applicable only at large cosmological scales, and under the regime of linear perturbation theory. While going to nonlinear scales, we must of course consider higher orders in perturbation theory and employ a better test of gravity that is more general in its approach. It will be interesting to see how important are general relativistic corrections in such tests which are easy to implement in the nonlinear regime as well.

Secondly, since angular power spectra are the truly observable quantities, we have made an attempt to model them in the redshift space, that is, with the inclusion of RSD effects. However, as already explained, it is not ideal to ignore lensing contributions in the main signal, which makes it imperative to consider them as well in the nonlinear regime. In the Appendix 3.C we have shown that even if the lensing contribution is negligible compared to RSD for wide redshift bins, it is of the same order as RSD for narrow bins and should not be neglected. It will be computationally challenging yet important to include these contributions for modelling angular power spectra in the nonlinear regime.

Finally, along with lensing contributions in the above-mentioned cases of testing gravity and modelling of angular power spectra, we should also take into consideration the systematic effects of astrophysical origin like intrinsic alignments that have a signature in our measurements. It is difficult to isolate them from weak lensing signals in which they are inherently included, and therefore measurements that involve the correlation of shear and galaxy number counts should be extended to take into account these intrinsic effects and the magnitude of their contribution should be assessed.

A

Useful mathematics

The sections below provide a brief introduction to a few mathematical concepts that have been used in the thesis. They can be studied in more detail in [94] and [21].

A.1 Fourier transform

The Fourier transform of any function $f(x)$ can be given to express it in a configurational space. According to the convention we use in this thesis, the Fourier transform of a spatial 3-vector can be give as:

$$f(\mathbf{k}) = \int d^3x f(\mathbf{x}) e^{i\mathbf{k}\cdot\mathbf{x}} \tag{A.1}$$

so that the inverse Fourier transform is

$$f(\mathbf{x}) = \frac{1}{(2\pi)^3} \int d^3k f(\mathbf{k}) e^{-i\mathbf{k}\cdot\mathbf{x}} \tag{A.2}$$

A.2 Legendre polynomials

The Legendre polynomials are defined in the interval [-1, 1] and formal an orthonormal set. The normalisation condition is the following:

$$\int_{-1}^{1} dx P_\ell(x) P'_\ell(x) = \frac{2}{2\ell+1} \delta_{\ell\ell'} \tag{A.3}$$

The Legendre polynomials obey the following differential equation:

$$(1-x^2)P''_\ell - 2xP'_\ell + \ell(\ell+1)P_\ell = 0 \tag{A.4}$$

We can obtain them via the recursion relation:

$$(\ell+1)P_{\ell+1}(x) = (2\ell+1)xP_\ell(x) - \ell P_{\ell-1}(x) \tag{A.5}$$

The Rodrigues' formula is:

$$P_\ell(x) = \frac{1}{2^\ell \ell!}\frac{d^\ell}{dx^\ell}(x^2-1)^\ell \tag{A.6}$$

Some of the lowest-order Legendre polynomials are as follows:

$$P_0 = 1, \tag{A.7}$$
$$P_1 = x, \tag{A.8}$$
$$P_2 = \frac{1}{2}(3x^2-1), \tag{A.9}$$
$$P_3 = \frac{1}{2}(5x^3-3x), \tag{A.10}$$
$$P_4 = \frac{1}{8}(35x^4-30x^2+3) \tag{A.11}$$

We also find that $P_\ell(-x) = (-1)^\ell P_\ell(x)$ and $P_\ell(1) = 1$.
Finally, we can define the associate Legendre functions by:

$$P_{\ell m}(x) = (1-x^2)^{m/2}\frac{d^m P_\ell(x)}{dx^m} = (1-x^2)^{m/2}\frac{1}{2^\ell \ell!}\frac{d^{\ell+m}}{dx^{\ell+m}}(x^2-1)^\ell \tag{A.12}$$

for $0 \leq m \leq \ell$. These Legendre functions are solutions of the following differential equation:

$$(1-x^2)P"_{\ell m} - 2xP'_{\ell m} + \left[\ell(\ell+1) - \frac{m^2}{1-x^2}\right]P_\ell m = 0 \tag{A.13}$$

The orthogonality relation holds as follows:

$$\int_{-1}^{1} P_{\ell m}(x)P_{\ell' m}(x)dx \tag{A.14}$$
$$= \int_0^\pi P_{\ell m}(\cos\vartheta)P_{\ell' m}(\cos\vartheta\sin\vartheta)d\vartheta = \frac{2}{2\ell+1}\frac{(\ell+m)!}{(\ell-m)!}\delta_{\ell\ell'} \tag{A.15}$$

A.3 Spherical harmonics

For our purpose, it is sufficient to be familiar with spherical harmonics of spin-0. If we have a unit vector $\mathbf{n}$ defined by its polar angles (ϑ, φ), we can write the spherical harmonics as:

$$Y_{\ell m} = (-1)^m\sqrt{\frac{2\ell+1}{4\pi}\frac{(\ell-m)!}{(\ell+m)!}}e^{im\varphi}P_{\ell m}(\mu), \quad \mu = \cos\vartheta \tag{A.16}$$

We can also prove that $Y_{\ell -m} = (-1)^m \bar{Y}_{\ell m}$ and the orthogonality relation holds as follows:

$$\int Y_{\ell m}(\mathbf{n})\hat{Y}_{\ell' m'}(\mathbf{n})d\Omega_{\mathbf{n}} = \delta_{\ell\ell'}\delta_{mm'} \tag{A.17}$$

The addition theorem for spherical harmonics is given by:

$$\frac{2\ell+1}{4\pi}P_\ell(\mathbf{n}_1\cdot\mathbf{n}_2)) = \sum_{m=-\ell}^{\ell}\hat{Y}_{\ell m}(\mathbf{n}_1)Y_{\ell m}(\mathbf{n}_2) \tag{A.18}$$

Some of the lower spherical harmonics are given by:

$$\ell = 0 \quad Y_{00} = \frac{1}{\sqrt{4\pi}}, \tag{A.19}$$

$$\ell = 1 \quad \begin{cases} Y_{11} &= -\sqrt{\frac{3}{8\pi}}\sin\vartheta e^{i\varphi}, \\ Y_{10} &= \sqrt{\frac{3}{4\pi}}\cos\vartheta, \end{cases} \tag{A.20}$$

$$\ell = 2 \quad \begin{cases} Y_{22} &= \sqrt{\frac{15}{32\pi}}\sin^2\vartheta e^{2i\varphi}, \\ Y_{21} &= -\sqrt{\frac{15}{8\pi}}\sin\vartheta\cos\vartheta e^{i\varphi}, \\ Y_{20} &= \sqrt{\frac{5}{4\pi}}\left(\frac{3}{2}\cos^2\vartheta - \frac{1}{2}\right), \end{cases} \tag{A.21}$$

$$\ell = 3 \quad \begin{cases} Y_{33} &= -\sqrt{\frac{35}{64\pi}}\sin^3\vartheta e^{3i\varphi}, \\ Y_{32} &= \sqrt{\frac{105}{32\pi}}\sin^2\vartheta\cos\vartheta e^{2i\varphi}, \\ Y_{31} &= -\sqrt{\frac{21}{16\pi}}\sin\vartheta\left(\frac{5}{2}\cos^2\vartheta - \frac{1}{2}\right)e^{i\varphi}, \\ Y_{30} &= \sqrt{\frac{7}{4\pi}}\cos\vartheta\left(\frac{5}{2}\cos^2\vartheta - \frac{3}{2}\right) \end{cases} \tag{A.22}$$

$$Y_{\ell-m} = (-1)^m Y^*_{\ell m} \tag{A.23}$$

A.4 Bessel functions and spherical Bessel functions

The two kinds of Bessel functions $J_\nu(x)$ and $Y_\nu(x)$ are real solutions to the following differential equation:

$$x^2\frac{d^f}{dx^2} + x\frac{df}{dx} + (x^2-\nu^2)f = 0 \tag{A.24}$$

The Hankel functions can be defined as:

$$H^{(1)}_\nu = J_\nu + iY_\nu, \quad H^{(2)}_\nu = J_\nu - iY_\nu \tag{A.25}$$

These functions satisfy the recurrence relations:

$$F_{\nu-1} + F_{\nu+1} = \frac{2\nu}{x}F_\nu, \tag{A.26}$$

$$F_{\nu-1} - F_{\nu+1} = 2F'_\nu, \tag{A.27}$$

$$F_{\nu-1} - \frac{\nu}{x}F_\nu = F'_\nu, \tag{A.28}$$

$$-F_{\nu+1} + \frac{\nu}{x}F_\nu = F'_\nu \tag{A.29}$$

We can represent the Bessel functions J_n, $n \in \mathbb{N}$ as the integral:

$$J_n(x) = \frac{(-i)^n}{\pi} \int_0^\pi e^{ix\cos\theta} \cos(n\theta) d\theta \tag{A.30}$$

from which we obtain the expansion:

$$e^{iy\cos\phi} = J_0(y) + 2\sum_{n=1}^{\infty} i^n J_n(y)\cos(n\phi) = \sum_{n=-\infty}^{\infty} i^n J_n(y) e^{in\phi} \tag{A.31}$$

The spherical Bessel and Hankel functions can be derived from the normal Bessel and Hankel functions as follows:

$$j_n(x) = \sqrt{(}\pi/2x) J_{n+1/2}(x), \tag{A.32}$$
$$y_n(x) = \sqrt{(}\pi/2x) Y_{n+1/2}(x), \tag{A.33}$$
$$h_n^{(1)} = j_n + iy_n, \tag{A.34}$$
$$h_n^{(2)} = j_n - iy_n. \tag{A.35}$$

They are solutions of the differential equation:

$$x^2 \frac{d^f}{dx^2} + 2x\frac{df}{dx} + (x^2 - n(n+1)))f = 0 \tag{A.36}$$

and they satisfy the following recurrence relations:

$$\frac{f_n}{x} = \frac{1}{2n+1}(f_{n-1} + f_{n+1}), \tag{A.37}$$
$$f_n' = \frac{1}{2n+1}(nf_{n-1} - (n+1)f_{n+1}), \tag{A.38}$$

The following expansion holds for an exponential function in terms of spherical Bessel functions and spherical harmonics:

$$e^{i\mathbf{x}\cdot\mathbf{k}} = e^{ikr\hat{x}\cdot\hat{k}} = \sum_{\ell m} j_{\ell m} j_{\ell m}(rk) Y_{\ell m}(\hat{x}) \tag{A.39}$$

Having determined the coefficients $c_{\ell m}$, we also find that

$$e^{i\mathbf{k}\cdot\mathbf{n}r} = \sum_{\ell=0}^{\infty} (2\ell+1) i^\ell j_\ell(kr) P_\ell(\mu) \tag{A.40}$$

where $P_\ell(\mu)$ are Legendre polynomials.

B

Derivation of kernels for one-loop SPT terms

This appendix can be seen as an extension to Appendix 4.A where we have not shown the detailed calculations for the kernels involved in the integration in Eq. (4.A25). Here we try to show explicitly the calculations for the same.

The kernels J_3^S and K_3^S are expressed in terms of the kernels J_2^S and K_2^S given in equations (4.A26) and (4.A27) respectively.

$$\begin{aligned} J_3^S(\mathbf{q}_1,\mathbf{q}_2,\mathbf{q}_3) = \frac{1}{3}\Bigg[& 7\frac{\mathbf{q}.\mathbf{q}_1}{q_1^2}J_2^S(\mathbf{q}_2,\mathbf{q}_3) + \frac{q^2\mathbf{q}_1.(\mathbf{q}_2+\mathbf{q}_3)}{q_1^2|\mathbf{q}_2+\mathbf{q}_3|2}K_2^S(\mathbf{q}_2,\mathbf{q}_3) \\ & + 7\frac{\mathbf{q}.\mathbf{q}_2}{q_2^2}J_2^S(\mathbf{q}_3,\mathbf{q}_1) + \frac{q^2\mathbf{q}_2.(\mathbf{q}_3+\mathbf{q}_1)}{q_2^2|\mathbf{q}_3+\mathbf{q}_1|^2}K_2^S(\mathbf{q}_3,\mathbf{q}_1) \\ & + 7\frac{\mathbf{q}.\mathbf{q}_3}{q_3^2}J_2^S(\mathbf{q}_1,\mathbf{q}_2) + \frac{q^2\mathbf{q}_3.(\mathbf{q}_1+\mathbf{q}_2)}{q_3^2|\mathbf{q}_1+\mathbf{q}_2|^2}K_2^S(\mathbf{q}_1,\mathbf{q}_2) \\ & + \left(7\frac{\mathbf{q}.(\mathbf{q}_1+\mathbf{q}_2)}{|\mathbf{q}_1+\mathbf{q}_2|^2} + \frac{q^2(\mathbf{q}_1+\mathbf{q}_2).\mathbf{q}_3}{|\mathbf{q}_1+\mathbf{q}_2|^2q_3^2}\right)K_2^S(\mathbf{q}_1,\mathbf{q}_2) \\ & + \left(7\frac{\mathbf{q}\cdot(\mathbf{q}_2+\mathbf{q}_3)}{|\mathbf{q}_2+\mathbf{q}_3|^2} + \frac{q^2(\mathbf{q}_2+\mathbf{q}_3).\mathbf{q}_1}{|\mathbf{q}_2+\mathbf{q}_3|^2q_1^2}\right)K_2^S(\mathbf{q}_2,\mathbf{q}_3) \\ & + \left(7\frac{\mathbf{q}\cdot(\mathbf{q}_3+\mathbf{q}_1)}{|\mathbf{q}_3+\mathbf{q}_1|^2} + \frac{q^2(\mathbf{q}_3+\mathbf{q}_1)\cdot\mathbf{q}_2}{|\mathbf{q}_3+\mathbf{q}_1|^2q_2^2}\right)K_2^S(\mathbf{q}_3,\mathbf{q}_1)\Bigg] \end{aligned} \tag{B.1}$$

$$\begin{aligned} K_3^S(\mathbf{q}_1,\mathbf{q}_2,\mathbf{q}_3) = \frac{1}{3}\Bigg[& \frac{\mathbf{q}_1.\mathbf{q}}{q_1^2}J_2^S(\mathbf{q}_2,\mathbf{q}_3) + \frac{q^2\mathbf{q}_1.(\mathbf{q}_2+\mathbf{q}_3)}{q_1^2|\mathbf{q}_2+\mathbf{q}_3|2}K_2^S(\mathbf{q}_2,\mathbf{q}_3) \\ & + \frac{\mathbf{q}_2.\mathbf{q}}{q_2^2}J_2^S(\mathbf{q}_3,\mathbf{q}_1) + \frac{q^2\mathbf{q}_2.(\mathbf{q}_3+\mathbf{q}_1)}{q_2^2|\mathbf{q}_3+\mathbf{q}_1|2}K_2^S(\mathbf{q}_3,\mathbf{q}_1) \\ & + \frac{\mathbf{q}_3.\mathbf{q}}{q_3^2}J_2^S(\mathbf{q}_1,\mathbf{q}_2) + \frac{q^2\mathbf{q}_3.(\mathbf{q}_1+\mathbf{q}_2)}{q_3^2|\mathbf{q}_1+\mathbf{q}_2|2}K_2^S(\mathbf{q}_1,\mathbf{q}_2) \\ & + \left(\frac{\mathbf{q}.(\mathbf{q}_1+\mathbf{q}_2)}{|\mathbf{q}_1+\mathbf{q}_2|^2} + \frac{q^2(\mathbf{q}_1+\mathbf{q}_2).\mathbf{q}_3}{|\mathbf{q}_1+\mathbf{q}_2|^2q_3^2}\right)K_2^S(\mathbf{q}_1,\mathbf{q}_2) \\ & + \left(\frac{\mathbf{q}.(\mathbf{q}_2+\mathbf{q}_3)}{|\mathbf{q}_2+\mathbf{q}_3|^2} + \frac{q^2(\mathbf{q}_2+\mathbf{q}_3).\mathbf{q}_1}{|\mathbf{q}_2+\mathbf{q}_3|^2q_1^2}\right)K_2^S(\mathbf{q}_2,\mathbf{q}_3) \end{aligned} \tag{B.2}$$

$$+\left(\frac{\mathbf{q}.(\mathbf{q}_3+\mathbf{q}_1)}{|\mathbf{q}_3+\mathbf{q}_1|^2}+\frac{q^2(\mathbf{q}_3+\mathbf{q}_1).\mathbf{q}_2}{|\mathbf{q}_3+\mathbf{q}_1|^2q_2^2}\right)K_2^S(\mathbf{q}_3,\mathbf{q}_1)\Bigg]$$

The angles between the vectors in question are given as μ_1, μ_2 and μ_3. Then we have,

$$\begin{aligned}F_2^S(\mathbf{q},\mathbf{k}\text{-}\mathbf{q}) = b_1J_2^S(\mathbf{q},\mathbf{k}\text{-}\mathbf{q}) + f\mu^2K_2^S(\mathbf{q},\mathbf{k}\text{-}\mathbf{q}) \\ + \frac{b_1f}{2}\left[\mu_1^2+\mu_2^2+\mu_1\mu_2\left(\frac{q}{k-q}+\frac{k-q}{q}\right)\right] \\ + f^2\left[\mu_1^2\mu_2^2+\frac{\mu_1\mu_2}{2}\left(\mu_1^2\frac{q}{k-q}+\mu_2^2\frac{k-q}{q}\right)\right]\end{aligned} \tag{B.3}$$

and a similar but much complicated expression for $F_3^S(\mathbf{q},\mathbf{-q},\mathbf{k})$ as can be seen in Eq. (10b) of [129]. We do not show this expression here because in the case of $F_3^S(\mathbf{q},\mathbf{-q},\mathbf{k})$, we integrate all the terms individually in our code.

Finally, the result of the integrations look like the following:

$$\begin{aligned}&\int_0^{2\pi}d\phi_q[F_2^S(q,\phi_q,x,\mu,b_1,f)]^2\\ =&\frac{1}{784}(4b_1^2(49(-f^2\mu^2(-1+\mu^2)+x^2(1+4f\mu^2+f^2\mu^2(-1+3\mu^2)))\\ &-28rx(-3-10f\mu^2+f^2(7\mu^2-14\mu^4)+x^2(10+24f\mu^2+7f^2\mu^2(-1+3\mu^2)))\\ &+2r^2((3+7f\mu^2)^2-2x^2(30+112f\mu^2+49f^2\mu^2(-1+3\mu^2))\\ &+2x^4(50+140f\mu^2+49f^2\mu^2(-1+3\mu^2))))+8b_1f\mu^2(49(-f^2\mu^2(-1+\mu^2)\\ &+x^2(2+4f\mu^2+f^2\mu^2(-1+3\mu^2)))+r^2(2(-3-8x^2+60x^4)\\ &+49f^2\mu^2(-1+\mu^2+x^2(7-9\mu^2)+2x^4(-3+5\mu^2))+7f(-3+\mu^2+x^2(13-27\mu^2)\\ &+2x^4(-5+27\mu^2)))-7rz(-4+32x^2+7f^2\mu^2(5-7\mu^2+x^2(-5+11\mu^2))\\ &f(7-25\mu^2+x^2(-7+81\mu^2))))+f^2\mu^4(196(-f^2\mu^2(-1+\mu^2)\\ &+x^2(2+4f\mu^2+f^2\mu^2(-1+3\mu^2)))-56rx(2+12x^2+7f^2\mu^2(3-3\mu^2+x^2(-3+5\mu^2))\\ &+f(7-5\mu^2+x^2(-7+33\mu^2)))\\ &r^2(8(1+6x^2)^2+56f(1+6x^2)(1-\mu^2+x^2(-1+3\mu^2))\\ &+49f^2(3(-1+\mu^2)^2-6x^2(1-6\mu^2+5\mu^4)\\ &+x^4(3-30\mu^2+35\mu^4))))).\end{aligned} \tag{B.4}$$

$$\begin{aligned}&\int_{-1}^1d\mu_q\int_0^{2\pi}d\phi_q[F_3^S(q,\phi_q,x,\mu,b_1,f)]^2\\ &=\pi\left[-\frac{4b_1f^2}{15}-\frac{8b_1f^2\mu^2}{9}-\frac{2b_1f^2\mu^2}{9r^2}-\frac{4b_1f(1+r^2)\mu^2}{9r^2}-\frac{2f^3\mu^4}{9r^2}+\frac{2}{3}b_1f^2\left(\frac{2}{5}+\frac{4\mu^2}{3}\right)\right.\\ &+\frac{f\mu^2(12r-82r^3+4r^5-6r^7+3(-1+r^2)^3(2+r^2)\log\left(\frac{1+r}{1-r}\right)}{252r^5}\\ &b_1\frac{2r(6-79r^2+50r^4-21r^6)+3(-1+r^2)^3(2+7r^2)\log\left(\frac{1+r}{1-r}\right)}{756r^5}\end{aligned}$$

$$\frac{1}{3}\left(\frac{1}{168k^8r^5}f\mu^2(18fk^8r-66fk^8r^3-66fk^8r^5+18fk^8r^7+8b_1k^4r^3(9k^4+52k^4r^2-9k^4r^4)\right.$$
$$-9fk^2(k-kr)^3(k+kr)^3\log\left(\frac{1+r}{1-r}\right)-36b_1k^2r^2(k-kr)^3(k+kr)^3\log\left(\frac{1+r}{1-r}\right)$$
$$+9fk^2r^2(k-kr)^3(k+kr)^3\log\left(\frac{1+r}{1-r}\right)+\frac{1}{168k^8r^5}f\mu^4\left(18fk^8r-218fk^8r^3+126fk^8r^5\right.$$
$$-54fk^8r^7-9fk^2(k-kr)^3(k+kr)^3\log\left(\frac{1+r}{1-r}\right)$$
$$\left.\left.-27fk^2r^2(k-kr)^3(k+kr)^3\log\left(\frac{1+r}{1-r}\right)\right)\right)\Bigg]\,. \tag{B.5}$$

Bibliography

[1] T. M. C. Abbott et al. "Dark Energy Survey Year 1 Results: Cosmological Constraints from Galaxy Clustering and Weak Lensing". In: *arXiv 1708.01530* (2017). arXiv: 1708.01530 [astro-ph.CO].

[2] Filipe Batoni Abdalla et al. "Cosmology from HI galaxy surveys with the SKA". In: *PoS* AASKA14 (2015), p. 017.

[3] Paul A. Abell et al. "LSST Science Book, Version 2.0". In: (2009). arXiv: 0912.0201 [astro-ph.IM].

[4] M. Abramowitz and I. Stegun. *Handbook of Mathematical Functions*. 9th Printing. Dover Publications, New York, 1970.

[5] Milton Abramowitz and Irene A. Stegun. *Handbook of Mathematical Functions*. New York, USA: Dover, 1972.

[6] Ixandra Achitouv et al. "Consistency of the growth rate in different environments with the 6-degree Field Galaxy Survey: Measurement of the void-galaxy and galaxy-galaxy correlation functions". In: *Phys. Rev.* D95.8 (2017), p. 083502. DOI: 10.1103/PhysRevD.95.083502. arXiv: 1606.03092 [astro-ph.CO].

[7] Julian Adamek, Ruth Durrer, and Martin Kunz. "Relativistic N-body simulations with massive neutrinos". In: *JCAP* 1711.11 (2017), p. 004. DOI: 10.1088/1475-7516/2017/11/004. arXiv: 1707.06938 [astro-ph.CO].

[8] Julian Adamek et al. "gevolution: a cosmological N-body code based on General Relativity". In: *Journal of Cosmology and Astroparticle Physics* 2016.07 (July 2016), pp. 053–053. ISSN: 1475-7516. DOI: 10.1088/1475-7516/2016/07/053. URL: http://dx.doi.org/10.1088/1475-7516/2016/07/053.

[9] Caitlin Adams and Chris Blake. "Improving constraints on the growth rate of structure by modelling the density-velocity cross-correlation in the 6dF Galaxy Survey". In: (2017). arXiv: 1706.05205 [astro-ph.CO].

[10] P. A. R. Ade et al. "Joint Analysis of BICEP2/*Keck Array* and *Planck* Data". In: *Phys.Rev.Lett.* 114.10 (2015), p. 101301. DOI: 10.1103/PhysRevLett.114.101301. arXiv: 1502.00612 [astro-ph.CO].

[11] P.A.R. Ade et al. "Planck 2013 results. I. Overview of products and scientific results". In: *Astron.Astrophys.* 571 (2014), A1. DOI: 10.1051/0004-6361/201321529. arXiv: 1303.5062 [astro-ph.CO].

[12] P.A.R. Ade et al. "Planck 2015 results. XIII. Cosmological parameters". In: (2015). arXiv: 1502.01589 [astro-ph.CO].

[13] Amir Aghamousa et al. "The DESI Experiment Part I: Science,Targeting, and Survey Design". In: (2016). arXiv: 1611.00036 [astro-ph.IM].

[14] Shadab Alam et al. "The clustering of galaxies in the completed SDSS-III Baryon Oscillation Spectroscopic Survey: cosmological analysis of the DR12 galaxy sample". In: *Mon. Not. Roy. Astron. Soc.* 470.3 (2017), pp. 2617–2652. DOI: 10.1093/mnras/stx721. arXiv: 1607.03155 [astro-ph.CO].

[15] R. A. Alpher, H. Bethe, and G. Gamow. "The origin of chemical elements". In: *Phys. Rev.* 73 (1948), pp. 803–804. DOI: 10.1103/PhysRev.73.803.

[16] Justin Alsing et al. "Weak Lensing with Sizes, Magnitudes and Shapes". In: *Mon. Not. Roy. Astron. Soc.* 452.2 (2015), pp. 1202–1216. DOI: 10.1093/mnras/stv1249. arXiv: 1410.7839 [astro-ph.CO].

[17] Gabriel Altay, Jorg M. Colberg, and Rupert A.C. Croft. "The Influence of Large-Scale Structure on Halo Shapes and Alignments". In: *Mon. Not. Roy. Astron. Soc.* 370 (2006), pp. 1422–1428. DOI: 10.1111/j.1365-2966.2006.10555.x. arXiv: astro-ph/0605296.

[18] Adam Amara and Alexandre Refregier. "Optimal Surveys for Weak Lensing Tomography". In: *Mon. Not. Roy. Astron. Soc.* 381 (2007), pp. 1018–1026. DOI: 10.1111/j.1365-2966.2007.12271.x. arXiv: astro-ph/0610127.

[19] Luca Amendola et al. "Cosmology and Fundamental Physics with the Euclid Satellite". In: *Living Reviews in Relativity* 21 (2018), p. 345. arXiv: 1606.00180 [astro-ph.CO].

[20] Lauren Anderson et al. "The clustering of galaxies in the SDSS-III Baryon Oscillation Spectroscopic Survey: Baryon Acoustic Oscillations in the Data Release 9 Spectroscopic Galaxy Sample". In: *Mon. Not. Roy. Astron. Soc.* 427.4 (2013), pp. 3435–3467. DOI: 10.1111/j.1365-2966.2012.22066.x. arXiv: 1203.6594 [astro-ph.CO].

[21] George B. Arfken and Hans J. Weber. *Mathematical Methods for Physicists.* Sixth Edition. Academic Press, New York, 2001.

[22] David J. Bacon et al. "Cosmology with Phase 1 of the Square Kilometre Array: Red Book 2018: Technical specifications and performance forecasts". In: *Submitted to: Publ. Astron. Soc. Austral.* (2018). arXiv: 1811.02743 [astro-ph.CO].

[23] Jeremy Bailin and Matthias Steinmetz. "Internal and external alignment of the shapes and angular momenta of lambda-CDM halos". In: *Astrophys. J.* 627 (2005), pp. 647–665. DOI: 10.1086/430397. arXiv: astro-ph/0408163.

[24] Kevin Bandura et al. "Canadian Hydrogen Intensity Mapping Experiment (CHIME) Pathfinder". In: *Proc. SPIE Int. Soc. Opt. Eng.* 9145 (2014), p. 22. DOI: 10.1117/12.2054950. arXiv: 1406.2288 [astro-ph.IM].

[25] Matthias Bartelmann. "Gravitational Lensing". In: *Class. Quant. Grav.* 27 (2010), p. 233001. DOI: 10.1088/0264-9381/27/23/233001. arXiv: 1010.3829 [astro-ph.CO].

[26] Matthias Bartelmann and Peter Schneider. "Weak gravitational lensing". In: *Phys. Rept.* 340 (2001), pp. 291–472. DOI: 10.1016/S0370-1573(00)00082-X. arXiv: astro-ph/9912508.

[27] James Bate et al. "When galaxies align: intrinsic alignments of the progenitors of elliptical galaxies in the Horizon-AGN simulation". In: *Mon. Not. Roy. Astron. Soc.* 491.3 (2020), pp. 4057–4068. DOI: 10.1093/mnras/stz3166. arXiv: 1911.04213 [astro-ph.CO].

[28] Daniel Baumann et al. "Cosmological Non-Linearities as an Effective Fluid". In: *JCAP* 1207 (2012), p. 051. DOI: 10.1088/1475-7516/2012/07/051. arXiv: 1004.2488 [astro-ph.CO].

[29] Lucía Fonseca de la Bella et al. "Impact of bias and redshift-space modelling for the halo power spectrum: Testing the effective field theory of large-scale structure". In: (2018). arXiv: 1805.12394 [astro-ph.CO].

[30] F. Bernardeau et al. "Large scale structure of the universe and cosmological perturbation theory". In: *Phys. Rept.* 367 (2002), pp. 1–248. DOI: 10.1016/S0370-1573(02)00135-7. arXiv: astro-ph/0112551 [astro-ph].

[31] G.M. Bernstein and M. Jarvis. "Shapes and shears, stars and smears: optimal measurements for weak lensing". In: *Astron. J.* 123 (2002), pp. 583–618. DOI: 10.1086/338085. arXiv: astro-ph/0107431.

[32] Gary M. Bernstein. "Comprehensive Two-Point Analyses of Weak Gravitational Lensing Surveys". In: *Astrophys. J.* 695 (2009), pp. 652–665. DOI: 10.1088/0004-637X/695/1/652. arXiv: 0808.3400 [astro-ph].

[33] Gary M. Bernstein and B. Jain. "Dark energy constraints from weak lensing cross - correlation cosmography". In: *Astrophys. J.* 600 (2004), pp. 17–25. DOI: 10.1086/379768. arXiv: astro-ph/0309332.

[34] Daniele Bertacca et al. "Beyond the plane-parallel and Newtonian approach: Wide-angle redshift distortions and convergence in general relativity". In: *JCAP* 1210 (2012), p. 025. DOI: 10.1088/1475-7516/2012/10/025. arXiv: 1205.5221 [astro-ph.CO].

[35] Florian Beutler et al. "The clustering of galaxies in the completed SDSS-III Baryon Oscillation Spectroscopic Survey: Anisotropic galaxy clustering in Fourier-space". In: *Mon. Not. Roy. Astron. Soc.* 466.2 (2017), pp. 2242–2260. DOI: 10.1093/mnras/stw3298. arXiv: 1607.03150 [astro-ph.CO].

[36] Florian Beutler et al. "The clustering of galaxies in the SDSS-III Baryon Oscillation Spectroscopic Survey: Testing gravity with redshift-space distortions using the power spectrum multipoles". In: *Mon. Not. Roy. Astron. Soc.* 443.2 (2014), pp. 1065–1089. DOI: 10.1093/mnras/stu1051. arXiv: 1312.4611 [astro-ph.CO].

[37] Somnath Bharadwaj and SK. Saiyad Ali. "On using visibility correlations to probe the HI distribution from the dark ages to the present epoch. 1. Formalism and the expected signal". In: *Mon. Not. Roy. Astron. Soc.* 356 (2005), p. 1519. DOI: 10.1111/j.1365-2966.2004.08604.x. arXiv: astro-ph/0406676 [astro-ph].

[38] Chris Blake et al. "RCSLenS: Testing gravitational physics through the cross-correlation of weak lensing and large-scale structure". In: *Mon. Not. Roy. Astron. Soc.* 456.3 (2016), pp. 2806–2828. DOI: 10.1093/mnras/stv2875. arXiv: 1507.03086 [astro-ph.CO].

[39] Chris Blake et al. "The WiggleZ Dark Energy Survey: the growth rate of cosmic structure since redshift z=0.9". In: *Mon. Not. Roy. Astron. Soc.* 415 (2011), p. 2876. DOI: 10.1111/j.1365-2966.2011.18903.x. arXiv: 1104.2948 [astro-ph.CO].

[40] Diego Blas, Mathias Garny, and Thomas Konstandin. "Cosmological perturbation theory at three-loop order". In: *JCAP* 1401.01 (2014), p. 010. DOI: 10.1088/1475-7516/2014/01/010. arXiv: 1309.3308 [astro-ph.CO].

[41] Diego Blas, Julien Lesgourgues, and Thomas Tram. "The Cosmic Linear Anisotropy Solving System (CLASS) II: Approximation schemes". In: *JCAP* 1107 (2011), p. 034. DOI: 10.1088/1475-7516/2011/07/034. arXiv: 1104.2933 [astro-ph.CO].

[42] Jonathan Blazek et al. "Beyond linear galaxy alignments". In: *Phys. Rev. D* 100.10 (2019), p. 103506. DOI: 10.1103/PhysRevD.100.103506. arXiv: 1708.09247 [astro-ph.CO].

[43] Jonathan Blazek et al. "Separating intrinsic alignment and galaxy-galaxy lensing". In: *JCAP* 05 (2012), p. 041. DOI: 10.1088/1475-7516/2012/05/041. arXiv: 1204.2264 [astro-ph.CO].

[44] Linda Blot et al. "Comparing approximate methods for mock catalogues and covariance matrices II: Power spectrum multipoles". In: *Mon. Not. Roy. Astron. Soc.* 485.2 (2019), pp. 2806–2824. DOI: 10.1093/mnras/stz507. arXiv: 1806.09497 [astro-ph.CO].

[45] G. R. Blumenthal et al. "Formation of galaxies and large-scale structure with cold dark matter." In: Nature 311 (Oct. 1984), pp. 517–525. DOI: 10.1038/311517a0.

[46] Camille Bonvin and Ruth Durrer. "What galaxy surveys really measure". In: *Phys.Rev.* D84 (2011), p. 063505. DOI: 10.1103/PhysRevD.84.063505. arXiv: 1105.5280 [astro-ph.CO].

[47] Camille Bonvin, Ruth Durrer, and M. Alice Gasparini. "Fluctuations of the luminosity distance". In: *Phys. Rev.* D73 (2006). [Erratum: Phys. Rev.D85,029901(2012)], p. 023523. DOI: 10.1103/PhysRevD.85.029901,10.1103/PhysRevD.73.023523. arXiv: astro-ph/0511183 [astro-ph].

[48] Camille Bonvin, Lam Hui, and Enrique Gaztanaga. "Asymmetric galaxy correlation functions". In: *Phys.Rev.* D89.8 (2014), p. 083535. DOI: 10.1103/PhysRevD.89.083535. arXiv: 1309.1321 [astro-ph.CO].

[49] Camille Bonvin, Lam Hui, and Enrique Gaztanaga. "Optimising the measurement of relativistic distortions in large-scale structure". In: *JCAP* 1608.08 (2016), p. 021. DOI: 10.1088/1475-7516/2016/08/021. arXiv: 1512.03566 [astro-ph.CO].

[50] Benjamin Bose and Kazuya Koyama. "A Perturbative Approach to the Redshift Space Power Spectrum: Beyond the Standard Model". In: *JCAP* 1608.08 (2016), p. 032. DOI: 10.1088/1475-7516/2016/08/032. arXiv: 1606.02520 [astro-ph.CO].

[51] Benjamin Bose, Kazuya Koyama, and Hans A. Winther. "Assessing non-linear models for galaxy clustering III: Theoretical accuracy for Stage IV surveys". In: (2019). arXiv: 1905.05135 [astro-ph.CO].

[52] Benjamin Bose et al. "Assessing non-linear models for galaxy clustering II: model selection and forecasts for Stage IV surveys". In: (2019). arXiv: 1905.05122 [astro-ph.CO].

[53] Benjamin Bose et al. "Theoretical accuracy in cosmological growth estimation". In: *Phys. Rev.* D96.2 (2017), p. 023519. DOI: 10.1103/PhysRevD.96.023519. arXiv: 1702.02348 [astro-ph.CO].

[54] C. Brans and R. H. Dicke. "Mach's Principle and a Relativistic Theory of Gravitation". In: *Physical Review* 124.3 (Nov. 1961), pp. 925–935. DOI: 10.1103/PhysRev.124.925.

[55] M.L. Brown et al. "Measurement of intrinsic alignments in galaxy ellipticities". In: *Mon. Not. Roy. Astron. Soc.* 333 (2002), p. 501. DOI: 10.1046/j.1365-8711.2002.05354.x. arXiv: astro-ph/0009499.

[56] Stefano Camera, Mario G. Santos, and Roy Maartens. "Probing primordial non-Gaussianity with SKA galaxy redshift surveys: a fully relativistic analysis". In: *Mon. Not. Roy. Astron. Soc.* 448.2 (2015), pp. 1035–1043. DOI: 10.1093/mnras/stv040,10.1093/mnras/stv040,10.1093/mnras/stx159. arXiv: 1409.8286 [astro-ph.CO].

[57] J. -E. Campagne, S. Plaszczynski, and J. Neveu. "The Galaxy Count Correlation Function in Redshift Space Revisited". In: *Astrophys. J.* 845.1 (2017), p. 28. DOI: 10.3847/1538-4357/aa7cf8. arXiv: 1703.02818 [astro-ph.CO].

[58] Federica Capranico, Philipp M. Merkel, and Björn Malte Schäfer. "Intrinsic ellipticity correlations of galaxies: models, likelihoods and interplay with weak lensing". In: *Mon. Not. Roy. Astron. Soc.* 435.1 (2013), pp. 194–206. DOI: 10.1093/mnras/stt1269. arXiv: 1207.5939 [astro-ph.CO].

[59] Wilmar Cardona et al. "Lensing convergence and the neutrino mass scale in galaxy redshift surveys". In: *Phys. Rev.* D94.4 (2016), p. 043007. DOI: 10.1103/PhysRevD.94.043007. arXiv: 1603.06481 [astro-ph.CO].

[60] Chris L. Carilli and S. Rawlings. "Science with the Square Kilometer Array: Motivation, key science projects, standards and assumptions". In: *New Astron. Rev.* 48 (2004), p. 979. DOI: 10.1016/j.newar.2004.09.001. arXiv: astro-ph/0409274 [astro-ph].

[61] Jordan Carlson, Martin White, and Nikhil Padmanabhan. "A critical look at cosmological perturbation theory techniques". In: *Phys. Rev.* D80 (2009), p. 043531. DOI: 10.1103/PhysRevD.80.043531. arXiv: 0905.0479 [astro-ph.CO].

[62] John Joseph M. Carrasco, Mark P. Hertzberg, and Leonardo Senatore. "The Effective Field Theory of Cosmological Large Scale Structures". In: *JHEP* 09 (2012), p. 082. DOI: 10.1007/JHEP09(2012)082. arXiv: 1206.2926 [astro-ph.CO].

[63] Luciano Casarini et al. "Non–linear weak lensing forecasts". In: *JCAP* 03 (2011), p. 026. DOI: 10.1088/1475-7516/2011/03/026. arXiv: 1102.3877 [astro-ph.CO].

[64] Emanuele Castorina and Martin White. "The Zeldovich approximation and wide-angle redshift-space distortions". In: *Mon. Not. Roy. Astron. Soc.* 479.1 (2018), pp. 741–752. DOI: 10.1093/mnras/sty1437. arXiv: 1803.08185 [astro-ph.CO].

[65] Paolo Catelan, Marc Kamionkowski, and Roger D. Blandford. "Intrinsic and extrinsic galaxy alignment". In: *Mon. Not. Roy. Astron. Soc.* 320 (2001), pp. L7–L13. DOI: 10.1046/j.1365-8711.2001.04105.x. arXiv: astro-ph/0005470.

[66] Riccardo Catena, Massimo Pietroni, and Luca Scarabello. "Einstein and Jordan reconciled: a frame-invariant approach to scalar-tensor cosmology". In: *Phys. Rev.* D76 (2007), p. 084039. DOI: 10.1103/PhysRevD.76.084039. arXiv: astro-ph/0604492 [astro-ph].

[67] Anthony Challinor and Antony Lewis. "The linear power spectrum of observed source number counts". In: *Phys.Rev.* D84 (2011), p. 043516. DOI: 10.1103/PhysRevD.84.043516. arXiv: 1105.5292 [astro-ph.CO].

[68] C. Chang et al. "Dark Energy Survey Year 1 Results: Curved-Sky Weak Lensing Mass Map". In: *Mon. Not. Roy. Astron. Soc.* 475.3 (2018), pp. 3165–3190. DOI: 10.1093/mnras/stx3363. arXiv: 1708.01535 [astro-ph.CO].

[69] Takeshi Chiba and Masahide Yamaguchi. "Conformal-Frame (In)dependence of Cosmological Observations in Scalar-Tensor Theory". In: *JCAP* 1310 (2013), p. 040. DOI: 10.1088/1475-7516/2013/10/040. arXiv: 1308.1142 [gr-qc].

[70] Nora Elisa Chisari and Cora Dvorkin. "Cosmological Information in the Intrinsic Alignments of Luminous Red Galaxies". In: *JCAP* 12 (2013), p. 029. DOI: 10.1088/1475-7516/2013/12/029. arXiv: 1308.5972 [astro-ph.CO].

[71] Nora Elisa Chisari and Andrew Pontzen. "Unequal time correlators and the Zeldovich approximation". In: (2019). arXiv: 1905.02078 [astro-ph.CO].

[72] Nora Elisa Chisari et al. "Contamination of early-type galaxy alignments to galaxy lensing–CMB lensing cross-correlation". In: *Mon. Not. Roy. Astron. Soc.* 453.1 (2015), pp. 682–689. DOI: 10.1093/mnras/stv1655. arXiv: 1507.03906 [astro-ph.CO].

[73] Nora Elisa Chisari et al. "Intrinsic alignments of galaxies in the Horizon-AGN cosmological hydrodynamical simulation". In: *Mon. Not. Roy. Astron. Soc.* 454.3 (2015), pp. 2736–2753. DOI: 10.1093/mnras/stv2154. arXiv: 1507.07843 [astro-ph.CO].

[74] Nora Elisa Chisari et al. "Intrinsic alignments of group and cluster galaxies in photometric surveys". In: *Mon. Not. Roy. Astron. Soc.* 445.1 (2014), pp. 726–748. DOI: 10.1093/mnras/stu1786. arXiv: 1407.4813 [astro-ph.CO].

[75] Nora Elisa Chisari et al. "Redshift and luminosity evolution of the intrinsic alignments of galaxies in Horizon-AGN". In: *Mon. Not. Roy. Astron. Soc.* 461.3 (2016), pp. 2702–2721. DOI: 10.1093/mnras/stw1409. arXiv: 1602.08373 [astro-ph.CO].

[76] Timothy Clifton et al. "Modified gravity and cosmology". In: *Physics Reports* 513.1-3 (Mar. 2012), pp. 1–189. ISSN: 0370-1573. DOI: 10.1016/j.physrep.2012.01.001. URL: http://dx.doi.org/10.1016/j.physrep.2012.01.001.

[77] Carlos Contreras et al. "The WiggleZ Dark Energy Survey: measuring the cosmic growth rate with the two-point galaxy correlation function". In: (2013). [Mon. Not. Roy. Astron. Soc.430,924(2013)]. DOI: 10.1093/mnras/sts608. arXiv: 1302.5178 [astro-ph.CO].

[78] Asantha Cooray and Wayne Hu. "Power spectrum covariance of weak gravitational lensing". In: *Astrophys. J.* 554 (2001), pp. 56–66. DOI: 10.1086/321376. arXiv: astro-ph/0012087.

[79] Asantha Cooray and Wayne Hu. "Second order corrections to weak lensing by large scale structure". In: *Astrophys. J.* 574 (2002), p. 19. DOI: 10.1086/340892. arXiv: astro-ph/0202411.

[80] Robert G. Crittenden et al. "Spin induced galaxy alignments and their implications for weak lensing measurements". In: *Astrophys. J.* 559 (2001), pp. 552–571. DOI: 10.1086/322370. arXiv: astro-ph/0009052.

[81] Kanan K. Datta, T. Roy Choudhury, and Somnath Bharadwaj. "The multi-frequency angular power spectrum of the epoch of reionization 21 cm signal". In: *Mon. Not. Roy. Astron. Soc.* 378 (2007), pp. 119–128. DOI: 10.1111/j.1365-2966.2007.11747.x. arXiv: astro-ph/0605546 [astro-ph].

[82] M. Davis et al. "The evolution of large-scale structure in a universe dominated by cold dark matter". In: ApJ 292 (May 1985), pp. 371–394. DOI: 10.1086/163168.

[83] Gerard de Vaucouleurs. "Recherches sur les Nebuleuses Extragalactiques". In: *Annales d'Astrophysique* 11 (Jan. 1948), p. 247.

[84] Victor P. Debattista et al. "Internal alignments of red versus blue discs in dark matter haloes". In: *Mon. Not. Roy. Astron. Soc.* 452.4 (2015), pp. 4094–4110. DOI: 10.1093/mnras/stv1563. arXiv: 1502.03429 [astro-ph.GA].

[85] Nathalie Deruelle and Misao Sasaki. "Conformal Equivalence in Classical Gravity: the Example of "Veiled" General Relativity". In: *Cosmology, Quantum Vacuum and Zeta Functions*. Ed. by Sergey D. Odintsov, Diego Sáez-Gómez, and Sebastian Xambó-Descamps. Berlin, Heidelberg: Springer Berlin Heidelberg, 2011, pp. 247–260. ISBN: 978-3-642-19760-4.

[86] Enea Di Dio et al. "Cosmological Parameter Estimation with Large Scale Structure Observations". In: *JCAP* 1401 (2014), p. 042. DOI: 10.1088/1475-7516/2014/01/042. arXiv: 1308.6186 [astro-ph.CO].

[87] Enea Di Dio et al. "Curvature constraints from Large Scale Structure". In: *JCAP* 1606.06 (2016), p. 013. DOI: 10.1088/1475-7516/2016/06/013. arXiv: 1603.09073 [astro-ph.CO].

[88] Enea Di Dio et al. "The CLASSgal code for Relativistic Cosmological Large Scale Structure". In: *JCAP* 1311 (2013), p. 044. DOI: 10.1088/1475-7516/2013/11/044. arXiv: 1307.1459 [astro-ph.CO].

[89] Enea Di Dio et al. "The Full-Sky Angular Bispectrum in Redshift Space". In: *JCAP* 1904 (2019), p. 053. DOI: 10.1088/1475-7516/2019/04/053. arXiv: 1812.09297 [astro-ph.CO].

[90] R. H. Dicke et al. "Cosmic Black-Body Radiation." In: ApJ 142 (July 1965), pp. 414–419. DOI: 10.1086/148306.

[91] Marian Douspis, Laura Salvati, and Nabila Aghanim. "On the Tension between Large Scale Structures and Cosmic Microwave Background". In: *PoS* EDSU2018 (2018), p. 037. DOI: 10.22323/1.335.0037. arXiv: 1901.05289 [astro-ph.CO].

[92] A. Drlica-Wagner et al. "Dark Energy Survey Year 1 Results: Photometric Data Set for Cosmology". In: *Astrophys. J. Suppl.* 235.2 (2018), p. 33. DOI: 10.3847/1538-4365/aab4f5. arXiv: 1708.01531 [astro-ph.CO].

[93] John Dubinski. "Cosmological Tidal Shear". In: ApJ 401 (Dec. 1992), p. 441. DOI: 10.1086/172076.

[94] R. Durrer. *The Cosmic Microwave Background*. Cambridge University Press, 2008.

[95] R. Durrer and W. Mathewson. "The flat sky approximation to the angular galaxy power spectra on the lightcone". In: *in preparation* (2019).

[96] Ruth Durrer. *The Cosmic Microwave Background*. Cambridge, UK: Cambridge University Press, 2008.

[97] Ruth Durrer. "The cosmic microwave background: the history of its experimental investigation and its significance for cosmology". In: *Class.Quant.Grav.* 32.12 (2015), p. 124007. DOI: 10.1088/0264-9381/32/12/124007. arXiv: 1506.01907 [astro-ph.CO].

[98] Albert Einstein. "Die Feldgleichungen der Gravitation. (German) [The Field Equations of Gravitation]". German. In: ???? (1915), pp. 844–847.

[99] Albert Einstein. "Zur Elektrodynamik bewegter Körper. (German) [On the electrodynamics of moving bodies]". German. In: 322.10 (1905), pp. 891–921. ISSN: 0003-3804. DOI: http://dx.doi.org/10.1002/andp.19053221004. URL: http://www.gsjournal.net/Science-Journals/Essays/View/2492;%20http://www.itba.edu.ar/cargrado/fismat/fismod/transf/htm/einstein_1.htm;%20http://www.zbp.univie.ac.at/einstein/einstein3.pdf.

[100] Daniel J. Eisenstein and Wayne Hu. "Baryonic features in the matter transfer function". In: *Astrophys.J.* 496 (1998), p. 605. DOI: 10.1086/305424. arXiv: astro-ph/9709112 [astro-ph].

[101] J. Elvin-Poole et al. "Dark Energy Survey year 1 results: Galaxy clustering for combined probes". In: *Phys. Rev.* D98.4 (2018), p. 042006. DOI: 10.1103/PhysRevD.98.042006. arXiv: 1708.01536 [astro-ph.CO].

[102] ESA. *(European Space Agency) Planck homepage*. http://www.rssd.esa.int/planck. Mar. 2012.

[103] *Euclid page*. https://www.euclid-ec.org/. Mar. 2017.

[104] Z.H. Fan. "Intrinsic alignments of galaxies and their effects on weak lensing detections of mass concentrations". In: *Astrophys. J.* 669 (2007), p. 10. DOI: 10.1086/521182. arXiv: 0706.3941 [astro-ph].

[105] Xiao Fang et al. "FAST-PT II: an algorithm to calculate convolution integrals of general tensor quantities in cosmological perturbation theory". In: *JCAP* 02 (2017), p. 030. DOI: 10.1088/1475-7516/2017/02/030. arXiv: 1609.05978 [astro-ph.CO].

[106] K. B. Fisher et al. "Clustering in the 1.2-JY IRAS Galaxy Redshift Survey - Part Two - Redshift Distortions and Xi/r/p, PI". In: *"Mon. Not. Roy. Astron. Soc."* 267 (Apr. 1994), p. 927. DOI: 10.1093/mnras/267.4.927. eprint: astro-ph/9308013.

[107] Simon Foreman, Hideki Perrier, and Leonardo Senatore. "Precision Comparison of the Power Spectrum in the EFTofLSS with Simulations". In: *JCAP* 1605.05 (2016), p. 027. DOI: 10.1088/1475-7516/2016/05/027. arXiv: 1507.05326 [astro-ph.CO].

[108] Jaime E. Forero-Romero, Sergio Contreras, and Nelson Padilla. "Cosmic web alignments with the shape, angular momentum and peculiar velocities of dark matter haloes". In: *Mon. Not. Roy. Astron. Soc.* 443.2 (2014), pp. 1090–1102. DOI: 10.1093/mnras/stu1150. arXiv: 1406.0508 [astro-ph.CO].

[109] Jérémie Francfort, Basundhara Ghosh, and Ruth Durrer. "Cosmological Number Counts in Einstein and Jordan frames". In: *JCAP* 1909.09 (2019), p. 071. DOI: 10.1088/1475-7516/2019/09/071. arXiv: 1907.03606 [gr-qc].

[110] A. Friedman. "On the Curvature of space". In: *Z. Phys.* 10 (1922). [Gen. Rel. Grav.31,1991(1999)], pp. 377–386. DOI: 10.1007/BF01332580.

[111] Y. Fujii and K. Maeda. *The scalar-tensor theory of gravitation*. Cambridge Monographs on Mathematical Physics. Cambridge University Press, 2007. ISBN: 9780521037525, 9780521811590, 9780511029882. DOI: 10.1017/CBO9780511535093. URL: http://www.cambridge.org/uk/catalogue/catalogue.asp?isbn=0521811597.

[112] Enrique Gaztanaga, Camille Bonvin, and Lam Hui. "Measurement of the dipole in the cross-correlation function of galaxies". In: *JCAP* 1701.01 (2017), p. 032. DOI: 10.1088/1475-7516/2017/01/032. arXiv: 1512.03918 [astro-ph.CO].

[113] Basundhara Ghosh and Ruth Durrer. "The observable E_g statistics". In: *JCAP* 1906.06 (2019), p. 010. DOI: 10.1088/1475-7516/2019/06/010. arXiv: 1812.09546 [astro-ph.CO].

[114] Basundhara Ghosh, Ruth Durrer, and Björn M. Schäfer. "7Intrinsic and extrinsic shape and sizecorrelations of galaxies in weak lensing data". In: *in Preparation* (2020).

[115] Basundhara Ghosh, Ruth Durrer, and Elena Sellentin. "General Relativistic corrections in density-shear correlations". In: *JCAP* 1806.06 (2018), p. 008. DOI: 10.1088/1475-7516/2018/06/008. arXiv: 1801.02518 [astro-ph.CO].

[116] Basundhara Ghosh, Mona Jalilvand, and Elisabetta Majerotto. *One loop standard perturbation theory calculations*. https://doi.org/10.5281/zenodo.3407616. Sept. 2019. DOI: 10.5281/zenodo.3407616.

[117] Aram Giahi-Saravani and Bjoern Malte Schaefer. "Evolution of intrinsic ellipticity correlations due to peculiar motion". In: *Mon. Not. Roy. Astron. Soc.* 428 (2013), pp. 1312–1320. DOI: 10.1093/mnras/sts110. arXiv: 1202.1196 [astro-ph.CO].

[118] Aram Giahi-Saravani and Björn Malte Schäfer. "Weak gravitational lensing of intrinsically aligned galaxies". In: *Mon. Not. Roy. Astron. Soc.* 437.2 (2014), pp. 1847–1857. DOI: 10.1093/mnras/stt2016. arXiv: 1302.2607 [astro-ph.CO].

[119] Hector Gil-Marín et al. "The clustering of galaxies in the SDSS-III Baryon Oscillation Spectroscopic Survey: RSD measurement from the LOS-dependent power spectrum of DR12 BOSS galaxies". In: *Mon. Not. Roy. Astron. Soc.* 460.4 (2016), pp. 4188–4209. DOI: 10.1093/mnras/stw1096. arXiv: 1509.06386 [astro-ph.CO].

[120] Héctor Gil-Marín et al. "The clustering of galaxies in the SDSS-III Baryon Oscillation Spectroscopic Survey: BAO measurement from the LOS-dependent power spectrum of DR12 BOSS galaxies". In: *Mon. Not. Roy. Astron. Soc.* 460.4 (2016), pp. 4210–4219. DOI: 10.1093/mnras/stw1264. arXiv: 1509.06373 [astro-ph.CO].

[121] R. L. Gilliland and M. M. Phillips. "Supernovae 1997ff and 1997fg". In: IAU Circ. 6810 (Jan. 1998), p. 1.

[122] L.S. Gradshteyn and L.M. Ryzhik. *Table of Integrals, Series and Products.* Sixth Edition. Academic Press, New York, 2000.

[123] Alister W. Graham and Simon P. Driver. "A Concise Reference to (Projected) Sérsic R1/n Quantities, Including Concentration, Profile Slopes, Petrosian Indices, and Kron Magnitudes". In: *Publications of the Astronomical Society of Australia* 22.2 (2005), pp. 118–127. ISSN: 1448-6083. DOI: 10.1071/as05001. URL: http://dx.doi.org/10.1071/AS05001.

[124] Alessandra Grassi and Björn Malte Schäfer. "Detecting baryon acoustic oscillations by 3d weak lensing". In: *Mon. Not. Roy. Astron. Soc.* 437.3 (2014), pp. 2632–2641. DOI: 10.1093/mnras/stt2075. arXiv: 1303.1024 [astro-ph.CO].

[125] Alex Hall and Camille Bonvin. "Measuring cosmic velocities with 21 cm intensity mapping and galaxy redshift survey cross-correlation dipoles". In: *Phys. Rev.* D95.4 (2017), p. 043530. DOI: 10.1103/PhysRevD.95.043530. arXiv: 1609.09252 [astro-ph.CO].

[126] Alex Hall, Camille Bonvin, and Anthony Challinor. "Testing General Relativity with 21-cm intensity mapping". In: *Phys.Rev.* D87.6 (2013), p. 064026. DOI: 10.1103/PhysRevD.87.064026. arXiv: 1212.0728 [astro-ph.CO].

[127] Alex Hall and Andy Taylor. "Intrinsic alignments in the cross-correlation of cosmic shear and CMB weak lensing". In: *Mon. Not. Roy. Astron. Soc.* 443 (2014), p. L119. DOI: 10.1093/mnrasl/slu094. arXiv: 1401.6018 [astro-ph.CO].

[128] A. J. S. Hamilton. "Linear redshift distortions: A Review". In: *Ringberg Workshop on Large Scale Structure Ringberg, Germany, September 23-28, 1996.* 1997. DOI: 10.1007/978-94-011-4960-0_17. arXiv: astro-ph/9708102 [astro-ph]. URL: http://alice.cern.ch/format/showfull?sysnb=0255366.

[129] A. F. Heavens, S. Matarrese, and Licia Verde. "The Nonlinear redshift-space power spectrum of galaxies". In: *Mon. Not. Roy. Astron. Soc.* 301 (1998), pp. 797–808. DOI: 10.1046/j.1365-8711.1998.02052.x. arXiv: astro-ph/9808016 [astro-ph].

[130] A. F. Heavens and A. N. Taylor. "A Spherical Harmonic Analysis of Redshift Space". In: *Mon. Not. Roy. Astron. Soc.* 275 (1995), pp. 483–497. DOI: 10.1093/mnras/275.2.483. arXiv: astro-ph/9409027 [astro-ph].

[131] A. F. Heavens and A. N. Taylor. "Design and analysis of redshift surveys". In: *Mon. Not. Roy. Astron. Soc.* 290 (1997), p. 456. DOI: 10.1093/mnras/290.3.456. arXiv: astro-ph/9705215 [astro-ph].

[132] A.F. Heavens, Thomas D. Kitching, and A.N. Taylor. "Measuring dark energy properties with 3D cosmic shear". In: *Mon. Not. Roy. Astron. Soc.* 373 (2006), pp. 105–120. DOI: 10.1111/j.1365-2966.2006.11006.x. arXiv: astro-ph/0606568.

[133] Alan Heavens. "3d weak lensing". In: *Mon. Not. Roy. Astron. Soc.* 343 (2003), p. 1327. DOI: 10.1046/j.1365-8711.2003.06780.x. arXiv: astro-ph/0304151.

[134] Alan Heavens, Justin Alsing, and Andrew Jaffe. "Combining Size and Shape in Weak Lensing". In: *Mon. Not. Roy. Astron. Soc.* 433 (2013), p. 6. DOI: 10.1093/mnrasl/slt045. arXiv: 1302.1584 [astro-ph.CO].

[135] Alan Heavens, Alexandre Refregier, and Catherine Heymans. "Intrinsic correlation of galaxy shapes: Implications for weak lensing measurements". In: *Mon. Not. Roy. Astron. Soc.* 319 (2000), p. 649. DOI: 10.1046/j.1365-8711.2000.03907.x. arXiv: astro-ph/0005269.

[136] Catherine Heymans et al. "CFHTLenS tomographic weak lensing cosmological parameter constraints: Mitigating the impact of intrinsic galaxy alignments". In: *Mon. Not. Roy. Astron. Soc.* 432 (2013), p. 2433. DOI: 10.1093/mnras/stt601. arXiv: 1303.1808 [astro-ph.CO].

[137] Catherine Heymans and Alan Heavens. "Weak gravitational lensing: Reducing the contamination by intrinsic alignments". In: *Mon. Not. Roy. Astron. Soc.* 339 (2003), p. 711. DOI: 10.1046/j.1365-8711.2003.06213.x. arXiv: astro-ph/0208220.

[138] Catherine Heymans et al. "Weak lensing with combo-17: estimation and removal of intrinsic alignments". In: *Mon. Not. Roy. Astron. Soc.* 347 (2004), p. 895. DOI: 10.1111/j.1365-2966.2004.07264.x. arXiv: astro-ph/0310174.

[139] Stefan Hilbert et al. "Intrinsic Alignments of Galaxies in the Illustris Simulation". In: *Mon. Not. Roy. Astron. Soc.* 468.1 (2017), pp. 790–823. DOI: 10.1093/mnras/stx482. arXiv: 1606.03216 [astro-ph.CO].

[140] Christopher M. Hirata et al. "Galaxy - galaxy weak lensing in SDSS: Intrinsic alignments and shear calibration errors". In: *Mon. Not. Roy. Astron. Soc.* 353 (2004), p. 529. DOI: 10.1111/j.1365-2966.2004.08090.x. arXiv: astro-ph/0403255.

[141] Christopher M. Hirata et al. "Cross-correlation of CMB with large-scale structure: Weak gravitational lensing". In: *Phys. Rev. D* 70 (2004), p. 103501. DOI: 10.1103/PhysRevD.70.103501. arXiv: astro-ph/0406004.

[142] Christopher M. Hirata et al. "Intrinsic galaxy alignments from the 2SLAQ and SDSS surveys: Luminosity and redshift scalings and implications for weak lensing surveys". In: *Mon. Not. Roy. Astron. Soc.* 381 (2007), pp. 1197–1218. DOI: 10.1111/j.1365-2966.2007.12312.x. arXiv: astro-ph/0701671.

[143] Cullan Howlett, Marc Manera, and Will J. Percival. "L-PICOLA: A parallel code for fast dark matter simulation". In: *Astron. Comput.* 12 (2015), pp. 109–126. DOI: 10.1016/j.ascom.2015.07.003. arXiv: 1506.03737 [astro-ph.CO].

[144] B. Hoyle et al. "Dark Energy Survey Year 1 Results: Redshift distributions of the weak lensing source galaxies". In: *Mon. Not. Roy. Astron. Soc.* 478.1 (2018), pp. 592–610. DOI: 10.1093/mnras/sty957. arXiv: 1708.01532 [astro-ph.CO].

[145] Wayne Hu. "Dark energy and matter evolution from lensing tomography". In: *Phys. Rev. D* 66 (2002), p. 083515. DOI: 10.1103/PhysRevD.66.083515. arXiv: astro-ph/0208093.

[146] Wayne Hu. "Dark synergy: Gravitational lensing and the CMB". In: *Phys. Rev. D* 65 (2002), p. 023003. DOI: 10.1103/PhysRevD.65.023003. arXiv: astro-ph/0108090.

[147] Wayne Hu and Max Tegmark. "Weak lensing: prospects for measuring cosmological parameters". In: *Astrophys. J. Lett.* 514 (1999), pp. L65–L68. DOI: 10.1086/311947. arXiv: astro-ph/9811168.

[148] Edwin Hubble. "A Relation between Distance and Radial Velocity among Extra-Galactic Nebulae". In: *Proceedings of the National Academy of Science* 15.3 (Mar. 1929), pp. 168–173. DOI: 10.1073/pnas.15.3.168.

[149] Eric M. Huff and Genevieve J. Graves. "Magnificent Magnification: Exploiting the Other Half of the Lensing Signal". In: *Astrophys. J. Lett.* 780 (2014), p. L16. DOI: 10.1088/2041-8205/780/2/L16. arXiv: 1111.1070 [astro-ph.CO].

[150] Lam Hui, Enrique Gaztanaga, and Marilena LoVerde. "Anisotropic Magnification Distortion of the 3D Galaxy Correlation: II. Fourier and Redshift Space". In: *Phys. Rev.* D77 (2008), p. 063526. DOI: 10.1103/PhysRevD.77.063526. arXiv: 0710.4191 [astro-ph].

[151] Lam Hui, Enrique Gaztanaga, and Marilena LoVerde. "Anisotropic Magnification Distortion of the 3D Galaxy Correlation. 1. Real Space". In: *Phys. Rev.* D76 (2007), p. 103502. DOI: 10.1103/PhysRevD.76.103502. arXiv: 0706.1071 [astro-ph].

[152] Lam Hui and Jun Zhang. "Intrinsic/extrinsic density-ellipticity correlations and galaxy-galaxy lensing". In: (May 2002). arXiv: astro-ph/0205512.

[153] Dragan Huterer. "Weak lensing and dark energy". In: *Phys. Rev. D* 65 (2002), p. 063001. DOI: 10.1103/PhysRevD.65.063001. arXiv: astro-ph/0106399.

[154] Dragan Huterer. "Weak lensing, dark matter and dark energy". In: *Gen. Rel. Grav.* 42 (2010), pp. 2177–2195. DOI: 10.1007/s10714-010-1051-z. arXiv: 1001.1758 [astro-ph.CO].

[155] Dragan Huterer and Masahiro Takada. "Calibrating the nonlinear matter power spectrum: Requirements for future weak lensing surveys". In: *Astropart. Phys.* 23 (2005), pp. 369–376. DOI: 10.1016/j.astropartphys.2005.02.006. arXiv: astro-ph/0412142.

[156] Dragan Huterer and Martin J. White. "Nulling tomography with weak gravitational lensing". In: *Phys. Rev. D* 72 (2005), p. 043002. DOI: 10.1103/PhysRevD.72.043002. arXiv: astro-ph/0501451.

[157] Takashi Ishikawa et al. "On the Systematic Errors of Cosmological-Scale Gravity Tests using Redshift Space Distortion: Non-linear Effects and the Halo Bias". In: *Mon. Not. Roy. Astron. Soc.* 443.4 (2014), pp. 3359–3367. DOI: 10.1093/mnras/stu1382. arXiv: 1308.6087 [astro-ph.CO].

[158] Albert Izard, Martin Crocce, and Pablo Fosalba. "ICE-COLA: Towards fast and accurate synthetic galaxy catalogues optimizing a quasi N-body method". In: *Mon. Not. Roy. Astron. Soc.* 459.3 (2016), pp. 2327–2341. DOI: 10.1093/mnras/stw797. arXiv: 1509.04685 [astro-ph.CO].

[159] Bhuvnesh Jain and Edmund Bertschinger. "Second order power spectrum and nonlinear evolution at high redshift". In: *Astrophys. J.* 431 (1994), p. 495. DOI: 10.1086/174502. arXiv: astro-ph/9311070 [astro-ph].

[160] Bhuvnesh Jain and Uros Seljak. "Cosmological model predictions for weak lensing: Linear and nonlinear regimes". In: *Astrophys. J.* 484 (1997), p. 560. DOI: 10.1086/304372. arXiv: astro-ph/9611077.

[161] Bhuvnesh Jain and Andy Taylor. "Cross-correlation tomography: measuring dark energy evolution with weak lensing". In: *Phys. Rev. Lett.* 91 (2003), p. 141302. DOI: 10.1103/PhysRevLett.91.141302. arXiv: astro-ph/0306046.

[162] Mona Jalilvand et al. "Intensity mapping of the 21 cm emission: lensing". In: *JCAP* 1901.01 (2019), p. 020. DOI: 10.1088/1475-7516/2019/01/020. arXiv: 1807.01351 [astro-ph.CO].

[163] Mona Jalilvand et al. "Non-linear contributions to angular power spectra". In: (2019). arXiv: 1907.13109 [astro-ph.CO].

[164] M.James Jee et al. "Cosmic shear results from the deep lens survey - I: Joint constraints on omega_m and sigma_8 with a two-dimensional analysis". In: *Astrophys. J.* 765 (2013), p. 74. DOI: 10.1088/0004-637X/765/1/74. arXiv: 1210.2732 [astro-ph.CO].

[165] Donghui Jeong, Fabian Schmidt, and Christopher M. Hirata. "Large-scale clustering of galaxies in general relativity". In: *Phys.Rev.* D85 (2012), p. 023504. DOI: 10.1103/PhysRevD.85.023504. arXiv: 1107.5427 [astro-ph.CO].

[166] Y.P. Jing. "Intrinsic correlation of halo ellipticity and its implications for large scale weak lensing surveys". In: *Mon. Not. Roy. Astron. Soc.* 335 (2002), p. L89. DOI: 10.1046/j.1365-8711.2002.05899.x. arXiv: astro-ph/0206098.

[167] B. Joachimi and P. Schneider. "Controlling intrinsic alignments in weak lensing statistics: The nulling and boosting techniques". In: (Sept. 2010). arXiv: 1009.2024 [astro-ph.CO].

[168] B. Joachimi and P. Schneider. "Intrinsic alignment boosting: Direct measurement of intrinsic alignments in cosmic shear data". In: *Astron. Astrophys.* 517 (2010), A4. DOI: 10.1051/0004-6361/201014482. arXiv: 1003.4211 [astro-ph.CO].

[169] B. Joachimi and P. Schneider. "The removal of shear-ellipticity correlations from the cosmic shear signal by nulling techniques". In: *Astron. Astrophys.* 488 (2008), p. 829. DOI: 10.1051/0004-6361:200809971. arXiv: 0804.2292 [astro-ph].

[170] B. Joachimi et al. "Constraints on intrinsic alignment contamination of weak lensing surveys using the MegaZ-LRG sample". In: *Astron. Astrophys.* 527 (2011), A26. DOI: 10.1051/0004-6361/201015621. arXiv: 1008.3491 [astro-ph.CO].

[171] Benjamin Joachimi et al. "Galaxy alignments: An overview". In: *Space Sci. Rev.* 193.1-4 (2015), pp. 1–65. DOI: 10.1007/s11214-015-0177-4. arXiv: 1504.05456 [astro-ph.GA].

[172] Harry Johnston et al. "KiDS+GAMA: Intrinsic alignment model constraints for current and future weak lensing cosmology". In: *Astron. Astrophys.* 624 (2019), A30. DOI: 10.1051/0004-6361/201834714. arXiv: 1811.09598 [astro-ph.CO].

[173] Jelte T.A. de Jong et al. "The Kilo-Degree Survey". In: *Exper. Astron.* 35 (2013), pp. 25–44. DOI: 10.1007/s10686-012-9306-1. arXiv: 1206.1254 [astro-ph.CO].

[174] Shahab Joudaki et al. "CFHTLenS revisited: assessing concordance with Planck including astrophysical systematics". In: *Mon. Not. Roy. Astron. Soc.* 465.2 (2017), pp. 2033–2052. DOI: 10.1093/mnras/stw2665. arXiv: 1601.05786 [astro-ph.CO].

[175] N. Kaiser. "Clustering in real space and in redshift space". In: *M.N.R.A.S.* 227 (July 1987), pp. 1–21.

[176] Nick Kaiser. "Weak gravitational lensing of distant galaxies". In: *Astrophys. J.* 388 (1992), p. 272. DOI: 10.1086/171151.

[177] Issha Kayo and Masahiro Takada. "Cosmological parameters from weak lensing power spectrum and bispectrum tomography: including the non-Gaussian errors". In: (June 2013). arXiv: 1306.4684 [astro-ph.CO].

[178] Issha Kayo, Masahiro Takada, and Bhuvnesh Jain. "Information content of weak lensing power spectrum and bispectrum: including the non-Gaussian error covariance matrix". In: *Mon. Not. Roy. Astron. Soc.* 429 (2013), pp. 344–371. DOI: 10.1093/mnras/sts340. arXiv: 1207.6322 [astro-ph.CO].

[179] Alina Kiessling et al. "Galaxy Alignments: Theory, Modelling & Simulations". In: *Space Sci. Rev.* 193.1-4 (2015). [Erratum: Space Sci.Rev. 193, 137 (2015)], pp. 67–136. DOI: 10.1007/s11214-015-0203-6. arXiv: 1504.05546 [astro-ph.GA].

[180] M. Kilbinger et al. "Dark energy constraints and correlations with systematics from CFHTLS weak lensing, SNLS supernovae Ia and WMAP5". In: *Astron. Astrophys.* 497 (2009), p. 677. DOI: 10.1051/0004-6361/200811247. arXiv: 0810.5129 [astro-ph].

[181] Martin Kilbinger. "Cosmology with cosmic shear observations: a review". In: *Rept. Prog. Phys.* 78 (2015), p. 086901. DOI: 10.1088/0034-4885/78/8/086901. arXiv: 1411.0115 [astro-ph.CO].

[182] Martin Kilbinger et al. "CFHTLenS: Combined probe cosmological model comparison using 2D weak gravitational lensing". In: *Mon. Not. Roy. Astron. Soc.* 430 (2013), pp. 2200–2220. DOI: 10.1093/mnras/stt041. arXiv: 1212.3338 [astro-ph.CO].

[183] D. Kirk et al. "Cross-correlation of gravitational lensing from DES Science Verification data with SPT and Planck lensing". In: *Mon. Not. Roy. Astron. Soc.* 459.1 (2016), pp. 21–34. DOI: 10.1093/mnras/stw570. arXiv: 1512.04535 [astro-ph.CO].

[184] Donnacha Kirk et al. "Galaxy alignments: Observations and impact on cosmology". In: *Space Sci. Rev.* 193.1-4 (2015), pp. 139–211. DOI: 10.1007/s11214-015-0213-4. arXiv: 1504.05465 [astro-ph.GA].

[185] Donnacha Kirk, Sarah Bridle, and Michael Schneider. "The Impact of Intrinsic Alignments: Cosmological Constraints from a Joint Analysis of Cosmic Shear and Galaxy Survey Data". In: *Mon. Not. Roy. Astron. Soc.* 408 (2010), pp. 1502–1515. DOI: 10.1111/j.1365-2966.2010.17213.x. arXiv: 1001.3787 [astro-ph.CO].

[186] Donnacha Kirk et al. "Optimizing cosmic shear surveys to measure modifications to gravity on cosmic scales". In: *Mon. Not. Roy. Astron. Soc.* 430.1 (2013), pp. 197–208. DOI: 10.1093/mnras/sts571. arXiv: 1109.4536 [astro-ph.CO].

[187] Thomas D. Kitching et al. "The Limits of Cosmic Shear". In: *Mon. Not. Roy. Astron. Soc.* 469.3 (2017), pp. 2737–2749. DOI: 10.1093/mnras/stx1039. arXiv: 1611.04954 [astro-ph.CO].

[188] Patricia Larsen and Anthony Challinor. "Intrinsic alignment contamination to CMB lensing–galaxy weak lensing correlations from tidal torquing". In: *Mon. Not. Roy. Astron. Soc.* 461.4 (2016), pp. 4343–4352. DOI: 10.1093/mnras/stw1645. arXiv: 1510.02617 [astro-ph.CO].

[189] R. Laureijs et al. "Euclid Definition Study Report". In: (2011). arXiv: 1110.3193 [astro-ph.CO].

[190] R. Laureijs et al. "Euclid Definition Study Report". In: *ArXiv e-prints* (Oct. 2011). arXiv: 1110.3193 [astro-ph.CO].

[191] Jounghun Lee and Pirin Erdogdu. "The Alignments of the Galaxy Spins with the Real-Space Tidal Field Reconstructed from the Two Mass Redshift Survey". In: *Astrophys. J.* 671 (2007), p. 1248. DOI: 10.1086/523351. arXiv: 0706.1412 [astro-ph].

[192] Jounghun Lee and Ue-Li Pen. "The Nonlinear Evolution of Galaxy Intrinsic Alignments". In: *Astrophys. J.* 681 (2008), p. 798. DOI: 10.1086/588646. arXiv: 0707.1690 [astro-ph].

[193] G. Lemaı tre. "Un Univers homogène de masse constante et de rayon croissant rendant compte de la vitesse radiale des nébuleuses extra-galactiques". In: *Annales de la Société Scientifique de Bruxelles* 47 (Jan. 1927), pp. 49–59.

[194] Julien Lesgourgues. "The Cosmic Linear Anisotropy Solving System (CLASS) I: Overview". In: (2011). arXiv: 1104.2932 [astro-ph.IM].

[195] Matthew Lewandowski et al. "EFT of large scale structures in redshift space". In: *Phys. Rev.* D97.6 (2018), p. 063526. DOI: 10.1103/PhysRevD.97.063526. arXiv: 1512.06831 [astro-ph.CO].

[196] Antony Lewis and Sarah Bridle. "Cosmological parameters from CMB and other data: A Monte Carlo approach". In: Phys. Rev. D 66 (2002), p. 103511. DOI: 10.1103/PhysRevD.66.103511. arXiv: astro-ph/0205436 [astro-ph].

[197] Antony Lewis, Anthony Challinor, and Anthony Lasenby. "Efficient computation of CMB anisotropies in closed FRW models". In: *Astrophys.J.* 538 (2000), pp. 473–476. DOI: 10.1086/309179. arXiv: astro-ph/9911177 [astro-ph].

[198] D. Nelson Limber. "The Analysis of Counts of the Extragalactic Nebulae in Terms of a Fluctuating Density Field. II". In: *Astrophys. J.* 119 (1954), p. 655. DOI: 10.1086/145870.

[199] Christiane S. Lorenz, David Alonso, and Pedro G. Ferreira. "The impact of relativistic effects on cosmological parameter estimation". In: (2017). arXiv: 1710.02477 [astro-ph.CO].

[200] Marilena LoVerde, Lam Hui, and Enrique Gaztanaga. "Lensing corrections to features in the angular two-point correlation function and power spectrum". In: *Phys. Rev.* D77 (2008), p. 023512. DOI: 10.1103/PhysRevD.77.023512. arXiv: 0708.0031 [astro-ph].

[201] LSST Dark Energy Science Collaboration. "Large Synoptic Survey Telescope: Dark Energy Science Collaboration". In: *ArXiv e-prints* (Nov. 2012). arXiv: 1211.0310 [astro-ph.CO].

[202] *LSST page*. https://www.lsst.org/. Nov. 2017.

[203] Roy Maartens et al. "Cosmology with the SKA – overview". In: (2015). arXiv: 1501.04076 [astro-ph.CO].

[204] Edward Macaulay, Ingunn Kathrine Wehus, and Hans Kristian Eriksen. "Lower Growth Rate from Recent Redshift Space Distortion Measurements than Expected from Planck". In: *Phys. Rev. Lett.* 111.16 (2013), p. 161301. DOI: 10.1103/PhysRevLett.111.161301. arXiv: 1303.6583 [astro-ph.CO].

[205] Niall MacCrann et al. "Cosmic Discordance: Are Planck CMB and CFHTLenS weak lensing measurements out of tune?" In: *Mon. Not. Roy. Astron. Soc.* 451.3 (2015), pp. 2877–2888. DOI: 10.1093/mnras/stv1154. arXiv: 1408.4742 [astro-ph.CO].

[206] Jonathan Mackey, Martin J. White, and Marc Kamionkowski. "Theoretical estimates of intrinsic galaxy alignment". In: *Mon. Not. Roy. Astron. Soc.* 332 (2002), p. 788. DOI: 10.1046/j.1365-8711.2002.05337.x. arXiv: astro-ph/0106364.

[207] Rachel Mandelbaum et al. "The WiggleZ Dark Energy Survey: Direct constraints on blue galaxy intrinsic alignments at intermediate redshifts". In: *Mon. Not. Roy. Astron. Soc.* 410 (2011), p. 844. DOI: 10.1111/j.1365-2966.2010.17485.x. arXiv: 0911.5347 [astro-ph.CO].

[208] Katarina Markovic, Benjamin Bose, and Alkistis Pourtsidou. "Assessing non-linear models for galaxy clustering I: unbiased growth forecasts from multipole expansion". In: (2019). arXiv: 1904.11448 [astro-ph.CO].

[209] Richard Massey et al. "Origins of weak lensing systematics, and requirements on future instrumentation (or knowledge of instrumentation)". In: *Mon. Not. Roy. Astron. Soc.* 429 (2013), p. 661. DOI: 10.1093/mnras/sts371. arXiv: 1210.7690 [astro-ph.CO].

[210] J. C. Mather et al. "A Preliminary Measurement of the Cosmic Microwave Background Spectrum by the Cosmic Background Explorer (COBE) Satellite". In: ApJ 354 (May 1990), p. L37. DOI: 10.1086/185717.

[211] T. Matsubara. "The Correlation Function in Redshift Space: General Formula with Wide-Angle Effects and Cosmological Distortions". In: *Astrophys.J.* 535 (May 2000), pp. 1–23. DOI: 10.1086/308827. eprint: astro-ph/9908056.

[212] Takahiko Matsubara. "Resumming Cosmological Perturbations via the Lagrangian Picture: One-loop Results in Real Space and in Redshift Space". In: *Phys. Rev.* D77 (2008), p. 063530. DOI: 10.1103/PhysRevD.77.063530. arXiv: 0711.2521 [astro-ph].

[213] William L. Matthewson and Ruth Durrer. "The Flat Sky Approximation for Galaxy Number Counts". In: *in Preparation* (2019).

[214] Patrick McDonald. "Gravitational redshift and other redshift-space distortions of the imaginary part of the power spectrum". In: *JCAP* 0911 (2009), p. 026. DOI: 10.1088/1475-7516/2009/11/026. arXiv: 0907.5220 [astro-ph.CO].

[215] Yannick Mellier. "Probing the universe with weak lensing". In: *Ann. Rev. Astron. Astrophys.* 37 (1999), pp. 127–189. DOI: 10.1146/annurev.astro.37.1.127. arXiv: astro-ph/9812172.

[216] Brice Menard et al. "Measuring the galaxy-mass and galaxy-dust correlations through magnification and reddening". In: *Mon. Not. Roy. Astron. Soc.* 405 (2010), pp. 1025–1039. DOI: 10.1111/j.1365-2966.2010.16486.x. arXiv: 0902.4240 [astro-ph.CO].

[217] Philipp M. Merkel and Bjoern Malte Schaefer. "Intrinsic alignments and 3d weak gravitational lensing". In: *Mon. Not. Roy. Astron. Soc.* 434 (2013), p. 1808. DOI: 10.1093/mnras/stt1151. arXiv: 1306.6466 [astro-ph.CO].

[218] Philipp M. Merkel and Björn Malte Schäfer. "Imitating intrinsic alignments: A bias to the CMB lensing-galaxy shape cross-correlation power spectrum induced by the large-scale structure bispectrum". In: *Mon. Not. Roy. Astron. Soc.* 471.2 (2017), pp. 2431–2437. DOI: 10.1093/mnras/stx1664. arXiv: 1709.04444 [astro-ph.CO].

[219] F. G. Mohammad et al. "The VIMOS Public Extragalactic Redshift Survey (VIPERS): An unbiased estimate of the growth rate of structure at using the clustering of luminous blue galaxies". In: *ArXiv e-prints* (2017). arXiv: 1708.00026.

[220] Francesco Montanari and Ruth Durrer. "An analytic approach to baryon acoustic oscillations". In: *Phys.Rev.* D84 (2011), p. 023522. DOI: 10.1103/PhysRevD.84.023522. arXiv: 1105.1514 [astro-ph.CO].

[221] Francesco Montanari and Ruth Durrer. "Measuring the lensing potential with tomographic galaxy number counts". In: *JCAP* 1510.10 (2015), p. 070. DOI: 10.1088/1475-7516/2015/10/070. arXiv: 1506.01369 [astro-ph.CO].

[222] Azadeh Moradinezhad Dizgah and Ruth Durrer. "Lensing corrections to the $E_g(z)$ statistics from large scale structure". In: *JCAP* 1609 (2016), p. 035. DOI: 10.1088/1475-7516/2016/09/035. arXiv: 1604.08914 [astro-ph.CO].

[223] Michael J. Mortonson, David H. Weinberg, and Martin White. "Dark Energy: A Short Review". In: (Dec. 2013). arXiv: 1401.0046 [astro-ph.CO].

[224] D. Munshi et al. "Cosmology with Weak Lensing Surveys". In: *Phys. Rept.* 462 (2008), pp. 67–121. DOI: 10.1016/j.physrep.2008.02.003. arXiv: astro-ph/0612667.

[225] Dipak Munshi, Peter Coles, and Martin Kilbinger. "Tomography and Weak lensing Statistics". In: *JCAP* 04 (2014), p. 004. DOI: 10.1088/1475-7516/2014/04/004. arXiv: 1112.0495 [astro-ph.CO].

[226] NASA. *(National Aeronautics and Space Administration) WMAP homepage.* http://map.gsfc.nasa.gov/. Jan. 2013.

[227] L. B. Newburgh et al. "HIRAX: A Probe of Dark Energy and Radio Transients". In: *Proc. SPIE Int. Soc. Opt. Eng.* 9906 (2016), p. 99065X. DOI: 10.1117/12.2234286. arXiv: 1607.02059 [astro-ph.IM].

[228] Takahiro Nishimichi and Atsushi Taruya. "Baryon Acoustic Oscillations in 2D II: Redshift-space halo clustering in N-body simulations". In: *Phys. Rev.* D84 (2011), p. 043526. DOI: 10.1103/PhysRevD.84.043526. arXiv: 1106.4562 [astro-ph.CO].

[229] Pierre Ocvirk et al. "Cosmic Dawn II (CoDa II): a new radiation-hydrodynamics simulation of the self-consistent coupling of galaxy formation and reionization". In: (2018). arXiv: 1811.11192 [astro-ph.GA].

[230] Akira Oka et al. "Simultaneous constraints on the growth of structure and cosmic expansion from the multipole power spectra of the SDSS DR7 LRG sample". In: *Mon. Not. Roy. Astron. Soc.* 439 (2014), pp. 2515–2530. DOI: 10.1093/mnras/stu111. arXiv: 1310.2820 [astro-ph.CO].

[231] Teppei Okumura et al. "Galaxy power spectrum in redshift space: combining perturbation theory with the halo model". In: *Phys. Rev.* D92.10 (2015), p. 103516. DOI: 10.1103/PhysRevD.92.103516. arXiv: 1506.05814 [astro-ph.CO].

[232] Isha Pahwa et al. "The alignment of galaxy spin with the shear field in observations". In: *Mon. Not. Roy. Astron. Soc.* 457.1 (2016), pp. 695–703. DOI: 10.1093/mnras/stv2930. arXiv: 1512.02236 [astro-ph.CO].

[233] Viraj Pandya et al. "Can intrinsic alignments of elongated low-mass galaxies be used to map the cosmic web at high redshift?" In: *Mon. Not. Roy. Astron. Soc.* 488.4 (2019), pp. 5580–5593. DOI: 10.1093/mnras/stz2129. arXiv: 1902.09559 [astro-ph.GA].

[234] P. Pápai and I. Szapudi. "Non-perturbative effects of geometry in wide-angle redshift distortions". In: *M.N.R.A.S.* 389 (Sept. 2008), pp. 292–296. DOI: 10.1111/j.1365-2966.2008.13572.x. arXiv: 0802.2940.

[235] J. A. Peacock and A. F. Heavens. "The statistics of maxima in primordial density perturbations". In: MNRAS 217 (Dec. 1985), pp. 805–820. DOI: 10.1093/mnras/217.4.805.

[236] Eske M. Pedersen et al. "First detection of the GI-type of intrinsic alignments of galaxies using the self-calibration method in a photometric galaxy survey". In: (Nov. 2019). arXiv: 1911.01614 [astro-ph.CO].

[237] A. A. Penzias and R. W. Wilson. "A Measurement of Excess Antenna Temperature at 4080 Mc/s." In: ApJ 142 (July 1965), pp. 419–421. DOI: 10.1086/148307.

[238] Ashley Perko et al. "Biased Tracers in Redshift Space in the EFT of Large-Scale Structure". In: (2016). arXiv: 1610.09321 [astro-ph.CO].

[239] A. Pezzotta et al. "The VIMOS Public Extragalactic Redshift Survey (VIPERS). The growth of structure at from redshift-space distortions in the clustering of the PDR-2 final sample". In: *Astron. & Astrophys.* 604, A33 (July 2017), A33. DOI: 10.1051/0004-6361/201630295. arXiv: 1612.05645.

[240] H.P. Robertson Ph.D. "LXXXVI. On relativistic cosmology". In: *The London, Edinburgh, and Dublin Philosophical Magazine and Journal of Science* 5.31 (1928), pp. 835–848. DOI: 10.1080/14786440508564528. eprint: https://doi.org/10.1080/14786440508564528. URL: https://doi.org/10.1080/14786440508564528.

[241] Davide Piras et al. "The mass dependence of dark matter halo alignments with large-scale structure". In: *Mon. Not. Roy. Astron. Soc.* 474.1 (2018), pp. 1165–1175. DOI: 10.1093/mnras/stx2846. arXiv: 1707.06559 [astro-ph.CO].

[242] Alkistis Pourtsidou. "Testing gravity at large scales with H*I* intensity mapping". In: *Mon. Not. Roy. Astron. Soc.* 461.2 (2016), pp. 1457–1464. DOI: 10.1093/mnras/stw1406. arXiv: 1511.05927 [astro-ph.CO].

[243] Anthony R. Pullen et al. "Constraining Gravity at the Largest Scales through CMB Lensing and Galaxy Velocities". In: *Mon. Not. Roy. Astron. Soc.* 460.4 (2016), pp. 4098–4108. DOI: 10.1093/mnras/stw1249. arXiv: 1511.04457 [astro-ph.CO].

[244] Manuel Rabold and Romain Teyssier. "Precision cosmology with baryons: non-radiative hydrodynamics of galaxy groups". In: *Mon. Not. Roy. Astron. Soc.* 467.3 (2017), pp. 3188–3211. DOI: 10.1093/mnras/stx266. arXiv: 1701.05337 [astro-ph.CO].

[245] A. Raccanelli, L. Samushia, and W. J. Percival. "Simulating redshift-space distortions for galaxy pairs with wide angular separation". In: *M.N.R.A.S.* 409 (Dec. 2010), pp. 1525–1533. DOI: 10.1111/j.1365-2966.2010.17388.x. arXiv: 1006.1652 [astro-ph.CO].

[246] Alvise Raccanelli et al. "Cosmological Measurements with General Relativistic Galaxy Correlations". In: (2015). arXiv: 1505.06179 [astro-ph.CO].

[247] Alvise Raccanelli et al. "Doppler term in the galaxy two-point correlation function: wide-angle, velocity, Doppler lensing and cosmic acceleration effects". In: (2016). arXiv: 1602.03186 [astro-ph.CO].

[248] Alvise Raccanelli et al. "Large-scale 3D galaxy correlation function and non-Gaussianity". In: *JCAP* 1408 (2014), p. 022. DOI: 10.1088/1475-7516/2014/08/022. arXiv: 1306.6646 [astro-ph.CO].

[249] Alvise Raccanelli et al. "Lensing and time-delay contributions to galaxy correlations". In: (2013). arXiv: 1311.6813 [astro-ph.CO].

[250] Anais Rassat et al. "Deconstructing Baryon Acoustic Oscillations: A Comparison of Methods". In: (2008). arXiv: 0810.0003 [astro-ph].

[251] Beth A. Reid et al. "The clustering of galaxies in the SDSS-III Baryon Oscillation Spectroscopic Survey: measurements of the growth of structure and expansion rate at z=0.57 from anisotropic clustering". In: (2012). arXiv: 1203.6641 [astro-ph.CO].

[252] Paulo H. F. Reimberg, Francis Bernardeau, and Cyril Pitrou. "Redshift-space distortions with wide angular separations". In: *JCAP* 1601.01 (2016), p. 048. DOI: 10.1088/1475-7516/2016/01/048. arXiv: 1506.06596 [astro-ph.CO].

[253] Robert Reischke and Björn Malte Schäfer. "Environmental dependence of ellipticity correlation functions of intrinsic alignments". In: *JCAP* 04 (2019), p. 031. DOI: 10.1088/1475-7516/2019/04/031. arXiv: 1812.06918 [astro-ph.CO].

[254] Reinabelle Reyes et al. "Confirmation of general relativity on large scales from weak lensing and galaxy velocities". In: *Nature* 464 (2010), pp. 256–258. DOI: 10.1038/nature08857. arXiv: 1003.2185 [astro-ph.CO].

[255] Vera C. Rubin and Jr. Ford W. Kent. "Rotation of the Andromeda Nebula from a Spectroscopic Survey of Emission Regions". In: ApJ 159 (Feb. 1970), p. 379. DOI: 10.1086/150317.

[256] Lado Samushia, Will J. Percival, and Alvise Raccanelli. "Interpreting large-scale redshift-space distortion measurements". In: *Mon. Not. Roy. Astron. Soc.* 420 (2012), pp. 2102–2119. DOI: 10.1111/j.1365-2966.2011.20169.x. arXiv: 1102.1014 [astro-ph.CO].

[257] Mario Santos et al. "Cosmology from a SKA HI intensity mapping survey". In: *PoS* AASKA14 (2015), p. 019. DOI: 10.22323/1.215.0019.

[258] Siddharth Satpathy et al. "The clustering of galaxies in the completed SDSS-III Baryon Oscillation Spectroscopic Survey: On the measurement of growth rate using galaxy correlation functions". In: *Mon. Not. Roy. Astron. Soc.* (2016). [Mon. Not. Roy. Astron. Soc.469,1369(2017)]. DOI: 10.1093/mnras/stx883. arXiv: 1607.03148 [astro-ph.CO].

[259] Bjoern Malte Schaefer. "Review: galactic angular momenta and angular momentum correlations in the cosmological large-scale structure". In: *Int. J. Mod. Phys. D* 18 (2009), pp. 173–222. DOI: 10.1142/S0218271809014388. arXiv: 0808.0203 [astro-ph].

[260] Bjoern Malte Schaefer and Philipp Merkel. "Galactic angular momenta and angular momentum couplings in the large-scale structure". In: *Mon. Not. Roy. Astron. Soc.* 421 (2012), pp. 2751–2762. DOI: 10.1111/j.1365-2966.2011.20224.x. arXiv: 1101.4584 [astro-ph.CO].

[261] Denise M. Schmitz et al. "Time evolution of intrinsic alignments of galaxies". In: *JCAP* 07 (2018), p. 030. DOI: 10.1088/1475-7516/2018/07/030. arXiv: 1805.02649 [astro-ph.CO].

[262] Aurel Schneider et al. "Quantifying baryon effects on the matter power spectrum and the weak lensing shear correlation". In: *JCAP* 1903.03 (2019), p. 020. DOI: 10.1088/1475-7516/2019/03/020. arXiv: 1810.08629 [astro-ph.CO].

[263] Michael D. Schneider et al. "Galaxy and Mass Assembly (GAMA): galaxy radial alignments in GAMA groups". In: *Mon. Not. Roy. Astron. Soc.* 433 (2013), p. 2727. DOI: 10.1093/mnras/stt855. arXiv: 1306.4963 [astro-ph.CO].

[264] Michael D. Schneider and Sarah Bridle. "A halo model for intrinsic alignments of galaxy ellipticities". In: *Monthly Notices of the Royal Astronomical Society* 402.4 (Mar. 2010), pp. 2127–2139. ISSN: 0035-8711. DOI: 10.1111/j.1365-2966.2009.15956.x. eprint: https://academic.oup.com/mnras/article-pdf/402/4/2127/4869000/mnras0402-2127.pdf. URL: https://doi.org/10.1111/j.1365-2966.2009.15956.x.

[265] Roman Scoccimarro. "Redshift-space distortions, pairwise velocities and nonlinearities". In: *Phys. Rev.* D70 (2004), p. 083007. DOI: 10.1103/PhysRevD.70.083007. arXiv: astro-ph/0407214 [astro-ph].

[266] Elena Sellentin and Björn Malte Schäfer. "Non-Gaussian forecasts of weak lensing with and without priors". In: *Mon. Not. Roy. Astron. Soc.* 456.2 (2016), pp. 1645–1653. DOI: 10.1093/mnras/stv2805. arXiv: 1506.05356 [astro-ph.CO].

[267] Elisabetta Semboloni et al. "Quantifying the effect of baryon physics on weak lensing tomography". In: *Mon. Not. Roy. Astron. Soc.* 417 (2011), p. 2020. DOI: 10.1111/j.1365-2966.2011.19385.x. arXiv: 1105.1075 [astro-ph.CO].

[268] Leonardo Senatore and Matias Zaldarriaga. "Redshift Space Distortions in the Effective Field Theory of Large Scale Structures". In: (2014). arXiv: 1409.1225 [astro-ph.CO].

[269] J. L. Sérsic. "Influence of the atmospheric and instrumental dispersion on the brightness distribution in a galaxy". In: *Boletin de la Asociacion Argentina de Astronomia La Plata Argentina* 6 (Feb. 1963), pp. 41–43.

[270] Ravi K. Sheth and Giuseppe Tormen. "Large scale bias and the peak background split". In: *Mon. Not. Roy. Astron. Soc.* 308 (1999), p. 119. DOI: 10.1046/j.1365-8711.1999.02692.x. arXiv: astro-ph/9901122.

[271] Fergus Simpson et al. "Galaxy and mass assembly: Redshift space distortions from the clipped galaxy field". In: *Phys. Rev.* D93.2 (2016), p. 023525. DOI: 10.1103/PhysRevD.93.023525. arXiv: 1505.03865 [astro-ph.CO].

[272] Yong-Seon Song et al. "Consistent Modified Gravity Analysis of Anisotropic Galaxy Clustering Using BOSS DR11". In: *Phys. Rev.* D92.4 (2015), p. 043522. DOI: 10.1103/PhysRevD.92.043522. arXiv: 1507.01592 [astro-ph.CO].

[273] Thomas P. Sotiriou. "Gravity and Scalar Fields". In: *Lect. Notes Phys.* 892 (2015), pp. 3–24. DOI: 10.1007/978-3-319-10070-8_1. arXiv: 1404.2955 [gr-qc].

[274] D. Spergel et al. "Wide-Field InfrarRed Survey Telescope-Astrophysics Focused Telescope Assets WFIRST-AFTA 2015 Report". In: (2015). arXiv: 1503.03757 [astro-ph.IM].

[275] Alexander S. Szalay, Takahiko Matsubara, and Stephen D. Landy. "Redshift space distortions of the correlation function in wide angle galaxy surveys". In: *Astrophys. J.* 498 (1998), p. L1. DOI: 10.1086/311293. arXiv: astro-ph/9712007 [astro-ph].

[276] Istvan Szapudi. "Wide angle redshift distortions revisited". In: *Astrophys. J.* 614 (2004), pp. 51–55. DOI: 10.1086/423168. arXiv: astro-ph/0404477 [astro-ph].

[277] Masahiro Takada and Bhuvnesh Jain. "The Impact of Non-Gaussian Errors on Weak Lensing Surveys". In: *Mon. Not. Roy. Astron. Soc.* 395 (2009), pp. 2065–2086. DOI: 10.1111/j.1365-2966.2009.14504.x. arXiv: 0810.4170 [astro-ph].

[278] Masahiro Takada and Martin J. White. "Tomography of lensing cross power spectra". In: *Astrophys. J. Lett.* 601 (2004), p. L1. DOI: 10.1086/381870. arXiv: astro-ph/0311104.

[279] Ryuichi Takahashi et al. "Probability Distribution Functions of Cosmological Lensing: Convergence, Shear, and Magnification". In: *Astrophys. J.* 742 (2011), p. 15. DOI: 10.1088/0004-637X/742/1/15. arXiv: 1106.3823 [astro-ph.CO].

[280] Ryuichi Takahashi et al. "Revising the Halofit Model for the Nonlinear Matter Power Spectrum". In: *Astrophys.J.* 761 (2012), p. 152. DOI: 10.1088/0004-637X/761/2/152. arXiv: 1208.2701 [astro-ph.CO].

[281] Vittorio Tansella et al. "The full-sky relativistic correlation function and power spectrum of galaxy number counts. Part I: theoretical aspects". In: *JCAP* 1803.03 (2018), p. 019. DOI: 10.1088/1475-7516/2018/03/019. arXiv: 1708.00492 [astro-ph.CO].

[282] Atsushi Taruya, Takahiro Nishimichi, and Francis Bernardeau. "Precision modeling of redshift-space distortions from a multipoint propagator expansion". In: *Phys. Rev.* D87.8 (2013), p. 083509. DOI: 10.1103/PhysRevD.87.083509. arXiv: 1301.3624 [astro-ph.CO].

[283] Atsushi Taruya, Takahiro Nishimichi, and Shun Saito. "Baryon Acoustic Oscillations in 2D: Modeling Redshift-space Power Spectrum from Perturbation Theory". In: *Phys. Rev.* D82 (2010), p. 063522. DOI: 10.1103/PhysRevD.82.063522. arXiv: 1006.0699 [astro-ph.CO].

[284] Atsushi Taruya and Teppei Okumura. "Improving geometric and dynamical constraints on cosmology with intrinsic alignments of galaxies". In: (Jan. 2020). DOI: 10.3847/2041-8213/ab7934. arXiv: 2001.05962 [astro-ph.CO].

[285] Svetlin Tassev, Matias Zaldarriaga, and Daniel Eisenstein. "Solving Large Scale Structure in Ten Easy Steps with COLA". In: *JCAP* 1306 (2013), p. 036. DOI: 10.1088/1475-7516/2013/06/036. arXiv: 1301.0322 [astro-ph.CO].

[286] Ananth Tenneti et al. "Galaxy Shapes and Intrinsic Alignments in The MassiveBlack-II Simulation". In: *Mon. Not. Roy. Astron. Soc.* 441.1 (2014), pp. 470–485. DOI: 10.1093/mnras/stu586. arXiv: 1403.4215 [astro-ph.CO].

[287] Ananth Tenneti et al. "Intrinsic alignments of galaxies in the MassiveBlack-II simulation: analysis of two-point statistics". In: *Mon. Not. Roy. Astron. Soc.* 448.4 (2015), pp. 3522–3544. DOI: 10.1093/mnras/stv272. arXiv: 1409.7297 [astro-ph.CO].

[288] Nicolas Tessore et al. "Weak lensing of large scale structure in the presence of screening". In: *JCAP* 10 (2015), p. 036. DOI: 10.1088/1475-7516/2015/10/036. arXiv: 1508.04011 [astro-ph.CO].

[289] Daniel B. Thomas, Marco Bruni, and David Wands. "Relativistic weak lensing from a fully non-linear cosmological density field". In: *JCAP* 09 (2015), p. 021. DOI: 10.1088/1475-7516/2015/9/021. arXiv: 1403.4947 [astro-ph.CO].

[290] M. A. Troxel et al. "Dark Energy Survey Year 1 results: Cosmological constraints from cosmic shear". In: *Phys. Rev.* D98.4 (2018), p. 043528. DOI: 10.1103/PhysRevD.98.043528. arXiv: 1708.01538 [astro-ph.CO].

[291] M.A. Troxel and Mustapha Ishak. "Self-Calibration for 3-point Intrinsic Alignment Auto-Correlations in Weak Lensing Surveys". In: *Mon. Not. Roy. Astron. Soc.* 423 (2012), pp. 1663–1673. DOI: 10.1111/j.1365-2966.2012.20987.x. arXiv: 1203.2138 [astro-ph.CO].

[292] M.A. Troxel and Mustapha Ishak. "The Intrinsic Alignment of Galaxies and its Impact on Weak Gravitational Lensing in an Era of Precision Cosmology". In: *Phys. Rept.* 558 (2014), pp. 1–59. DOI: 10.1016/j.physrep.2014.11.001. arXiv: 1407.6990 [astro-ph.CO].

[293] Tim M. Tugendhat and Björn Malte Schäfer. "Angular ellipticity correlations in a composite alignment model for elliptical and spiral galaxies and inference from weak lensing". In: *Mon. Not. Roy. Astron. Soc.* 476.3 (2018), pp. 3460–3477. DOI: 10.1093/mnras/sty323. arXiv: 1709.02630 [astro-ph.CO].

[294] Edo van Uitert et al. "KiDS+GAMA: Cosmology constraints from a joint analysis of cosmic shear, galaxy-galaxy lensing and angular clustering". In: (2017). arXiv: 1706.05004 [astro-ph.CO].

[295] Georgios Valogiannis and Rachel Bean. "Efficient simulations of large scale structure in modified gravity cosmologies with comoving Lagrangian acceleration". In: *Phys. Rev.* D95.10 (2017), p. 103515. DOI: 10.1103/PhysRevD.95.103515. arXiv: 1612.06469 [astro-ph.CO].

[296] Ludovic Van Waerbeke, F. Bernardeau, and Y. Mellier. "Efficiency of weak lensing surveys to probe cosmological models". In: *Astron. Astrophys.* 342 (1999), pp. 15–33. arXiv: astro-ph/9807007.

[297] Eleonora Villa, Enea Di Dio, and Francesca Lepori. "Lensing convergence in galaxy clustering in LambdaCDM and beyond". In: (2017). arXiv: 1711.07466 [astro-ph.CO].

[298] Zvonimir Vlah, Nora Elisa Chisari, and Fabian Schmidt. "An EFT description of galaxy intrinsic alignments". In: *JCAP* 01 (2020), p. 025. DOI: 10.1088/1475-7516/2020/01/025. arXiv: 1910.08085 [astro-ph.CO].

[299] C. J. Walcher et al. "4MOST Scientific Operations". In: *The Messenger* 175 (Mar. 2019), pp. 12–16. DOI: 10.18727/0722-6691/5118. arXiv: 1903.02465 [astro-ph.IM].

[300] Robert M. Wald. *General Relativity*. Chicago, USA: Chicago University Press, 1984.

[301] Martin J. White. "Baryons and weak lensing power spectra". In: *Astropart. Phys.* 22 (2004), pp. 211–217. DOI: 10.1016/j.astropartphys.2004.06.001. arXiv: astro-ph/0405593.

[302] Hans A. Winther et al. "COLA with scale-dependent growth: applications to screened modified gravity models". In: *JCAP* 1708.08 (2017), p. 006. DOI: 10.1088/1475-7516/2017/08/006. arXiv: 1703.00879 [astro-ph.CO].

[303] Xiaoying Xu et al. "Measuring DA and H at z=0.35 from the SDSS DR7 LRGs using baryon acoustic oscillations". In: *Mon. Not. Roy. Astron. Soc.* 431 (2013), p. 2834. DOI: 10.1093/mnras/stt379. arXiv: 1206.6732 [astro-ph.CO].

[304] Kazuhiro Yamamoto et al. "A Measurement of the quadrupole power spectrum in the clustering of the 2dF QSO Survey". In: *Publ. Astron. Soc. Jap.* 58 (2006), pp. 93–102. DOI: 10.1093/pasj/58.1.93. arXiv: astro-ph/0505115 [astro-ph].

[305] Shengqi Yang and Anthony R. Pullen. "Calibrating magnification bias for the E_G statistic to test general relativity". In: *Mon. Not. Roy. Astron. Soc.* 481 (2018), p. 1441. DOI: 10.1093/mnras/ty2353. arXiv: 1807.05639 [astro-ph.CO].

[306] Ji Yao, Mustapha Ishak, and M.A. Troxel. "Self-calibration method for II and GI types of intrinsic alignments of galaxies". In: *Mon. Not. Roy. Astron. Soc.* 483.1 (2019), pp. 276–288. DOI: 10.1093/mnras/sty3188. arXiv: 1809.07273 [astro-ph.CO].

[307] Ji Yao et al. "Effects of Self-Calibration of Intrinsic Alignment on Cosmological Parameter Constraints from Future Cosmic Shear Surveys". In: *JCAP* 10 (2017), p. 056. DOI: 10.1088/1475-7516/2017/10/056. arXiv: 1707.01072 [astro-ph.CO].

[308] Ji Yao et al. "Separating the Intrinsic Alignment Signal and the Lensing Signal using Self-Calibration in Photo-z Surveys with KiDS450 and KV450 Data". In: (Nov. 2019). arXiv: 1911.01582 [astro-ph.CO].

[309] Jaiyul Yoo. "General Relativistic Description of the Observed Galaxy Power Spectrum: Do We Understand What We Measure?" In: *Phys. Rev.* D82 (2010), p. 083508. DOI: 10.1103/PhysRevD.82.083508. arXiv: 1009.3021 [astro-ph.CO].

[310] Jaiyul Yoo, A. Liam Fitzpatrick, and Matias Zaldarriaga. "A New Perspective on Galaxy Clustering as a Cosmological Probe: General Relativistic Effects". In: *Phys.Rev.* D80 (2009), p. 083514. DOI: 10.1103/PhysRevD.80.083514. arXiv: 0907.0707 [astro-ph.CO].

[311] Jaiyul Yoo and Uroš Seljak. "Wide-Angle Effects in Future Galaxy Surveys". In: *Mon.Not.Roy.Astron.Soc.* 447.2 (2015), pp. 1789–1805. DOI: 10.1093/mnras/stu2491. arXiv: 1308.1093 [astro-ph.CO].

[312] Jaiyul Yoo et al. "Going beyond the Kaiser redshift-space distortion formula: a full general relativistic account of the effects and their detectability in galaxy clustering". In: *Phys.Rev.* D86 (2012), p. 063514. DOI: 10.1103/PhysRevD.86.063514. arXiv: 1206.5809 [astro-ph.CO].

[313] Pengjie Zhang et al. "Probing Gravity at Cosmological Scales by Measurements which Test the Relationship between Gravitational Lensing and Matter Overdensity". In: *Phys. Rev. Lett.* 99 (2007), p. 141302. DOI: 10.1103/PhysRevLett.99.141302. arXiv: 0704.1932 [astro-ph].

[314] Yi Zheng and Yong-Seon Song. "Study on the mapping of dark matter clustering from real space to redshift space". In: *JCAP* 1608.08 (2016), p. 050. DOI: 10.1088/1475-7516/2016/08/050. arXiv: 1603.00101 [astro-ph.CO].

[315] R. Ziour and L. Hui. "Magnification Bias Corrections to Galaxy-Lensing Cross-Correlations". In: *Phys. Rev.* D78 (2008), p. 123517. DOI: 10.1103/PhysRevD.78.123517. arXiv: 0809.3101 [astro-ph].

[316] Jolanta Zjupa, Bjoern Malte Schaefer, and Oliver Hahn. "Intrinsic alignments in the IllustrisTNG simulations and their implications for weak lensing". In: *to be submitted to MNRAS* (May 21, 2018).

[317] F. Zwicky. "Die Rotverschiebung von extragalaktischen Nebeln". In: *Helvetica Physica Acta* 6 (Jan. 1933), pp. 110–127.